Simulating Areal Snowcover Depletion and Snowmelt Runoff in Alpine Terrain

A Thesis submitted to the College of
Graduate Studies and Research
in partial fulfillment of the requirements
for the degree of Doctorate of Philosophy
in the Department of Geography and Planning
(Centre for Hydrology)
University of Saskatchewan
Saskatoon, SK

by

Chris M. DeBeer

May 2012

PERMISSION TO USE

In presenting this thesis in partial fulfilment of the requirements for a Postgraduate degree from the University of Saskatchewan, I agree that the Libraries of this University may make it freely available for inspection. I further agree that permission for copying of this thesis in any manner, in whole or in part, for scholarly purposes may be granted by the professor or professors who supervised my thesis work or, in their absence, by the Head of the Department or the Dean of the College in which my thesis work was done. It is understood that any copying or publication or use of this thesis or parts thereof for financial gain shall not be allowed without my written permission. It is also understood that due recognition shall be given to me and to the University of Saskatchewan in any scholarly use which may be made of any material in my thesis.

Requests for permission to copy or to make other use of material in this thesis in whole or part should be addressed to:

Head of the Department of Geography and Planning
University of Saskatchewan
117 Science Place
Saskatoon, Saskatchewan
S7N 5C8

ABSTRACT

An overwhelming proportion of the flow of some of the major rivers in the western Canadian Prairies (e.g., the South Saskatchewan River) is derived from runoff in the headwaters of the Rocky Mountains, where snowmelt represents the greatest single contribution. Increasing concerns over future regional water resource stresses require better understanding and prediction of some alpine snow hydrology components, which are currently limited due to the large spatial heterogeneity of snow accumulation and melt processes, and problems with the scaling of these processes in hydrological models. The work presented in this thesis was aimed at improving the representation and effects of this variability on simulated areal snowcover depletion (SCD) and snowmelt runoff generation at different spatial scales in alpine environments. To accomplish this, a focused field data collection campaign was carried out at a small (1.2 km^2) alpine cirque basin within the Marmot Creek Research Basin in the Front Ranges of the Canadian Rockies in the Kananaskis Valley, Alberta. Measurements here included detailed hydro-meteorological observations, snowcover (spatially distributed snow surveys, LiDAR-derived snowcover mapping, and daily acquisition of terrestrial-based photography of the alpine landscape for spatial–temporal snowcover mapping), and streamflow measurement at the alpine basin outlet. A theoretical framework was developed to upscale physically based point-scale snowmelt simulations for the prediction of areal SCD and meltwater generation, and was based on the lognormal probability distribution for values of snow water equivalent (SWE). The framework was applied and tested using a point-scale snowmelt model (Snobal) developed within the Cold Regions Hydrological Model (CRHM) platform. Finally, a conceptual/process-based hydrological model was developed for this basin using CRHM, and the spatial snowmelt framework was used together with this model to simulate the streamflow hydrograph at the outlet of the basin.

This work has led to a number of important findings that advance the state of understanding of alpine snow hydrology, and provide useful tools for prediction outside of well-studied research basins. First, it was shown how the spatial and temporal variability in both pre-melt snowcover and snowmelt energetics control the evolution of

the alpine snowcovered area (SCA) during the spring, which is an important variable for both hydrological and climatological applications. Daily terrestrial photographs were re-projected orthogonally over the landscape, and comparison of model predictions of areal SCD with observations from this imagery showed that improvements resulted from considering separate SWE distributions and applied energy to the snowcover on different slope-based landscape units in the basin, relative to using a single, basin-wide distribution with uniform applied energy. It was further shown that at certain times, such as early in spring, the effects of differential warming, ripening, and melt of different initial classes of SWE within a single landscape unit cause an "acceleration" of areal SCD due to the earlier and more rapid melt of areas with a relatively shallow snowpack, and that models that do not properly account for this effect may be in error. This is a feature that is common to all "cold" snowcovers, yet currently this can only be represented by fully distributed simulations applied at a fine spatial scale (i.e., 10 – 25 m), and where difficulties arise in establishing initial snowcover patterns outside of well-studied basins. However, the framework developed here provides a useful approach for resolving all major sources of SWE and melt rate variability, while retaining spatial and computational simplicity, and physical integrity. This is done by making explicit snowmelt computations for different initial classes of SWE (with unique mass and energy states) on different slope-based landscape units; the framework only requires values of $\overline{\text{SWE}}$ (i.e., mean SWE) and CV (coefficient of variation) to establish initial snowcover conditions in a model. Thus, it can easily be applied in other basins by using "representative" landscape-based CV values.

Lastly, the work provided insight on how the variability in both pre-melt snowcover and meltwater inputs over the basin influence the snowmelt hydrograph at the basin outlet. Through a comparison of different approaches for representing snowcover, snowmelt, and lower basin forest canopy effects, it was shown that the best correspondence with observed hydrographs was achieved when explicitly accounting for the differential timing, location, and extent of source areas for snowmelt runoff. However, in many other cases realistic appearing hydrographs were obtained, but for the wrong reasons due to cancellation of model errors. The approach here maintains internal "correctness" of the alpine snow components, which is beneficial towards development

and parameterization of other process components in hydrological models applied elsewhere in alpine landscapes. The results also showed that the effects of differential melt timing and rate over different SWE classes within a single landscape unit (i.e., inhomogeneous melt) did not become manifested in the overall hydrograph response, despite having an important influence on areal SCD. Thus, if the primary goal of model application is to predict the hydrograph only, then this effect can likely be neglected without serious errors.

ACKNOWLEDGEMENTS

First, I would like to thank my supervisor, Professor John Pomeroy for his guidance and support throughout all stages of my graduate studies at the University of Saskatchewan. It has been a rewarding experience to work with him and I am grateful for his continued commitment to my scientific career. I would also like to thank the students and staff of the Centre for Hydrology for their contributions in many different aspects of this thesis work and my graduate studies. In particular, I am very grateful to Kevin Shook, Joni Onclin, Chad Ellis, Matt MacDonald, Jimmy MacDonald, Chris Marsh, May Guan, Logan Fang, Brad Williams, Erin Shaw, and Kim Janzen. I am especially grateful to Michael Solohub and Tom Brown for help with the field instrumentation/data collection and CRHM model development, respectively. I thank Anne Sabourin and Pascal Hagenmuller (Ècole Polytechnique, France), Richard Essery (U. Edinburgh) and Greg Langston (U. Calgary) for help with field data collection at Marmot Creek, and Javier Corripio (U. Innsbruck) for help with instruction for the camera setup and terrestrial image processing. My academic committee, consisting of Professors Cherie Westbrook and Xulin Guo, and Dr. Al Pietroniro, provided valuable feedback and advice, and all had an important role in my graduate training that I am grateful for. My external examiner, Professor Jessica Lundquist (U. Washington), provided helpful feedback and suggestions on this thesis, for which I thank her. I also thank Chris Hopkinson (AGRG, Nova Scotia) and C-CLEAR for processed LiDAR data over Marmot Creek. Finally, I wish to thank my family, my parents Andy and Jean, and particularly my partner Sheri Korpess, who supported me during this time, and without whom I could not have reached this stage.

Funding for this work was provided by the Canadian Foundation for Climate and Atmospheric Sciences (CFCAS) through support of the IP3 Research Network, the Canada Research Chairs Programme, the University of Calgary Biogeoscience Institute (BGSI), and the Natural Sciences and Engineering Research Council (NSERC). The Nakiska Ski Resort and the University of Calgary BGSI kindly provided logistical support for the field work. I am also very grateful to the University of Saskatchewan and to NSERC for a Dean's Scholarship and an Alexander Graham Bell CGS-D Scholarship, which supported me during my graduate programme at this University.

For Chandler and Rylan, and for Sheri

Who inspired and motivated me, and helped me achieve this goal

TABLE OF CONTENTS

LIST OF FIGURES

LIST OF TABLES

LIST OF SYMBOLS AND ABBREVIATIONS

Symbols

A	Slope azimuth (degrees clockwise from north)
C	Environment coefficient
C_p	Specific heat (kJ/kg·°C)
C_s	Coefficient of skew
D_{100}	Mean snowcover depth at transition from incomplete to complete snowcover
D_m	Modelled depth
d_o	Observed depth
d_s	Depth of snow (cm)
e	Base of natural logarithm
E	Mass flux of evaporation
$f()$	Probability distribution of variable in parentheses
H	Hour angle of sun; Sensible heat flux (W/m^2)
h	Canopy height (m)
h_f	Latent heat of fusion (334 kJ/kg)
I	Inflow
K	Frequency factor
K^*	Net shortwave radiation flux (W/m^2)
K_{min}	K value corresponding to SWE = 0
K_s	Linear storage constant (days)
K_y	Frequency factor of log transformed values
L	Monin–Obukhov stability length (m)
L^*	Net longwave flux (W/m^2)
$L\uparrow$	Outgoing longwave radiation flux (W/m^2)
$L\downarrow$	Incoming longwave radiation flux (W/m^2)
L_0	Observation longwave radiation (W/m^2)
L_v	Latent heat of vaporization (2.501×10^6 J/kg)
m	Optical air mass
m_a	Accumulated snowmelt
$max_{z,s0}$	Maximum active layer thickness of snowpack
m_r	Snowmelt rate (mm/d)
n	Number of observations or bins
O	Outflow
P	Probability (cumulative)
p	Mean zenith path transmissivity
$P()$	Exceedence probability of variable in parentheses
Q_{dir}	Direct beam component of solar radiation
Q_E	Latent heat flux (W/m^2)
Q_G	Ground heat flux (W/m^2)
Q_H	Sensible heat flux (W/m^2)
Q_{li}	Incoming longwave radiation (W/m^2)

$Q_{\ln}$	Net longwave radiation (W/m^2)
Q_m	Energy available for melting snow (W/m^2)
Q_{net}	Net all-wave radiation flux (W/m^2)
Q_P	Energy added to the snowpack by precipitation (W/m^2)
Q_{si}	Incident shortwave radiation (W/m^2)
r	Rank of observation
R^2	Coefficient of determination
r_a	Average radius of visible horizon on hemispheric photograph or image
R_a	Radius of hemispherical photograph
R_f	Redistribution factor
S	Storage
S_0	Surface saturation
S_f	New snowfall amount (mm)
S_{I}	Average soil saturation in upper 0.4 m soil layer
$S_{\min,\alpha}$	Minimum snowfall to refresh albedo
T	Snowpack temperature (°C or K)
t_0	Infiltration opportunity time (h)
T_f	Temperature of forest canopy elements (K)
$T_{s,0}$	Snow surface temperature (K)
U	Internal energy of the snowpack (kJ/m^2); wind speed (m/s)
u^*	Friction velocity (m/s)
w_c	Liquid water content of snow
$w_{c,\ \max}$	Maximum liquid water holding capacity
x	Fetch distance
y	Natural logarithm of SWE values
$\bar{y}$	Mean of logarithmic values of SWE
Z	Zenith angle (degrees)
z_0	Snow surface roughness height (m)

Greek Symbols

α	Snow albedo; slope of line segment; shape parameter for Gamma distribution
$\alpha_{\max}$	Maximum snow albedo following new snowfall events
$\alpha_{\min}$	Minimum snow albedo for exponential decay
β	Thermal quality or fraction of ice in unit mass of snow; Scale parameter for Gamma distribution
$\Gamma(\alpha)$	Gamma function
δ	Solar declination
Δt	Timestep length
ε_f	Emissivity of forest canopy elements
ε_s	Snow Emissivity or surface emissivity
θ	Latitude; Solar angle above horizon
ρ_{s}	Snow density (kg/m^3)
σ	Stefan-Boltzman constant (5.67×10^{-8} W/m^2·K^4)
σ_y	Standard deviation of logarithmic values of SWE

τ	Time constant applied to melting snow; forest transmittance
υ	Canopy sky view factor
υ_{eff}	Effective terrain view factor

Abbreviations

ADC	Areal Distribution Curve
CRHM	Cold Regions Hydrological Model
CV	Coefficient of Variation
DEM	Digital Elevation Model
ENSO	El Niño/Southern Oscillation
GIS	Geographic Information Systems
GPS	Global Positioning System
GRU	Grouped Response Unit
HRU	Hydrological Response Unit
LAI	Leaf Area Index
LAI′	Effective Leaf Area Index
LiDAR	Light Detection And Ranging
MB	Model Bias
MCRB	Marmot Creek Research Basin
MGA	Meltwater Generating Area
NS	Nash–Sutcliffe model efficiency coefficient
PBSM	Prairie Blowing Snow Model
PDO	Pacific Decadal Oscillation
REA	Representative Elementary Area
RH	Relative Humidity
RMSE	Root Mean Squared Error
SCA	Snowcovered Area
SCD	Snowcover Depletion
Snobal	Snowmelt Energy Balance Model
SWE	Snow Water Equivalent
$\overline{\text{SWE}}$	Mean SWE
WSC	Water Survey of Canada

1. INTRODUCTION

1.1 Background

Many of the major rivers that flow through the western prairie region of North America originate in the Rocky Mountains, and this relatively small headwater region contributes a disproportionately large fraction of their total flow volume (Comeau, 2009). Here, snowmelt runoff during the spring represents the primary source of streamflow (Hauer et al., 1997; Stewart et al., 2004). In the Canadian Rockies, for example, the Bow River at the town of Banff discharges an average of ~55% of its total annual runoff during the months of May through July (Water Survey of Canada, 2010). The average flow rate for this three month period is nearly 2.5 times the average annual rate, and nearly 9.5 times the mean low flow. Snowmelt and runoff typically begin in March and April at lower elevations and peak in May and June, when deeper snowpacks at higher elevations in the headwaters are melting (Woo and Thorne, 2006). During this period, mountain streams are fed by surface runoff, outflow from saturated soils, and snowmelt water moving rapidly through unconsolidated till and talus (Liu et al., 2004; McClymont et al., 2010). A recession to baseflow occurs in snowmelt dominated basins through July and August as remaining isolated snow patches at higher elevations melt and disappear. Snowmelt during the spring also provides a major source of recharge for groundwater aquifers (Clow et al., 2003; Hood et al., 2006), which sustain streamflow throughout the year, as well as over longer time scales (Rademacher et al., 2005).

Because most of the flow is due to snowmelt runoff, the hydrological regime of these mountain streams is highly sensitive to climatic change (Barnett et al., 2005). Within temperate mid-latitude alpine basins, snowpack temperature generally remains near the melting point and is therefore sensitive to even minor changes in air temperature (Beniston, 2003). Increasing cold season temperatures could lead to more frequent mid-winter snowmelt events and a shift in the timing of the primary snowmelt period to earlier times in the spring (Stewart et al., 2004). Warmer air temperatures also lead to a greater fraction of the winter and spring precipitation falling as rain rather than snow, and thus

reduce snow accumulation and snowpack volume. In the absence of changes in the total precipitation, this would result in higher winter and early spring runoff rates and diminish the late spring and summer season flows. Changes in winter and spring precipitation may significantly complicate the response in runoff, however, depending on how these changes are manifested (Stewart, 2009). Climate models generally suggest an increase in both mean winter precipitation and precipitation variability for western North America (Giorgi and Bi, 2005; Solomon et al., 2007). Greater snowfall could potentially dampen the effects of modest warming, while increased winter and spring precipitation with a greater mix of rain and snow, coupled with changes in the snowmelt regime, could lead to an increased risk of flooding. Furthermore, an increase in the inter-annual variability of precipitation decreases the reliability of mountain snowpacks, and reduced snowpack volume could, in some years, lead to critical water shortages in downstream areas. Many studies have investigated the response of mountain hydrological regimes to climatic variability and found that these changes have already been occurring to some degree over the last several decades (e.g., Cayan et al., 2001; Mote et al., 2005; Hamlet et al., 2007; Moore et al., 2007; Stewart et al., 2005; Barnett et al., 2008; Stewart, 2009).

For these reasons there is increasing concern over the effects of ongoing and future climate change in the mountain regions of western North America. Many of the downstream areas are highly populated and depend on the flow from these rivers for municipal, agricultural, and industrial supply, while continuing economic development and population growth place additional pressure on regional water resources. In some semi-arid and arid regions, these resources are already under stress and the potential for future conflict between water users and jurisdictions is high. For example, east of the Rocky Mountains in south-western Alberta, new water license allocations are no longer available in the Bow and Oldman River basins, while demand from various sectors is expected to grow markedly in coming decades (Sauchyn and Kulshrestha, 2008). Thus, long term water management and policy in such areas require better predictive tools and understanding of the processes of snow accumulation, snowmelt, and runoff in the mountains, as well as the hydrologic impacts of climate variability that might be expected in the future (e.g., Viviroli et al., 2011).

1.1.1 Difficulties in Spatial Modelling of Alpine Snowmelt

Understanding of snow processes in alpine areas is limited at the present time, and complicated by a number of factors that make it difficult to accurately predict how the hydrology of mountain basins will respond to climatic variation. This variation in western North America is influenced by superimposed natural modes of variability such as El Niño/Southern Oscillation (ENSO) and Pacific Decadal Oscillation (PDO), which can perturb the mean precipitation conditions on various time scales ranging from individual seasons to decades (Moore, 1996; Moore and McKendry, 1996). Geographic setting exerts a strong influence on climate and hydrology, as regional climate patterns exhibit sharp gradients, and local conditions are influenced considerably by surrounding topography (Barry, 2008). Thus, it is difficult to project the changes in temperature and precipitation regime in different localities and over different elevation ranges, yet such projections are important as the spatial distribution of these changes will have a significant impact on changes in mountain snowcover dynamics and hydrology. These problems are exacerbated by the sparse network of climate monitoring stations and lack of instrumental records at high elevations in areas such as the southern Canadian Rockies. For example, the Meteorological Service of Canada has only one long term operational weather station above tree-line in this region, which is vastly less than other mountain areas such as the Swiss Alps.

In addition to these uncertainties, predictions of the hydrological response of mountain watersheds are hindered by limitations in understanding of alpine snow processes, as well as their representation in most hydrological models (Bales et al., 2006; Pomeroy et al., 2009a). In above tree line alpine environments, snow accumulation, redistribution, melt, and runoff are significantly affected by variations and complexities in the terrain. The combined influence of elevation, slope, aspect, topographic shelter, and shrub vegetation structure give rise to complex patterns of both snowcover development throughout the winter and surface energetics during melt (Elder et al., 1991; Blöschl and Kirnbauer, 1992; Winstral et al., 2002; Anderton et al., 2004; Lehning et al., 2011). These processes are therefore often more difficult to parameterize for numerical models in alpine terrain than in low relief areas. Topographic depressions, areas of

exposed alpine shrubs and vegetation, and leeward slopes tend to accumulate snow drifts up to several metres or more in depth over the winter, while adjacent and more exposed terrain is scoured by wind and may accumulate little or no snow (Pomeroy, 1991; Mott et al., 2010). As the snow melts, this heterogeneity, together with spatial variability in applied melt energetics, leads to the development of a patchy snowcover with intermittent areas of exposed vegetation and bare rock and soil. Local advection of sensible heat from snow-free areas and increased net radiation and/or sensible heat exchange to the snowpack from exposed vegetation complicate the energy balance and potentially introduce feedbacks that enhance melt (Liston, 1995; Marsh et al., 1997; Shook and Gray, 1997a; Essery, 1999; Grünewald et al., 2010; Mott et al., 2011a). Together with variations in radiation and wind speed with topography, these effects produce a highly variable pattern of melt energy over the landscape. The combined variability in accumulation and ablation processes is important hydrologically as it controls the spatial–temporal patterns of areal snowcover depletion (SCD) and the meltwater generating area (MGA) over the landscape. This affects the location, as well as the timing, rate, and magnitude of meltwater input to the land surface and snowmelt runoff.

Problems exist in terms of the representation of this variability and the spatial scaling of snow processes over complex alpine terrain. The variation in these processes and the dominant factors controlling their spatial patterns are strongly dependent on scale (Blöschl, 1999; Deems et al., 2006; Mott et al., 2011b), as well as location in the landscape. Such scale effects are poorly understood in mountain environments, but have significant implications for hydrological modelling (Cline et al., 1998). As model scales are changed, for example, and processes such as snow accumulation and ablation are considered over larger areas, the non-linear nature of complex process interactions may lead to large errors in model representation of areal SCD and snowmelt runoff generation. Since the processes do not aggregate linearly, it cannot be assumed that $E(f(x)) = f(E(x))$, where E is the mathematical expectation (i.e., mean), x is location, and f is a function or variable (Blöschl, 1999). For these reasons it is important to represent the processes in a manner that is consistent with the natural underlying variability, and avoid inappropriate spatial averaging of model inputs, variables, and state conditions (Seyfried and Wilcox, 1995).

Much of the variability in the processes affecting areal SCD and snowmelt runoff generation in alpine terrain occurs over very small spatial scales. An approach to dealing with these problems is to explicitly model the spatial and temporal variability in snow processes at fine scales using fully distributed models (e.g., Marks et al., 1999; Lehning et al., 2006). These models may be run at scales as small as several metres and hence account for detailed variations in snow accumulation and melt over the landscape. Application of these models provides useful insight on the hydrological behaviour and response of small, intensively studied research basins, but this level of detail requires considerable spatial information on model parameters, initial conditions, forcing data, and calibration and validation data. Difficulties are frequently encountered in realistically representing the patterns and areal variations in the wind speed/direction, temperature, and humidity fields over complex terrain. For these reasons as well as the computational demands, the approach is not yet, and likely may never be suitable for regional scale applications.

Rather, most hydrological models and land surface schemes are applied at larger spatial scales, and to account for the smaller scale variability they incorporate some type of sub-grid parameterization of the processes and the areal snowcover state. However, such representations are generally poor as the physics of the processes are often not realistically described (e.g., Pomeroy et al., 1998), while the inherent assumptions may be violated at even small spatial scales in sharp alpine terrain. For example, sub-grid snowcover heterogeneities and areal SCD are often represented assuming spatially uniform melt rates over the model domain or computational grid cell area, and a single, unimodal frequency distribution of snow water equivalent (SWE) depth over the landscape (e.g., Donald et al., 1995; Liston, 1999, 2004; Luce et al., 1999; Luce and Tarboton, 2004; Egli et al., 2011). No model includes representation at the sub-grid level of the small scale differences in warming and ripening, overnight cooling and refreezing, and the associated effects on melt rates and timing, areal SCD, and snowmelt runoff over a heterogeneous snowcover, although this has been shown to be highly important in many environments (Gray and O'Neil, 1974; Male and Gray, 1975; Marsh and Pomeroy, 1996; Fierz et al., 1997, 2003). Thus, the current state of development of these models is limited, and their applicability at large scales in complex alpine environments is

questionable due to the substantial variability in the seasonal snowcover development, snowmelt energetics, and melt.

Spatial associations between accumulation and ablation processes may also arise at various scales due to the common underlying factors that influence them (e.g., topography, vegetation, etc., [Faria et al., 2000; Pomeroy et al., 2003]). A stochastic approach to handle the joint variability and covariance of both SWE and snowmelt may be applied (Essery and Pomeroy, 2004b), but such an approach may be intractable and lack an analytical solution in mountainous environments. Here, the frequency distributions of these variables and their statistical association are not constant over time due to the considerable spatial–temporal variations in melt energetics and frequent snowfall events during the late winter and spring.

It is likely that hydrological modelling applications dealing with snow processes in alpine terrain can be applied at intermediate spatial scales and objectively chosen landscape units for computation. This can avoid some of the limitations of fully distributed representations, whilst at the same time utilizing a means of landscape stratification that conforms to the natural scales and location of the terrain, the snow processes, and their variability, rather than an arbitrarily selected model grid (e.g., Dornes et al., 2008a, 2008b). By properly accounting for the variability (i.e., both stochastic and deterministic components), scale dependence, and interaction of snow accumulation and ablation processes, physically-based point-scale models may be effectively upscaled and applied over larger areas. An improved understanding of the nature of the processes and their variability over the landscape is therefore needed to determine how to best represent the effects of landscape heterogeneity and identify an appropriate means of terrain stratification for modelling. This is necessary in order to conduct a proper and rigorous assessment of the potential response of streams and rivers in the Rocky Mountains to various future climate scenarios.

1.2 Thesis Objectives

The purpose of this thesis is to address some of the issues stated above and improve the understanding of the nature and variability of processes related to areal SCD and

snowmelt runoff in alpine terrain. The investigation here focuses specifically on the scale dependence of the variability and association between late winter SWE and spring ablation rates, as well as the representation of this variability in modelling applications. A key premise is that snow processes in complex alpine terrain are not always conservative (i.e., simple arithmetic averaging cannot always be applied to upscale process representation), and that different physical factors control the spatial patterns of these processes at different locations, scales, and times. In this context, this research will help to reveal how model representations of areal SCD and snowmelt runoff generation may be subject to error when applied at large scales without properly accounting for variability in the relevant processes and the non-linear spatial scaling effects. The specific objectives of this research are as follows:

1. Develop a theoretical framework for examining the influence of spatial variability of snow accumulation and ablation, and covariance between these variables, on areal snowmelt and SCD at differing scales over mountainous terrain;
2. Determine how the variability and covariance of snow accumulation and melt processes affect the generation of snowmelt runoff;
3. Develop and test a spatial snowmelt parameterization over an alpine basin using distributed observations of snow accumulation, snowmelt timing, rate, and duration, and areal SCD; and
4. Incorporate the new theoretical framework within a simple hydrological model to represent this basin, and use it to examine the influence of different spatial snowcover and snowmelt representations on the basin hydrograph.

The fulfillment of these objectives will help to identify key sources and effects of non-linearity in spatial snow hydrology modelling over mountainous terrain. It is anticipated that the findings of this research will lead to suggestions for improvements in the representation of mountain SCD in regional scale hydrological models and land surface schemes. In particular, a major new contribution of this thesis to alpine snow hydrology will be the development of a new theoretical approach for dealing with the effects of sub-grid variability in snowmelt rates and timing due to non-uniform warming and ripening of cold and highly redistributed snowcovers. This has not been previously considered for

any upscaled model parameterization of areal SCD or snowmelt runoff, although it is likely of importance in alpine regions such as the Canadian Rocky Mountains.

1.3 Scope and Organization of Thesis

The work presented in this thesis describes theoretical developments and the application of a new spatial snowmelt parameterization towards simulating areal SCD and meltwater runoff generation in an alpine environment. The approach is meant to be applied over sparsely vegetated alpine terrain with moderate to steep slopes and/or sharp arêtes; the inherent assumptions may not hold for sub-alpine forested areas or highly complex and incised terrain characterized by extensive cliffs. The snowmelt and SCD parameterization developed here is not intended to be applied over alpine glacier surfaces, although it could theoretically be extended to include some glacierized areas. However, this is beyond the scope of this thesis and is not further considered here. This thesis deals primarily with the snowcover processes occurring in the late winter and spring melt period, and does not explicitly address the over-winter development of spatial snowcover patterns due to blowing snow redistribution. It is noted that some of the work presented in this thesis has been previously published by DeBeer and Pomeroy (2009, 2010).

The thesis is organized into eight major sections. Section Two of this thesis presents a review of the theory and recent literature dealing with the accumulation and distribution of seasonal snowcovers, the snowpack energy balance and snowmelt modelling, and areal SCD and meltwater runoff generation in various environments. Section Three develops the theoretical framework for handling spatial variability of both snowmelt and SWE (for prediction of areal SCD and snowmelt runoff) in alpine terrain, and discusses various considerations and implications of the framework. Section Four describes the study site for this research in the Canadian Rocky Mountains and its physical/climatological characteristics, along with the data collection and monitoring programme that was carried out here to obtain the necessary data to apply and test the theoretical framework. A point-scale snowmelt model that was used to simulate melt rates is presented in Section Five. The parameterization and validation of the model is described here, and analysis of the variability of melt rates at the point-scale is presented.

In Section Six, the spatial snowmelt framework is applied to the test basin using the previously described model to examine the effects of spatial variability of snowmelt and SWE at different spatial scales and locations on areal SCD, the meltwater generating area (MGA), and overall meltwater production. Section Seven describes how this framework has been incorporated within a hydrological model for the purpose of simulating basin scale runoff and the snowmelt hydrograph, and tests the model. A number of different approaches to representing the variability in snowmelt over the basin are compared here in order to gain insight on how the overall streamflow response is influenced by such variability. Finally, Section Eight presents a synthesis of the findings in this research, and considers future research directions for alpine snow hydrology and modelling.

2. Review of Theory and Literature

2.1 Formation and Distribution of Seasonal Snowcovers

A seasonal snowpack typically develops over the winter period in cold regions through the accumulation of multiple snowfall events, which are subsequently modified through the action of wind, metamorphism, and melt/refreezing at the surface and within the pack. Thus, seasonal snowpacks are characterized by a distinctive layered structure with a highly varied stratification depending on factors such as the type of snow deposited and the meteorological conditions during and between snowfall events (Male, 1980). The spatial distribution of snowpack properties and structure also varies considerably over a range of different scales. Over large regions (100s to 1000s of kilometres) this is due to latitude, synoptic scale meteorology, distance from moisture sources, orography, etc. At intermediate and local scales (100s to 1000s of metres) differences in deposition, redistribution, and accumulation are related to meso-scale terrain features, physiography, and vegetation type, density, extent, etc. Surface roughness and small scale variations in vegetation influence the micro-scale (up to 10s of metres) patterns of snowpack variability, mainly through redistribution and transport phenomena. There has been a great deal of work to investigate characteristics of seasonal snowcovers, including their formation, measurement, and areal distribution. In this section some of the relevant work and recent studies dealing with this topic are reviewed.

2.1.1 Snow Deposition and Measurement

The amount of snowfall and the accumulation of the snowpack are important hydrological and climatological variables. Measurements are routinely made at principal climate stations as part of the meteorological observation programs in many cold regions countries (Brown and Goodison, 2005), and generally focus on the depth and snow water equivalent (SWE), which is the equivalent depth of water if the snow were melted. Together with the density of the snowpack, these are some of the most important physical

properties of the snowcover (Pomeroy and Gray, 1995). These properties are interrelated through the expression:

$$\text{SWE(mm)} = 0.01(d_s \cdot \rho_s), \tag{2.1}$$

where d_s is the depth of snow (cm) and ρ_s is the snow density (kg/m^3). This expression holds due to the fact that 1 mm of SWE spread over an area of 1 m^2 weighs 1 kg. Typical rates of snowfall are on the order of 1 cm/h of depth or 0.8 mm/h of SWE, but vary widely with the types of storms producing the snowfall (Jordan et al., 2008).

There are numerous approaches to measuring snow and designing observation strategies, and many of the *in situ* methods are reviewed by Goodison et al. (1981), Doekson and Judson (1997), and Pomeroy and Gray (2005). Standard approaches at a point include manual depth measurements with a snow probe or ultrasonic sensor; density measurements using microwave radar, gamma ray attenuation, or a snow pit and gravimetric sampling; and SWE measurements using a snow pillow. The operation of snowfall gauges is complicated by the fact that gauge measurements are strongly affected by wind due to the movement of turbulent eddies around the orifice of the gauge. Snowfall gauges are therefore generally shielded from wind exposure to reduce snow undercatch, but problems remain with even some of the better shields such as the Nipher or Tretyakov (Goodison, 1978; Pomeroy and Goodison, 1997). These gauges require regular maintenance to ensure their proper operation, which means they must be located at accessible sites. Other problems and sources of error in snowfall and ground snowpack measurements arise, and are related to blowing and drifting snow, melting or rapid settling of the snow on the ground, representativeness of the measurement site, and highly variable densities of freshly fallen snow (Doekson and Judson, 1997; Pomeroy and Goodison, 1997).

The density of freshly fallen snow varies widely, ranging from 20 to over 300 kg/m^3, depending on wind speed, snow type, and other meteorological factors during deposition. Higher densities occur for warm, wet snow, while lower densities are characteristic of snow falling in cold and dry conditions. The U.S. Army Corps of Engineers (1956) reported that the density of freshly fallen snow decreases exponentially as air temperature declines below freezing. Wind also has a significant effect on new snow density. Snow crystals falling and being redistributed in strong winds are

fragmented and tend to more be densely packed (Jordan et al., 1999). In general, densities of fresh snow vary between 50 and 120 kg/m^3 for dry snow falling in low to moderate winds (Jordan et al., 2008). Goodison et al. (1981) reported values of 70 to 165 kg/m^3 as typical values for fresh snow density in Canada, and an average density for new snowfall of 100 kg/m^3 is often assumed (Pomeroy and Gray, 1995).

After deposition on the ground surface or on a previous snow layer, the accumulated snow forms a new layer. The individual snow crystals are rapidly transformed through metamorphism into a matrix of ice grains with interconnected pores filled with humid air, and characterized by a relatively high porosity (i.e., volume ratio between solid and fluid components) (Male, 1980; Jordan et al., 2008). The snow particles continue to change their size, shape, and bonding, and the new snow layer rapidly evolves in texture and structure (Colbeck, 1987). Thus, shortly after being deposited, the new snow layer bears little resemblance to the original snow crystals that it formed from. For dry snow with a temperature below 0 °C, two primary mechanisms have been identified in controlling metamorphism within the pack: equitemperature and temperature gradient metamorphism (Sommerfeld and LaChapelle, 1970). Different physical processes are important under each of these idealized conditions. Generally, the movement of molecules through the vapour phase is the dominant process, acting either across or between individual grains (equitemperature), or between different parts of the snowpack (temperature gradient) (Langham, 1981).

Snowpacks also undergo rapid changes after deposition due to the strain and compaction under the pressure of overlying layers of snow, as well as wind compaction. Sturm and Holmgren (1998) examined differences in the densities and compaction rates of snow, and suggested that differences in compaction behaviour arise primarily from climatically controlled differences in the character of the snow. Therefore, snow grain, bond, and stratigraphic characteristics develop reliably in a given climate region from one winter to the next, and should give rise to characteristic time–density curves. Several authors have examined the rates of snow density increase in different regions within Canada and under various meteorological conditions, reporting rates of increase of 7 – 9 kg/m^3 per hour (Gray et al., 1970; Goodison et al., 1981). Gray and Prowse (1993) report various curves for describing the increase of mean snow density in different

environments. Density changes as a result of wind packing and settlement have been noted to exhibit dramatic and episodic increases (Pomeroy et al., 1998).

2.1.2 Snow Redistribution

During and after snowfall events, wind transport and sublimation, interception by vegetation canopies, and in steep terrain, avalanches, act to redistribute the snow and often lead to the development of a highly heterogeneous snowpack distribution over the landscape. These processes are important for the formation of seasonal snowcovers, and vary widely in different environments and under different physiographic and meteorological conditions (McKay and Gray, 1981). In open and exposed regions, such as alpine terrain, prairies or steppes, tundra, and ice sheets, blowing snow processes are important and may redistribute or remove a significant proportion of the total annual snowfall (Dyunin, 1967; Tabler, 1975; Mott et al., 2010). Interception and unloading are important within forested environments, where a considerable fraction of the cumulative snowfall can be stored and lost to sublimation (Pomeroy and Gray, 1995; Hardy et al., 1997). Understanding of these processes is important to snow hydrology since they have a large effect on the distribution of meltwater generation and runoff in spring.

Many processes are involved in the redistribution of snow by wind. The transport process is initiated when the shear force of the wind exceeds the inter-particle cohesive forces and particle weights, which oppose motion (Kind, 1981). The surface shear strength of the snow depends on the conditions of the snowcover such as degree of metamorphism, bonding of ice crystals, wetness, surface hardness, and wind packing. Threshold wind speeds for snow transport are higher for wet, icy, or aged snow than for fresh, dry snow, and reach a minimum at temperatures near –25 °C (Li and Pomeroy, 1997a). Wind shear stress is greater in areas where the wind converges and accelerates, such as the crest of a ridge or around surface obstacles, and thus erosion of any deposited snow prevails at these locations and limits snowcover development.

The overall transport of blowing snow is greatest over extensive open areas, free of obstructions to the airflow (Miller, 1976). At the same time, the mass flux over wind-scoured terrain can be considerably less than that over a complete snowcover (Pomeroy,

1991). Three major modes of transport are commonly recognized: turbulent diffusion (i.e., suspension), saltation, and creep (Pomeroy and Gray, 1995; Lehning et al., 2008). A considerable amount of research has been done to investigate various aspects of these transport mechanisms, and studies have shown that snow saltation and suspension are the dominant processes, and that transport rates can be described by relationships with wind speed (e.g., Dyunin, 1959; Budd et al., 1966; Budd, 1966; Schmidt, 1986; Pomeroy, 1989; Pomeroy and Gray, 1990; Tabler et al., 1990). Saltation occurs within the lowest few centimetres above the surface, and involves the motion of snow particles by skipping or jumping. Saltating snow is the source of suspended snow, which moves by turbulent diffusion at approximately the same velocity as the mean horizontal wind. These particles are held in suspension when vertical velocity components in the air flow are approximately equal to or greater than the terminal fall velocity of the snow particles (Kind, 1981).

Sublimation of blowing snow particles occurs during transport and can return a significant portion of the mass back to the atmosphere as water vapour. High rates of sublimation of blowing snow, in comparison to a stationary surface snowcover, are due to the much higher exposure and ventilation, and higher ratio of surface area to mass for a particle removed from the pack (Pomeroy and Brun, 2001). Much of the theory of this process has been described by Dyunin (1959), Schmidt (1972), Male (1980), Pomeroy (1988), and Pomeroy et al. (1993). Some recent work has focused on the importance of snow sublimation in alpine areas, and shown that losses due to sublimation of snow in transport are significant and highly variable over the landscape (Strasser et al., 2008; Groot Zwaaftink and Lehning, 2010; MacDonald et al., 2010). MacDonald et al. (2010) reported that modelled blowing snow sublimation loss amounted to 17 – 19% of cumulative snowfall over an alpine ridge in the Front Ranges of the Canadian Rocky Mountain, but noted this is likely a conservative estimate because the study transect was situated in an area of relatively moderate topography without air-flow separation. Work by Groot Zwaaftink and Lehning (2010) in the Swiss Alps showed that implementation of sublimation into the snow-transport model of Alpine 3D (Lehning et al., 2006) correctly reproduced local snow depths, which were considerably overestimated if sublimation was neglected. Pomeroy (1991) concluded that the decay of blowing snow mass in high-

wind-speed alpine environments is largely due to vertical transport of snow out of the surface boundary layer, where it sublimates before settling back to the surface. Strasser et al. (2008) reported local blowing snow sublimation losses in a mountainous region in southeast Germany ranging from 10 to 20% of winter snowfall in large valley areas, up to 90% at the highest mountain crests.

Snow deposition occurs and drifts form in locations where the air-flow diverges and the wind slows, thereby reducing the shear stress (Kind, 1981). Variations in surface topography and terrain features have a major effect on the boundary-layer flow, and therefore exert a large influence on deposition of snow and preferential locations of drifts over the landscape (Winstral and Marks, 2002; Dadic et al., 2010; Mott et al., 2010). McKay and Gray (1981; p. 156) noted that "in areas with no major changes in land use, and where the wind distributions are repeated seasonally, the drifts tend to form in approximately the same shapes and locations from year-to-year". Schirmer et al. (2011) and Schirmer and Lehning (2011) studied snow depth distributions and their scaling behaviour (see below) in a small alpine basin in the Swiss Alps and found very strong inter-annual correlations. Wind speeds tend to be reduced on leeward slopes and lead to increased deposition and development of wind-slab layers. For example, Föhn and Meister (1983) reported mean snow accumulation on a lee slope oriented perpendicular to the prevailing wind to be roughly twice that on the windward slope at a site in the Swiss Alps. The maximum accumulation was roughly six times the minimum observed on the windward slope and occurred just below the ridge crest. Abrupt changes in topography such as sharp ridge crests lead to local acceleration of the wind and air-flow separation, which are responsible for such patterns of erosion and deposition in complex terrain, and often result in the formation of cornices (e.g., Mott et al., 2010).

Local surface depressions and gullies also favour the deposition of wind-transported snow due to sheltering. Gray (1979) and Gray et al. (1979) showed how drainage-ways and gullies act as major collection areas for wind-transported snow in prairie landscapes, retaining up to four and a half times the amount as adjacent gradual slopes and level plains. Other studies have shown how relative topographic position, orientation, and sheltering influence the spatial patterns of snow accumulation in low relief terrain (Pomeroy and Gray, 1995; Lapen and Martz, 1996; Essery and Pomeroy,

2004a). Surface curvature has been noted as an important index for snow accumulation (Elder et al., 1989; Blöschl et al., 1991), with convex and concave profiles representing ridges and gullies respectively, and being associated with below and above average values of SWE. Blöschl and Kirnbauer (1992) observed this pattern when examining maps of curvature and snow distribution over an alpine catchment in the Austrian Alps. Numerous other studies in alpine regions have examined and/or modelled the effects of terrain features such as curvature, terrain sheltering, and upwind and downwind features, and found these to be important controls on snow distribution (e.g., Elder et al., 1991; Cline, 1992; Liston and Sturm, 1998; Purves et al., 1998; Anderton et al., 2004; Marks et al., 2002; Winstral and Marks, 2002; Winstral et al., 2002). Anderton et al. (2004) examined spatial variability in patterns of SWE in a high alpine catchment in the Spanish Pyrenees, and related the patterns to topographic variables extracted from a LiDAR (Light Detection And Ranging) derived digital elevation model (DEM). They discussed how divergence of airflow caused by breaks in slope in the micro-topography has an important effect on snow redistribution, and therefore, even subtle variations in the terrain can induce the formation of drifts over exposed and windswept terrain. Lehning et al. (2008) introduced the process of preferential deposition, which is deposition in lee slopes during snowfall in the absence of erosion of already deposited snow and thus also in the absence of saltation. They reported a main conclusion from their modelling at an alpine site in the Swiss Alps was that preferential deposition is very significant for snow distribution at the scale of a ridge, but that saltation dominated the smaller scale snow deposition patterns.

In addition to topography, characteristics of the surface vegetation cover have a significant influence on the deposition and accumulation of wind-blown snow. Exposed vegetation, mechanical barriers such as rocks, snowfences, etc., or crop stubble protruding through the snowcover reduce the shear stress since part of the force of the wind is expended on these non-erodible elements (Steppuhn, 1981; Pomeroy and Gray, 1995). Thus, deeper accumulations of snow occur over certain parts of the landscape in relatively open and windy environments where these features are present. Walker et al. (2001) provide an extensive review of snow–vegetation interactions in windswept alpine and tundra regions. In these environments, krummholz vegetation (i.e., isolated wind-

shaped shrub and tree "islands") has a significant influence on patterns of snow deposition as snow drifts form in the sheltered leeward side of these obstacles (Hiemstra et al., 2002, 2006). McFadden et al. (2001) examined interactions between shrubs and snow along several transects in arctic Alaska and found that snow depths correlated closely with shrub characteristics, and that shrubs increased snow depths by 27% independent of local variations in topographic relief. Similarly, Essery and Pomeroy (2004a) and Hiemstra et al. (2002, 2006) have shown how the presence of shrubs in arctic tundra and alpine environments affects spatial patterns of snow drifts over various terrain features, and increases snow accumulation on the landscape. Relatively high accumulation of wind-transported snow also often occurs near treeline in mountainous environments, where there is a sharp transition from exposed alpine tundra to denser stands of subalpine larch (*Larix lyalli*), spruce (*Picea engelmannii* or *Picea glauca*), or fir (*Pseudotsuga menziesii* var. *glauca*) forest (Fisera, 1977; Walker et al., 2001). Deciduous larch trees trap blowing snow effectively and have lower interception losses than other species. In the treeline area, various assemblages of vegetation such as parallel ribbon forests act as snow fences and accumulate deep and persistent drifts of snow, resulting in grassy "snow glades" between tree stands (Billings, 1969).

In forested areas, interception of snow by the forest canopy has a major role in the accumulation and distribution of the snowcover on the ground (Hedstrom and Pomeroy, 1998). Intercepted snow is more readily lost to sublimation due to its higher exposure and increased net radiation to snow held in the canopy, and thus large amounts of snowfall are returned to the atmosphere in subalpine and boreal forests rather than accumulating on the surface (Harding and Pomeroy, 1996; Schmidt and Troendle, 1992). Some studies have compared snow accumulation under forest canopies to that in nearby canopy clearings (see Pomeroy et al., 1998). For example, Toews and Gluns (1986) reported an average of 37% more snow in clear-cut logged areas from in southern British Columbia. Golding and Swanson (1986) reported that accumulation was 20 to 45% greater in clearings than adjacent forest areas in the foothill region of southern Alberta. Although there was uncertainty about the processes responsible for such differences in much of the early literature (e.g., Meiman, 1970), it is now accepted that interception and

sublimation are the primary factors that contribute to these forest–clearing differences in accumulation (Pomeroy and Gray, 1995).

Interception and unloading of the snow creates distinct spatial patterns of SWE around individual trees. This is influenced by atmospheric turbulence, radiation, humidity, and temperature within the canopy during snowfall events and between storms. Sturm (1992), Woo and Steer (1986), and Pomeroy and Goodison (1997), showed how snow depth varies with distance from conifer trunks in a variety of boreal ecosystems. In general, snow depth and SWE are low directly under the canopy foliage, and increase rapidly outward from the trees to a maximum depth shortly past the edge of the branches. At the forest stand scale, differences in accumulation occur between different tree species and winter leaf area index (LAI) values (Pomeroy and Goodison, 1997). Faria et al. (2000) reported differences in mean SWE ($\overline{SWE}$) and coefficient of variation (CV; i.e., standard deviation/mean) of SWE prior to melt in different forest stands within the boreal forest in central Saskatchewan. They observed that the variability of SWE tended to increase with increasing canopy density, with the exception of a burned stand, and that $\overline{SWE}$ was generally greater for more open forest stands. Because of the underlying processes affecting snow interception and unloading, SWE distribution patterns within particular regions and forest stands are likely to be consistent from year to year.

In steep alpine terrain, avalanches and redistribution of snow by gravity are important processes that affect the distribution of seasonal snowcovers. Perla (1980), Schaerer (1981), and McClung and Schaerer (1993), provide detailed reviews on the mechanisms of avalanche release, snow stability, avalanche motion, as well as many other aspects related to this phenomenon. In general, avalanches occur on steep slopes (i.e., > 30° for the most part) where deep snowpacks develop from the accumulation of heavy snowfall or drifting snow. Weaknesses within the snowpack as a result of metamorphism, surface melt, or buried layers with weak bonds between grains cause the snow to fail when the stress due to the weight of overlying snow becomes high. Due to the highly variable snow and terrain conditions over the landscape, however, avalanches exhibit a wide range of forms and magnitude (Haegeli and McClung, 2007). In locations where frequent avalanches occur on extensive and steep slopes, large amounts of snow are transported to the base of the slopes where deep accumulations develop over the

winter (de Scally, 1996). For example, using a terrestrial laser rangefinder, Hood and Hayashi (2010) measured snow depths of 6 – 9 m on talus slopes in a high alpine catchment in the Canadian Rockies, and attributed this to the redistribution of snow from avalanches.

While large scale avalanches are capable of substantially altering the distribution and patterns of snow accumulation in steep alpine catchments, gravitational redistribution of snow also influences local patterns and prevents snow from accumulating in certain steep parts of the catchment. Elder et al. (1998) found that snow accumulations in a montane watershed in California were generally greater on slopes less than 37°, and attributed this to the fact that steeper slopes avalanche more frequently. In an alpine basin in the Swiss Alps, Mittaz et al. (2002) noted that the maximum percentage of area covered by snow during the winter is difficult to determine and depends strongly on the fraction of the surface with slope values exceeding about 45°. Again, this is because snow does not remain on terrain steeper than this value. Kirnbauer et al. (1991) analyzed snowcover patterns in an alpine basin in the Austrian Alps from oblique photographs, and reported that slopes steeper than 60° were virtually never snowcovered. Blöschl et al. (1991) noted that the threshold slope beyond which slopes are permanently snow free depends on climatic conditions and varies between 45 and 70°. In climatic regions where snow deposition generally occurs at relatively warm temperatures close to 0 °C, snow tends to stick to and accumulate on steeper surfaces, while in colder regions where snowfall occurs at lower temperatures, the snow is more easily redistributed.

2.1.3 Statistical Description of Snowcover Variability

The processes of snow accumulation and redistribution discussed in the previous sections lead to the development of a highly heterogeneous snowcover over the landscape, especially in alpine environments. Understanding and characterizing the variability of SWE is important, as this affects the melt and depletion of the snowcover, and the generation of snowmelt runoff (Luce et al., 1998; Anderton et al., 2002). Classification approaches have been pursued in many studies, where a catchment is divided into a number of areal units with similar topographic, vegetation/land use, and other

characteristics, and within which snowcover displays relatively uniform characteristics and patterns (McKay, 1970; Steppuhn and Dyck, 1974; Woo and Marsh, 1978). For example, Steppuhn and Dyck (1974) reported that the areal variations of snowcovers exhibit consistent similarities within areal units having similar landscape features. They found that the variability in snow depth and density, expressed by the CV, was considerably lower for individual landscape classes than when combined, and suggested that stratified sampling schemes have merit over random sampling for this reason. Pomeroy et al. (1998) and Clark et al. (2011) listed representative average values for the CV of SWE calculated from thousands of samples in seasonal snowcovers near the time of peak accumulation on various landscape units in prairie, arctic, and boreal forest environments. Values have been found to range from <0.05 in certain boreal forest stands to 0.58 in prairie fallow fields on the crests of hills, knolls, and ridges. Killingveit and Sand (1991) showed how values of average SWE and CV varied with elevation in open and forested areas within mountain catchments in Norway. In general, CV values were found to increase with elevation in open areas, up to an average value of approximately 1.0, while observations from individual snow courses indicated a wide range of values from 0.17 to over 2.0.

The landscape classification approach of many of these studies has been noted to be qualitative and subjective (Pomeroy et al., 1998). Some work has been done to investigate the use of objective terrain classification approaches based on combinations of variables derived from DEMs (Blöschl et al., 1991; Elder et al., 1991; Lapen and Martz, 1996). In general, these studies reported a reduction in the total snow depth and SWE variance, and success in delineating major patterns of snow accumulation over the landscape based on terrain features. Lehning et al. (2011) presented a model of the mean snow depth in topographic control units as a function of two terrain parameters: the elevation plus a fractal roughness parameter (see discussion on fractal geometry below). Regression tree approaches, where snow distribution is related to various terrain variables in a non-linear and hierarchical manner, have also been explored as a means for spatial interpolation and estimating snow distribution in alpine environments (Elder et al., 1998; Erxleben et al., 2002). These methods have been shown to yield good predictions of the

variance in SWE, and are useful to incorporate within the sampling strategy for characterizing snow distribution over complex terrain.

The spatial variability of SWE over individual landscape units or catchments can be characterized using various parametric statistical frequency distributions. This has been the focus of many recent studies in snow hydrology since the shape of the distribution is important in order to describe the development of snow-free areas in spring (Essery and Pomeroy, 2004b). A common feature of these distributions in open environments is the relatively high frequency of smaller values of SWE and the tendency for the distributions to exhibit positive skew. Numerous studies within a wide variety of environments have found that distributions of SWE prior to melt can be approximated by the lognormal distribution (discussed in detail in Section 3.2) when stratified by terrain feature classes (e.g., Killingveit and Sand, 1991; Donald et al., 1995; Shook, 1995; Faria et al., 2000; Janowicz et al., 2003; Shook and Gray, 1997b; Pomeroy et al., 1998, 2001, 2004). Others have used alternative distributions to characterize the spatial variability of the snowcover, including normal, beta, and gamma distributions (e.g., Steppuhn and Dyck, 1974; Kuchment and Gelfan, 1996; Brubaker and Menoes, 2001; Alfnes et al., 2004; Skaugen et al., 2004; Skaugen, 2007; Egli et al., 2011). Essery and Pomeroy (2004b; p. 262) stated that "the scales on which such unimodal distributions can be applied will depend on the complexity and length scales of the landscape under consideration." At the catchment scale, for example, Marchand and Killingveit (2003) showed that a weighted mixed distribution combining two separate lognormal distributions gave the best approximation to the snowcover variation in several mountainous catchments in Norway.

Although the frequency characteristics of snow depth and SWE can be considered as spatially random, it is well established that the spatial structures of seasonal snowcovers exhibit distinct regularities in their pattern over various scale ranges. These variables are often highly autocorrelated at certain scales and tend to display statistical self-similarity (i.e., the variability and structure appear the same when examined over multiple scales of observation). This type of scale invariance can be described by the theory of fractal geometry (Mandelbrot, 1983), and many studies have used this approach in their investigation of the spatial structure and distribution of snow (Shook, 1995;

Shook et al., 1993; Shook and Gray, 1996, 1997b; Kuchment and Gelfan, 1997, 2001; Deems et al., 2006, 2008; Mott et al., 2011b; Schirmer and Lehning, 2011). For example, Shook et al. (1993) demonstrated that snow and soil patches that formed during the ablation of shallow snowcovers show fractal characteristics in the area–frequency and perimeter–area relationships. This was attributed to an underlying fractal distribution of SWE. Shook and Gray (1996) examined snow transect data in prairie and arctic environments and showed that the spatial distribution of snow depth is fractal at small scales, becoming random at scales greater than about 30 m. Deems et al. (2006) used a high resolution airborne LiDAR dataset over alpine sites in Colorado, and showed that snow depth variability exhibits fractal scaling behaviour over two distinct scale ranges separated by a break at around 15 – 40 m. Such changes in the scaling behaviour at some cutoff length can point to important changes in the processes controlling spatial patterns at different scales (e.g., Blöschl, 1999). Deems et al. (2006) and Shook and Gray (1996) suggested that this scale break is related to the variation of underlying topography, and found that it is greater where the overall relief of the landscape is higher. Mott et al. (2011b) used high resolution simulations and airborne and terrestrial laser scans in an alpine basin in Switzerland to explore the links between the scaling behaviour of snow depths and the wind induced processes driving the spatial structure of the snowcover. They found, similar to Deems et al. (2006), that the direction of the strongest autocorrelation of both wind velocity and snow depth was perpendicular to the direction of the prevailing winds. Their modelling showed that wind fields, calculated snow depths, and modelled snow depths have similar fractal behaviour, which is because topographically modified flow fields strongly influence snow depth spatial structure. Deems et al. (2008) used a subsequent LiDAR dataset and showed that fractal dimensions and scale break distances were consistent between years with different snow accumulation histories. They suggested that the scaling features in snow depth distributions are largely determined by physiography and vegetation, and are relatively insensitive to year-to-year variations in snowfall. This finding is supported by the work of Schirmer et al. (2011) and Schirmer and Lehning (2011), who used multi-temporal terrestrial laser scans of several unvegetated alpine slopes in Switzerland to investigate persistence in snow depth distributions. They reported that the final snow distribution at

the time of peak accumulation is mainly shaped by "master" storms (i.e., from the north-east) and that these storms create persistent accumulation patterns.

2.2 Snowmelt Energy Balance and Modelling

The ablation of a snowpack is defined as the net volumetric decrease in its water equivalent, and is governed by several processes including snowmelt, sublimation and condensation, vertical and lateral transmission of water through the snowpack, and infiltration of water to the underlying substrate (Male and Gray, 1981). For seasonal snowcovers, snowmelt becomes an important process in the spring, and the rate at which this occurs is controlled by the energy balance of the snowpack. This balance, in turn, is controlled primarily by energy fluxes at the air–snow interface, which depend on meteorological conditions, snowcover state, terrain, and vegetation, giving rise to a high degree of spatial–temporal heterogeneity in melt rates. Representing these processes and defining the appropriate level of complexity and detail in modelling applications has been the focus of a large amount of research in recent decades (Brun et al., 2008).

2.2.1 Snowpack Energy Balance

When applying the energy balance principle to snowcovers, it is common to consider a small control volume with boundaries at the air–snow and ground–snow interfaces. Such an approach is necessary to completely describe the thermal regime of the pack (Male, 1980). The amount of energy available for melting snow, Q_m (generally expressed in units of W/m^2 or kJ/m^2·d), is determined for this volume as:

$$Q_m = K^* + L^* + Q_H + Q_E + Q_G + Q_P - \frac{dU}{dt}, \tag{2.2}$$

where K^* is the net shortwave radiation flux, L^* is the net longwave flux, Q_H, Q_E, and Q_G are the sensible, latent, and ground heat fluxes, respectively, Q_P is the energy added to the snowpack by precipitation, and U is the internal energy of the snowpack.

Incoming shortwave radiation is often the most important energy source to the snowcover. The amount received at the surface varies widely depending on time of day,

season, slope and aspect of the terrain, vegetation, cloudiness, and atmospheric conditions. In highly complex terrain, the contribution from the sky, reflection from surrounding topography, and local shadows have an important effect on the variation of direct solar radiation at a given point (Dozier, 1980). A diffuse shortwave component also contributes to the radiation received at the surface (Kuz'min, 1961; List, 1968), which may contribute ~10% on clear days, and up to 100% on completely overcast days. Net shortwave radiation depends on the albedo of the snow (i.e., the ratio of reflected radiation to incident radiation), which can be as high as 0.9 for fresh snow, decreasing to 0.3 – 0.4 for older dirty snow (Pomeroy and Brun, 2001). Albedo also varies as a function of wavelength and snow grain size (Warren and Wiscombe, 1980). Studies have shown how the albedo decays exponentially as the snow ages and undergoes metamorphism (U.S. Army Corps of Engineers, 1956; O'Neil and Gray, 1973), but melting of the snowcover also exposes bare ground and vegetation surfaces, which has an influence on the areal albedo as shown by O'Neil and Gray (1973).

Longwave radiation to the surface is emitted by various atmospheric constituents and related primarily to the air temperature and vapour pressure, particularly within the lowest several hundred meters. In mountainous environments, part of the sky is obscured by surrounding terrain while at the same time the terrain contributes longwave fluxes according to its temperature and emissivity, resulting in further spatial variations in longwave radiation receipt at a point (Olyphant, 1986; Plüss and Ohmura, 1997; Sicart et al., 2006). The snowcover surface radiates as a nearly perfect black body with an emissivity in the range of 0.97 – 0.99 and surface temperature confined to 0 °C for melting snow. Over seasonal snowcovers the upward flux emitted from the snow surface is usually greater than the incoming longwave radiation so that the net flux is usually negative (Male and Granger, 1979).

In comparison to radiative fluxes, the turbulent fluxes of sensible and latent heat are of secondary importance in the snowcover energy balance, but turbulent transfer may still represent an important source of energy for snowmelt in some situations (Mott et al., 2011a). These fluxes depend on air temperature and humidity gradients above the snow surface, wind speed, surface roughness, and stability of the air. Profile or direct flux measurements are generally not available in most experimental and modelling studies,

leading investigators to parameterize the fluxes using bulk transfer calculations, together with Monin–Obukhov similarity theory to account for atmospheric stability effects. Helgason (2009) recently demonstrated problems with this approach in mountainous regions due to non-local sources of turbulence in the surface boundary layer. He noted that the bulk transfer approach can still provide adequate results if prior information regarding the heat transfer process is available and site-specific effective transfer coefficients are used. In areas with relatively dry air, some studies have shown that latent and sensible energy exchanges are often approximately balanced with opposing sign, leading to a zero net turbulent flux (Marks and Dozier, 1992; Pomeroy et al., 1998; Marks et al., 2008; Helgason, 2009). However, turbulent energy transfer may play a more important role later in the melt period. For example, as a snowcover becomes patchy during melt, areas of exposed ground significantly alter the energy balance through local advection sensible heat, which becomes increasingly important as the snowcover disintegrates (Marsh and Pomeroy, 1996; Marsh et al., 1997; Shook et al., 1997b; Neumann and Marsh, 1998 Grünewald et al., 2010; Mott et al., 2011a).

The ground heat flux is usually a negligible component of the snowpack energy balance in comparison to the radiative and turbulent fluxes. However, because it is persistent, its cumulative effect can be significant over a season and play an important role in controlling the thermal regime at the bottom of the snowpack and its conditioning for melt (Male and Gray, 1981). During the snowmelt period, infiltration of meltwater into unsaturated frozen soil releases latent heat upon refreezing and reduces temperature gradients in the soil, leading to very small values of Q_G, (Zhao et al., 1997; Pomeroy et al., 1998).

Rainfall adds energy to the snowpack through the addition of sensible heat, and in the case of a sub-freezing pack, through the refreezing and release of latent heat. This can, in some situations, exert a considerable influence on the thermal regime of the pack. Condensation on the surface as a result of the high humidity often associated with rainfall can also represent a significant source of energy for snowmelt (Marks et al., 1998).

Consideration of the changes in the internal energy, U (kJ/m^2), is essential to successfully apply the energy balance principle to shallow seasonal snowcovers (Male

and Gray, 1975; Norum et al., 1976). This term consists of components for the solid, liquid, and vapour phases of the snowpack, and is given by Male and Gray (1981) as:

$$U = d(\rho_i C_{pi} + \rho_l C_{pl} + \rho_v C_{pv})T_m, \tag{2.3}$$

where d is the snow depth (m), ρ is density (kg/m^3), C_p is specific heat (kJ/(kg·°C)), T_m is mean snowpack temperature (°C), and i, l, and v refer to the solid (ice), liquid, and vapour phases respectively. The internal energetics of the snowpack prior to and during melt are quite complex. Energy inputs to initially sub-freezing snow are first used to raise the temperature to 0 °C throughout the depth of the snowpack before further inputs can be used towards phase change. However, melt can occur in the upper layers of the pack while lower layers are still below 0 °C, resulting in percolation of meltwater along preferential flow paths into the pack (Marsh and Woo, 1984). As this meltwater encounters cold internal snow layers, it refreezes and releases latent heat, rapidly warming the snow towards the melting point. Overnight cooling and refreezing at the surface due to longwave radiation losses also result in internal energy deficits, which must be compensated for the following day to bring the snowpack back to 0 °C and resume melting conditions. This depth of refreezing is usually confined to the upper 20 cm of the snowpack (Pomeroy and Brun, 2001).

Meltwater is produced in appreciable quantities once the snowpack is ripe (i.e., isothermal conditions at 0 °C and holding water at about 3 – 5% of the snow by weight). The melt energy can be expressed on a daily basis from Q_m (kJ/m^2·d) as a depth of melt, m (m), by:

$$m = \frac{Q_m}{\rho h_f \beta}, \tag{2.4}$$

where ρ is the density of the snow (kg/m^3), h_f is the latent heat of fusion (334 kJ/kg), and β (dimensionless) is the thermal quality or the fraction of ice in a unit mass of wet snow. Since a melting snowpack will hold about 3 – 5% liquid water as it drains by gravity, the value of β is generally between 0.95 and 0.97 (Male and Gray, 1981).

2.2.2 Snowmelt Modelling and Scaling Issues

Over the previous several decades, a wide variety of numerical snowmelt models have been developed and applied in various aspects of snow hydrology, climatology, and avalanche forecasting. Early applications of the energy balance principle for continuous simulation of snowmelt were simplified in terms of the representation of physical snowpack properties and basin heterogeneity (e.g., Anderson, 1968). However, this was a considerable advance from previous empirical approaches that used air temperature as the sole index to energy exchange and snowmelt. Temperature index, or degree day approaches are still widely used due to their simplicity (Rango and Martinec, 1995; Hock, 2003), but severe limitations are encountered due to the lack of a physical basis, non-consideration of snowpack internal energy and spatial variability in energy fluxes, and difficulty in determining and transferring empirical melt factors. Following the early efforts on energy balance snowmelt modelling, significant progress has been made towards representing energy transfer mechanisms, internal snowpack processes, and spatial variability of fluxes and snowcover conditions (e.g., see Brun et al., 2008 and references therein). Recent model intercomparison projects have helped to demonstrate the performance of various models in different environments, as well as shed insight on the optimum level of model complexity for different purposes (Etchevers et al., 2004; Essery et al., 2009).

Current models differ widely in their structure and complexity. Kampf and Burges (2007) provide a framework for classifying and comparing distributed models, partly based on the nature of their process representation. Most models only consider snow processes in the vertical direction, while the representation of layering and internal processes within the snowpack varies between models. Some of the more sophisticated snow-physics models with treatment of multiple layers and snow phases include CROCUS (Brun et al., 1989, 1992) and SNOWPACK (Bartlet and Lehning, 2002), developed primarily for use in avalanche forecasting, and SNTHERM (Jordan, 1991), which is a detailed energy and mass balance model for understanding snow processes and runoff forecasting. This type of modelling framework followed the work of Anderson (1976), who was the first to develop such a detailed multiple-layer model that explicitly

accounted for internal snow processes. A somewhat simpler model is Snobal (Marks and Dozier, 1992; Marks et al., 1998), and its distributed counterpart Isnobal (Marks et al., 1999), which approximate the snowpack as being composed of two layers for mass and energy balance computations and runoff predictions. This model is similar to the approach of Anderson (1976), but is designed to be run on simpler and more generalizable inputs. Other models such as UEB (Tarboton and Luce, 1996), or land surface schemes such as CLASS (Verseghy, 1991), represent the snowpack using only a single layer. These models greatly simplify the treatment of internal snow processes such as meltwater retention and percolation, density changes, vapour transfer, and thermal diffusion. Some models such as EBSM (Gray and Landine, 1988) utilize the energy balance equation within their framework, but employ empirical procedures for evaluating some of the terms. Thus, their use outside of the regions for which they were developed may be problematic. Common models applied in mountainous regions have included UEB, DHSVM (Wigmosta et al., 1994), Isnobal, and SNOWPACK within the Alpine 3D model described by Lehning et al. (2006); the latter two of these three models are typically applied in a fully distributed manner.

An important issue that is central to applying any numerical snowmelt model over an extended area or a catchment is the spatial discretization and model element size chosen to represent the landscape and processes. In terms of spatial representation, models may be distinguished as either lumped or distributed (Grayson and Blöschl, 2000). Lumped models represent the conditions and processes within a catchment using a single set of parameter values, state variables, and mass and energy fluxes, and therefore treat the catchment as a single unit without consideration of spatial variability of the processes. In contrast, distributed models attempt to represent these processes in a spatially explicit manner by dividing the catchment into a number of sub-units, and computing snowmelt for each of these independently using corresponding parameters and variables. Often, models use a uniform and finely spaced grid or mesh system to divide the area into elements, and solve balance equations analytically or numerically at the nodal points of this mesh. Freeze and Harlan (1969) were the first to propose this type of "blueprint" for physically-based, distributed hydrological models, and since then a wide range of catchment models have been implemented based on their approach (e.g., SHE

model; Abbott et al., 1986). Marks et al. (1999) and Lehning et al. (2006) described the use of a similar modelling approach for snowmelt and runoff simulations in mountainous catchments. However, fully distributed simulations require a considerable effort, with difficulties in determining the necessary parameters, obtaining high quality spatial data, and meeting the high numerical and computational demands.

Simpler approaches for spatially distributed modelling have been developed, including the hydrological response unit (HRU; e.g., Leavesley and Stannard, 1995) and grouped response unit (GRU; e.g., Kouwen et al., 1993) concepts. The HRU approach assumes that a catchment can be split into distinct units corresponding to variations in elevation, land cover, slope, aspect, soils, and/or precipitation distribution, for example. Each HRU is then treated as a lumped model element for numerical computation. This allows for relatively detailed spatial representation of patterns and processes, depending on the selection and number of HRUs, and is better suited for relatively smaller catchments. The Cold Regions Hydrological Model (CRHM) platform, described by Pomeroy et al. (2007), is based on this approach. In the GRU approach, all areas with a similar land cover (or other hydrological attribute) are grouped, and a grid system is used within which each individual grid cell may contain a number of distinct GRUs. Thus, each grid cell is not necessarily considered as a distinct hydrological unit. This is a more sensible approach for larger basins because the data requirements are fewer while still allowing for reasonably detailed physical descriptions (Pietroniro and Soulis, 2003). Both the HRU and GRU approaches have the advantage that they simplify the modelling process and yet still allow spatial patterns and the dominant processes to be represented in a distributed manner. Some of the disadvantages are that it may be difficult and somewhat subjective to define the units, and that the units themselves are considered as spatially homogeneous in terms of their properties.

All models must conceptualize and simplify the physical processes governing snowmelt to some degree. The equations and parameters describing the processes are meant to apply at the point-scale or over a small control volume, and therefore regardless of how spatially explicit, the models are lumped to some degree and deal with processes in an aggregated manner over space and time (Gupta et al., 2005). This has forced model developers and users to seek effective parameter values that reproduce the bulk behaviour

of the model elements. These are generally derived through calibration with some integrated form of catchment response and do not necessarily correspond to point-scale measurements, although they may still contain some physical relevance. Beven (1989) discussed the problems of parameter interaction, difficulty of determining the correct combination of parameters, and the compensating effects of different parameters in complex hydrological models. There may be many combinations of equally plausible parameter values that yield model simulations that are consistent with observations; this is referred to as problems of non-uniqueness or "equifinality" (Beven and Binley, 1992).

No matter the level of detail in the spatial representation, there will be some "sub-grid" variability that is not resolved by the model. Effective parameters represent one approach to handling this, but understanding of the scale of the processes and their variability (e.g., Blöschl, 1999) is important when trying to explicitly represent the spatial patterns of important or dominant processes. The theoretical notion of a representative elementary area (REA) developed by Wood et al. (1988) essentially defines a minimum scale or measurement area needed to capture the underlying spatial variability, below which representation of explicit spatial patterns of the relevant variables becomes less important. Studies have considered the existence of an REA for snow depth distribution and snowmelt (Cline et al., 1998; Leydecker et al., 2001). Cline et al. (1998) reported that a possible explanation for the scale effects seen in their grid-based snowmelt model over a mountain basin in the Sierra Nevada could be the existence of an REA-type scale threshold between 90 and 250 m. It stands that if such an REA can be defined for a given location it is unlikely that it will be transferrable as it will depend on the nature of the specific processes, climate, terrain, and vegetation.

Nevertheless, this type of notion has merit for discretizing a catchment or defining HRUs. Seyfried and Wilcox (1995) noted that data requirements can be reduced by recognizing the nature and sources of variability, focusing on important sources of deterministic variability, and representing variability at scales smaller than the deterministic length either stochastically or as uniform. Proper understanding and representation of the relevant sources of variability, specific to a particular catchment and modelling objective, can have a large effect on the degree of modelling success. For example, Dornes et al. (2008a, 2008b) disaggregated a small subarctic mountain

headwater basin into HRUs based on slope, aspect, and landcover for the simulation of snowmelt and runoff generation, and compared the results with various spatially aggregated simulations. They found that the distributed model based on these HRUs best described the observed magnitudes of snowcover ablation and basin runoff, whereas the aggregated simulations failed to represent the differential snowmelt and meltwater production between slopes. It has been argued that if the effects of important large scale deterministic variability are depicted, models may more truly depict the actual physical processes than fully distributed traditional Freeze–Harlan (1969) type models (Seyfried and Wilcox, 1995).

It is clear from this discussion that the effects of scale are particularly important to consider in snowmelt modelling. Blöschl and Sivapalan (1995) discussed issues of scaling in hydrological modelling and defined upscaling in a hydrological context as transferring information from a given scale to a larger scale. Scale refers to some characteristic length or time, and can be distinguished by process, measurement, and model scales (Blöschl, 1999). As has already been discussed, model scales are generally inconsistent with process and measurement scales, with important implications for the predictions. Blöschl (1999) examined the effects of measurement and model scale on data and predictions, and showed that biases occur in the results of snow models due to improper representation of the true process scale. He also examined scale effects inherent in distributed models and showed how non-linearity present in the natural system and/or models can significantly bias the mean of variables such as SWE over a catchment. Others have considered the effects of non-linear interactions between snow processes, showing, for example, how spatial covariance between snow mass and melt energy can cause substantial deviations from point-scale physical predictions of snowmelt flux and duration in upscaled simulations (Faria et al., 2000; Pomeroy et al., 2001; Pomeroy et al., 2004; Essery and Pomeroy, 2004b). These deviations occur due to the fact that the processes do not aggregate linearly, so that $E(f(x)) \neq f(E(x))$, where E is the mathematical expectation (i.e., mean), x is location, and f is a function or variable describing the process interaction. Therefore, it is important to take the nature of the process interactions into account when choosing a strategy to discretize a catchment and represent sub-grid variability.

The variability in processes and variables at the sub-grid scale is often directly parameterized based on other resolved quantities. An example of this in many numerical snowmelt models is the areal snowcover depletion (SCD) within individual model elements or over the landscape. The substantial heterogeneity in the pre-melt snowcover is well recognized (Section 2.1) and results in a complex patchwork or mosaic of snowcovered and snow-free surfaces as the snow melts. This has led many investigators to develop parameterizations of the fractional snowcovered area (SCA) using variables such as $\overline{\text{SWE}}$ or accumulated depth of snowmelt over a model element, often in combination with statistical descriptions of the pre-melt snowcover variability over the landscape. (This is discussed more thoroughly in the following section of this review). Other processes and variables that are commonly parameterized at sub-grid scales include spatial average turbulent energy fluxes; surface albedo decay and refresh with subsequent snowfall events; interception and sublimation of snowfall, heat fluxes from, and radiation transmission through vegetation canopies; and thermal and hydraulic characteristics of the snowpack (Essery, 2008, *Snow Parameterization in GCMs*, In: Brun et al., 2008). These are typically related to model variables such as air/snow temperature, precipitation amount, and mean snow depth or SWE, while the parameterizations depend on upscaled characteristics of surface and canopy properties. Non-linearities associated with the scaling behaviour of all of these processes are important to consider in the context of sub-grid parameterization to avoid biasing mean conditions at larger scales.

2.3 Areal Snowcover Depletion and Snowmelt Runoff

The spatial variability of SWE over the landscape leads to the development of a patchy snowcover as the snow melts. If snowcover were uniformly distributed and melt energy was applied evenly across the landscape, the result would be an "instant bare ground" effect as the snowcover melts in spring, which is an obvious oversimplification of reality (Donald et al., 1995). The disintegration of the snowcover over time is among the most important processes to represent from both a hydrological and climatological perspective. The fraction of SCA controls the meltwater generating area (MGA), thereby affecting the rate and magnitude of meltwater production, while this fraction is used in models to

calculate fluxes separately over snowcovered and snow-free terrain (Liston, 1995). Therefore, proper representation of the sub-grid or sub-model element snowcover extent is crucial for modelling success. There have been a number of different approaches for estimating areal SCD described in the literature, and some of the more prominent of these are reviewed in this section.

2.3.1 Remote Sensing of Snowcovered Area

Observations from satellite platforms or using other remote sensing techniques are highly valuable for obtaining information on a variety of physical characteristics and the spatial–temporal variability of the snowcover, especially in remote, inaccessible, or data sparse regions. There exists a wide range of passive and active sensors onboard different satellite and aircraft platforms, which are suited to obtaining information on variables such as SCA, SWE, snow depth, snow albedo, temperature, liquid water presence, and various other snow characteristics. König et al. (2001), Dozier and Painter (2004) and Scherer et al. (2005) provide detailed reviews on this topic. One of the particularly useful applications of remote sensing in snow hydrology is the measurement of SCA over areas ranging from drainage basin to continental scales. Early work by Hall and Martinec (1985) demonstrated the capability of optical sensors for SCA determination in mountainous areas using a classified Landsat-MSS (Multispectral Scanning Subsystem) image over part of the Swiss Alps. Other sensors have also been used to classify snowcovered areas, including for example Landsat-TM (Thematic Mapper), the NOAA Advanced Very High Resolution Radiometer (AVHRR), and the ASTER (Advanced Spaceborne Thermal Emission and Reflection Radiometer) and MODIS (Moderate Resolution Imaging Spectrometer) sensors. The approaches for classification of multi-spectral imagery generally make use of the high reflectance of snow in the visible portion of the spectrum and the sharp decrease in reflectance into the near-infrared.

Although there are many sensors well-suited for snowcover mapping, there is a trade-off between spatial resolution and swath width (which affects the frequency of observations). In alpine areas, hydrological applications require regular, frequent observations at a high spatial resolution in order to resolve much of the small scale

variability in snow processes that characterize these regions (Dozier and Painter, 2004). Sensors with spatial resolution suitable for SCA mapping in alpine areas (e.g., Landsat-TM, ASTER; resolutions of 30 m or less for visible and near-infrared bands) tend to have return periods of 16 days or more. This can severely restrict the acquisition of imagery due to the presence of cloud cover during satellite overpasses, and even under clear skies may not be sufficient for some hydrological applications during the spring. MODIS snowcover products are available at 500 m resolution as daily and eight day composite products, which have been shown to have a high degree of accuracy (Hall et al., 2002; Hall and Riggs, 2007). Although this is a coarse resolution for snow mapping in alpine areas, sub-pixel SCA can be quantified reliably through spectral mixing analysis and statistical techniques (Rosenthal and Dozier, 1996; Kaufman et al., 2002; Painter et al., 2009). Thus, MODIS can provide a useful tool for deriving snowcover information in mountainous environments in support of hydrological modelling and analysis (e.g., Akyurek et al., 2011; Homan et al., 2011).

For applications dealing with smaller watersheds or headwater alpine basins, aerial or terrestrial-based photography methods provide a useful means for deriving information on the snowcover. Kirnbauer et al. (1991) and Blöschl and Kirnbauer (1992) used oblique aerial photographs to monitor snowcover patterns in a high alpine basin in the Austrian Alps. Parajka et al. (in press) showed how time-lapse photography provides an attractive source of information about snow cover, especially at the small catchment scale. Corripio (2004) developed a technique to re-project terrestrial-based digital photographs orthogonally onto a DEM, and used this for areal albedo estimation and validation on an alpine glacier in the French Alps. Others have subsequently used this approach to characterize snow accumulation or depletion patterns in alpine regions (Schmidt et al., 2009; DeBeer and Pomeroy 2009; 2010; Farinotti et al., 2010). These studies have shown how this technique provides a useful, reliable, and inexpensive means of obtaining SCA measurements over small alpine basins where other remote sensing approaches may fail.

2.3.2 Snowcover Depletion Curves

Snowcover depletion curves are used to relate the percent areal coverage of the snow pack to time, average snow depth or SWE, accumulated snowmelt, or some other relevant variable. Early work in snow hydrology recognized SCA as a prime variable in many applications, and focused on techniques to develop curves for an entire watershed based on indirect relationships with other observed data such as $\overline{\text{SWE}}$ (U.S. Army Corps of Engineers, 1956; Anderson, 1973). Using observations of the snowcover over a sufficient period of record, these studies suggested that it is possible to derive SCD curves because snow accumulation and melt patterns are consistent from one year to the next across a watershed. However, these relationships are difficult to establish and require calibration specific to each watershed. They represent the characteristic response of the watershed to snowmelt, which is in turn related to the specific topographic and surface cover characteristics of the basin. Martinec (1980) later showed that an unequivocal relationship between SCA and $\overline{\text{SWE}}$ is not theoretically possible, and that the areal extent of snowcover seems to be linked to the ratio of the current SWE to its maximum of the respective year.

Subsequent work focused on developing solutions to some of these problems and applying SCD curves in runoff forecasts. Rather than using a single depletion curve for an entire basin, many studies instead adopted the approach of dividing a basin into zones of equal elevation, and developing and applying the curves separately over each zone. For example, Rango and Martinec (1982) divided a mountain basin in southwest Colorado (elevation range from 2605 – 3914 m) into three elevation zones for runoff simulations. They used modified depletion curves to relate the SCA to the cumulative snowmelt depth, and suggested how these can be used for either estimating initial snow accumulation or for seasonal runoff forecasts. Instead of a single curve for each zone, a family of curves derived for years with different conditions (including extreme years) accounts for the year-to-year variation of initial SWE and weather conditions, while consideration of separate elevation zones accounts for differences in melt rate over the basin due to elevation (Martinec and Rango, 1987). Runoff forecasts can be provided with some estimate of the initial SWE by selecting an appropriate modified depletion

curve, which can later be updated as satellite images become available. Martinec (1985) and Rango and van Katwijk (1990) provided more detailed descriptions of these procedures for operational forecasts using the snowmelt runoff model (SRM; Martinec et al., 1998). This model uses satellite snowcover data to determine or update the SCA in forecasts for up to nine elevation zones over a basin.

In contrast to watershed-wide or elevation zone depletion curves, Donald et al. (1995) developed a general model for landcover-based curves using observed snow distribution data from a low relief watershed in southern Ontario. They described, from both a conceptual and mathematical standpoint, how the snow depth distribution on various land units could be uniformly melted to produce the SCD curve. Their approach was based on the assumption that snow depths follow a three-parameter lognormal distribution, and it required specification of the D_{100} (i.e., the mean snowcover depth at the transition from incomplete to complete snowcover), as well as the standard deviation of snow depths corresponding to this condition. The land unit areal average snow depth could then be directly related to the SCA for that unit (Fig. 2.1a). Donald et al. suggested that landcover-based depletion curves should result in snowcover parameters in runoff models that are more stable than those based on watershed-wide curves.

In the studies by Luce et al. (1999) and Luce and Tarboton (2004), a dimensionless depletion curve was introduced to account for inter-annual variations in

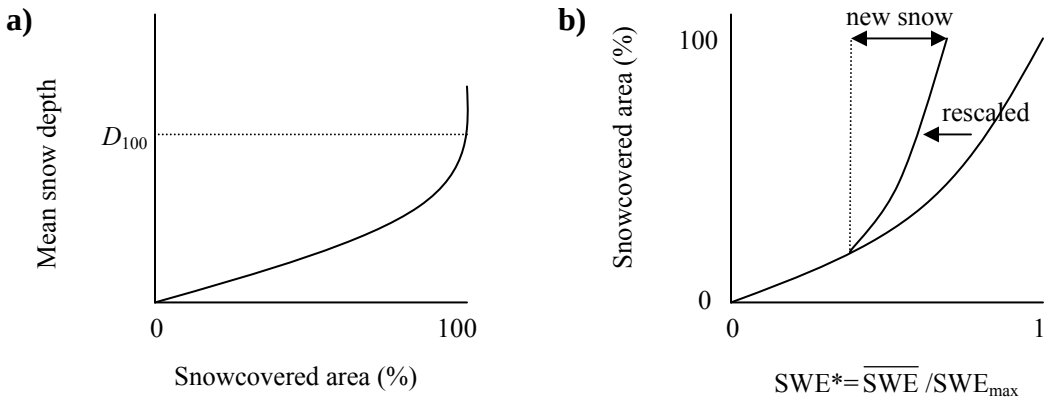

Figure 2.1. Snowcover depletion curves modified from a) Donald et al. (1995), and b) Luce et al. (1999) and Luce and Tarboton (2004).

snow accumulation. They related SCA to the areal $\overline{\mathrm{SWE}}$, scaled by the maximum SWE since the beginning of the snow season (Fig. 2.1b), and thereby avoided the problem of assigning a new curve for each season. It was shown how the dimensionless depletion curve could be derived mathematically from the SWE distribution at peak accumulation, and further, how the effects of snowfall during melt could be handled with a rescaled depletion curve. As indicated in figure 2.1b, SCA is defined to revert to 100% with a new snowfall event and the system returns along a rescaled curve until the point of original departure. Using data from a small (26 ha) basin within the Reynolds Creek watershed in southern Idaho, Luce et al. (1999) demonstrated that this approach provided results of areal SCD and surface water input that compared well with periodic measurements and results of a fully distributed mass and energy balance simulation. Luce and Tarboton (2004) presented a series of dimensionless depletion curves at this site from several years and showed that the curves are stable over time.

The issue of snowfall events during the melt period has been considered in other studies as well. Anderson (1973) and Moore et al. (1999) assumed new snowfall to temporarily increase SCA to 100% until 25% of the new snow had melted, after which SCA was linearly interpolated back to the original depletion curve. The choice to use 25% of the new snowfall for the beginning of this linear reversion was arbitrary and could vary between watersheds. Liston (2004) used an approach where new accumulation is used to reduce the melt depth values, effectively moving back along the depletion curve towards 100%. This will generally produce smaller snowcovered fractions than Anderson's and Moore et al.'s approach and does not account for the fact that snowfall is distributed over an entire grid cell or model element. Davison (2003) presented a theoretical framework for handling fresh snowfall within a GRU-based hydrological model, and introduced a D_{100} term for snow accumulation, D_{100A}, which is lower than that for snow depletion. This results in a hysteresis zone for the depletion curve of Donald et al. (1995), and at any time a measurement of snow depth vs. SCA could fall anywhere within this zone, depending on the history of the pack.

Many studies have investigated how the shape of the depletion curve is related to the underlying frequency distribution of SWE at peak accumulation. It has been established that under uniform melting conditions, the fractional area retaining snow at a

given time may be described by a shift in the probability distribution, $f(\mathrm{SWE})$, equal to the accumulated snowmelt, m_a, up to that time (Donald et al., 1995; Shook, 1995; Pomeroy et al., 1998; Liston, 1999; Luce et al., 1999; Essery and Pomeroy, 2004b). The remaining SCA may then be obtained as:

$$\mathrm{SCA} = \int_{m_a}^{\infty} f(\mathrm{SWE}) d\mathrm{SWE}\,, \tag{2.5}$$

and the average remaining SWE is:

$$\overline{\mathrm{SWE}} = \int_{m_a}^{\infty} (\mathrm{SWE} - m_a) f(\mathrm{SWE}) d\mathrm{SWE}\ . \tag{2.6}$$

By Equation (2.5) the SCD curve can be obtained by applying the snowmelt rate evenly over the SWE distribution. In this context, differing values of CV have a direct effect on the rate of SCA depletion and the overall shape of the depletion curve. Lower values of CV are associated with a more peaked distribution that has values grouped more closely to the mean, and therefore result in a more rapid depletion. Luce and Tarboton (2004) noted that in windswept environments, patterns of snow accumulation are relatively consistent between years such that the standard deviation should track with the $\overline{\mathrm{SWE}}$, yielding small changes in CV from year to year. Pomeroy et al. (2004) showed this effect during the accumulation phase using snow survey data from a series of winters in a subarctic mountainous basin in the Yukon Territory. This helps, in part, to explain the relative stability of dimensionless depletion curves over time.

Equations (2.5) and (2.6) show that the pre-melt frequency distribution of SWE is both an initial condition that defines the snow distribution at the start of melt, as well as a boundary condition that persists throughout the melt period until the snowcover disappears (Liston, 2004). For example, Liston (1999) showed that under conditions of uniform melt, the temporal evolution of the snowcover in spring can be characterized by three interrelated and fundamental features: 1) the pre-melt distribution of SWE, 2) the melt rate, and 3) the depletion of SCA. These interrelations were defined mathematically and it was shown how knowledge of any two of the features allows determination of the third. The main limitation with this framework is that within areas of complex terrain, it may be unrealistic to assume a uniform melt rate over a basin or even a model grid cell.

Some more recent work has continued to explore combining remotely sensed snowcover information and snowmelt modelling for improving hydrological and runoff models and for reconstructing pre-melt SWE. For example, Farinotti et al. (2010) used a distributed temperature index melt model together with oblique terrestrial photography to infer the initial snow accumulation patterns in a small alpine catchment in the Swiss Alps. At a much larger scale over the mountainous Rio Grande headwaters in Colorado, Molotch (2009) used SCA observations from the Landsat Enhanced Thematic Mapper in combination with spatially distributed temperature index melt modelling to estimate SWE. This illustrated the utility of such an approach for obtaining high resolution SWE estimates in remote locations where detailed hydro-meteorological observations are scarce. However, these studies were limited either by the small spatial extent or the infrequent return period of the satellite sensor, and by the use of empirical temperature index snowmelt modelling. Other recent studies have made use of MODIS snowcover products towards investigation of areal SCD patterns (Kuchment et al., 2010; Akyurek et al., 2011; Homan et al., 2011). Homan et al. (2011) demonstrated the use of MODIS products together with melt modelling using the UEB model for obtaining modified depletion curves (Rango and Martinec, 1982) in the foothills of south-western Idaho and the Brooks Range of northern Alaska. Their model results were comparable to the results from ground based observation of these curves for three 500-m square study areas, confirming the potential to use MODIS information where the spatial variability of snow is known to occur at scales much smaller than the MODIS footprint. Kuchment et al. (2010) described a physically based model of snowpack formation and ablation with adoption of available satellite data such as SWE and fractional SCA. They applied this model to a large (~124,000 km^2) forested river basin in Russia using a 0.01° grid cell resolution, and noted that the advantage of this approach is in the detailed physical description of snow processes as compared to snow products derived solely from satellite data.

These studies did not incorporate spatially varying snowmelt computations at a sub-grid level in their approach. In the Swiss Alps, Grünewald et al. (2010) recently investigated the small scale (~2.5 m) spatial patterns of snow ablation in an alpine catchment using terrestrial laser scanning, and although they found highly variable

ablation rates, the correlation with meteorological and terrain parameters was reported to be weak. At this same site, Egli et al. (2011) showed that despite the spatial variation of ablation rates, the development of SCA through the spring could be predicted by spatially uniform melt rates if the initial snow depth distribution at the start of the melt period is established. Grünewald et al. (2010) attributed the patterns of ablation to significant lateral energy fluxes; however, this may also have been partly attributable to the terrestrial laser scanning approach which based ablation rates on measured depth changes together with a spatially uniform snow density. To this author's knowledge, no recent studies since Essery and Pomeroy (2004b) and Pomeroy et al. (2004) have considered the implications of inhomogeneous melt at small scales on areal SCD or suggested an approach for dealing with this issue in upscaled model applications. Rather, the issue remains somewhat unresolved and represents a gap in the understanding and prediction of alpine snowmelt hydrology. This is explored further in the following section.

2.3.3 Inhomogeneous Snowmelt

Melt rates are often variable over the landscape due to the effects of terrain and vegetation, as well as differences in the energy state for different depths over the SWE distribution (e.g., Male and Gray, 1975). For conditions of non-uniform melt, Equations (2.5) and (2.6) may be replaced by double integrals over the joint SWE and melt rate distributions (Essery and Pomeroy, 2004b). Essery and Pomeroy (2004b) noted that these integrals will generally be intractable, but that SCD curves can still be obtained by numerical integration or simulation. Part of the difficulty is due to the fact that melt rates and their spatial distribution are continuously changing over time, and therefore cannot generally be used as a boundary condition persisting throughout the spring in the same context as the pre-melt SWE distributions, as discussed above. An alternative approach is to apply the above SCD framework to sub-regions of the model domain over which melt rates can be assumed to be uniform (Liston, 1999). Dividing a basin into elevation zones has generally been a common approach used in many studies. However, if very fine scale variations in melt energy or melt rates exist, then the approach may fail.

Some degree of spatial association may be expected between the distributions of SWE and melt rates due to the fact that snow accumulation and ablation processes are often influenced by common underlying factors. The nature of the association between these variables has important consequences for the depletion of the snowcover, and has been investigated by a number of recent studies. Essery and Pomeroy (2004b) and Pomeroy et al. (2001) used theoretical analyses and simulation to examine the influence of melt rate variability on the rate of SCD, and showed that negative correlation tends to initially accelerate SCD as the shallow patches of snow are subjected to higher melt rates and melt out more rapidly. Positive correlation would have the opposite effect, but with greater melt rates to deeper snow, this eventually leads to a faster overall depletion of the snowcover. Faria et al. (2000) reported a negative correlation between melt rates and SWE in the southern boreal forest of Saskatchewan, and showed that this association further accelerated SCD relative to the case with uniform melt rates. They developed a model for upscaled simulation of SCD that presumed a lognormal distribution of SWE and melt rates as a linear function of the rank of the pre-melt SWE values. Pomeroy et al. (2003, 2004) observed a negative correlation between melt rate and SWE at scales of up to 2000 m using transect data in a shrub tundra environment. This was attributed to the effects of slope and aspect on solar radiation receipt, together with the particular orientation of the slopes with respect to the predominant wind direction. They noted that other topographic orientations and blowing snow regimes might lead to quite different associations between melt rates and SWE at this scale. All of this work was based on the underlying condition that the association between melt rates and pre-melt SWE is constant throughout the duration of the melt season.

In addition to spatial variability in the energy supplied to a snowcover, differences in the temporal evolution of the internal snowpack energy state can have a large effect on the timing and rate of snowmelt. Male and Gray (1975) and Norum et al. (1976) discussed the importance of the internal energy term, U, in applying the energy balance principle to shallow prairie snowcovers. During the melt period, runoff is commonly produced in the afternoon, but cooling and refreezing of the snowpack overnight cause large changes in its internal energy content. By Equation (2.3) (p. 26), it is clear that U varies with the depth and density (and thus SWE) of the snowpack, which complicates

the determination of the energy balance and melt rate over an areal SWE distribution. For deeper snow, the magnitude of the internal energy change is relatively minor in comparison to the other components of the energy balance, and therefore is frequently neglected (Male and Gray, 1981). However, this snow takes longer to warm in spring so that melt is often first produced from shallow snow, which may completely disappear before the areas with a deeper snowpack begin to produce melt (Gray and O'Neil, 1974; Male and Gray, 1975; Marsh and Pomeroy, 1996). Horne and Kavvas (1997) suggested that upscaled models are in error by utilizing point-scale energy balance equations and not accounting for the spatially heterogeneous snowmelt process over a grid area surrounding a computational node. They developed areally averaged mass and energy balance equations by assuming the snowmelt process is spatially ergodic, and considered snow temperature and density as stochastic variables.

Within complex windswept alpine environments, the importance of variable snow mass and internal energetics is likely even greater than within the prairies due to the more extreme spatial variability in snowpack depth. Overnight longwave radiation losses, cooling, and refreezing of areas with a shallow snowpack or the upper layers of deep packs are generally greater at higher altitudes. Norum et al. (1976) noted that large differences exist in the energetics and computation of snowmelt between "shallow" prairie snowpacks and "deep" mountain packs; but in windswept alpine terrain, the snowcover exhibits characteristics of both over short distances. Fierz et al. (1997, 2003) applied an energy balance model to simulate the internal energetics and melt of the snowcover in an alpine basin in Switzerland. They showed that in addition to variation in radiative and turbulent fluxes, internal processes such as heat conduction and phase changes need to be accounted for to properly simulate the evolution of initially sub-freezing snowcovers and the effects of refreezing overnight. Many applications of energy balance snowmelt models, however, are restricted to the main melt season and so-called "ripe" snowcovers. Walland and Simmonds (1996) used sub-grid topographic information to divide grid cells into cold snow, melting snow, and snow-free fractions based on a diagnosed freezing level. No studies have considered the effects of differences in internal energy content on melt rate computations over a SWE distribution

for the determination of SCD curves, which is an oversimplification of reality in light of this discussion.

2.3.4 Meltwater Generation and Snowmelt Runoff

The hydrological response at the outlet of a watershed depends on all processes acting within the basin and the pathways and storages of water within it, which act to control the integrated basin response (i.e., runoff) (Blöschl, 2005). For snowmelt, a distinction is made here between meltwater generation and snowmelt runoff, with the former referring to the input of meltwater at the ground surface from the base of the snowpack and the later referring to the water that travels through the basin, with temporary storages and abstractions, to contribute to streamflow at the basin outlet. Alpine catchments are characterized by highly variable surface topography, vegetation, soils and other surface deposits, and by large spatial and temporal variability in hydro-meteorological conditions, and therefore exhibit large spatial differences in snowmelt runoff generation that influence the overall basin hydrograph. Understanding and quantification of this variability is crucial towards successfully representing or modelling snowmelt runoff generation.

Heterogeneity in snow accumulation, and melt timing and rates has an important effect on the generation of meltwater and snowmelt runoff over the landscape. Many studies in a wide variety of environments have focused on this variability along with the integrated response of runoff at the basin scale. In a small prairie watershed, Gray and O'Neil (1974) found that the definition of major sources areas of snowmelt runoff was essential when attempting to relate energy balance predictions with measured basin discharge. Marsh and Pomeroy (1996) investigated the meltwater fluxes at an arctic–forest tundra site in the Northwest Territories. Their results showed that the initial release of meltwater occurred first on upland tundra sites with shallow snow, but meltwater release did not occur until nearly two weeks later in areas with deep snowdrifts. Thus, during the early melt period, the snowcover was only partially contributing to runoff. Pohl et al. (2005, 2006) and Pohl and Marsh (2006) also modelled spatially variable meltwater production and runoff at this site, and demonstrated the

relative importance of variability of the pre-melt snowcover, melt energy fluxes, and local advection processes for the development of a patchy snowcover and for runoff during the spring melt period. The location, timing, and amount of meltwater release depend on these processes and correspond to landscape type and topography (Davison et al., 2006).

In alpine landscapes, the high spatial heterogeneity of both the initial snowcover and the snowmelt energetics are important for basin-averaged snowmelt and runoff (Luce et al., 1998; Anderton et al., 2002; Marks et al., 2002; Lehning et al., 2006; Dornes et al., 2008a, 2008b; Lott and Lundquist, 2008). Marks et al. (2002), for example, investigated patterns of snow accumulation, snowcover energy balance, and melt over a small headwater basin within the Reynolds Creek watershed, and showed how these are influenced by patterns of topographic variation and vegetation shelter. Wind exposed areas melted out prior to the onset of melt-out in wind sheltered areas, providing runoff in the late winter and early spring. Sheltered and drift areas acted as source areas for runoff in late spring and early summer. In this way, the presence of late lying drifts, which can hold a significant amount of the total basin SWE, provides a source for late-season runoff. Within the Colorado Rocky Mountain Front Ranges, Kampf et al. (2010) reported that a hillslope with an east facing aspect produced snowmelt runoff primarily in late May and early June at roughly the same time as the maximum basin scale runoff production. In contrast, a hillslope with a north facing aspect produced runoff in late June to early July as the basin scale runoff was receding. Lehning et al. (2006) used the Alpine 3D snow model together with the calibrated HRU-based PREVAH model (Zappa et al., 2003) in an alpine basin in Switzerland to examine the sensitivity of runoff generation to vegetation, soils, and radiation energy balance. They showed that when the effects of mountain shading, exposure, and slope angle on the local radiation balance were ignored, the efficiency of the modelled discharge was significantly reduced. Thus the differential timing and magnitude of runoff generation from different locations within a watershed play a vital role in the overall hydrograph response. Lott and Lundquist (2008) modelled the spatial differences in snowmelt runoff timing in the Sierra-Nevada Mountains, California, and showed that the effects of shading and aspect play a key role in the sensitivity of different sub-basins to climate change.

In addition to variability in snowmelt rate and timing, the release of meltwater from the base of the snowpack depends on the routing of water through the pack, which can exhibit spatial variability as controlled by snowcover patterns. The daily cycle of net all-wave radiation drives diurnal pulses of melt water from the snowpack, which in turn controls the daily pulse of flow through the hillslope subsurface and into the stream channel. Marsh and Pomeroy (1996) applied a variable flow path meltwater percolation model in their study of meltwater fluxes. Differences in the ripening, retention of meltwater, and flow of water through the pack helped to explain the differences in meltwater release from the different landscape types. In the Sierra-Nevada Mountains, California, Lundquist and Dettinger (2005) and Lundquist et al. (2005) showed how snowpack heterogeneity affects the timing of diurnal pulses of meltwater at the basin outlet. Generally, in small basins, travel times through the snowpack dominate diurnal streamflow timing. They noted that as snowcover heterogeneity increases over larger basins with a greater range of elevation, the timing of streamflow becomes more consistent due to the slower decrease in average depths over the snowcovered areas. Snowpack and melt rate heterogeneity also mean that areas with faster melt rates to dominate the net timing of the snowmelt hydrograph. Therefore, it is important for snowmelt runoff models to include representation of the patchy and heterogeneous snowcover over a basin to properly simulate the meltwater release and streamflow timing.

After meltwater is released from the snowpack, it reaches the landscape surface and travels via several different pathways to the stream network, which gives rise to important differences in the timing and magnitude of water delivery at the basin outlet depending on the path. In areas with relatively impermeable substrate or frozen ground, outflows can be quickly translated to the stream as overland flow or rapid subsurface flows through porous organic horizons near the surface (Carey and Woo, 1998). In many alpine areas, subsurface flow tends to be relatively important where soils are poorly developed or absent, and surface deposits are highly permeable. In the Colorado Front Ranges, Kampf et al. (2010) reported that hillslope and plot runoff was produced mainly by rapid shallow subsurface flow and saturation excess overland flow. A common feature in most high alpine watersheds is the presence of moraines, talus, and bedrock,

which have a large influence on the movement and storage of meltwater (Clow et al., 2003; Liu et al., 2004; Hood et al., 2006; McClymont et al., 2010). Clow et al (2003), for example, showed that groundwater was an important contributor to flow in an alpine catchment in the Colorado Rockies, and that talus slopes within the catchment represented the primary reservoir. These areas were estimated to have a maximum storage capacity as large as the total annual discharge from the catchment. In contrast, McClymont et al. (2010) reported that the total input volume of snowmelt and rainfall to an alpine meadow – talus complex along the continental divide of the Canadian Rockies was several times larger than its groundwater storage capacity. This resulted in a rapid response of the water table and streamflow discharge to snowmelt during the spring. This emphasizes how local bedrock, moraine deposits, and talus slopes are hydrologically important in different watersheds, and how differences in surface cover and geology can influence the storages and transfers within these watersheds. Spatial and temporal patterns of hydrological connections and contributing areas are also an important factor influencing overall basin discharge. For example, in a high elevation meadow system in the Sierra Nevada Mountains, California, Lowry et al. (2010) discussed the hydrological connections and groundwater flux between hillslope and meadow aquifers, and noted that the seasonal variability in water levels was controlled by the spatial and temporal distribution of snowmelt within the watershed and groundwater flux entering the meadow. They suggested that for numerical simulations, it is important to avoid both spatial averaging of groundwater fluxes and temporal averaging of snowmelt pulses entering the boundaries of a model as watershed processes are strongly linked to local scale processes. Finally, baseflow is a slow and stable runoff component of alpine catchments that represents most of the total discharge in winter. The dynamics of this flow component depend on groundwater storage in different aquifers and the amount of groundwater recharge (Clow et al., 2003; Liu et al., 2004; Lehning et al., 2006).

Another feature that affects the delivery of meltwater to the basin outlet is the presence of snow in the stream channels. In windswept areas with incised gulleys and stream channels, snow dams can have a significant influence on the timing and magnitude of meltwater delivery downstream (e.g., Woo, 1998). These channel blockages delay runoff by several days or weeks as the snow acts as a dam for meltwater

flow and as water refreezes in the compacted snow deposits. Ponding of water may occur, with subsequent failure of the snow dam and release of larger quantities of meltwater. In addition, this presents a special difficulty for modelling snowmelt runoff (e.g., Hinzman and Kane, 1991) and currently there is no satisfactory technique to represent this phenomenon in a physically based manner in hydrological models.

3. Development of a Theoretical Framework for Areal Snowcover Depletion and Surface Meltwater Inputs

3.1 Introduction

The purpose of this section is to address the first objective of this thesis. The developments here build upon the theory and literature discussed in Section Two, with a specific focus on complex alpine terrain. This framework is meant to be a simple yet robust approach for handling certain characteristics that are known or hypothesized to be important for the melt and depletion of heterogeneous snowcovers, but which are not currently addressed in a realistic way in most upscaled representations of snowmelt (i.e., differences in SWE distribution patterns across the landscape, variable applied energy to these distributions, small-scale spatial differences in internal snowpack energy content and melt timing/rate, and new snowfall during melt). Consideration is given to the previous work and current understanding of spatial variability, scaling, and snow process representation throughout the development of this framework. It is anticipated that the approach can provide a useful means of upscaling physically-based point-scale snowmelt models, and can be used to examine the influence of spatial variability of snow accumulation and ablation on areal snowmelt and SCD at differing spatial scales.

This framework is based on the lognormal distribution for pre-melt SWE, and the section begins with a description of this distribution. The approach for representing areal SCD under both spatially uniform applied melt and inhomogeneous melt (due to differences in internal snowpack energy) is then presented. Where there is significant spatial variability of incident radiation, areal SCD must be calculated based on separate applied energy and SWE distributions amongst landscape units. An approach for handling the effects of snowfall events during the melt period is discussed as well. It is then shown how the framework can be applied towards representing surface meltwater

inputs over the landscape, which can be used within hydrological models to ultimately predict snowmelt runoff at the basin outlet. Finally, it is shown how the framework can be extended to other distributions.

Before describing the specific technical details of how this framework is applied, it is useful to present a conceptual overview of the approach so that the reader has a sense of how each step fits into the overall procedure. Figure 3.1 below shows a flowchart that highlights the key steps involved with this theoretical framework. It begins with an initial distribution of SWE or multiple distributions stratified by landscape units, and proceeds with the simulation of snowmelt over these distributions. During this step, characteristics of the melt and depletion of cold, heterogeneous snowcovers listed above are explicitly represented. The end result of the framework is a prediction of the basin-wide areal SCD and surface meltwater inputs.

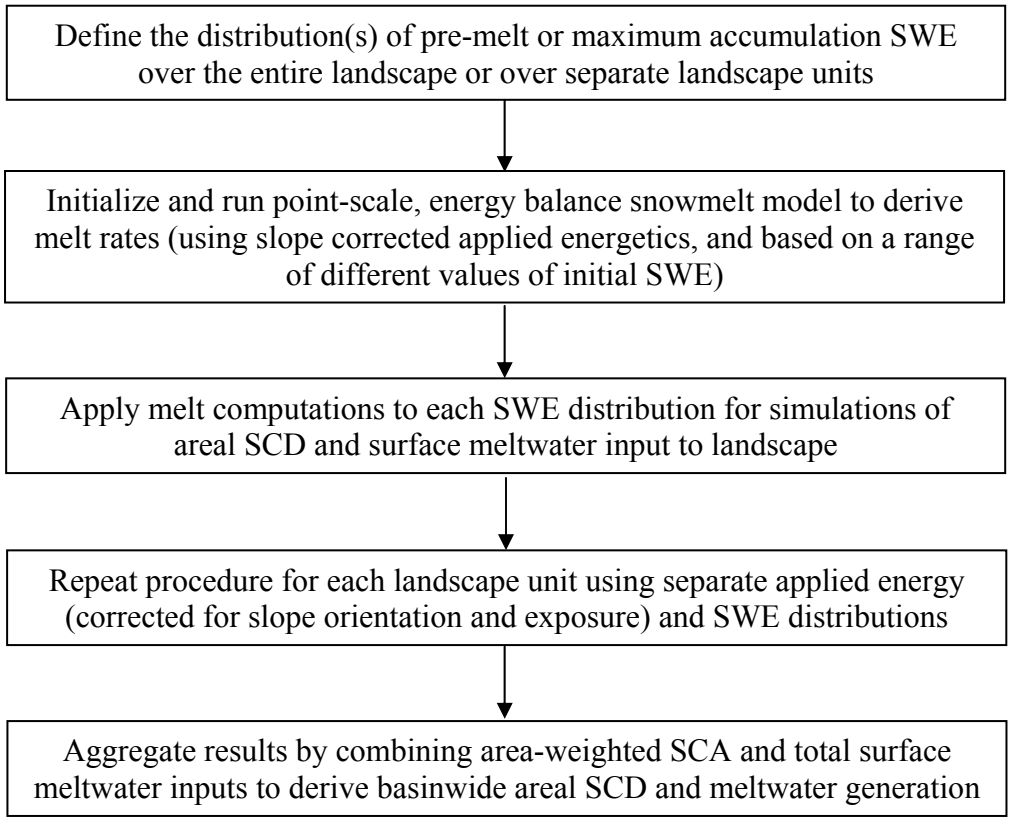

Figure 3.1. Conceptual flowchart describing the key steps involved with application of the theoretical framework for areal SCD and surface meltwater inputs.

3.2 The Lognormal Distribution

As discussed in Section 2.1.3, a wide range of studies have found that pre-melt distributions of SWE can be approximated reasonably well by the lognormal distribution when stratified by terrain features. The framework described here is therefore based on this distribution. Brutsaert (2005, p. 518) noted that:

> "The application of most theoretical distribution functions can be justified on strict probabilistic considerations. Unfortunately it is rare that that such considerations are rigorously valid for data sets of hydrologic concern, and in most cases the actual mathematical form of the distribution function, that represents the population, is unknown. Thus the best that can be hoped for is that the selected distribution is simple enough and also physically plausible to be useful in practice."

The lognormal distribution has the advantage of being a relatively simple distribution that is not difficult to characterize mathematically. Also, only two parameters – the mean and coefficient of variation (CV; i.e., standard deviation/mean) – are needed to specify this distribution, and these can be obtained from field transect surveys of SWE.

For SWE values, the lognormal distribution is expressed in terms of the probability density function of the transformed variable, $y = \ln(\text{SWE})$ as:

$$f(y) = \frac{1}{\sigma_y^2\sqrt{2\pi}} \exp\left(-\frac{(y-\bar{y})^2}{2\sigma_y^2}\right), \tag{3.1}$$

where $\bar{y}$ and σ_y are the mean and standard deviation of the logarithmic values of SWE respectively. These values can be determined from the $\overline{\text{SWE}}$ and CV of the natural values using the following equations:

$$\bar{y} = \frac{1}{2}\ln\left(\frac{\overline{\text{SWE}}^2}{1+\text{CV}^2}\right), \tag{3.2}$$

and

$$\sigma_y = \sqrt{\ln(\text{CV}^2+1)}\ . \tag{3.3}$$

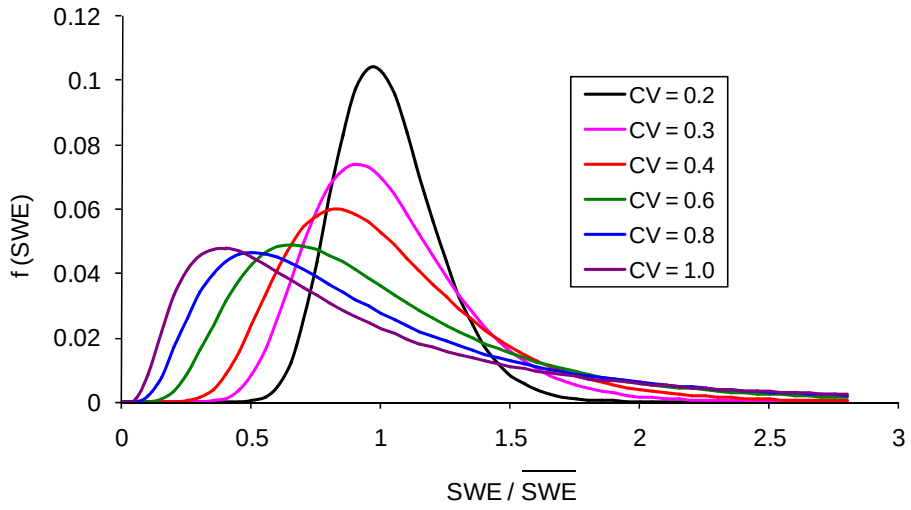

Figure 3.2. Graphical representations of the lognormal probability density function for different values of CV, normalized by $\overline{\text{SWE}}$.

Figure 3.2 provides some examples of this distribution for different values of CV, showing how the distribution becomes less peaked as the CV increases. Chow (1954) showed how the lognormal distribution can be conveniently expressed in the following linear form (in this case for SWE):

$$\text{SWE} = \overline{\text{SWE}}(1 + K\text{CV}), \text{ or} \tag{3.4a}$$

$$\text{SWE} = (\overline{\text{SWE}} + K\sigma), \tag{3.4b}$$

where SWE is the value of the snow water equivalent having an exceedence probability equal to that of the frequency factor, K, and σ is the standard deviation of the natural values. When the values of the transformed variable are normally distributed, K in Equation (3.4) is the well-known z-statistic of the normal distribution, and is given by:

$$K = \frac{1}{CV}\left[\exp\left(\sigma_y K_y - \frac{\sigma_y^2}{2}\right) - 1\right], \tag{3.5}$$

where $K_y = (y - \bar{y})/\sigma_y$, the frequency factor of the transformed data.

Equation (3.4) describes the theoretical two-parameter lognormal distribution. Thus, observed values of SWE plotted against K should approximate a straight line with a slope equal to the standard deviation of SWE and an intercept at K = 0 equal to $\overline{\text{SWE}}$

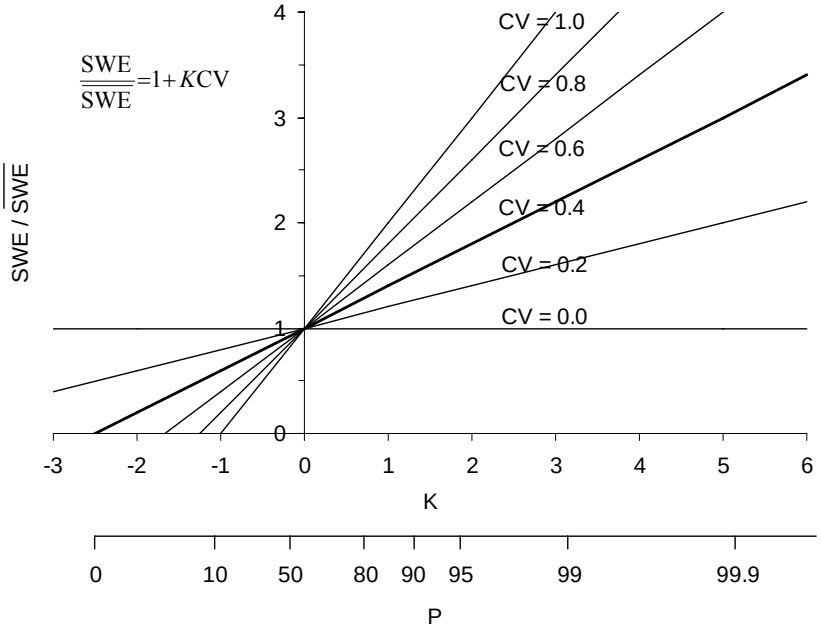

Figure 3.3. Plots of the lognormal distribution for SWE expressed by Equation (3.4). Secondary horizontal scale shows the cumulative probability for the distribution with CV = 0.4.

provided that the underlying distribution is lognormal. Figure 3.3 shows normalized plots of Equation (3.4) for various values of CV to provide a sense of how this distribution appears when expressed in this form.

To use snow survey data within this framework and compare observations with this theoretical distribution, observed values of K and SWE should be used. Values of K for observed data (excluding observations of zero SWE depth) can be calculated as (Chow, 1954):

$$K = \frac{\exp\left(\sigma_y K_y - \frac{\sigma_y^2}{2}\right) - 1}{\sqrt{\exp\left(\sigma_y^2\right) - 1}}. \tag{3.6}$$

A value for observed K_y is required for Equation (3.6); this may be determined by noting that the exceedence probability, P, of K_y and SWE are equal for a given sample of n observations. The probability of K_y being exceeded, $P(K_y)$, is:

$$P(K_y) = \frac{1}{\sqrt{2\pi}} \int_{K_y}^{\infty} \exp\left(-\frac{K_y^2}{2}\right) dK_y \,. \tag{3.7}$$

The exceedence probability of each measurement for a set of observations of SWE can be determined following Gumbel (1954) as:

$$P(\text{SWE}) = \frac{r}{n+1}, \tag{3.8}$$

where r is the rank of the SWE observation when arranged in decreasing order of magnitude and n is the number of observations. Given that P(SWE) = $P(K_y)$, corresponding values for observed K_y can be determined by taking the inverse of the standard normal cumulative distribution for the values of 1 – P(SWE) for each SWE observation (e.g., P(SWE) is the exceedence probability and therefore 1 – P(SWE) is the cumulative probability).

Figure 3.3 on the previous page also shows how the cumulative probability of SWE theoretically varies across the distribution (specifically in this case for a CV value of 0.4) using a secondary horizontal scale. This is determined for K values by solving for the corresponding K_y value, evaluating Equation (3.5), and setting P(SWE) = $P(K_y)$. More than 50% of the distribution has values less than the mean, and is characterized by negative K values. Chow (1954) showed how the probability density varies over the distribution as a function of the coefficient of skew, C_s, which is given as $C_s = 3 \cdot CV + CV^3$. The probability at the mean is only equal to 50% under the condition of $C_s = 0$, and is otherwise less than 50%. The positive skew is also clearly evident through the gradual decline in the proportion of the higher values of SWE and K.

For this distribution to provide a useful approximation to the true snowcover variability, it may be necessary to stratify the landscape according to terrain and land use features. This can reduce the overall CV and has merit as it improves the confidence of the fit of the distribution, reduces the necessary field sampling, and can produce a more unimodal distribution (e.g., Steppuhn and Dyck, 1974). Therefore, appropriate landscape stratification is an important consideration in order to successfully apply this framework.

The lognormal distribution can only be defined for $0 < \text{SWE} \leq \infty$. Thus, the entire landscape or areal unit should be snowcovered for an approximation based on this distribution. This may be a problem in complex terrain where there are cliffs or other

features that are permanently snow-free (e.g., Blöschl et al., 1991). If these features occupy only a very small percentage of the total landscape area, then this can likely be neglected without causing significant error, but if the area occupied by cliffs, etc., is relatively large it will be necessary to exclude these areas and only consider the distribution over the remainder of the landscape.

3.3 Areal Snowcover Depletion

Approximations of the snowcover distribution based on the lognormal distribution are well suited for the calculation of SCA and areal SCD over the landscape. Expressed in the linear form of Equation (3.4), the value of K is related to the exceedence probability of the corresponding value of SWE. Therefore, the frequency factor corresponding to specific SWE values can be used as an index of the probability of that particular value of SWE being exceeded, or alternatively, the areal fraction of the snowcover with a value of SWE exceeding that particular value. As previously noted in Section 2.3.2, the SWE distribution at the start of melt is both an initial condition as well as a boundary condition that persists throughout the melt period. In this regard, as the snowcover melts, the probabilities and area fractions defined for the initial distribution can be used together with the amount of melt over time to track the state of the snowcover. For instance, as areas with a shallow snowcover melt out and expose the underlying ground, the value of K from the initial distribution corresponding to SWE = 0 (i.e., K_{min}) at a given time provides an index of the snowcovered area over the landscape. This holds for melt rates applied uniformly or for inhomogeneous melt across the distribution, as well as following new snowfall events during the melt period. These features and their mathematical representation are explained here, together with some specific examples to help elucidate the procedures.

3.3.1 Uniform Applied Melt

The SCD curve can be derived from an initial distribution of SWE (defined by $\overline{\text{SWE}}$ and CV) and a one dimensional uniform melt rate applied to the distribution over time. The

application of a uniform melt rate has been the standard approach used in most lumped models for handling sub-grid SCA. The steps involved are as follows:

1. Establish the values of $\overline{\text{SWE}}$ and CV that describe the pre-melt SWE distribution.
2. Plot the distribution based on the condition that SWE = $\overline{\text{SWE}}$ at $K = 0$, and SWE = 0 at $K = K_{min}$; at this initial condition, SCA = $0.\overline{99}$.
3. The line representing the SWE distribution is then shifted downwards by the amount of melt in the next timestep, and the x-intercept is recalculated.
4. From the value of K at this new x-intercept, calculate K_y using the following modification of Equation (3.5):

$$K_y = \frac{\ln(1 + K\text{CV})}{\sigma_y} + \frac{\sigma_y}{2}. \tag{3.9}$$

5. Based on this value of K_y, the SCA fraction (equivalent to P(SWE)) is quantified as $P(K_y)$, which can be solved using Equation (3.7) or equivalently determined as one minus the value of the standard normal cumulative distribution function evaluated for K_y.
6. For each successive timestep, the distribution is shifted down further by the amount of melt and the procedure is repeated.

The following simplified example illustrates this procedure. Initial conditions of $\overline{\text{SWE}}$ = 200 mm, CV = 0.4, and a constant melt rate of 30 mm/day are assumed. Figure 3.4a shows this initial distribution and its melt over time, while Table 3.1 provides some of the corresponding values used in the calculation of SCA for the times depicted in the figure. The slope of the line is equal to the standard deviation of the pre-melt distribution (i.e., 80 mm), giving an initial K_{min} of –2.5 corresponding to SCA of $0.\overline{99}$. As the distribution is uniformly melted and the line is shifted downwards, the value of the x-intercept each subsequent day is used to determine the SCA.

The depletion of SCA over time is shown in Fig. 3.4b, which includes points indicating the specific days shown in Fig. 3.4a. For the first few days SCD is negligible, but then the rate rapidly increases after the third day, and gradually declines later in the melt period. The shape of this curve is directly linked to the probability distribution,

Table 3.1. Values of some of the variables for SCA calculation over time under uniform melt conditions.

Days after melt onset	Accumulated melt depth (mm)	*K* value (i.e., x-intercept)	K_y value	SCA (i.e., *P*(SWE))
0	0	–2.5	-	$0.\overline{99}$
2	60	–1.75	–2.94	0.99
5	150	–0.625	–0.55	0.71
10	300	1.25	1.26	0.11
15	450	3.125	2.30	0.01

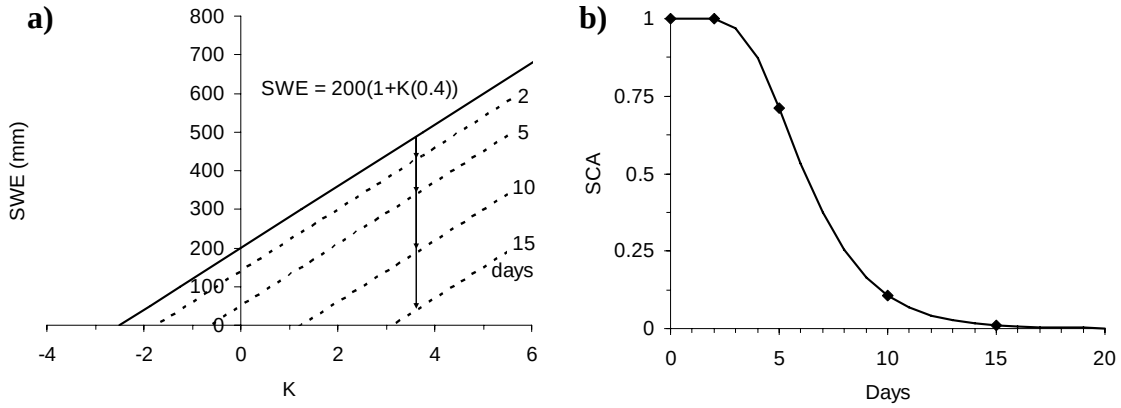

Figure 3.4. a) Representation of initial distribution with parameters $\overline{SWE}$ = 200 mm and CV = 0.4 (solid line), and uniform melt of this distribution over time (dashed lines); b) SCD curve derived from the melting of this distribution.

which has a high density for shallow SWE values below the mean, and is skewed with a gradually declining proportion of greater values of SWE.

This example used a constant melt rate over time, while in reality this rate would vary from day to day and over different parts of the day. Any point-scale snowmelt model could be used to provide an estimate of the melt rate to be applied over the distribution, but the assumption is that the melt rate is applied to all parts of the distribution and the landscape or areal unit evenly. Thus, the energy supply to the surface and the internal energy changes must be assumed to be spatially uniform. This can be a major limitation in areas of complex terrain with an initially cold and highly heterogeneous snowcover.

3.3.2 Inhomogeneous Melt

Often, the most important energy source in the snowmelt energy balance is the net shortwave radiation flux, and to a lesser degree, the net longwave flux. Stratification of the landscape into terrain-based features such as areal units of relatively uniform slope, aspect, and elevation may therefore resolve much of the variability in energy supply to the surface. At the same time, this stratified approach can reduce the CV and improve confidence in the goodness of fit of the distribution, as previously described. This is the first step towards successfully applying such a framework, and requires some consideration for the choice of spatial units and the degree of disaggregation of the landscape. By separately accounting for SWE distributions according to landscape/ terrain units and resolving the primary sources of variability in shortwave and longwave radiation, the assumption of uniform energy supply to the distribution becomes more justified.

A remaining problem is the determination of the melt rate to apply to the distribution on each areal unit. Physically based snowmelt models utilizing the energy balance equation must account for the internal energy state of the snowpack to properly determine the timing and magnitude of melt. Even under the assumption of uniform energy receipt at the surface, differences in snowmelt are inevitable over a cold (i.e., < 0 °C) and heterogeneous snowcover as a result of variability in U (Equation (2.3); p. 26) and dU/dt (Equation (2.2); p. 23) across the distribution. Therefore, this framework must be extended to include an approach for handling this effect.

The problem can be addressed by considering separate classes, or bins, of SWE for the computation of melt rates. This allows variability in melt timing and rates due to differences in the internal energy content to be resolved over a SWE distribution. Since all that is required to track the SCA state over time are the pre-melt SWE distribution and the x-intercept (K_{min}) of the line in a plot of K vs. SWE, a similar approach to that for uniform melt can be used. Essentially, the line representing the pre-melt distribution can be discretized into a number of individual segments connected by nodes, which are specific (K, SWE) pairs along the initial distribution. The SWE values are tracked over time by the snowmelt model to adjust the location of these nodes as well as the line

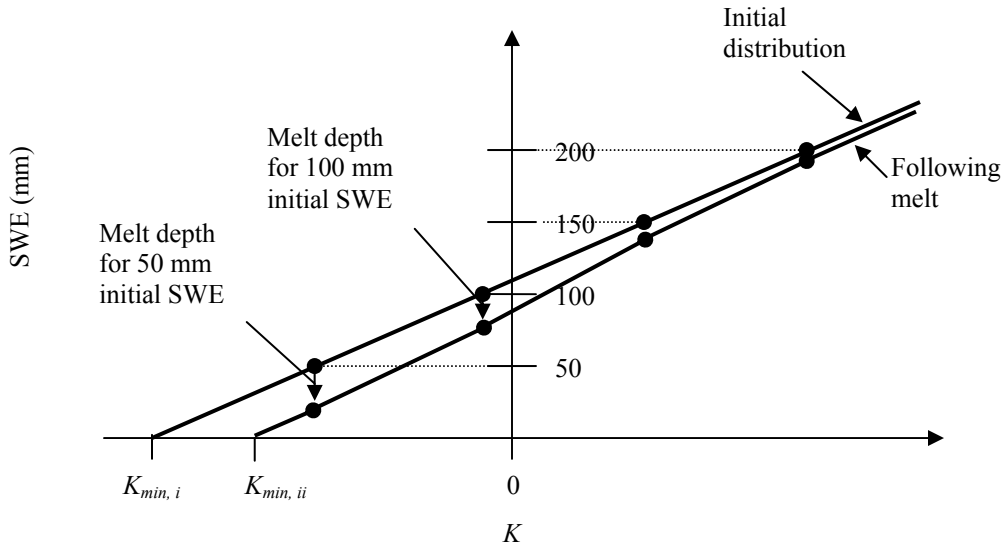

Figure 3.5. Conceptual framework for handling inhomogeneous melt over a SWE distribution by computing melt rates separately for different SWE values.

segments between them. Figure 3.5 shows a conceptual representation of this approach for a hypothetical K–SWE plot. In this case, shallower SWE has either begun to melt earlier or has melted at a faster rate than the deeper SWE. Nodes are initially defined for SWE values at 50 mm intervals, together with their corresponding values of K, and point-scale melt rate computations are used to reduce these values of SWE individually. The value of K_{min} increases over time as in the case for uniform applied melt.

An important aspect is to be able to determine the x-intercept over time using this framework, but it is not readily clear how this should be done. The slope of each segment of the line is initially equal to the standard deviation; however, this will change once the individual SWE depths begin to undergo differential melt. A possible approach for predicting the intercept would be to use this initial slope for the segment representing the shallowest SWE. Once the first simulated SWE depth (i.e., the first node) melts out, a new slope can be determined and used for the intercept over the subsequent K interval. This can be found at the time of melt out using the following variation of the point–slope formula for the line:

$$a = \frac{\mathrm{SWE}_2 - \mathrm{SWE}_1}{K_2 - K_1}, \tag{3.10}$$

where a is the slope for the segment, $SWE_1 = 0$ and SWE_2 is the next lowest value being tracked, and K_1 and K_2 are the corresponding values of the frequency factor. Once the x-intercept is determined, the procedure described for uniform melt conditions can be used to solve for SCA.

To provide an example of how inhomogeneous melt over a SWE distribution (due to either earlier or more rapid melt of shallow snow) theoretically influences the rate and timing of areal SCD, Figure 3.6 shows SCD curves derived from two different snowmelt scenarios using various approaches to generating the curves. Daily SCA values were based on an initial lognormal SWE distribution with parameters $\overline{SWE}$ = 200 mm, CV = 0.4. To compute SCA values each day, the distribution was discretized into 50 mm wide SWE classes with initial values of 50, 100,… 500 mm. The first hypothetical scenario assumed melt rates (m_r) to vary with remaining SWE according to $m_r = -0.06(SWE) + 43$, such that melt rates ranged from ~43 mm/d for SWE depths near zero to 13 mm/d for SWE depths with 500 mm (Fig. 3.6a). Under this approach, melt rates gradually increased over time as each initial value of SWE progressively became smaller. The second approach assumed uniform melt of 30 mm/d, but that melt of each SWE class began progressively one day later than the previous shallower class (Fig. 3.6b). For each of these two hypothetical snowmelt scenarios, areal SCD curves were derived using the approach described above by tracking each SWE value over time and predicting K_{min} and SCA each day (inhomogeneous melt of SWE classes). For comparison, approaches assuming uniform melt rate and timing over the distribution were used to derive SCD curves. In these instances the initial distribution was shifted downwards by the daily melt depth for either the initial 300 mm or 500 mm SWE values to predict daily SCA values.

The results show an acceleration of areal SCD when explicitly accounting for this inhomogeneous melt, and that when melt rates based on progressively deeper snowpacks are used to predict the depletion of the snowcover, the delay in SCD timing becomes larger. In reality, the variation in melt timing and rates over a natural SWE distribution might differ from these hypothetical scenarios and would change considerably over time, but this highlights an important point. In order to use a point-scale snowmelt model to predict melt rates for which to uniformly apply over a SWE distribution, the model simulation must be based on sufficient initial SWE to represent the deepest areas of the

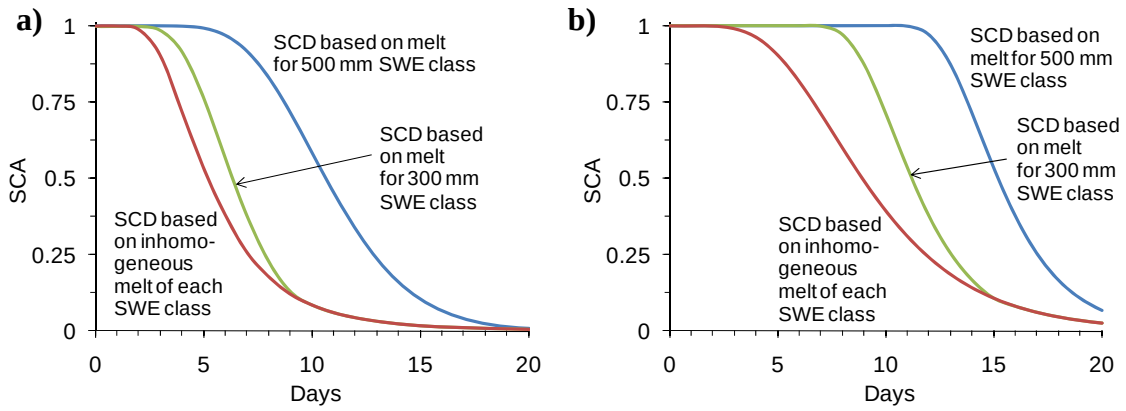

Figure 3.6. Areal SCD curves generated from melt of initial SWE distribution with parameters $\overline{\text{SWE}}$ = 200 mm and CV = 0.4: a) melt rates vary with remaining SWE as m_r = –0.06(SWE) + 43; b) melt rates of 30 mm/d with progressively one day later melt initiation per SWE class.

snowcover over the landscape. In the example above, this was 500 mm, as the snow based on 300 mm initial SWE melted out prior to the end of the 20 day simulation and subsequent SCA computations had to be based on initially deeper SWE values. Therefore if melt timing and/or rate varies in reality over a SWE distribution, modelling approaches using uniform melt based on deeper snowpacks will be subject to this error.

In considering inhomogeneous melt across a SWE distribution, it would also be possible to discretize the probability distribution, f(SWE), into classes or segments, solve Equation (2.5) (p. 38) for each of these individually, and sum the results for the overall SCA. The novel approach presented in this section has several advantages though. First, it produces a smooth and continuous representation of the depletion of SCA, while allowing for unique melt timing and rates for different SWE depths over the distribution. It is also possible to include the effects of smaller scale variability in melt energy to the surface if there is a quantifiable relationship between melt energy and initial SWE that is persistent over time (e.g., Faria et al., 2000; Pomeroy et al., 2001). Provided that areas of deeper snow do not melt out before areas of shallow snow, a positive association between melt energy and SWE can be represented as well. Even under such circumstances, it is more common in nature for the shallowest SWE within a given landscape unit to melt out before areas with deeper snowcover, so in general this would not pose a problem.

Another advantage of this approach is that it can be used further to handle the effects of snowfall events that take place after melt and SCD have begun to occur. This is discussed in the following section.

3.3.3 Effects of Snowfall Events during Melt

In environments where it is common for snowfall events to occur part way through the melt period, it is important to include representation of these effects. This framework can easily be adapted to handle this in a conceptual manner, based on the peak accumulation SWE distribution and the evolution of K_{min} over time. In the cases of both uniform and inhomogeneous melt, the initial distribution specifies the proportion of the total area covered by different SWE depths, and can be used to track the changes in these areal fractions as the distribution is melted. This feature can be similarly used for the reverse condition of snow accumulation, the only consideration being on how the snow is redistributed over the landscape.

Figure 3.7 provides a representation of how a late spring snowfall event might add SWE uniformly over the landscape following a period of uniform melt. The initial distribution is defined by curve 1 and melts over a period of time to curve 2, exposing some of the underlying surface and producing a new K_{min}. Uniform snowfall shifts the curve upwards by the amount of new SWE to curve 3 and produces a horizontal "foot" for the portion of the initial distribution that had become snow-free. This conceptually represents the fact that the new snowfall covers the entire landscape. There is no longer an x-intercept, but the K_{min} for this state can be taken as the original K_{min} of the peak distribution. As melting conditions resume, the curve may be shifted back down to simulate the depletion of SCA once again. It is noted that by this approach, once the new SWE depth has melted the effect will be an instant transition from complete snowcover to the previous SCA just prior to the snowfall event.

The conceptualization of how new SWE is redistributed over the landscape (and across the K–SWE plot) can be redefined to more realistically simulate the depletion of SCA following snowfall events. Rather than defining a horizontal foot, it is possible to set the accumulation at the original K_{min} equivalent to some arbitrary fraction of the total

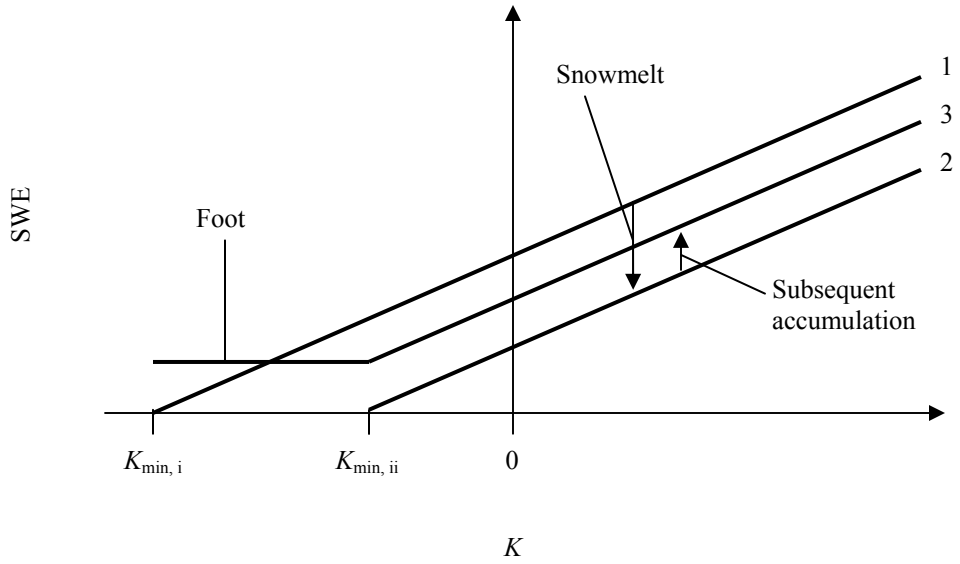

Figure 3.7. Theoretical lognormal SWE distribution showing the effects of uniform applied melt and uniform new snowfall accumulation.

snowfall depth, and linearly interpolate the segment of the line between this value and the SWE added at the previous K_{min} just prior to the snowfall event. This approach is similar in some respects to many of the previous conceptual approaches in the literature for handling new snowfall (e.g., Luce et al., 1999; Moore et al., 1999; Davison, 2003). For example, it establishes a type of D_{100A}, or depth of snow/SWE for accumulation events by specifying an amount of SWE to be melted before any SCD occurs. It also acts as a rescaled depletion curve that follows the shape of the original depletion curve defined by the relationship between K and P(SWE), but which is scaled by the snowfall amount. What is different in this case from the approaches developed in these previous studies is that here the approach is based on information from the maximum accumulation, or peak SWE distribution (i.e., K vs. SWE plot), where values of K_{min} based on this distribution correspond to specific values of P(SWE) and SCA. Therefore all that is required to track the evolution of SCA following new snowfall events is the value of K_{min}, which can be determined according to the shape of the foot described above as snowmelt resumes.

A key advantage of this approach is that it allows the system to retain some "memory" of previous melt conditions over the distribution. Depending on how accumulation is specified over previous snow-free areas as well as the remainder of the

distribution, any prior variability in snowmelt is preserved as the new snow depth may be added to the simulated (K, SWE) nodes and the line segments readjusted. Hysteresis-type effects can also be represented when snowfall events occur in succession during the melt period, such that the snow from one event does not completely melt before the next event occurs. For these reasons, the technique should provide a simple and robust approach for handling the effects of spring snowfall events. It should be able to produce realistic results of SCA; however, it is noted that the approach is conceptual and does not necessarily conserve mass over the landscape at all times. The condition of mass continuity is only met when new snow accumulation is distributed uniformly, or is redistributed by properly accounting for the amount of snow transported amongst SWE classes together with the area that these classes occupy. This is discussed further in the following section.

3.4 Surface Meltwater Generation

It has been shown how the framework here provides an approach for representing areal SCD and investigating the effects of melt rate and SWE variability, but a further extension for use in hydrological studies is required. Within this context, understanding of the location, extent, and timing of primary runoff generating areas, as well as the rate of meltwater production within them, is required to predict the snowmelt inputs to the basin for use within a hydrological model. This is possible based on the pre-melt SWE distribution and melt rate computations over this distribution, in a similar manner as for the determination of SCD curves. This again is because the initial distribution provides information on the areal extent of different SWE depths over a landscape unit, which can be tracked over time. Here, an approach for using the framework for the purpose of predicting meltwater generation and runoff is described.

For the case of spatially uniform melt within a landscape or terrain unit, the total volume of meltwater production is simply the product of the SCA and the melt rate. However, even if uniform melt can be assumed, this may oversimplify the reality of melt-water release and timing from the variable snowcover due to differences in water retention and transit time through the snowpack (e.g., Colbeck, 1972; Colbeck and

Davidson, 1973). Thus, it is ultimately necessary to consider different classes of SWE in order to properly represent the meltwater inputs to the ground surface.

Beginning with the distribution of SWE at peak accumulation, the areal fraction occupied by the different classes of SWE chosen for snowmelt computations must be established. This can be based on either pre-selected values of SWE or alternatively, specified probability intervals over the distribution. For set values of SWE, the area is determined by solving for K and the corresponding exceedence probability based on the initial distribution, and taking the difference in probability of the upper and lower limits of a class. To use specified probability (and hence area) intervals, the associated K and SWE values need to be determined. This is somewhat more complex, but can be done iteratively by solving the inverse of Equation (3.7) to obtain K_y, and then evaluating Equations (3.4) and (3.5) to obtain K and SWE respectively. Spreadsheet programs such as Microsoft® Office Excel, however, include a function to directly solve for the value at a given probability based on the lognormal distribution (e.g., the LOGINV function in Excel).

Figure 3.8 shows graphical examples of both approaches to breaking up a SWE distribution and obtaining the values of K, SWE, and P. For this particular distribution, the use of SWE at 100 mm intervals beginning from 50 mm results in large variation of the probability within each of the classes (Fig. 3.8 a). A single class contains nearly 50% of the total distribution, while other classes representing deeper SWE contain only a negligible proportion. Thus both finer and coarser resolution of classes is needed for the shallow and deeper parts of the SWE distribution, respectively. Taking equal probability intervals of 0.2 results in considerable variation in the width of SWE classes (Fig. 3.8 b). For example, one class has a range of only 34 mm, while all snow deeper than 257 mm is represented by a single SWE class. Instead of taking equal probability intervals across the entire distribution, Figure 3.8 c shows how the upper range of the distribution can be divided so that the deepest 5% of SWE values are represented in a separate class. This is a more appropriate means of representing the range of SWE values and the probability density over this range. It allows for improved resolution of the small areas with the deepest snow drifts and adds another SWE class for the above average, mid-range part of

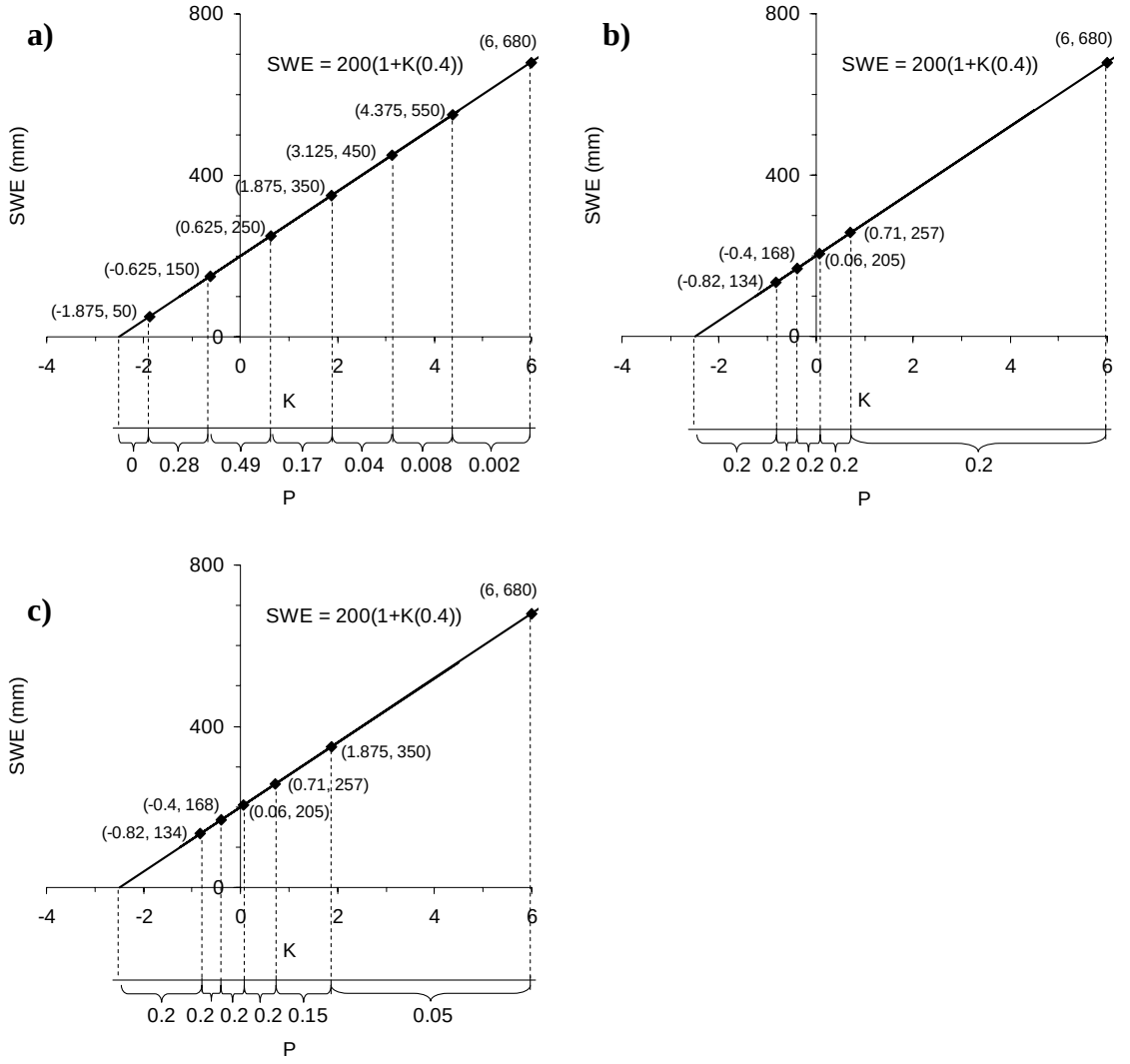

Figure 3.8. Calculations of *K*, SWE, and *P* values for lognormal SWE distribution with $\overline{SWE}$ = 200 mm and CV = 0.4: a) based on equal SWE intervals; b) based on equal probability intervals; c) based on a combination of the two approaches. Labels for the nodes represent the values for each (*K*, SWE) pair.

the distribution. Analysis in Section Five of this thesis shows that differences in internal energy and melt timing/rates vary most strongly for SWE values of less than approximately 400 mm. Therefore, adding another SWE class to this range of the distribution is beneficial towards improving resolution and capturing this variability, rather than grouping these values together with the uppermost SWE values in the distribution.

Once the area of the bins associated with various initial SWE depths is established, a point-scale snowmelt model can be used to represent melt rates and meltwater transmission through the snowpack. The results can then be weighted by the relative area that the bin occupies and aggregated together over the landscape unit to give the meltwater input to an HRU. If snowfall events occur during the melt period, their effects can be handled by adding the new SWE to each of the bins either uniformly or according to some pre-determined redistribution factor. The assumption of uniform snowfall inherently preserves mass continuity; to achieve this using an approach based on redistribution factors, it must be ensured that:

$$\sum_{i=1}^{n} R_{f,i} P_i = 1, \tag{3.11}$$

where R_f is the value of the redistribution factor, P is the probability (or relative area), and n is the number of bins. Snowfall redistribution may also occur between landscape units, or even between basins, while the relative degree of redistribution may also vary depending on the meteorological conditions and probability of occurrence of blowing snow (e.g., Li and Pomeroy, 1997b). Therefore, such an approach will require careful consideration. The assumption of uniform snow may be more justifiable for spring snowfall events as the threshold wind speed for blowing snow transport is high and therefore probability of blowing snow is very low for warm/wet snow (Li and Pomeroy, 1997a, b).

A challenge may arise in instances where melt and runoff begin to occur prior to the time of maximum accumulation, which would occur in mountainous environments that characteristically receive abundant spring snowfall amounts. This makes it somewhat difficult to determine the area of bins to use at these times. One approach to handling this situation could be to base the relative areas on the distribution present at the time when melt begins, and later update these areas for the maximum accumulation SWE distribution. Although this preserves continuity due to the fact that the areas are intrinsically linked to the SWE distribution, it does not ensure model simplicity and may be difficult to implement. Alternatively, the bin areas can simply be derived from estimates of the parameters of the peak distribution and used throughout the entire simulation period. In particular, values of CV may be assumed to be conserved over time

since the standard deviation generally tracks with the $\overline{SWE}$, yielding small changes in CV (Pomeroy et al., 2004; Egli and Jonas, 2009). This is a simpler approach and retains forecasting capabilities of the model, but may result in slight errors due to the misrepresentation of the true areas of each SWE class prior to maximum accumulation. In the case of either approach in these situations, the overall error should not be too large since most of the meltwater generation and runoff should occur after the time of maximum snow accumulation (Woo and Thorne, 2006).

Many previous studies have considered the variability in SWE and applied snowmelt energetics over a watershed to define different meltwater and runoff producing areas (e.g., see Section 2.3.4). The framework described here is unique and novel in two key ways. First, it represents the small scale, sub-unit variability in snowmelt runoff generation over a SWE distribution in a stochastic manner, rather than treating the timing and magnitude of snowpack outflow as uniform over the landscape unit, constrained only by the SCA. This is important for windswept alpine environments that are characterized by extreme variability in SWE over short distances and variability in radiation inputs between slopes. It also allows characterization of a meltwater generating area (MGA) that is not equal to the SCA at times when shallow snow has begun to release meltwater, but deeper snow is still warming and ripening and not yet producing outflow. Secondly, it allows the areas of the different SWE bins (which produce runoff at different times and rates) to be determined uniquely each year according to the snow conditions of a given year (i.e., $\overline{SWE}$ and CV). This is in contrast to assuming the major meltwater producing zones to occupy the same location and spatial extent year after year, with snow amounts in different locations scaled by a drift factor as in previous studies (e.g., Luce et al., 1998 Tarboton et al., 2000). Under the assumption that the CV value is relatively consistent between years, differences in the extent of the runoff contributing areas on each unit are then primarily related to year-to-year differences in $\overline{SWE}$. This effectively captures the dynamic behaviour of spatial patterns of SWE and snowmelt runoff generation, yet is simple and easy to represent within a hydrological model.

3.5 Extension to Other Distributions

The framework described in this section has been developed for the lognormal distribution, which has been widely reported as a useful approximation to the true pre-melt snowcover variability. However, the methods described here for areal SCD and snowmelt runoff generation are not limited to this distribution. They can, in fact, be applied in a similar manner for any theoretical or empirical distribution used to describe SWE variability. The framework is extended here to include all statistical frequency distributions. An example is provided using the gamma distribution, which has been another common distribution used in the literature to describe snowcover variability.

Expressing any probability density function for SWE values in cumulative form gives the areal distribution curve (ADC; Donald et al., 1995). The ADC can easily be plotted for any parametric distribution; alternatively, an empirical set of survey data can be used to generate this curve from a histogram of SWE values. ADC curves provide information on the proportion of the landscape with SWE values greater than a specified amount, and can therefore be used together with the amount of melt over time to track the SCA. The method is equivalent to solving Equation (2.5) (p. 38), and has been widely applied in the past. However, only a few studies have considered the effects of varying melt rates over a distribution (e.g., Faria et al., 2000; Pomeroy et al., 2001; Essery and Pomeroy, 2004b), and here the emphasis is on the consideration of internal energetics and melt rate computations for different SWE values over a distribution.

In this thesis, the approach developed for the lognormal distribution (expressed in the form of a linear K–SWE plot) has been to discretize the line into segments defined between nodes of (K, SWE) pairs. This approach can similarly be applied for any ADC by discretizing the curve into linear segments defined by points of SWE and corresponding P at peak accumulation. The choice must be made, as in the case of the lognormal distribution, of how to segment the distribution to achieve an optimal representation of SWE classes and probability intervals over the distribution. Melt rate computations can then be applied to each of the (P, SWE) pairs independently to simulate the melt and depletion of the SWE distribution, with the segments continuously adjusted between nodes. SCA estimates can be made from the intercept at SWE = 0, while

snowmelt runoff amounts can be determined using weighted inputs from the different SWE bins based on their pre-melt areal extent. The effects of snowfall events during melt can also be handled by adding the new SWE to the bins and snow-free areas as described in Section 3.3.3. In this way, the extension to other distributions retains all of the components of the framework based on the lognormal distribution. The following section illustrates some of these concepts for a hypothetical SWE distribution based on the gamma distribution.

3.5.1 The Gamma Distribution

The gamma distribution has been another common distribution used to represent SWE variability over the landscape (Alfnes et al., 2004; Kuchment and Gelfan, 1996; Skaugen, 2007; Skaugen et al., 2004). This parametric form has the advantage that it describes a distribution with positive skew without the need for log transformation, and is limited to values in the range SWE ≥ 0. This distribution for continuous values of SWE is given by:

$$f(\mathrm{SWE}) = \frac{1}{\beta^{\alpha}\Gamma(\alpha)}\mathrm{SWE}^{\alpha-1}e^{-\mathrm{SWE}/\beta}, \tag{3.12}$$

where α and β are the shape and scale parameters respectively, and $\Gamma(\alpha)$ is the gamma function, defined by:

$$\Gamma(\alpha) = \int_0^{\infty} \mathrm{SWE}^{\alpha\text{-}1}e^{-\mathrm{SWE}}d\mathrm{SWE}\,. \tag{3.13}$$

The parameters of this distribution have the properties that $\alpha\beta = \overline{\mathrm{SWE}}$, and the variance of the natural values, σ^2, is equal to $\alpha\beta^2$. The main limitation of the gamma distribution for use in snow hydrology is that these parameters may be difficult to estimate.

Figure 3.9a shows a hypothetical probability distribution of SWE and its corresponding ADC based on the gamma distribution with parameters $\alpha = 6$, $\beta = 33.33$. This gives $\overline{\mathrm{SWE}}$ = 200 mm and CV = $\sqrt{\alpha\beta^2}/\alpha\beta \approx 0.4$. Figure 3.9b shows an approximation of the ADC with linear segments based on SWE values taken at 100 mm intervals from zero. Suppose, for example, the distribution is uniformly melted by 150 mm, effectively shifting the ADC to the left. At this time, the initial SWE value of 200

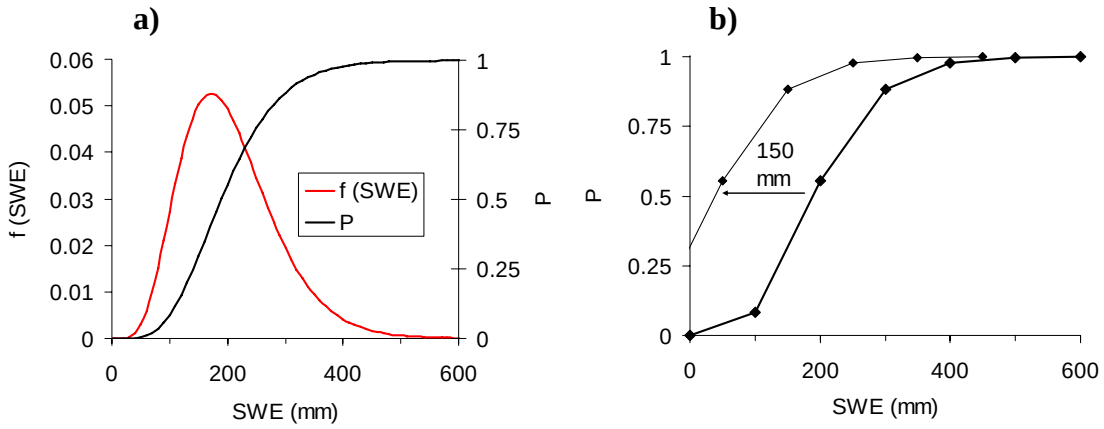

Figure 3.9. a) Hypothetical SWE distribution and cumulative distribution (i.e., ADC) based on the gamma distribution with parameters $\alpha = 6$ and $\beta = 33.33$; b) approximation of the ADC based on SWE values at 100 mm intervals, and simulated shift in the distribution after 150 mm of uniform applied melt.

mm and $P = 0.554$ has become reduced to 50 mm. The slope, a, of the line segment representing initial SWE values between 100 – 200 mm is ~0.005 mm^{-1}, so the y-intercept after 150 mm melt is:

$$P_{int} = P_1 - \text{SWE}_1 \cdot a$$
$$= 0.554 - (50 \text{ mm})(0.005 \text{ mm}^{-1})$$
$$= 0.319.$$

Therefore the predicted SCA is 1 – 0.319 = 0.681, whereas the actual distribution yields values of $P = 0.297$ and SCA = 0.703 at 150 mm. For a lognormal distribution with $\overline{\text{SWE}}$ = 200 mm and CV = 0.4, the predicted SCA after 150 mm of uniform melt would be 0.71. The procedure based on the approximated ADC could also be carried out for inhomogeneous melt. In this case, the slope of the individual line segments would need to be recomputed each time a simulated SWE value becomes zero. For snowmelt runoff simulations, all that is required is the simulated meltwater outflow from each SWE bin and the corresponding probability of the bin for weighted inputs to the areal unit.

3.6 Remote Sensing Applications

It is important to be able to link this theory with remote sensing techniques for SCA determination so that it can be applied toward hydrological modelling efforts in large, remote, inaccessible, or data sparse regions. Throughout the literature there have been various approaches presented to combine snowmelt modelling with remotely sensed SCA in order to derive the peak accumulation snow distribution and/or use towards seasonal runoff forecasts (e.g., Rango and Martinec, 1982; Martinec, 1985; Martinec and Rango, 1987; Liston, 1999; Turpin et al., 1999; Farinotti et al., 2010). The fundamental basis for this method has been, without exception, the assumption of uniform melt rate and timing over a SWE distribution, using either temperature index or energy balance melt models. Thus, the effects of non-uniform warming, ripening, and melt over an initially cold and heterogeneous snowcover are not captured. This can lead to errors such as underestimating SWE depths in the shallow part of the distribution and overestimating the deeper SWE depths, and can introduce uncertainty in selecting the proper depletion curve from a set of curves for hydrological forecasts (e.g., Martinec and Rango, 1987). For these reasons it may be important to consider these effects. A possible approach to using the framework presented here together with acquisition of remotely sensed SCA is described below.

To begin, it is useful to analyze the variation in melt rate and timing due to differences in SWE and internal energy, as predicted by a point-scale energy balance snowmelt model, in order to gain insight on the potential importance of such inhomogeneous melt. This requires some initial conditions to be set, which can be done either by allowing the model to run for a sufficient period of time through the winter, or by obtaining field measurements. To run a model and allow it to develop a realistic pre-melt snowpack state for different SWE classes, the model must account for differences in accumulation and snow transport over various parts of the landscape (i.e., sheltered vs. exposed). If this modelling reveals non-uniform melt rates and timing that cannot be considered insignificant, then it is necessary to account for this variation when attempting to reconstruct pre-melt SWE distributions.

As satellite measurements of SCA become available during the spring, the SCD curve with respect to time can be generated. Martinec (1985) explained how replacing time on the *x*-axis with accumulated snowmelt produces a modified depletion curve (Section 2.3.2), which can be used to estimate the initial $\overline{\mathrm{SWE}}$ at the end of the snowmelt season. Under uniform melt, the decrease in the SCA fraction over time is equivalent to the fraction of the landscape covered by a depth of SWE equal to or less than the accumulated melt up to that time, following from Equation (2.5) (p. 38). A similar approach can be employed under inhomogeneous melt since areas with shallower snowcover melt out first; however, in this case the accumulated melt of separate classes of initial SWE need to be used.

The following example shown in Figure 3.10 and Table 3.2 illustrates how remotely sensed values of SCA over time can be used together with differential snowmelt modelling for separate SWE classes to estimate the pre-melt distribution. Initial SWE values (and associated snowpack state variables) are taken at 50 mm intervals and snowmelt modelling is applied to each. Figure 3.10 a – c shows this for eight different classes, revealing some earlier and more rapid melt of shallow snow. By tracking the timing of melt out from the different SWE classes and comparing with the SCA at the times of each image acquisition, the percentage of the landscape covered by the various depths of SWE can be estimated. In this hypothetical example, by the time of the second image acquisition no SWE class had yet melted out (Fig. 3.10a), but by the third image the first two classes were depleted (Fig. 3.10b). The 100 mm initial class was therefore the maximum class observed to melt out, and the total decline in SCA up to this time of 0.18 was attributed equally to the melt out of both the 50 and 100 mm classes. Subsequently observed SCA and melt out of different classes were used generate an ADC (see previous section), from which the frequency distribution can be derived (Fig. 3.10 e).

From image eight to image nine there is no melt out of a SWE class, and so the total decrease in SCA following the melt out of the 350 mm initial SWE class is equal to the change between image seven (0.13) and image nine (0.06) (Table 3.2). This produces more uncertainty in the actual SWE distribution. Along with problems of multiple SWE classes melting out between image acquisitions, these issues show how better and more reliable estimates of the true distribution can be made by increasing the resolution of

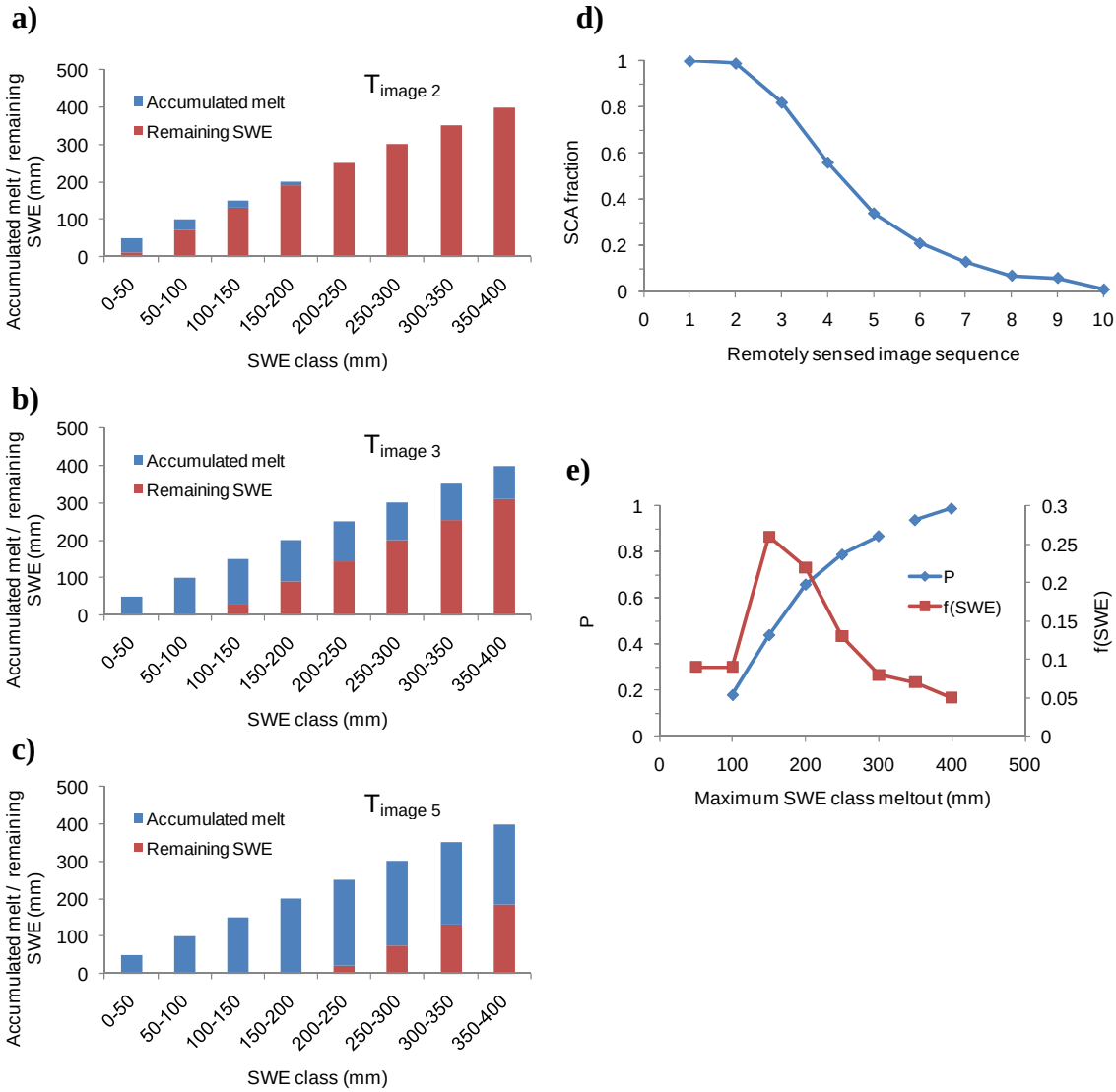

Figure 3.10. a) – c) Hypothetical variation in accumulated melt for different initial SWE classes (showing times of different image acquisitions); d) observed SCD curve from remotely sensed image series; e) cumulative distribution (i.e., ADC) and inferred SWE distribution.

image sequence	Observed SCA	Change in SCA	max SWE class to melt out	P
1	1			
2	0.99	0.01		
3	0.82	0.17	100	0.18
4	0.56	0.26	150	0.44
5	0.34	0.22	200	0.66
6	0.21	0.13	250	0.79
7	0.13	0.08	300	0.87
8	0.07	0.06	350	
9	0.06	0.01	350	0.94
10	0.01	0.05	400	0.99

Table 3.2. Values of SCA from remotely sensed image series, along with change in SCA between images, tracking of melt out of SWE classes, and estimated cumulative probability of SWE classes over the landscape.

SWE classes for modelling and by obtaining more frequent imagery. Snowcover products from sensors such as MODIS (Section 2.3.1) therefore can likely provide a useful tool for this type of hydrological research. In selecting curves from a set of curves for hydrological forecasting, the information during the early melt period is most crucial (Martinec and Rango, 1987). Given that this is the time when inhomogeneous melt over a cold, non-isothermal, and highly redistributed snowcover would be most pronounced, it may be very important to take these effects into consideration and apply differential melt computations to determine the true nature of SCD in relation to accumulated snowmelt.

3.7 Conclusions

The theoretical framework presented in this section is based upon the application of a point-scale energy balance snowmelt model over a parametric or empirical SWE distribution for the computation of areal SCD, and for the estimation of meltwater inputs to the land surface. Although many of the technical components are based upon the previous work of other authors and the framework appears to simply integrate these together, it is novel and unique in several important ways. First, it uses the maximum accumulation SWE distribution to base areal fractions of features over the landscape such as SCA, meltwater generation, and new snowfall over previously exposed ground surfaces, and in doing so scales these areas based on the year-to-year differences in snow distribution parameters such as $\overline{SWE}$ and CV. Secondly, other than in the case of fully distributed models, it is the first reported approach for using multiple snowpack states (internal energy and available energy for melt) and initial SWE to simulate the variability in melt rates and timing over a SWE distribution. Together, these allow the extent of different meltwater generating areas due to snowpack variability to be defined across the landscape, rather than be set as equal to the SCA with uniform melt. This is a significant contribution as inhomogeneous melt due to spatial variation in SWE and internal energy is known to occur in a range of environments, and is to be expected in high alpine regions such as the Canadian Rocky Mountains. Until now, however, there has been no sub-grid model parameterization to deal with this phenomenon and only modelling applications using fully distributed energy balance approaches have been able to account for this.

4. Study Area and Field Methods

4.1 Introduction

Several of the stated objectives of this thesis involve application of the theoretical framework developed in Section Three towards investigating the effects of SWE and melt rate variability on areal SCD and snowmelt runoff. This was done using a set of observational data collected over several years from a well-studied alpine basin in the Canadian Rocky Mountains – the Marmot Creek Research Basin (MCRB) in Kananaskis, Alberta. The purpose of this section is to describe the physical and climatological characteristics of this basin, and to explain the details of the field data collection programme that was carried out.

A description is first given of the MCRB and its research history. Fisera Ridge and the adjacent Upper Middle Creek Basin within MCRB are described, along with the network of meteorological stations over the ridge and the measurements obtained. This site was the primary focus of this thesis. Following this, some of the other data collection initiatives are discussed, which included snow surveys over parts of the basin and streamflow measurement at the basin outlet, as well as acquisition of terrestrial-based photography and airborne LiDAR snowcover mapping.

4.2 Marmot Creek Research Basin

The MRCB is located in the Front Ranges of the Canadian Rocky Mountains, in Kananaskis, Alberta (Fig. 4.1). Marmot Creek is a tributary to the Kananaskis River, which in turn flows into the Bow River. The basin is approximately 9.6 km^2 in area and is comprised of three tributary sub-basins (i.e., Cabin, Middle, and Twin Creeks) with approximately the same area and relief. Elevations range from 1587 m at the Water Survey of Canada (WSC) gauge, to 2831 m at the summit of Mt. Allan. Most of the basin is covered by forest stands of lodgepole pine, spruce, and fir, giving way to thin band of alpine larch in the treeline area, which occurs between the elevations of 2100 and

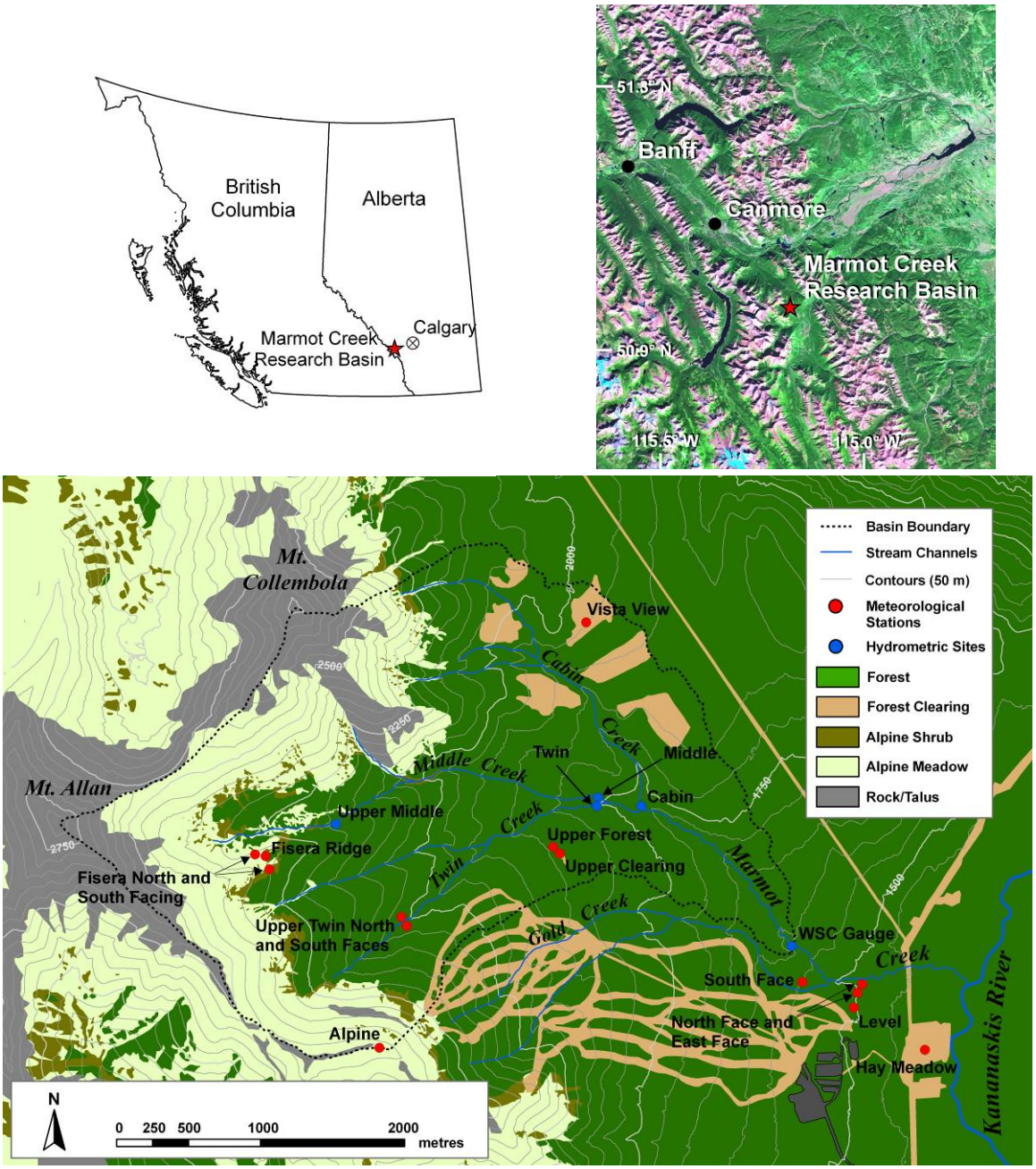

Figure 4.1. Location and overview of the Marmot Creek Research Basin, showing the present and recent past network of hydro-meteorological stations operated by the Centre for Hydrology, University of Saskatchewan. Top right image is a 2001 Landsat scene indicating the location of the basin within the Rocky Mountain Front Ranges.

2300 m. The alpine zone is characterized by isolated and exposed stands of krummholz vegetation and grassy meadows, with talus slopes and bare rock at higher elevations. The

basin is covered by seasonally frozen soils, and underlain with glacial and post-glacial deposits that blanket the bedrock except at high elevations and along parts of the stream channels. These deposits of unconsolidated material range in depth from 10 to 30 m over the lower basin and have a large storage capacity that dampens hydrograph peaks and supplies baseflow throughout much of the year (Stevenson, 1967).

Climatic conditions at Marmot Creek are classified as humid continental and are characterized by long, cold winters and cool, wet summers. Mean January and July temperatures are –10 °C and 14 °C respectively (based on extrapolated readings from Kananaskis, AES Sta. 3053600, 1391 m), while April, May, and June temperatures are –2.4 °C, 2.3 °C, and 6.0 °C respectively. During the winter months, warm and dry Chinook winds often leads to large temperature variations, and there are many days in mid-winter when the air temperature exceeds 0 °C over much of the basin. Annual precipitation has been observed to range from <600 mm in the lowermost portions of the basin to >1140 mm near treeline at the boundary between Twin and Middle Creeks (Storr, 1967). The basin average annual precipitation, weighted by area/elevation, is estimated to be roughly 900 mm, and 70 to 75% of this falls as snow. Observations during the study period of this thesis (2007, 2008, and 2009) more-or-less conform to this fraction. Climatic data from Kananaskis station 3053600 (1979 – 2009) show that monthly average air temperature was one to two degrees below average during April in each of the years of this study. In 2007, May and June air temperatures were roughly one degree above average, while in 2008 and 2009, May temperatures were average and June temperatures roughly half a degree cooler than normal. Monthly precipitation totals were slightly above average during 2007, while in 2008, precipitation was slightly lower than normal in April but well above average in May and June (nearly two and a half times the average total for May). In 2009, precipitation was slightly higher than average in April, but much below average in May and June.

Marmot Creek has a rich history of hydrological research. The basin was established in 1962 as part of the International Hydrological Decade and was the first project undertaken by the Eastern Slopes (Alberta) Watershed Research Program. Each of the three sub-basins, along with the lower confluence area, was instrumented for research into various hydrological effects of forest management. Instrumentation

included 4 permanent meteorological stations, 10 snow pillows, 40 shallow groundwater wells, and 5 weirs for monitoring streamflow on Marmot Creek and its tributaries. In the summer of 1974, a simulated commercial cutting operation was carried out on the Cabin Creek sub-basin in which roughly 40% of its forested area was clearcut in six blocks ranging from 3 to 13 ha. Between the fall of 1977 and winter of 1979, roughly 40% of the forested area on the Twin Creek sub-basin was also removed, but here an experimental forest treatment was carried out that consisted of over 2100 circular clearings of 15 or 20 m diameter. This treatment was designed to modify snow accumulation and melt and thereby alter the streamflow regime in favor of late season runoff (Swanson and Golding, 1982). In the summer of 1984, clearing began for the Nakiska Ski Resort on Mt. Allan, which was to become the site of the 1988 Winter Olympic downhill events. This development encroached on the southern portion of the basin, and following review, the Marmot Creek experimental watershed study was ended in 1986. Most meteorological, hydrometric, and groundwater monitoring sites were closed, however, several wells and the main weir at the basin outlet remained in operation.

Beginning in 2004, a number of meteorological stations were installed in and adjacent to the basin (Fig. 4.1), and a monitoring programme was re-established here by members of the Centre for Hydrology, University of Saskatchewan. At the time of writing of this thesis, there are ten permanent meteorological stations at elevations from 1450 m to 2500 m collecting precipitation, snow depth, soil moisture, soil temperature, short and longwave radiation, air temperature, humidity, wind speed, and turbulent fluxes of heat and water vapour. Observations of groundwater levels and streamflow at the basin outlet are made by the federal and provincial governments, and streamflow is measured on each tributary using pressure transducers deployed by Centre for Hydrology staff.

4.2.1 Fisera Ridge Site and Upper Middle Creek Basin

Data collection efforts for this work were concentrated on Fisera Ridge and the adjacent Upper Middle Creek Basin within the alpine zone of MCRB. Figure 4.2 shows a map and an aerial photograph of this small (1.2 km^2) sub-basin, together with a detailed map

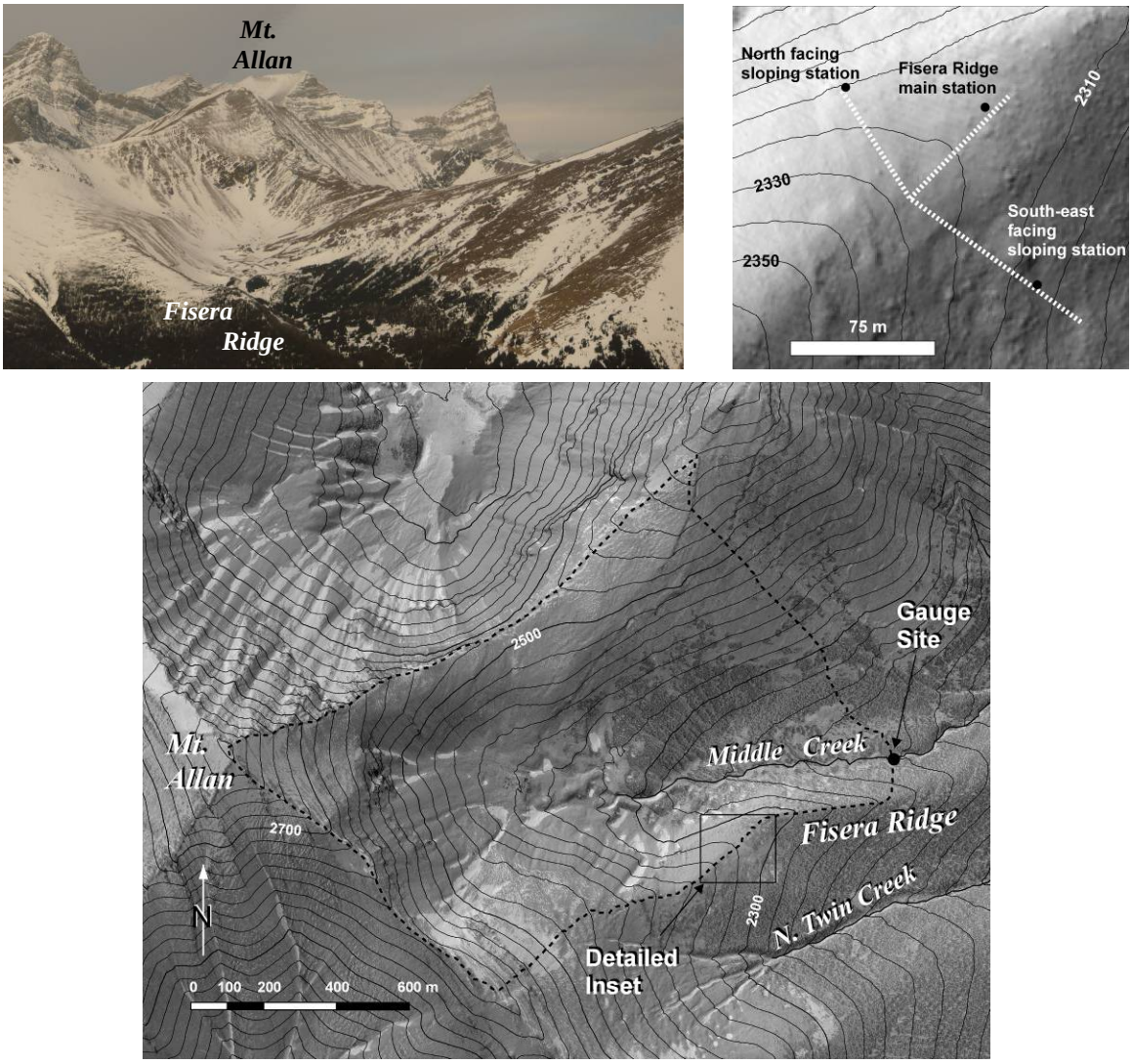

Figure 4.2. Aerial photograph and map of Fisera Ridge and Upper Middle Creek Basin (dashed line indicates the basin boundary; 25 m contour interval). A detailed map of the ridge-top area at top right shows the locations of the main station and two sloping stations, along with the snow survey transect used in 2008 and 2009 (dashed line).

of the ridge-top area. This specific site provided an ideal location to conduct this study as the ridgetop offers a good vantage point to overlook most of the small basin (see Section 4.4.1), and is representative of the alpine – forest transition zone in the Front Ranges of the Rockies. The Upper Middle Creek Basin has many slopes of different orientation, which is useful for testing components of the theory developed previously in this thesis,

and further this basin was not subject to any land cover manipulation as were the other sub-basins within MCRB during the Alberta Watershed Research Program.

Several meteorological stations were in operation here during the course of the study (Figs. 4.2, 4.3, 4.4); these consisted of a main station located on level terrain on the ridge-top, and two sloping stations on south-east (SE) and north (N) facing slopes, either side of the ridge. The main station was installed in October 2006 to enhance the network coverage of stations within MCRB and provide data for various studies within the basin, while the two sloping stations were installed in October 2007 specifically to support the work in this thesis. Measurements of incoming/outgoing shortwave and longwave radiation, wind speed/direction, air temperature and humidity, precipitation, and snow depth were made at the main station, while the sloping stations recorded snow depth, wind speed, air temperature and humidity, and internal snowpack temperature. Table 4.1 provides further details on the instrumentation and measurements.

The Upper Middle Creek Basin is a glacial cirque situated below Mt. Allan, and is mostly covered by alpine meadow, talus, and exposed rock outcrops. (Fig. 4.5; Table 4.2) The lower part of the basin is forested with sub-alpine fir and larch stands in the tree-line area. The basin is comprised of several distinct slopes of different orientation, with a valley bottom area above treeline that is relatively gentle in slope. There are several steep cliffs in the upper part of the basin that remain virtually snow free, but these only occupy a marginal proportion of the total area (~one – two percent). A number of incised gullies and topographic depressions in the alpine part of this basin trap blowing snow and develop drifts several meters deep over the winter. Subtle variations in the micro-topography and exposed krummholz also develop drifts over the winter in seasonally repeating patterns. Avalanching is not a major factor in the redistribution of snow here, although parts of some slopes are prone to small (i.e., class 1 – 2) avalanches. A large part of the terrain is exposed to the wind and is scoured free of snow through most of the winter. However, late winter and spring snowfalls, which are typically wetter and less subject to wind scouring, generally cover these areas just prior to and during the main snowmelt period.

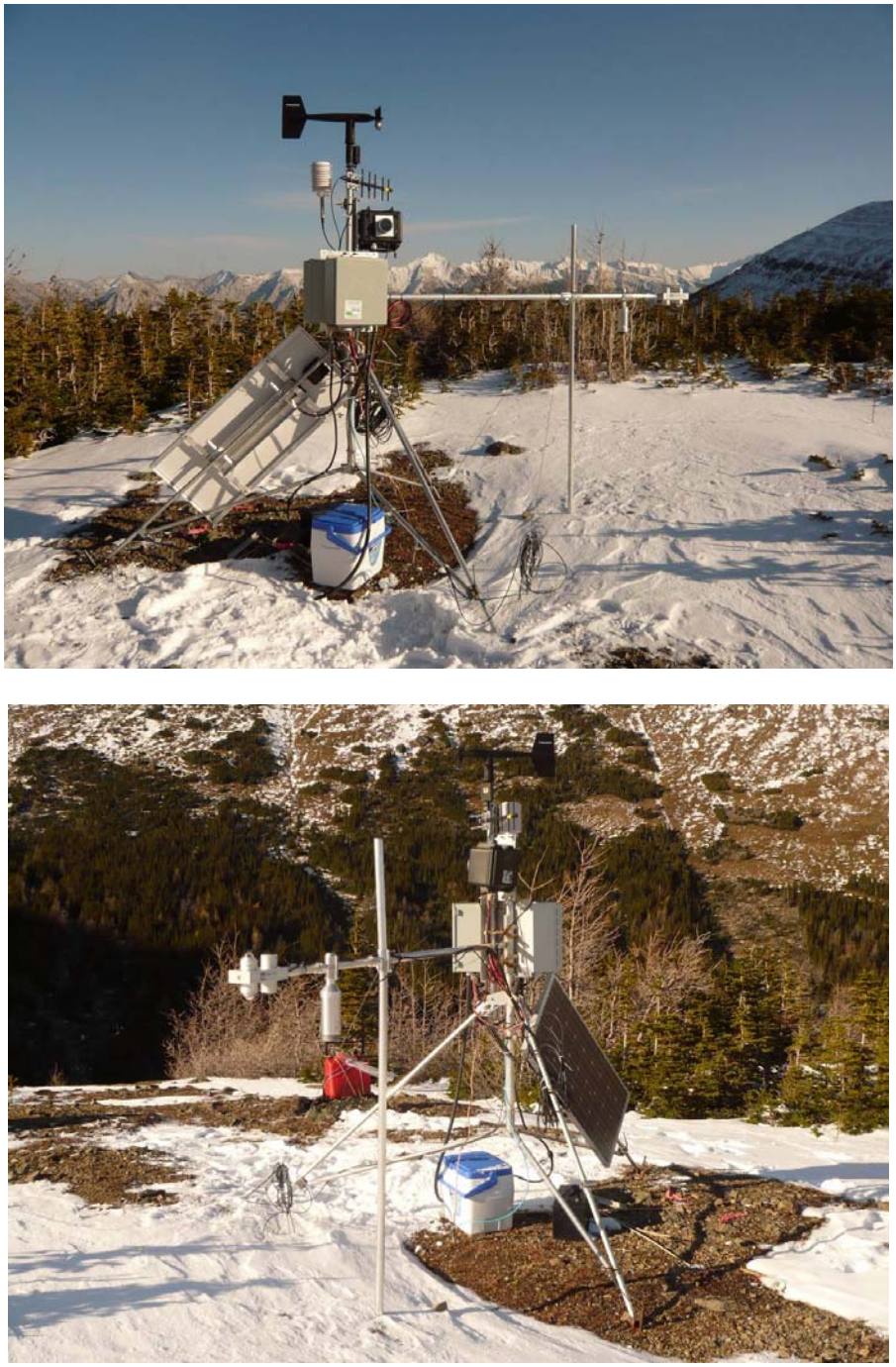

Figure 4.3. Fisera Ridge station (October 15, 2008).

Figure 4.4. Fisera North facing (top) and South-east facing (bottom) sloping stations (October 15, 2008).

Table 4.1. Fisera Ridge instrumentation details. All observations collected at 15-min frequency.

Station	Variable	Instrument Model	Sensor Height (m)	Comments
Fisera Ridge main station	Net Radiation	Kipp & Zonen CNR1 (CM3 pyranometer, and CG3 pyrgeometer)	1.4	4-component radiometer (installed Oct 2007)
	Incoming shortwave	Kipp & Zonen CM21 pyranometer	1.5	Replaced in Oct 2007 by CNR1
	Incoming longwave	Kipp & Zonen CG1 pyrgeometer	1.5	Replaced in Oct 2007 by CNR1
	Air temperature and humidity	Campbell Sci. HMP45C212	2.25	
	Wind speed and direction	RM Young anemometer (Model 05103-10)	2.55	
	Rainfall	Campbell Sci. TB4-L tipping bucket gauge		
	Total precipitation	Geonor T-200B alter shielded strain gauge		Installed in Aug 2008; located ~25 m away in sheltered area
	Soil temperature	Type-E fine-wire (24 gauge) thermocouples	–0.05 –0.15	
	Snow depth	Campbell Sci. SR-50 sonic ranger	1.15	
	Data logger	Campbell Sci. 23X and CR3000		23X replaced by CR3000 in 2008
Sloping stations	Snowpack internal temperature	Type-E fine-wire (24 gauge) thermocouples		Positioned every 20 cm up from 2 cm above ground
	Air temperature and humidity	Campbell Sci. HMP45C212	1.9 (N face) 2.85 (S face)	Instrument heights varied due to tower adjustments at S facing site
	Wind speed	Met-One 014A 3-cup anemometer	2.4 (N face) 3.15 (S face)	
	Snow depth	Campbell Sci. SR-50 sonic ranger	2.2 (N face) 2.45 (S face)	Heights are perpendicular distance to ground surface
	Data logger	Campbell Sci. 10X		

Table 4.2. Landcover types over Upper Middle Creek Basin. Areas based on cover types shown in Fig. 4.5.

Cover type	Area (10^4 m^2)	Area (% of total)
Alpine meadow	44.5	36.6
Rock and talus	52.1	42.8
Fir – Larch forest	25.1	20.6
total	121.7	100

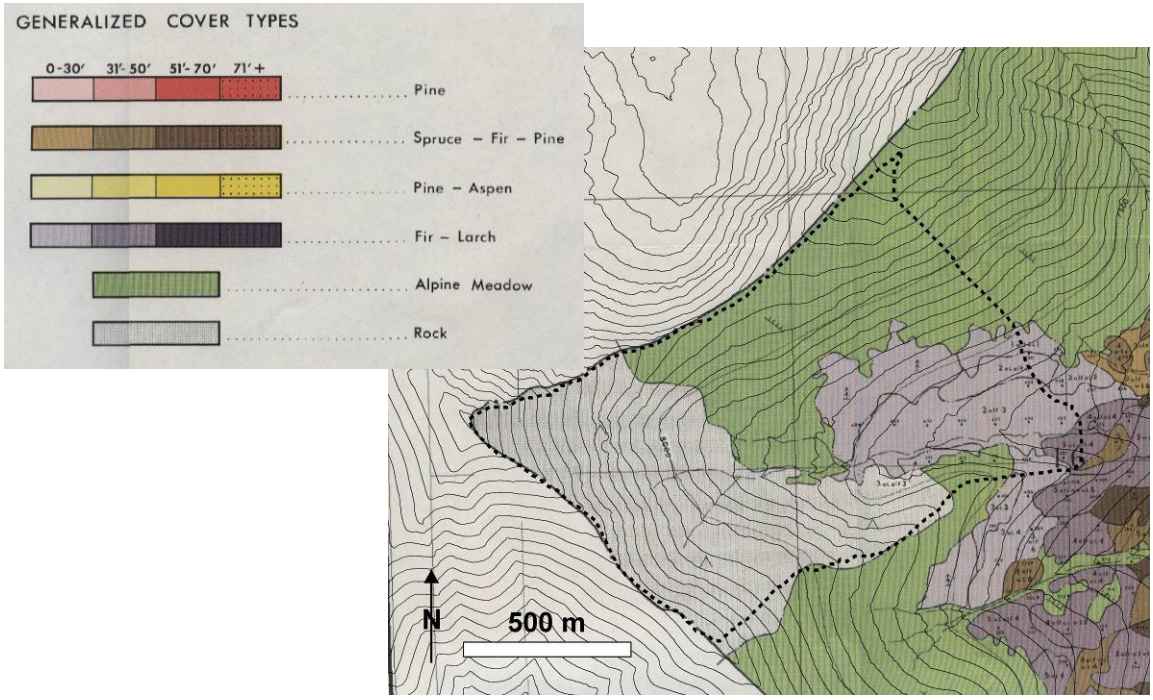

Figure 4.5. Map of lancover type over Upper Middle Creek Basin; original map and photography by the Alberta Forest Service, 1963, and the Calgary Regional Laboratory, Department of Forestry, 1965. Dashed line represents basin boundary.

4.3 Field Survey Measurements

4.3.1 Snow Surveys and Snow Pits

As part of the development of this thesis, a number of snow surveys were carried out over various parts of the Upper Middle Creek Basin during the winter and spring periods in 2007, 2008, and 2009. These were done to characterize the variability in pre-melt and

melt period SWE on different slopes and in different localities. The surveys supported the broader measurement campaigns over the whole MCRB, but transects crossing Fisera Ridge and the Mt. Allan cirque beginning in 2008 were specifically designed by this author to support the work of this thesis (see Appendix A). Surveys were carried out along linear transects with measurement points spaced evenly at regular intervals anywhere from 1 – 5 m, and ranging from tens to several hundred meters in length. The locations were selected based on accessibility and avoidance of hazards, with an attempt to represent, as best as possible, the variability in terrain features over the basin. Several of the transects were repeated a number of times at semi-regular intervals in the winter/spring periods of 2008 and 2009. Figure 4.6 shows the locations of these transects in and adjacent to the basin.

Snow depth measurements were obtained using a snow probe, which is a graduated aluminum rod etched with one cm increments, and is assembled together from individual one metre segments for portability. Measurements of bulk snow density were obtained for relatively shallow snow (<~1.5 m) using a mount rose snow tube or an ESC-30 snow tube together with a calibrated spring scale. These measurements were taken roughly every fifth depth measurement, where possible. Shallow snow density was sometimes also measured with a fixed volume triangular cutting device, with a volume of 1000 cm^3 such that the mass of snow in grams is equivalent to the density in kg/m^3. The density measurements were used to convert snow depth to SWE using either mean density or relationships between depth and density, if any were apparent.

Several snow pits were dug at various positions along some of the regular survey transects (Fig. 4.5) in an effort to examine the vertical snowpack structure and measure the density of individual strata within the pack. These pits also provided bulk density measurements for deeper snow, which could not be reliably measured with snow tubes. Sampling was done by identifying individual layers within the snowpack and noting their characteristics, then taking one or more density measurements in each layer with the triangular cutter, and finally taking the weighted average density based on the thickness of each layer as the bulk density of the pack. When previously excavated pits were returned to for sampling at later dates, the shaded wall of the pit was cut away a sufficient amount to avoid sampling snow that had melted along the sides of the pit.

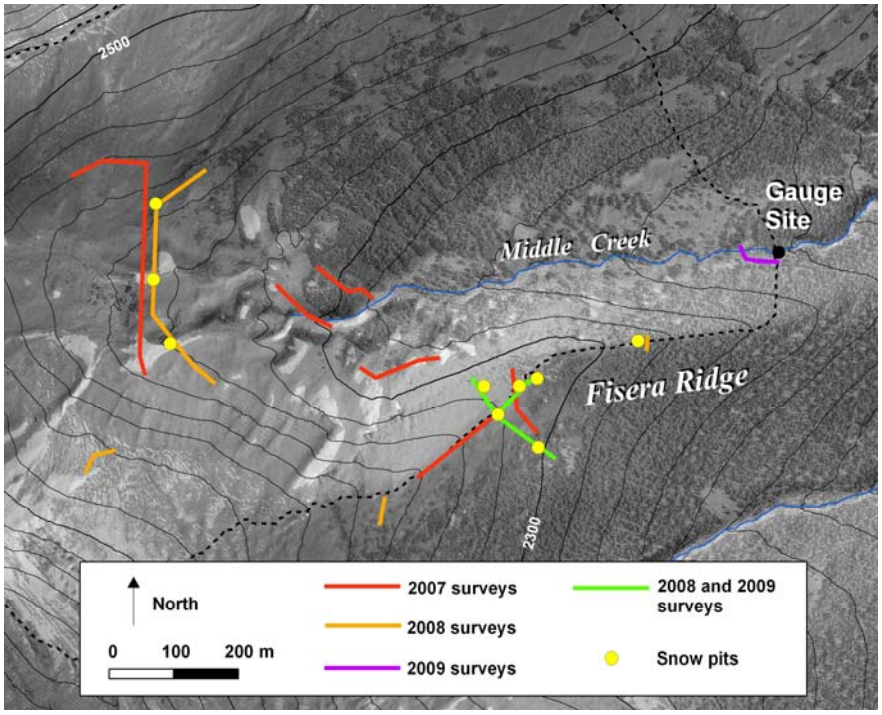

Figure 4.6. Locations of snow surveys and snow pits on Fisera Ridge and within the Upper Middle Creek Basin.

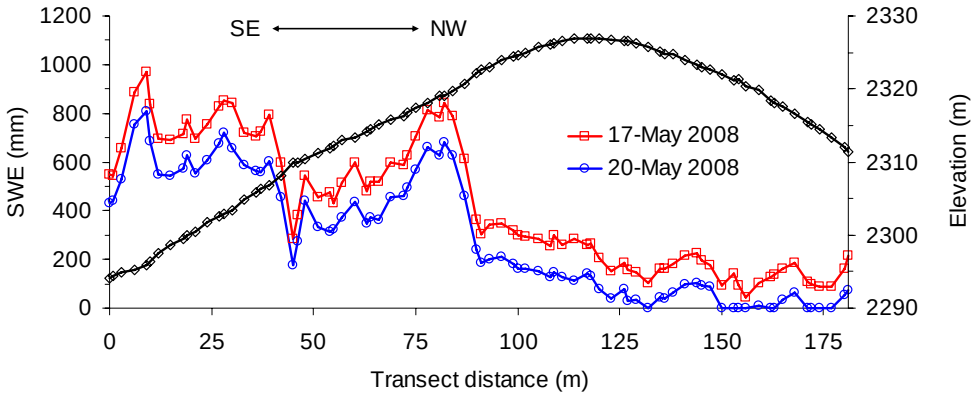

Figure 4.7. Survey measurements of SWE over Fisera ridge transect in spring 2008. Ground surface topography along the transect, which was derived from a LiDAR DEM, is also shown.

Figure 4.7 provides an example of two consecutive survey measurements over Fisera Ridge during a melt period just following the time of maximum accumulation. The high degree of SWE variability over the landscape is readily apparent. Wind

directions here are predominantly from the north and north-west (MacDonald et al., 2010), and it can be seen how small variations in the micro-topography and breaks in the slope of the terrain lead to the formation of drifts on the lee (south-east facing) slope. Some of the other snow survey and snow pit data are provided in Appendix A.1, and examined in more detail in Section Six of this thesis.

4.3.2 Stream Gauging and Streamflow Measurement

Continuous measurements of streamflow were obtained during the spring and summer months for each of the three tributaries to Marmot Creek, as well as the Upper Middle Creek near the forest – alpine transition (Fig. 4.1). Streamflow measurements at the Marmot Creek outlet are available through the WSC. The location of the gauge sites was selected to coincide with the previous locations of gauges used during the Alberta Watershed Research Program study at Marmot Creek.

Measurements of stream velocity and depth were obtained in 2007 and 2008 using Unidata Starflow™ ultrasonic Doppler devices mounted on aluminum plates, which were secured to the channel bed. Measurements were recorded using a 120K Starlog™ MicroLogger at a 15 minute frequency. These instruments were deployed as soon as the stream channels became clear of snow in the spring, and were placed near the center of the stream in locations with uniform flow along the channel and a simple channel cross-sectional profile. The product of the depth and velocity provided a useful index of stream discharge rates.

In 2008, most of the Starflow devices failed due to rupture and water leakage, thereby limiting the data available for that spring and summer. These were replaced for the 2009 season with Solinst Levelogger® pressure transducers to measure stream depth only. Measurements were obtained at a 15 minute frequency. These were placed inside PVC tubes installed vertically along the sides of the channel, or in some cases near the center of the channel if there was a structure present to mount the tube on.

Discharge rates were measured a number of times throughout the spring and summer each year for each of the streams. This was done by dividing the width of the channel into 0.1 or 0.2 m segments and measuring the depth and velocity (at a depth

above the bed of 0.4 times the total depth) for each. The increment lengths were chosen so that no more than ~20% of the total flow passed through any individual segment, and the total discharge was determined from the sum of all segments. Depth was measured using a standard aluminum ruler and velocity was measured using a Sigma portable ultrasonic velocity meter. Comparison tests were also made using a SonTek FlowTracker^{TM} acoustic Doppler velocimeter. The discharge measurements were then used to develop rating curves on each stream to relate discharge rate to depth or velocity, which were continuously measured.

Figure 4.8 shows the Upper Middle Creek gauging site in 2009, and Figure 4.9 shows the depth and discharge measurements from this site used to predict the hydrograph. A linear relationship was fitted to the measured data over the range of depths from ~0 to 0.15 m, and was used to generate the hydrograph from continuous measurements of stream depth. However, below a stream stage of about 0.04 m this relationship predicts negative discharge values, which were set as zero, and thus the

Figure 4.8. Photograph of Upper Middle Creek gauging site showing the PVC tube housing the pressure transducer and a Starflow device mounted nearby (July 3, 2009). The channel width is approximately 2.5 m at this location.

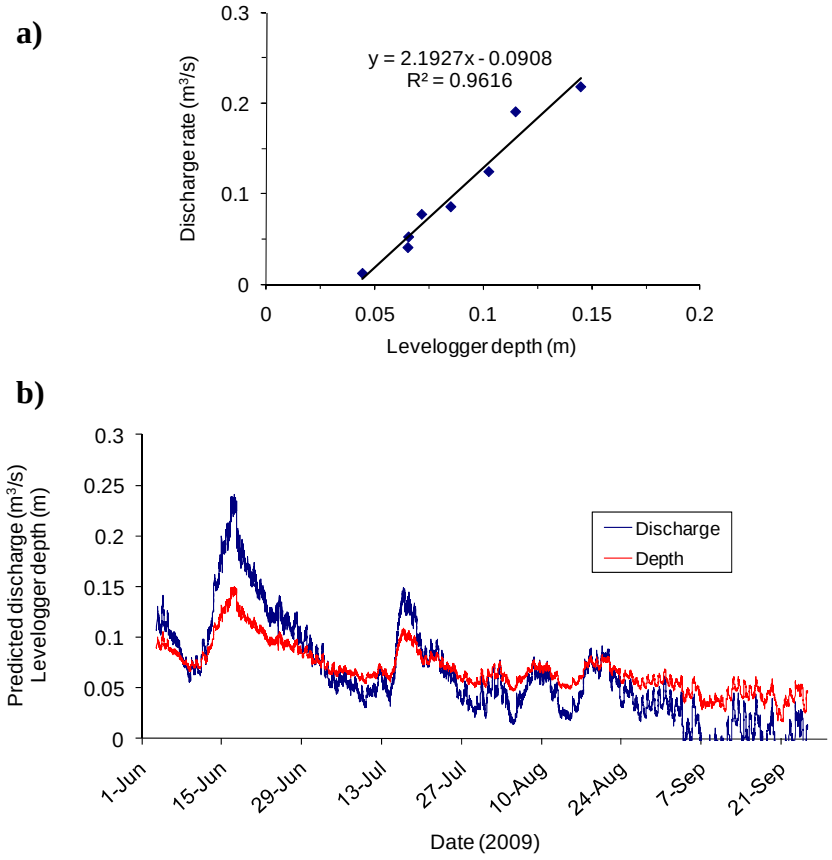

Figure 4.9. a) Discharge measurements and rating curve for Upper Middle Creek in 2009; b) Depth series and predicted hydrograph using the rating curve in (a).

values toward the end of summer and beginning of fall are subject to greater relative error. The period of interest for this work is only until the mid summer when the snowmelt period has largely ended, and so this should not have a major impact on the results presented in Section Seven.

Data for 2008 is limited at this site due to the failure of the Starflow device. The hydrographs developed from these procedures are used in Section Seven of this thesis to compare with simulation results from a hydrological model for Upper Middle Creek Basin.

4.4 Remotely Sensed Data Acquisition

4.4.1 Terrestrial Based Photography

To support the work of this thesis and obtain frequent observations of the SCA over Upper Middle Creek Basin, digital time-lapse photography was used. In early May of 2007 a digital single lens reflex camera (Pentax model K110D) with a high precision lens to minimize radial image distortion (Pentax DA 21mm F3.2AL Limited) was mounted to the Fisera Ridge station inside a weatherproof housing (Fig. 4.3). Another camera was similarly mounted to a chairlift station at ~2250 m within the Nakiska ski area boundary. The two cameras provided a clear view over most of the alpine portion above treeline of the Upper Middle Creek Basin from the different vantage points (Figs. 4.10, 4.11). At Fisera Ridge, the camera's shutter release was controlled remotely using the stations datalogger, which was programmed to take photos several times daily. At the chairlift station, a Canon TC-80N3 remote timer was used to control the camera shutter to take one photo daily. Photos taken at 12:00 p.m. local time each day were selected for analysis, except in situations when low cloud cover or snowfall obscured the terrain.

To derive SCA measurements from the digital photography, the images were projected orthogonally onto a 1 m resolution DEM that was generated from airborne

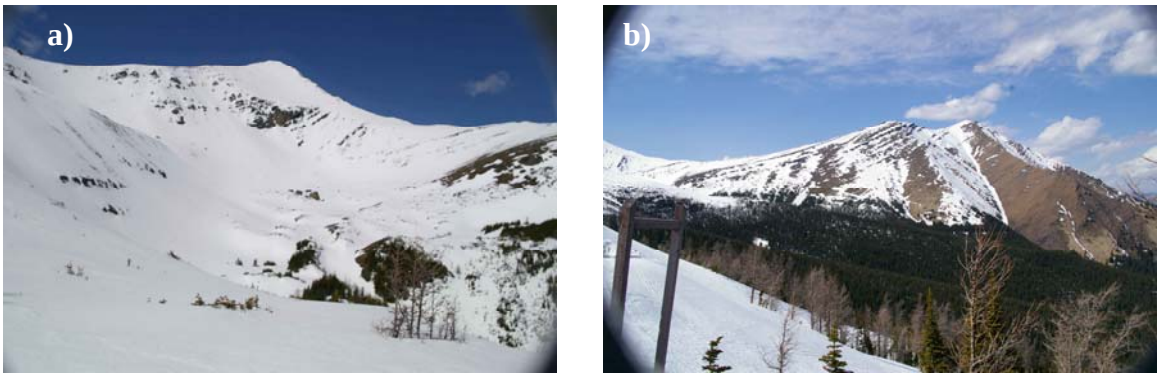

Figure 4.10. Terrestrial photographs over alpine portion of Middle Creek sub-basin: a) Mt. Allan and Upper Middle Creek Basin; b) Mt. Collembola and upper forested portions of Twin Creek sub-basin.

LiDAR using a technique described in detail by Corripio (2004). Initially, a viewshed map must be created for the location of the camera using GIS software. The DEM is then projected virtually from the perspective of the camera position and orientation so that it forms a two-dimensional representation of the relief information contained in the DEM. Orientation data consisting of three rotation parameters for spatial rotations of the camera, location of the camera (x, y, z) and the central pixel of the photographic image in the DEM coordinate system, and principal distance (i.e., camera focal length) are required to achieve this representation. This virtual projection of the DEM is then scaled by the resolution of the image, and the correspondence between image pixels, the projected coordinates of the DEM cells, and their geographic location is established. Finally, based on this information, the image pixels are re-projected over the DEM to the geographic location that they correspond to.

Orientation parameters were derived manually by trial and error for each image in order to achieve optimal correspondence between the image pixels and their geographic coordinates. This was necessary since very subtle movements of the camera due to wind and periodic operator access into the camera housing caused significant movements of the geographic locations of individual pixels between subsequent images. Comparison of a series of ground control points within the cirque obtained using a differential GPS (Global Positioning System) and clearly identifiable objects within the georeferenced images (e.g., bushes, small rock outcrops, etc.) revealed a root mean square error (RMSE) of ~3 m, but this error tended to be directionally consistent, and thus the area of features was preserved. Visual inspection of the georeferenced image series and a 1 m resolution shaded relief image of the DEM also indicated a very close correspondence between data sets over nearly all visible parts of the alpine landscape.

Together, the two cameras provided good coverage over most of the slopes above treeline within the Upper Middle Creek Basin and the adjacent slopes on Mt. Collembola (Fig. 4.11). Daily SCA measurements were derived from the georeferenced imagery for different slopes within the basin. These measurements were made using ESRI® ArcMap™ 9.3, in which a threshold was applied to classify snow and non-snow areas. This classification could be easily performed because of the large difference in brightness values of the cells representing snow and those representing bare ground or vegetation.

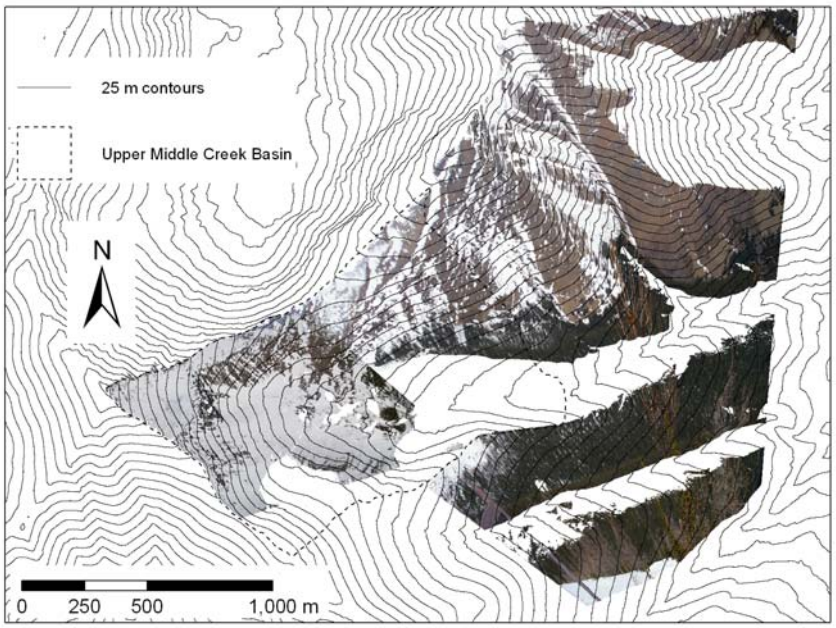

Figure 4.11. Spatial coverage of re-projected terrestrial-based photos over parts of the alpine terrain within MCRB (from photos taken May 4, 2008).

SCA was then determined as the ratio of the number of "snow" cells to the total number of pixels over the relevant area (excluding pixels containing "no-data" values which were hidden from view of the camera). The process is described in more detail in Appendix B.

4.4.2 Repeat LiDAR Acquisition and Snowcover Mapping

Spatial patterns of snow depth were mapped over the MCRB and surrounding area in the late winter of 2008 using multi-temporal LiDAR data acquisition. The first dataset was collected during snow-free conditions in August 2007 to derive a base DEM of the basin, while the second dataset was collected in the late winter during March 2008. The second dataset produced a snow surface model, which, after subtraction of the bare ground DEM, yielded a 1 m resolution raster snow depth model. The procedures are described in detail by Hopkinson et al. (in press).

Snow survey data from the Fisera Ridge transect on 27 and 28-March were used as partial validation data for the alpine zone of MCRB. GPS readings were made at a number of points along the transect using a Trimble Pro-XL differential GPS, and the

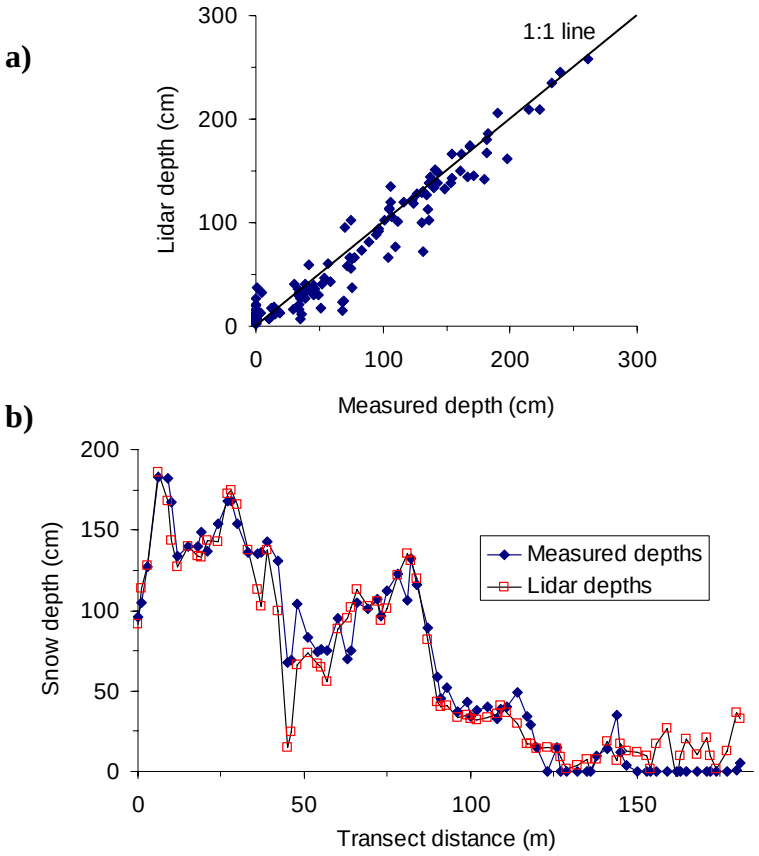

Figure 4.12.[1] Validation of LiDAR derived snow depths along the Fisera Ridge survey transect in late March 2008: a) correspondence between measured and LiDAR-derived depths; b) spatial pattern of depth values along transect. (See also Fig. A.7 in Appendix A).

location of other points was interpolated between these "benchmark" points. The positional accuracy of individual points was estimated to be within ±0.5 m by this method. Snow depths were measured every 3 m along the transect crossing the ridge and every 2 m on the ridge crest transect, and were compared with the LiDAR derived snow depths at the location of each survey point. (See Appendix A.2 for more information on the validation of these data). This comparison is shown in Figure 4.12, and it is clear that the repeat LiDAR technique yielded favourable results. Individual depths showed good correspondence (R^2 = 0.94; n = 137; RMS error = 0.17 m) over the range of measured

[1] Parts of the analysis here and Fig. 4.12a are adapted from Hopkinson et al. (in press), and was the primary work of the author of this thesis. The specific role of other co-authors was in reviewing and approval.

snow depths from 0 to 2.88 m, and the LiDAR depths reproduced the observed spatial pattern over the ridge very well. There were no apparent biases in error due to slope or aspect, but the LiDAR snow depths had greater error (up to ~0.6 m) in locations with exposed alpine shrubs (e.g., near the 45 m transect distance). The favourable results are likely due the high elevation of the terrain and the fact that it was relatively close to the sensor platform, and the minimal surface vegetation cover (Hopkinson et al., in press). Thus, the LiDAR snow depth raster model provides a useful tool for examining the spatial pattern and distribution of snow depth over most of the sparsely vegetated and open alpine part of MCRB.

Figure 4.13 shows the snowcover patterns derived from the LiDAR over the Upper Middle Creek Basin and adjacent alpine terrain. It is clear from this image how gullies and depressions trap and accumulate snowdrifts as deep as several meters or more, while adjacent windswept terrain is scoured free of snow. At the particular time of acquisition of the March 2008 LiDAR dataset, much of the exposed alpine landscape was snow-free. The image also shows major wind loading of snow onto slopes, such as the Upper North Twin Creek Basin, and the deep snowpack that accumulates in the treeline area. The observed spatial patterns of drifts and scoured areas are consistent with patterns observed in historical aerial photographs and the observations during the course of this work, suggesting that these patterns are consistently repeated from year to year.

Finally, the snow depths were converted to SWE using measurements of snow density from a variety of sites across the alpine portion of MCRB near the time of the LiDAR acquisition. Data from 10 snow pits ranging in depth from 0.21 to 1.63 m showed little variation in bulk density (mean = 355.3 kg/m^3, standard deviation = 32.5 kg/m^3), and no association with depth (see Appendix A.2). Thus, the snow depth raster model was multiplied by the mean density to derive a SWE raster model for the alpine zone, which could then be used to analyze SWE patterns over the basin for use in Section Six of this thesis.

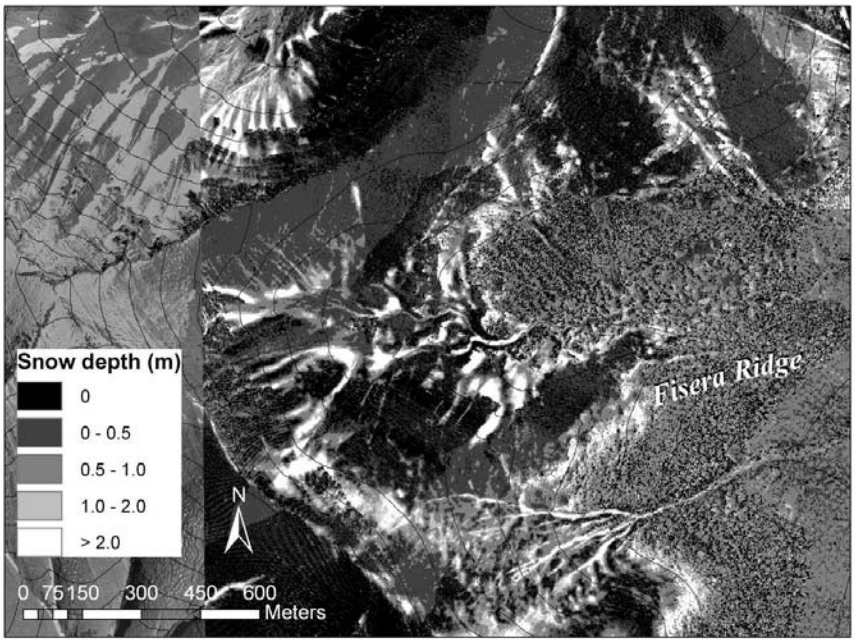

Figure 4.13. Map of snow depth over upper portion of MCRB derived from the repeat LiDAR datasets in 2007 and 2008.

5. POINT-SCALE SNOWMELT MODELLING

5.1 Introduction

A physically-based energy balance snowmelt model was used in this thesis to examine the spatial variability of snowmelt and the effects of this variability on areal SCD and snowmelt runoff generation. The development of this model involved combining selected process algorithms for the mass and energy balance of the snowpack into a functional point-scale snowmelt model within the Cold Regions Hydrological Model (CRHM) platform. The model was tested and validated using meteorological and snowpack observation series from the three sites at Fisera Ridge, and subsequently used to examine the influence of differences in energy receipt and snowpack state on melt timing and rates at these sites. The purpose of this section of the thesis is to explain and describe the development, parameterization, and testing of this model, along with its use in examining melt rate variability at the point-scale. The application of the model beyond the point-scale using the theoretical framework of Section Three is described later within Sections Six and Seven.

First, the basic model structure is described, including a brief discussion of CRHM and its operation, the energy balance snowmelt routine *Snobal*, which has been incorporated as a module within CRHM, and the other modules used for estimating incoming radiation and evaluating some of the terms in the energy balance equation. The meteorological conditions at Fisera Ridge and some of the dataset collected during the study period are then presented, and the parameterization and validation of the model based on this observed data are discussed. Following this, the spatial and temporal variability of simulated snowmelt at the three sites over the ridge are examined to investigate the effects of differences in meteorological conditions, surface energy receipt, and snowpack state on melt timing and rates. Finally, the section concludes with a discussion of these results and the considerations that these may imply for snowmelt modelling in such environments.

5.2 Model Structure and Routines

5.2.1 The Cold Regions Hydrological Model (CRHM) Platform

The model used in this work was developed and applied using CRHM, which is a flexible, object oriented modelling system that can be used to generate an operational model of a hydrological system, specific to the needs of the user. The features, functions, and structure of this model platform are described in detail by Pomeroy et al. (2007). CRHM is a modular tool where users can build a model by selecting various hydrological process modules from a library based on several decades of hydrological research in western and northern Canada. Process algorithms within this library cover a wide range of phenomenon that are specific to cold regions hydrology, and range from physically-based to conceptual in nature. The modules are then linked together to represent specific elements of the hydrological cycle and system behaviour over hydrological response units (HRUs). The HRU concept was discussed briefly on page 29 in Section Two; for CRHM, HRUs are defined as homogeneous landscape units characterized by their surface properties and terrain features, and within which conditions and processes are represented by single sets of parameters, state variables, and energy and mass fluxes. Because process modules can be chosen to create a purpose-built model, and spatial representation can be varied from lumped to distributed, CRHM provides a high level of flexibility.

CRHM also has the advantages of a user-friendly interface and relatively easy operation. The model platform checks and configures the linkage of the selected process modules to ensure a functional model is generated with appropriate structure and data flow. The interface allows the model developer/user to set parameters and basin characteristics, and specify initial conditions and observational forcing data, while a graphical display of the output is provided to easily visualize results. These results can be saved for comparison with other simulations and/or exported for use in other programs such as Microsoft® Office Excel. Analysis of the data can also be performed within CRHM to examine the performance of the model, or to convert or scale observation data for use in the model. Thus, a model can be quickly created, run, and tested using an

observational time series, and can be modified according to any deficiencies that are found.

The mass and energy balance snowmelt model developed for this work was based on existing modules already within the CRHM library. In particular, the model Snobal, which was developed by D. Marks and is described in detail by Marks et al. (1998, 1999, 2008), was recently incorporated as a module within CRHM, and was used for snowmelt computations in this study. Other routines were added to handle observation data, blowing snow redistribution, and components of the energy balance, such as incoming shortwave and longwave radiation in complex terrain, and snow surface albedo. These components and their linkages within CRHM form an operational model for snowmelt simulations, as described below.

5.2.2 Snobal (Snowmelt Energy Balance Model)

Snobal simulates each component to calculate a coupled snowpack energy balance (Equation (2.2); p. 23) and mass balance for each model time-step to predict the development of, or melting and runoff from the snowpack. The pack is approximated as being composed of two layers for simplicity of representation, including a surface active layer of fixed maximum thickness, and a lower layer representing the remaining portion of the snowpack. Energy and mass exchanges to and from the atmosphere are accounted for within the active snow layer, while the lower layer does not interact with the atmosphere directly, but rather, with both the ground and the active snow layers. Snobal solves for the temperature (°C) and the specific mass (kg/m^2) or water equivalent depth per unit area (mm) of each layer for each time-step. Melt is computed in either layer once the accumulated energy exceeds that required to bring the snowpack to 0 °C, at which point positive values of Q_m in Equation (2.2) result in snowmelt. Runoff occurs once the accumulated melt and liquid water content exceed a specified threshold for maximum water holding capacity. Figure 5.1 depicts this representation of the snowpack and the fluxes that are considered by Snobal.

The model is initialized by setting parameters specifying the measurement heights and snowpack state variables (i.e., snow depth, density, temperature, and liquid water

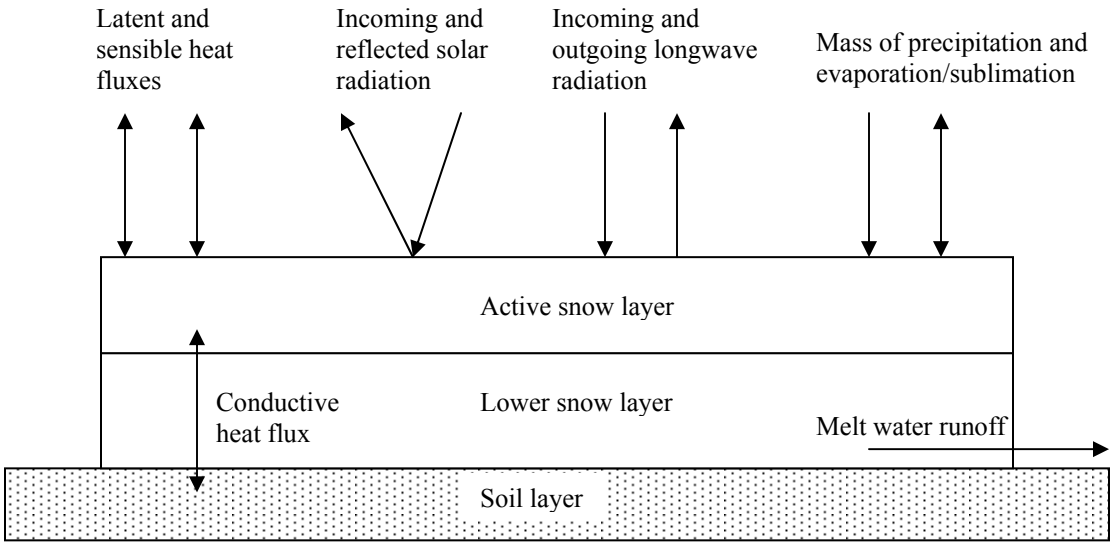

Figure 5.1. Conceptual representation of the two-layer snowpack simulated by Snobal, and the mass and energy fluxes to and from the snowpack. Modified from: Marks et al. (1998, 1999).

content). With each time-step, these conditions are updated as the snowpack evolves. Measurement heights can be set as relative to the snow surface to allow them to change, and the physical characteristics of both layers are adjusted according to the melt or accumulation of the pack. The thickness of the lower layer is set as the difference between the total snow depth and the maximum active layer thickness, or as zero if the total depth is less than the maximum depth of the active layer. Snow surface roughness height, z_0, is set as a constant that is preserved throughout the simulation. The liquid water content is determined as:

$$w_c = \frac{\text{volume of water}}{\text{volume of snow} - \text{volume of ice}}, \tag{5.1}$$

and the relative saturation of the snowpack is determined from its ratio to the maximum liquid water holding capacity, $w_{c,\,\max}$ (i.e., the capacity of the void fraction to retain liquid water). After setting the initial relative saturation, which for a cold and dry snowpack should be equal to zero, the liquid water content is continuously updated for each model time-step.

Snobal handles the mass and energy fluxes to and from the snowpack using a number of sub-routines. For precipitation events, the model determines the temperature

and form (i.e., solid, liquid, mixed) to adjust the depth and density, water content, and temperature of the snowpack. For the Snobal module within CRHM, the net shortwave and incident longwave radiation fluxes are provided through other modules (described below), while the outgoing longwave component is determined by:

$$L\uparrow = \varepsilon_s \sigma T_{s,0}^4 , \tag{5.2}$$

where ε_s is the snow emissivity, σ is the Stefan-Boltzman constant (5.67×10^{-8} W/m^2·K^4), and $T_{s,0}$ is the snow surface temperature (K), which is calculated by the model for each time-step. The turbulent transfers of latent and sensible heat are evaluated using a bulk transfer approach, where the model solves a system of non-linear equations based on Monin–Obukhov similarity theory. The method was adapted from Marks and Dozier (1992) and uses an iterative solution to simultaneously derive the Obukhov stability length, L, the friction velocity, u*, and the sensible and latent heat fluxes, H and L_vE, respectively, where L_v is the latent heat of vaporization (2.501×10^6 J/kg at 0 °C). This also provides the mass flux, E, by evaporation or condensation to the snow surface. Energy transfers between the snowpack and the underlying ground surface are also considered. A temperature and vapour pressure gradient are established in the model, and used to compute vapour diffusion and heat conduction between the ground and the lower layer, as well as between the lower layer and the active layer.

This model is intermediate in complexity in comparison to other physically-based energy and mass balance snowmelt models. It is ideally suited for the purposes of this study because it explicitly accounts for a number of important physical features of the snowpack. For example, it treats water retention and percolation within the pack, and accounts for the changes in internal energy, effects of refreezing, and associated changes in liquid water content. Snowpack density and thermal characteristics (such as overall specific heat) change with time in the model. Vapour transfer and heat diffusion within the pack and at the snow/ground interface are also simulated. Although these features are represented in a somewhat simplified manner, Snobal offers an advantage over other models that include only crude or no representation of these features. The division of the snowpack into two layers maintains numerical efficiency and simplifies the model structure and parameter selection processes, as opposed to more complex models, which include numerous snowpack layers. However, the two-layer snowpack greatly improves

the representation of snowpack vertical structure from a single-layer treatment. Because it can be run on relatively generalized inputs, is robust and adaptable, and has a moderate to high level of physical realism in comparison to other models, Snobal provides a useful tool for this research.

5.2.3 Other Model Routines and Linkages

To generate a working snowmelt model within CRHM, a number of other routines had to be added to supplement Snobal and provide some of the mass and energy fluxes to the snow surface. These included modules to handle meteorological observations and basin characteristics, blowing snow redistribution, radiative fluxes on sloping surfaces in complex terrain, and snow surface albedo decay.

Observation series of meteorological data at 15 minute intervals from each of the stations on Fisera Ridge were input to CRHM using the *Observation* module. This included observation of incoming shortwave and longwave radiation, air temperature, humidity, wind speed, precipitation, snow depth, and snowpack temperature. The *Basin* module specifies characteristics for each of the HRU (or points), including latitude, slope and aspect, elevation, and area. Together, these modules handle the basic model forcing and project setup by extrapolating observations to individual HRU (e.g., using a lapse-rate correction for air temperature) and defining the basic physical characteristics of the basin.

The *Prairie Blowing Snow Model* (*PBSM*; Pomeroy and Gray, 1990; Pomeroy et al., 1993; Pomeroy and Li, 2000) was incorporated into CRHM as a module and linked to Snobal (as described in MacDonald et al. (2010)) in order to simulate the erosion or deposition of snow due to wind redistribution. Although the focus of this work is not on the development of the snowcover over the winter, but rather its melt in spring, it is important to adequately represent the initial state of the snowpack near the time of melt onset. This is done by considering the energy and mass transfer for a period of time in late winter to allow the model to develop the initial pre-melt conditions. PBSM represents the snow mass balance of an HRU as:

$$\frac{d(\mathrm{SWE})}{dt} = P - p\left(\nabla_H \cdot F(x) + \frac{\int E_B(x)dx}{x}\right) - E - m_r\,, \tag{5.3}$$

where $d(\mathrm{SWE})/dt$, P, E, E_B, and m_r are the surface snow accumulation, snowfall, surface sublimation, blowing snow sublimation, and melt rates respectively (kg/m^2·s), p is the probability of blowing snow occurrence, ∇_H is the horizontal divergence , F is the downwind blowing snow transport rate (kg/m^2·s), and x is the fetch distance. Transport by both saltation and suspension processes are considered, and PBSM specifies an aerodynamic roughness height that depends on the saltation layer height. The probability of occurrence of blowing snow is used to account for the unsteady nature of blowing snow events and the differences in meteorological/surface conditions that restrict these events (Li and Pomeroy, 1997b). Although the model was designed to be used in prairie and arctic environments, MacDonald et al. (2010) recently demonstrated its ability to perform well for snow mass balance and blowing snow sublimation and transport rates at Fisera Ridge.

PBSM is linked to Snobal in CRHM in a simple way. A special PBSM module compatible with Snobal, *PBSM_Snobal*, produces outputs of HRU sublimation and HRU snow drift, which are used as basic inputs to the modified Snobal routine. Other inputs to Snobal are provided through the Observation module, as well as the following modules described below.

To simulate incoming shortwave radiation on sloping terrain, the direct and diffuse beam components of solar radiation were adjusted using the modules *Global*, and *Slope_Qsi* within CRHM. Global calculates the theoretical direct beam component of solar radiation to slopes, Q_{dir}, using an expression proposed by Garnier and Ohmura (1970):

$$\begin{aligned} Q_{dir} = I \cdot p^m \big[&(\sin\theta\cos H)(-\cos A\sin Z) - \sin H(\sin A\cos Z) \\ &+ (\cos\theta\cos H)\cos Z\big]\cos\delta + \big[\cos\theta(\cos A\sin Z) \\ &+ (\sin\theta\cos Z)\big]\sin\delta \end{aligned} \tag{5.4}$$

where I is the intensity of extraterrestrial radiation, p is the mean zenith path transmissivity of the atmosphere, m is the optical air mass, δ is the declination of the sun, θ is the latitude, H is the hour angle measured from solar noon positively towards west, A

is the slope azimuth (i.e., aspect) measured from the north through east, and Z is the angle of the slope. Global uses a simple means of calculating the diffuse clear-sky radiation, Q_{dif} (W/m^2), given by List (1968) as:

$$Q_{dif} = 0.5((1 - aw - ac)Q_{ext} - Q_{dir}) , \quad (5.5)$$

where aw is the radiation absorbed by water vapour (7 %), ac is the radiation absorbed by ozone (2 %), Q_{ext} (W/m^2) is the extra-terrestrial radiation on a horizontal surface at the outer limit of the earth's atmosphere, and Q_{dir} (W/m^2) is the direct clear-sky radiation reaching the earth's surface on a horizontal surface. The Slope_Qsi module estimates shortwave radiation for a slope from the measured incoming shortwave radiation on the level. The ratio of measured shortwave radiation and the calculated theoretical clear sky direct and diffuse radiation on a horizontal plane is used to adjust the calculated clear sky shortwave radiation value on the slope.

The reflected shortwave radiation was determined from the albedo of the snow (i.e., the ratio of reflected radiation to incident radiation), which was computed using a specific albedo module. This module parameterizes the albedo as an exponential decay during the melt period using the following expressions from Essery and Etchevers (2004). For each timestep with snowmelt, the albedo is updated according to:

$$\alpha \rightarrow (\alpha - \alpha_{\min}) \exp\left(\frac{-\Delta t}{\tau}\right) + \alpha_{\min} , \quad (5.6)$$

where Δt is the timestep length, τ is a time constant applied to melting snow, and $\alpha_{\min}$ is the minimum albedo that the decay declines asymptotically toward. For time steps with snowfall, the albedo is increased by:

$$\alpha \rightarrow \alpha + (\alpha_{\max} - \alpha)\frac{S_f \Delta t}{S_{\min,\alpha}}, \quad (5.7)$$

where S_f is the snowfall amount during the timestep, and $S_{\min,\alpha}$ is the minimum snowfall amount required to refresh the albedo to $\alpha_{\max}$.

Incoming longwave radiation was adjusted for the location within the landscape using a modified version of the parameterization suggested by Sicart et al. (2006), in which the effect of varying sky view is accounted for. The sky view factor is the fraction of sky visible from a specific point, and is defined as the ratio of the projected area of the

visible hemisphere to the projected area of the whole hemisphere. In this model, longwave irradiance on the slopes, $L\downarrow$, was calculated as:

$$L\downarrow = L_0 + \upsilon_{eff}\varepsilon_s\sigma T_s^4, \tag{5.8}$$

where L_0 is the observed incoming longwave radiation, υ_{eff} is the effective terrain view factor (i.e., the difference between sky view factor at the observation site and that over the slope), ε_s is the emissivity of the surface (taken as 0.98), σ is the Stefan-Boltzmann constant, and T_s is the surface temperature (K). The daily average air temperature was used as an approximation of the surface temperature. The parameter υ_{eff} accounts for the fact that a component of the observed longwave radiation is contributed from adjacent terrain. This parameter effectively represents the relative increase (or decrease) in exposure to surrounding terrain, and thus provides a useful means for extrapolating longwave radiation measurements to nearby locations with different sky view factors. This adjusted longwave irradiance was computed outside of CRHM using Microsoft® Office Excel and added to the observation files.

Figure 5.2 shows the linkages and data flow within this model, highlighting the main variables as inputs and outputs to and from the various modules for simplicity. Within each of the modules, the model tracks state variables and parameters must be set for the computations made at each time-step. This is described in the following section.

5.3 Model Parameterization and Validation

5.3.1 Observed Meteorological Conditions

The model was set up and tested using conditions and observations at Fisera Ridge for the late winter and spring periods of 2007, 2008, and 2009. Figures 5.3 and 5.4 show the meteorological conditions during these periods for the latter two years as daily averages or totals for measured variables. Several features are common between the different observation years, and have a significant influence on the snowcover evolution here. The local conditions are characterized in general by relatively high wind speeds throughout the winter and spring. Cold temperatures and light snowfall events generally occur in March, while early and short duration melt events begin more so in April as air

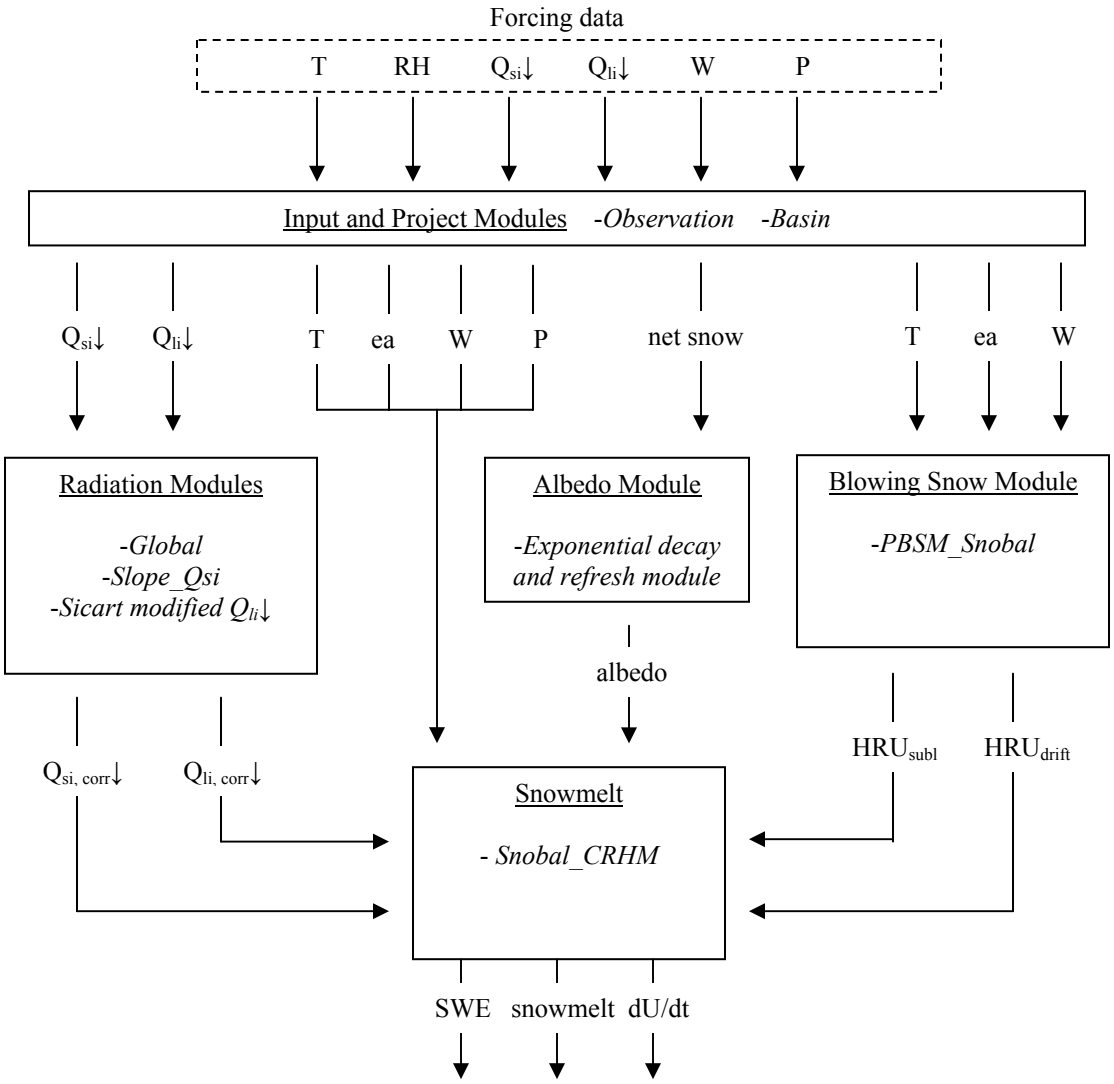

Figure 5.2. Flow diagram of the modules and linkages within CRHM to construct an operational snowmelt model for the study. Variables are: wind speed (W), relative humidity (RH), specific humidity (ea), air temperature (T), precipitation (P), incoming longwave radiation ($Q_{li}\downarrow$), and incident shortwave radiation ($Q_{si}\downarrow$).

temperatures become positive for up to several days. These early melt events are interrupted by snowfall events and/or cooler conditions, which build up the snowcover to peak accumulation, usually sometime in early or mid-May. Snowmelt conditions and the primary melt period usually begin in mid to late-May, when warmer air masses sustain positive air temperatures and shortwave radiation receipt becomes larger due to higher

sun angles and longer day lengths. Net longwave radiation generally represents an energy loss from the surface, except during a few instances when there is high humidity and cloud cover, such as during precipitation events.

Snowmelt is frequently interrupted by spring snowfall events in May and June, which can deposit 100 mm or more of SWE. These events are usually characterized by relatively warm conditions, leading to the accumulation of wet and dense snow over the landscape, and refreshing the snowcover. It may then take up to several days or a week for melting conditions to resume. This pattern during the late winter and spring period is characteristic of most seasons in the alpine zone of MCRB and common across the Rocky Mountain Front Ranges.

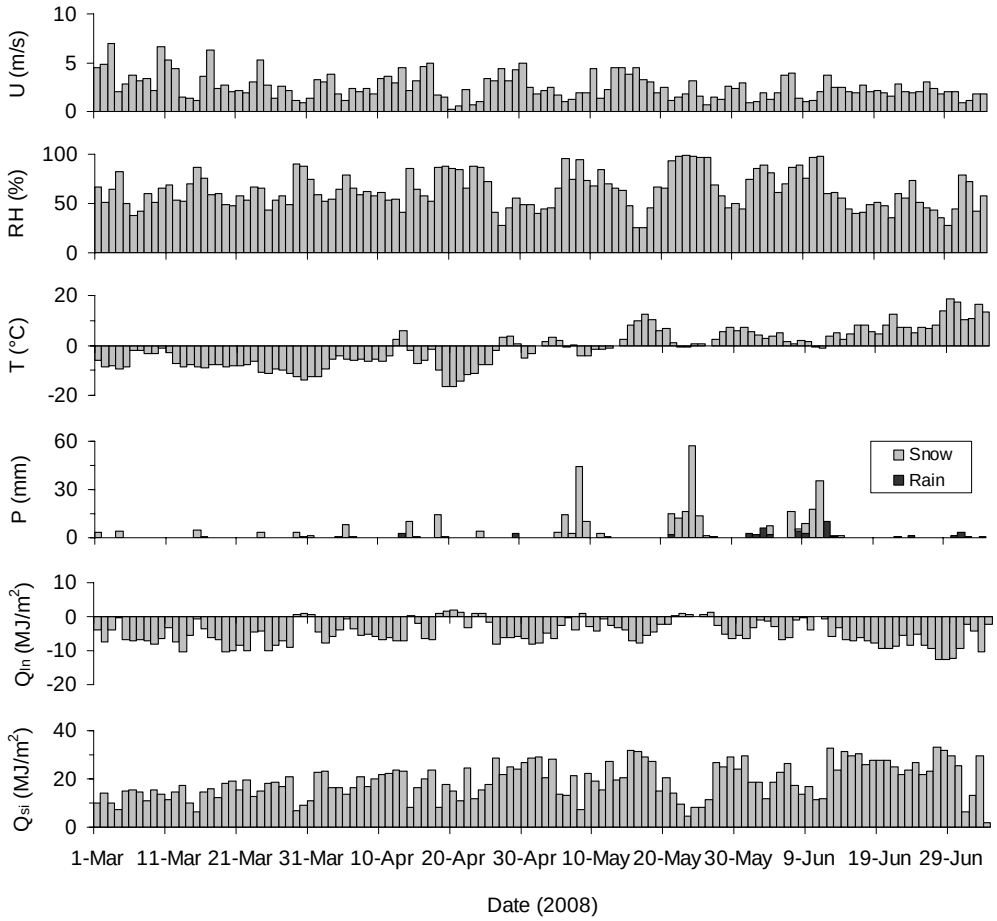

Figure 5.3. Observed daily meteorological conditions at Fisera Ridge during the late winter and spring period in 2008. Variables are: wind speed (U), relative humidity (RH), air temperature (T), precipitation (P), net longwave radiation (Q_{ln}), and incident shortwave radiation (Q_{si}).

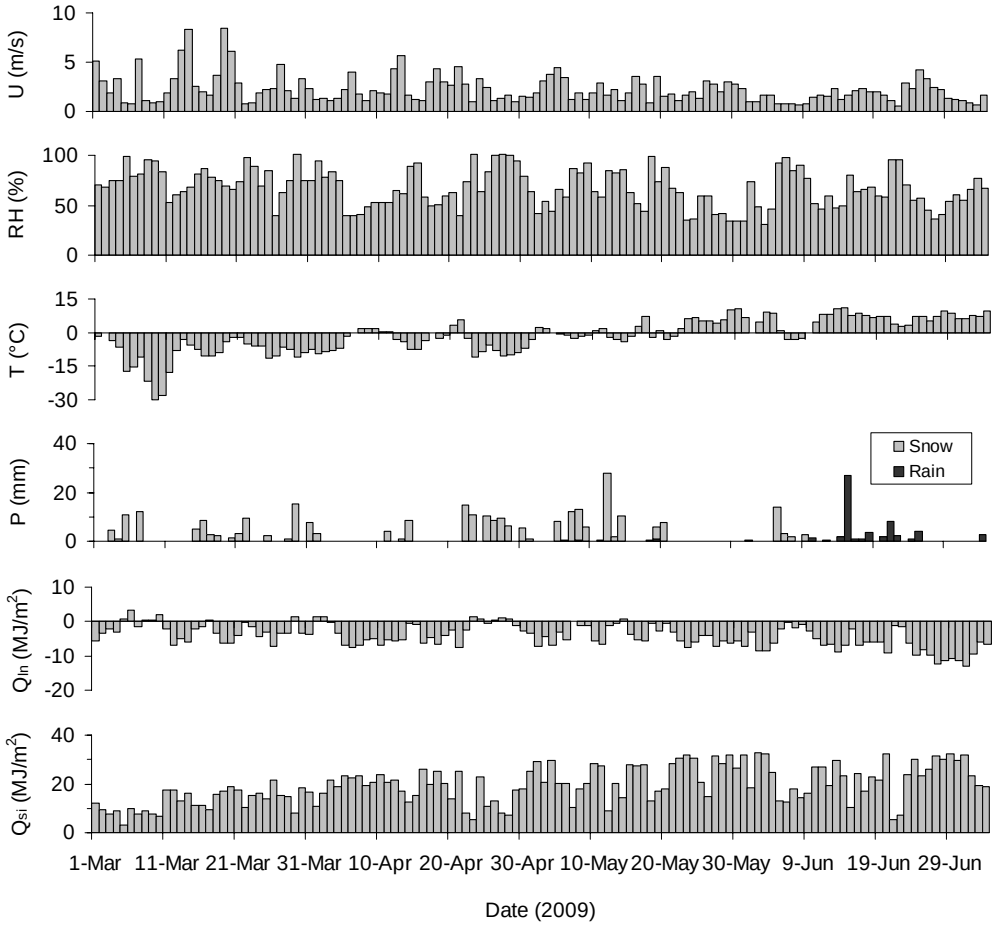

Figure 5.4. Observed daily meteorological conditions at Fisera Ridge during the late winter and spring period in 2009. Variables are the same as in Fig. 5.3.

5.3.2 Initialization and Parameterization of Model

For each model run, the initial conditions were set from observations at each station on or as near as possible to March 1 of the respective season. This was the start date for each run in order to provide sufficient time for the model to develop the pre-melt snowcover state. Thus, the simulated snowpack was able to adjust to the prevailing meteorological conditions and reach a quasi-stable internal state during the period prior to melt. The model was run for the late winter and spring periods of 2007 at the main station, and the same periods in 2008 and 2009 at all stations. The first 2 years of observations were used

to identify and select the most suitable parameter values, while observations from the final year were used to evaluate the model performance.

Model parameter selection was performed by setting parameters from field measurements, using standard or default values associated with some modules, or by manual calibration in some instances. Measurements of some standard terrain parameters were made in ArcMap^{TM} 9.1 GIS, and are listed in Table 5.1. To obtain measurements of sky view factor at each site on Fisera Ridge, digital hemispheric photographs were taken and the view factor was calculated from them following Corripio (2003). These were determined from the ratio r_a^2 / R_a^2, where r_a is the average radius of the visible horizon, and R_a is the radius of the image. Vegetation parameters at each site, used for PBSM routines, were set following MacDonald et al. (2010), and the minimum fetch distance of 300 m for PBSM was also set following their study.

Parameter selection also focused on three parameters related to snowpack properties represented by Snobal, and four parameters related to the decay function for snow albedo (Table 5.2). The first of these parameters, specific to Snobal, are the roughness height of the snow surface, z_0, the maximum active layer thickness of the snowpack, $max_{z,s0}$, and the maximum liquid water holding capacity of the snowpack, $w_{c,max}$, (i.e., the irreducible water content). The value for roughness height was taken as 1.0×10^{-3} m, which worked well in the simulations using PBSM together with Snobal. This value is physically realistic for the actual roughness of the pure snow surface, as measurements of z_0 over seasonal snowcovers generally indicate small values on the order of 10^{-4} to 10^{-3} m (Harding, 1986). The default value of the maximum active layer thickness in Snobal is 0.25 m. However, Marks et al. (2008) found that reducing the value of $max_{z,s0}$ from 0.25 to 0.1 m improved simulations of sensible and latent heat fluxes under a pine canopy within the Fraser Experimental Forest. Further, the value of 0.1 m is more physically representative of the upper exchange layer of the snowpack within which turbulent energy exchange and short-wave radiation penetration occur, and therefore used here. Maximum water holding capacity, which is defined as the ratio of the volume of liquid water to the volume of pore space within the snowpack, was set following Marks et al. (1998; 2008). In the absence of ice layering, evidence suggests that it rarely exceeds 1% of the snowcover void space, although with ice layering in a

Table 5.1. Surface terrain and vegetation cover parameters at each of the three meteorological stations on Fisera Ridge.

Parameter	Ridge-top	N-Facing	SE-Facing
Terrain slope (°)	0	26	24
Aspect (° clockwise from north)	-	346	102
Elevation (m)	2318	2311	2304
Sky view factor / v_{eff}	0.76	0.71 / 0.05	0.74 / 0.02
Vegetation height (m)	0.14	0.17	0.92
Vegetation density (shrubs/m^2)	0.1	0.1	0.6

Table 5.2. Snowmelt parameters used for Snobal and Albedo modules at Fisera Ridge.

Parameter	Module	Value
Roughness height (m)	Snobal	1.0×10^{-3}
Max. active layer thickness (m)	Snobal	0.1
Max. liquid water content (m^3/m^3)	Snobal	0.01
Time constant for melting snow (s)	Albedo	1.0×10^{6}
Minimum albedo	Albedo	0.3
Initial/maximum albedo	Albedo	0.85
Minimum snowfall to refresh (mm)	Albedo	10

wet, melting snowpack it can be as much as 5% (Marks et al., 2008). The value of 0.01 yielded good results, while higher values were found to delay simulated snowpack ablation by retaining too much liquid water.

Albedo parameters for Equations (5.6) and (5.7) were set primarily by calibration with observed snowmelt. The values allow the albedo to decline to artificially low values for pure snow (i.e., 0.3), but in doing so effectively represent an areal albedo that is characteristic of the mixed snow, vegetation, and bare ground surface supplying energy to the melting snow. It was noted that for times when snowcover was present at the main station, these values produced a reasonable correspondence between predicted and observed albedo. The observed albedo was determined on a daily basis using accumulated shortwave measurements from the upward, as well as a downward facing CM3 pyranometer.

5.3.3 Evaluation of Model Performance

Assessment of the model's performance was based on the correspondence between measured and simulated snow depth, SWE, internal snowpack temperature (sloping stations), melt rates, and timing of melt onset. Figures 5.5, 5.6, and 5.7 show time series of some of these variables during the late winter and spring periods in 2008 and 2009. SWE measurements were obtained using the bulk density from nearby snow pits at survey times together with the associated SR-50 depth at each station. The model clearly appears capable of representing the late winter and spring snowpack evolution on different slopes over multiple seasons. Some discrepancies between the observations and the simulation results can be seen in a number of cases (e.g., internal snowpack temperature and SWE in 2009), but overall, the model performs well and tracks the major variations over time. In particular, the model does well at predicting the timing of the

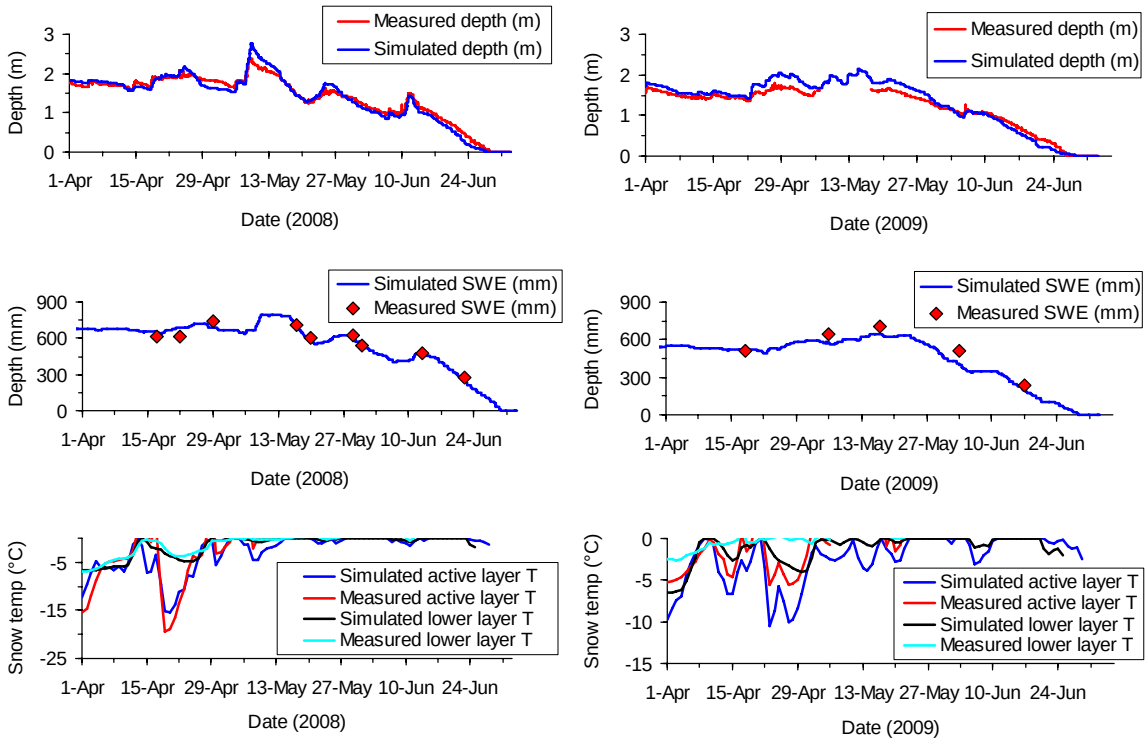

Figure 5.5. Comparisons of measured and simulated snow depth, SWE, and internal snowpack temperature at the South-East facing station for 2008 and 2009 late winter and spring seasons.

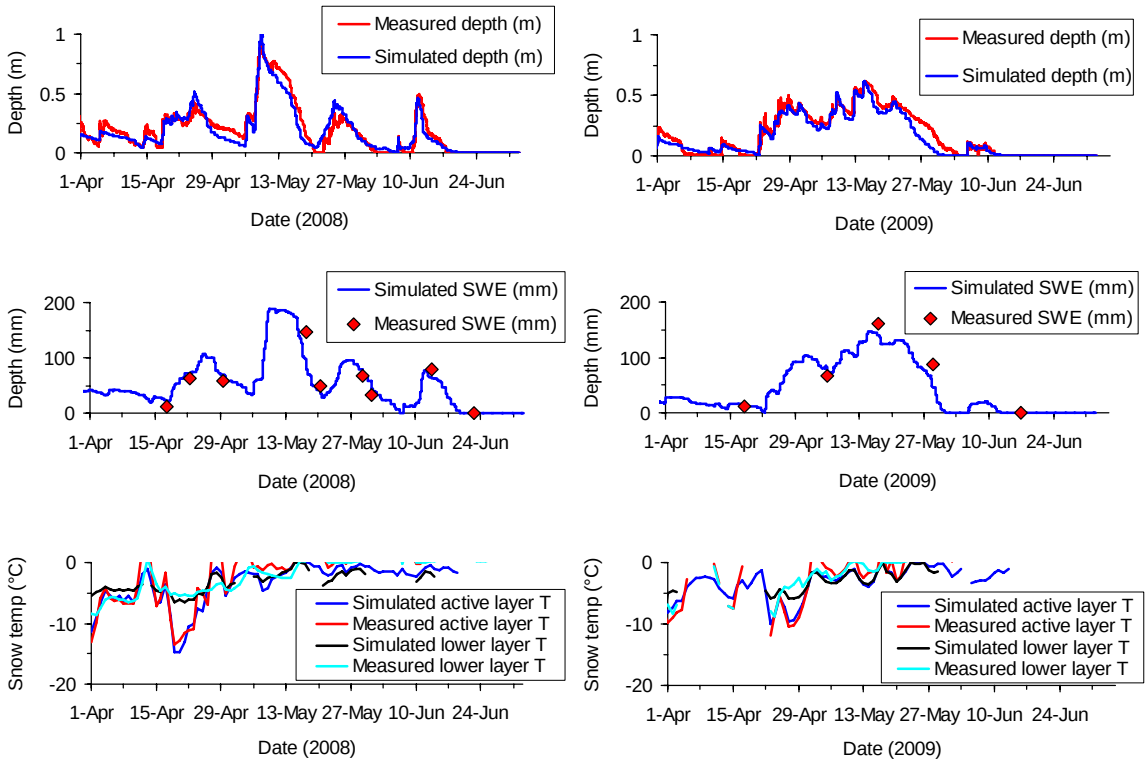

Figure 5.6. Comparisons of measured and simulated snow depth, SWE, and internal snowpack temperature at the North facing station for 2008 and 2009 late winter and spring seasons.

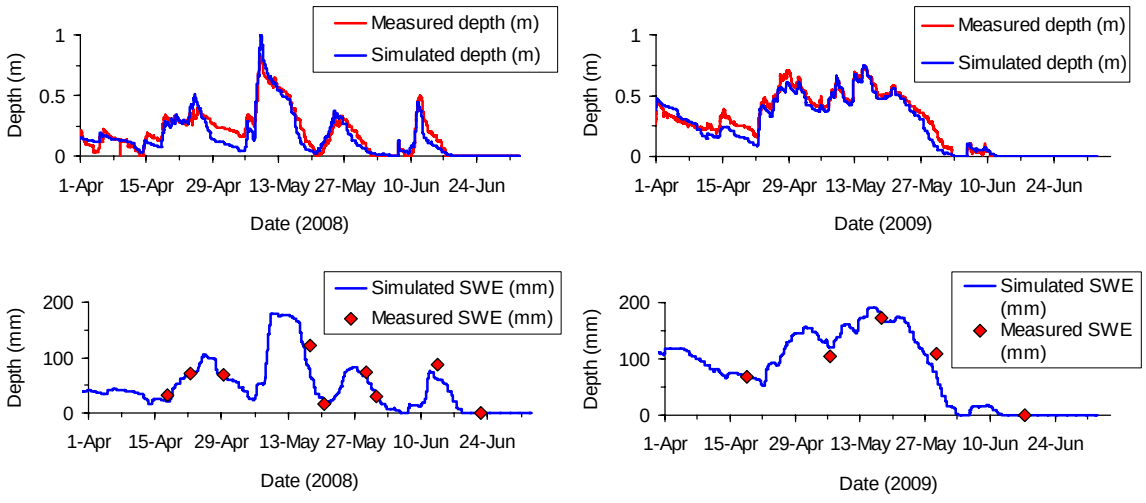

Figure 5.7. Comparisons of measured and simulated snow depth and SWE at the main ridge-top station for 2008 and 2009 late winter and spring seasons.

snowpack reaching an isothermal state of 0 °C and melt onset. In each case, the timing of simulated melting conditions was within ± 1 – 2 days at the most of observed snowpack ripening based on the thermocouple measurements.

Statistical evaluation of the model performance was made using the Nash–Sutcliffe model efficiency coefficient (Nash and Sutcliffe, 1970), *NS*, and the root mean square error (*RMSE*) for snow depth series and individual SWE measurements. *NS* values were calculated as follows:

$$NS = 1 - \frac{\sum_{i=1}^{n}(d_{o,i} - d_{m,i})^2}{\sum_{i=1}^{n}(d_{o,i} - \overline{d_o})^2}, \tag{5.9}$$

where d_o is observed snow depth, d_m is modelled depth, i is an index for the observation – simulation data pair, and n is the total number of pairs. *NS* values range from $-\infty$ to 1.0; an efficiency of 1.0 indicates the model is a perfect match to the observed data, while a value of 0 indicates the model captures none of the observed variability and the predictions are as accurate as the mean of the observed depths. Negative *NS* values occur when the observed mean is a better predictor than the model. The *RMSE* was determined by:

$$RMSE = \sqrt{\frac{\sum_{i=1}^{n}(d_{o,i} - d_{m,i})^2}{n}}. \tag{5.10}$$

This parameter gives a weighted measure (i.e., by the squared term in Equation 5.10) of the residuals between simulated and observed depths. These values are given in Table 5.3 for each station and simulation year. The combination of relatively high *NS* and low *RMSE* values indicates the model generally reproduced both the magnitude and variability of observations quite well.

Melt rates were determined in a number of instances at each site based on the change in SWE between consecutive surveys, or until the time of snow disappearance observed by the SR-50s. These rates were computed over periods ranging in duration from 2 to 10 days, and characterized by relatively continuous and steady melting conditions uninterrupted by snowfall or blowing snow. Figure 5.8 shows the correspondence between simulated and measured snowmelt rates. Although there were not many instances where melt rates could be determined in this manner, the

Table 5.3. *NS* and *RMSE* values for snow depth series (for the period April 1 until final snow disappearance), and for SWE measurements at each site during each of the three years.

	Model year	*NS*			*RMSE* (m)		
		Ridge-top	N-facing	SE-facing	Ridge-top	N-facing	SE-facing
Snow depth	2007	0.83	-	-	0.08	-	-
	2008	0.84	0.88	0.96	0.07	0.07	0.12
	2009	0.90	0.90	0.94	0.06	0.06	0.15
		NS			*RMSE* (mm)		
		Ridge-top	N-facing	SE-facing	Ridge-top	N-facing	SE-facing
SWE	2007	0.76	-	-	22.5	-	-
	2008	0.73	0.67	0.89	18.9	23.2	43.4
	2009	0.88	0.80	0.78	19.6	25.6	77.0

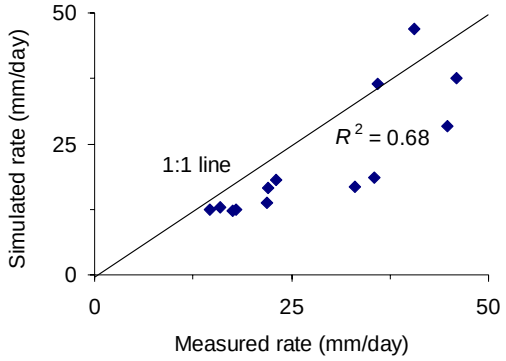

Figure 5.8. Comparison of simulated and measured snowmelt rates at the three stations for various periods in 2008 and 2009. R^2 value is based on a best fit linear trendline (y = 0.83x–1.9).

results indicate a reasonable agreement with the measurements (R^2 = 0.68, n = 13). Simulated melt rates were under-predicted by roughly 5 mm/day on average, but it is noted that the measured rates are subject to some uncertainty due to the difficulty in precisely determining the actual SWE at any given time.

This evaluation of this model is important, and shows that it is robust and able to adequately capture some of the essential features of the snowpack evolution on different slopes and seasons at Fisera Ridge. Its success in predicting snowmelt timing and melt rates under various conditions here indicates that it can be used towards examining the influence of energy receipt and snowpack state on snowmelt variability in more detail. The model should also be able to be applied elsewhere within the surrounding alpine landscape with reasonable confidence.

5.4 Simulated Variability of Snowmelt

It is clear from the results in the previous section that there is a high degree of local variability in the snowcover evolution over Fisera Ridge. Differences in snow accumulation arise from vegetation and topographic influences on wind and blowing snow regimes, while differences in snowmelt arise primarily from spatial variability in the dominant terms of the snowpack energy balance and snowpack characteristics. This section examines some of the differences in snowmelt features over the ridge and other parts of the alpine landscape in Upper Middle Creek Basin, as simulated by the model, to develop a better understanding of the sources and effects of this variation.

5.4.1 Spatial – Temporal Variability in Melt Energy and Snowmelt

Figure 5.9 shows the simulated energy fluxes to a deep snowpack at Fisera Ridge in the late winter and spring of 2008 to provide a sense of the relative magnitude of the various sources of energy for snowmelt. Throughout most of March and early April, net shortwave radiation inputs to the surface were relatively low due to frequent snowfall events together with cold air temperatures and non-melting conditions, which maintained a high albedo. Net shortwave receipt during the day was nearly balanced with nighttime longwave radiation losses from the surface, so that daily net all-wave radiation during this time was approximately zero or negative (Fig. 5.9 c). Melting conditions began to occur later in April with the onset of warmer air temperatures, greater incoming solar radiation, and a decrease in the albedo, causing the net shortwave radiation to increase. During May and June the shortwave component was the dominant term providing most of the energy to the surface, except after snowfall events when high albedo values were temporarily restored. Net longwave radiation was generally negative, but losses were constrained in magnitude somewhat due to the fact that the simulated surface temperature did not exceed 0 °C. At certain times it represented a positive flux to the surface. The turbulent heat fluxes were also nearly balanced in general, with positive sensible and negative latent fluxes. This pattern was also found at the Hay Meadow site (Fig. 4.1) in the valley bottom area here by Helgason (2009), and has been reported elsewhere (e.g.,

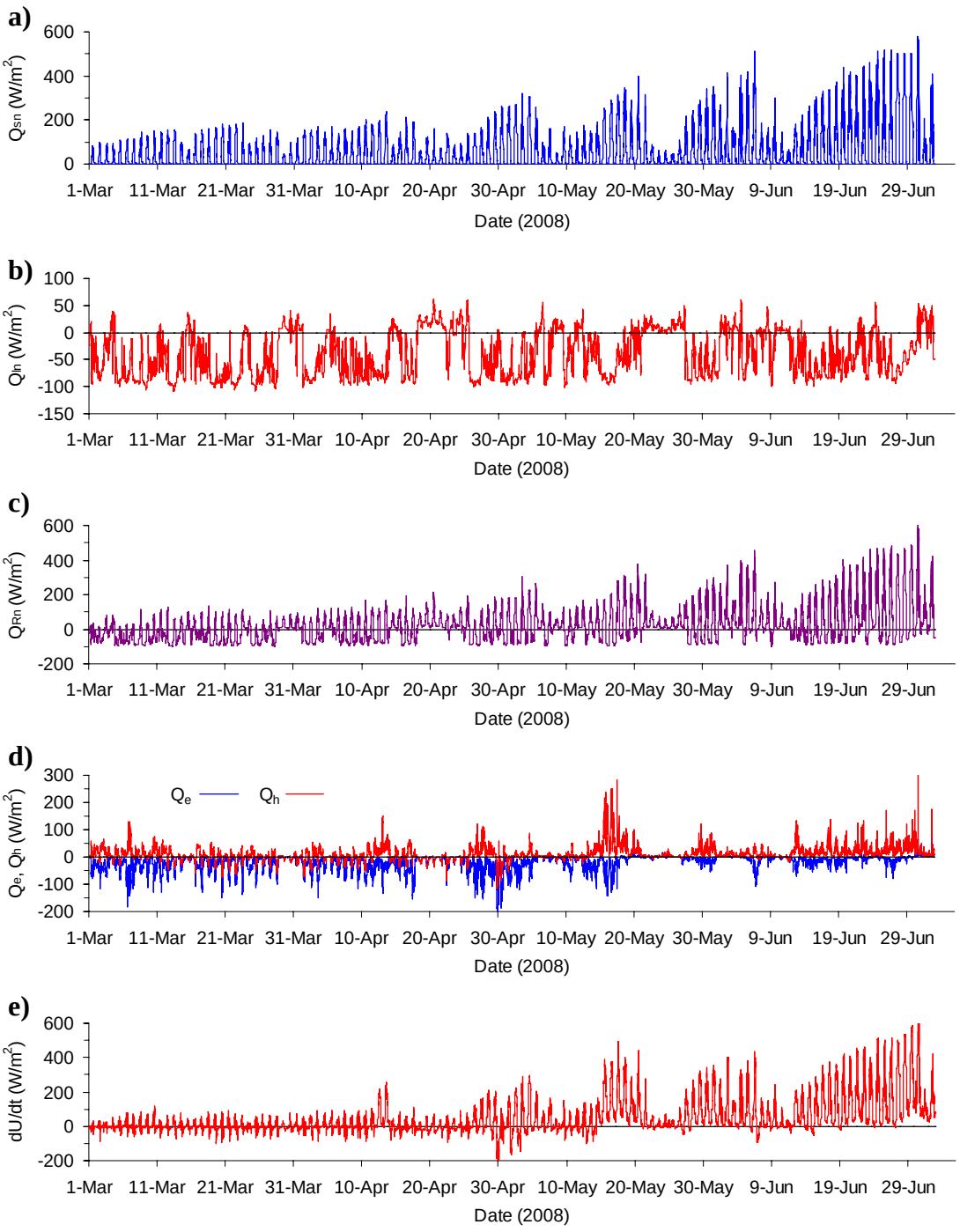

Figure 5.9. Simulated radiant and turbulent energy fluxes and internal snowpack energy changes at the main station on Fisera Ridge during the late winter and spring period in 2008. a) net shortwave radiation (Q_{sn}), b) net longwave radiation (Q_{ln}), c) net all-wave radiation (Q_{Rn}), d) latent heat flux (Q_e) and sensible heat flux (Q_h), and e) internal energy change (dU/dt).

Marks and Dozier, 1992; Marks et al. 1998, 1999, 2008; Pomeroy et al., 1998). Throughout most of March and April, sublimation and latent heat losses were dominant over sensible heat transfer to the pack, but this was reversed in May and June with warmer air temperatures and greater sensible heat fluxes. Finally, the pattern of internal energy changes generally followed that of net radiation over the season. During March and early April, positive daytime values were in balance with negative nighttime values. Later in the season, the positive daytime values became greater in magnitude, and by late May and into June the values of dU/dt were positive at all times.

The dominant source of energy for snowmelt here is net radiation, with the magnitude and temporal pattern of Q_{Rn} being driven mainly by shortwave inputs. The longwave radiation balance is also important when considering nighttime surface losses and given the relative balance between sensible and latent heat fluxes. Therefore, spatial variability in radiation receipt amongst slopes of different aspect, gradient, and sky view in the open, sparsely vegetated alpine landscape likely has the most significant influence on snowmelt variability across the landscape. Differences in simulated incident shortwave and longwave radiation between a number of locations at Fisera Ridge and within the Upper Middle Creek Basin were examined to gain insight on the spatial patterns and variability in these sources of energy for snowmelt. To do this, the modules *Global* and *Slope_Qsi*, and the modified Sicart et al. (2006) module were used to correct radiation inputs on different slopes in the basin, as for the various points over Fisera Ridge. Terrain parameters were defined for each slope-based unit using ESRI® ArcMap™ 9.3 GIS by taking spatial average values over the extent of each slope unit. Skyview was calculated over these slopes using the *Solar Radiation Graphics* tool in ArcMap™, which creates a virtual hemispherical viewshed based on a DEM for the locations of specified points. A number of points were analyzed across each unit to obtain a representative average, and skyview was determined for each as the ratio r_a^2 / R_a^2, where r_a is the average radius of the visible horizon and R_a is the radius of the virtual image. The values of average slope and aspect, as well as sky view and effective terrain view factors (i.e., the difference in sky view between a location and that of the longwave measurement, v_{eff}) calculated for three different slopes within the basin (north, south, and east facing) are given in Table 5.4. The radiation modules were used in a point-scale

Table 5.4. Spatial average values of terrain parameters over individual slope-based units in the alpine part of Upper Middle Creek Basin.

Parameter	N facing slope	S facing slope	E facing slope
Terrain slope (°)	28	26.5	33
Aspect (° clockwise from north)	24	155	76
Sky view factor / V_{eff}	0.72 / 0.04	0.74 / 0.02	0.72 / 0.04

mode with these parameter values.

Figures 5.10 and 5.11 show the simulated daily incident shortwave and longwave radiation to each of the stations over Fisera Ridge and the slopes in the adjacent basin, while Table 5.5 provides values of accumulated radiation receipt over the late winter and spring, along with the relative differences between each station or slope unit and the horizontal ridge-top station. Incoming shortwave radiation to the north facing locations was considerably less than to the horizontal and south facing locations, with an accumulated difference over the late winter and spring of up to –41% compared to a horizontal surface. Daily incident shortwave was very similar between the ridge-top and south-east facing locations on Fisera Ridge, as a slope with this particular orientation (i.e., slightly south of east-facing) receives more direct radiation in the early part of the day, but less in the afternoon compared to the horizontal. The south facing slope within the adjacent basin received the greatest amount of total shortwave radiation, while the east facing slope received less than the horizontal, but more than the north facing locations. Simulated incident longwave radiation was slightly greater at each of the sloping sites due to the parameterization based on differences in local sky view from the measurement location (i.e., the ridge-top site). The greatest difference (i.e., ~6%) was between the ridge-top site and the north and east facing slopes, which have the lowest sky view (highest effective terrain view factor). However, the actual magnitude of differences amongst the sites was considerably less than that for incoming shortwave radiation. For example, differences in accumulated longwave inputs ranged up to as high as 164 MJ/m^2, whereas those of simulated shortwave radiation to the surface were up to 865 MJ/m^2 between sloping and horizontal sites. Therefore a much greater portion of the variance in energy receipt over the landscape is due to shortwave radiation differences.

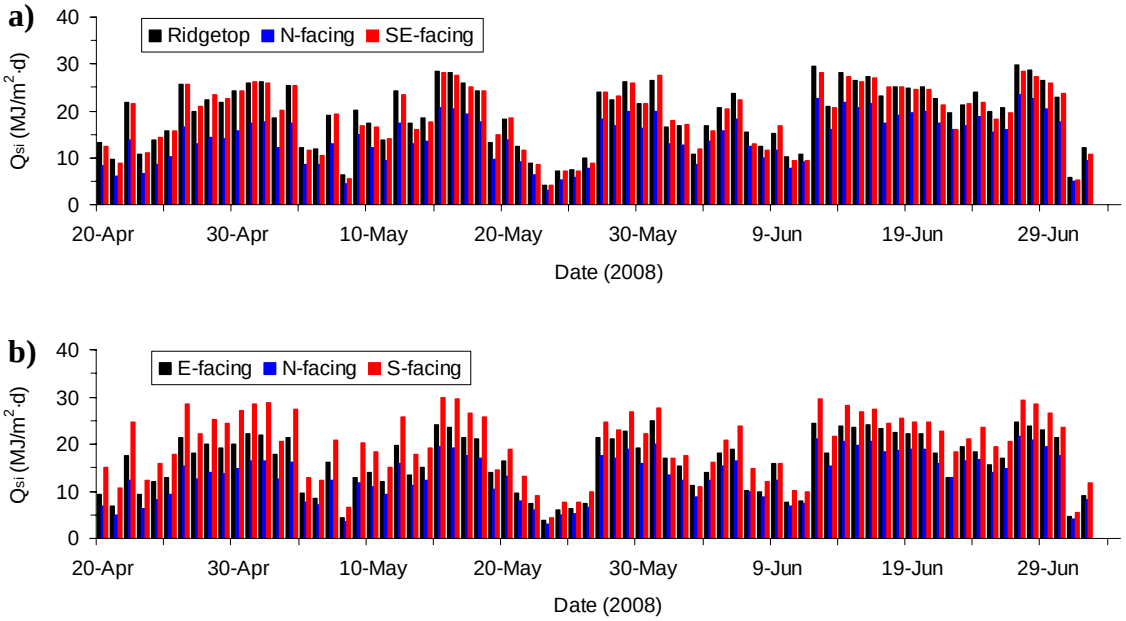

Figure 5.10. Simulated daily incident shortwave radiation (Q_{si}) during the melt period in 2008 at various locations in the alpine landscape: a) at stations on Fisera Ridge, b) for points representing different slope units in the Upper Middle Creek Basin.

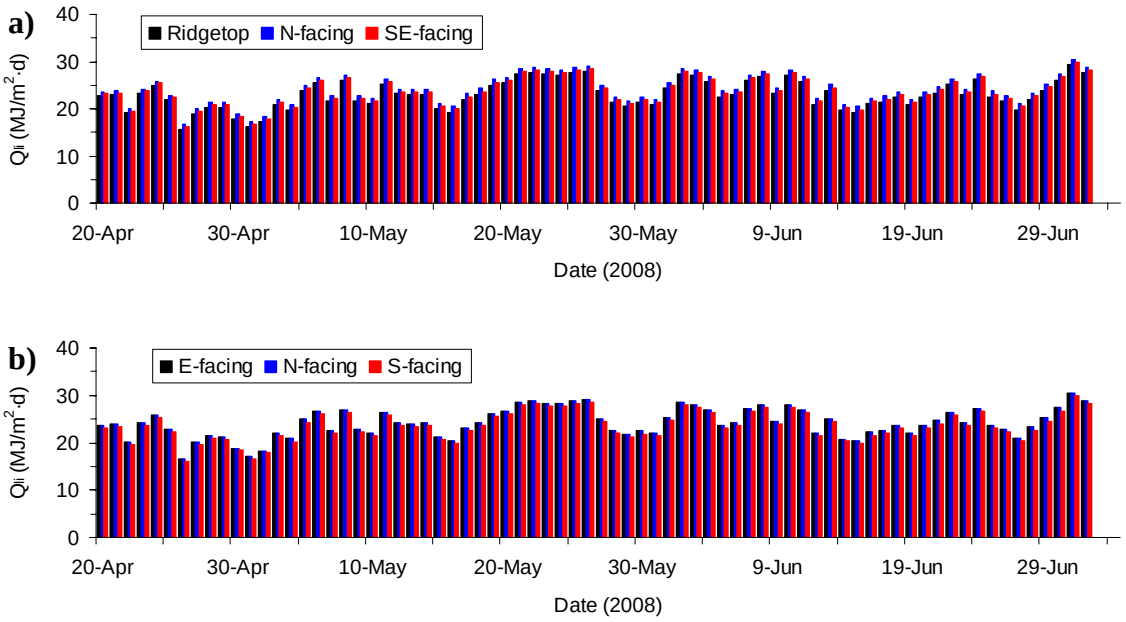

Figure 5.11. Simulated daily incident longwave radiation (Q_{li}) during the melt period in 2008 at various locations in the alpine landscape, as in Fig. 5.10: a) at stations on Fisera Ridge, b) for points representing different slope units in the Upper Middle Creek Basin.

Table 5.5. Accumulated incident radiation and snowmelt over the late winter and spring of 2008 (1-Mar – 2-Jul) amongst the three Fisera Ridge sites and the three slope units. The differences between the value at each sloping station or slope unit and the ridge-top station are expressed as a percentage.

Site/slope	Q_{si}(MJ/m^2)	Diff. (%)	Q_{li}(MJ/m^2)	Diff. (%)	Melt(mm)	Diff. (%)
Fisera ridge-top station	2122	-	2624	-	922	-
North facing station	1369	–35.5	2755	5.0	794	–13.9
South-east facing station	2119	–0.2	2690	2.5	954	3.5
North facing slope	1257	–40.8	2788	6.2	703	–23.7
South facing slope	2379	12.1	2690	2.5	1032	11.9
East facing slope	1755	–17.3	2788	6.2	874	–5.2

Differences in simulated snowmelt as a result of the variability in radiation receipt at the various locations over the alpine landscape were examined using the model described and validated in the previous sections. The model was run with slope-corrected radiation inputs and adjusted air temperatures based on a constant lapse rate (6.5 °C per 1000 m) for slopes in the adjacent basin. Other observations, such as wind speed, humidity, and precipitation were not adjusted and values measured at the main ridge-top station were used. The results of this modelling in terms of snowmelt rates and timing are shown in Figure 5.12, where daily melt rate values were derived from simulations when SWE depths were between ~100 and 200 mm on that particular date. According to this model, snowmelt began later and at a lesser rate at northerly facing locations, while melt rates were greater in magnitude at south and south-east, as well as horizontal locations. Daily melt depths generally remained higher at those sites with greater shortwave radiation receipt throughout the spring, although there were notable patterns in the spatial and temporal variability of snowmelt. For example, periods of active snowmelt conditions with high rates of melt in general at each of the locations were interrupted by periods with relatively low melt during cooler weather or following snowfall events. Local differences in melt at each of the sites indicate that the spatial pattern varies over time as a result of changing meteorological conditions. At times in the spring when the conditions were characterized as warm and sunny, and the magnitude of snowmelt was the greatest, melt rate variability between the different slopes was more pronounced, while under cloudier or cooler conditions with reduced melt rates this variability was greatly reduced. Furthermore, as time progressed toward the summer

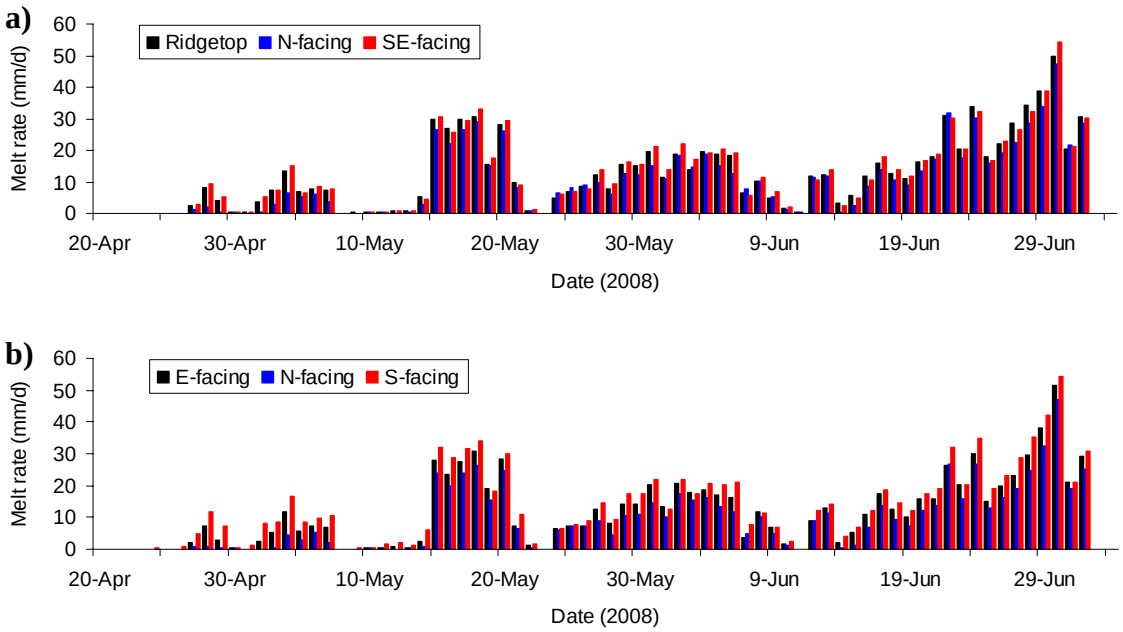

Figure 5.12. Simulated daily melt rates during the melt period in 2008 at various locations in the alpine landscape, as in Figs 5.10 and 5.11: a) at stations on Fisera Ridge, b) for points representing different slope units in the Upper Middle Creek Basin.

solstice, higher solar angles, longer day lengths, and a solar path with more northerly azimuths in the morning and late afternoon lead to more uniform receipt of shortwave radiation between slopes of different orientation. At this time, the presence of warmer air masses is more common as well; both the higher and more uniform insolation, and the relatively warmer air temperatures lead to a reduction in the variability of snowmelt energy and melt rates between slopes.

Differences in simulated longwave radiation receipt also had an influence on the variability of rates of snowmelt over the landscape. The greater incoming longwave to the north and east facing slopes, in comparison to the south, south-east, and horizontal slopes and sites on Fisera Ridge acted to somewhat reduce the variability in melt that otherwise would have resulted from differences in shortwave radiation alone. However, these effects were less important overall. By the end of the simulation in early July, total accumulated snowmelt at the various locations ranged from 703 to 1031 mm, with relative differences from the horizontal site ranging from –24 to 12% (Table 5.5; Figure 5.13).

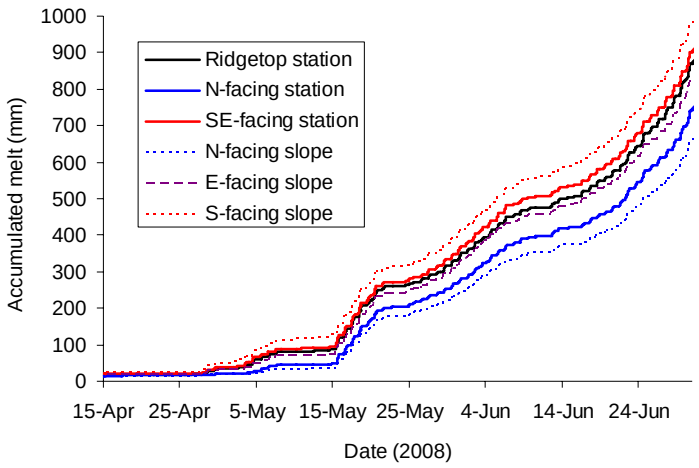

Figure 5.13. Accumulated potential snowmelt at each of the simulated points over Fisera Ridge and within the alpine basin in the spring of 2008.

5.4.2 Effects of Snow Mass and Internal Energy on Snowmelt

In addition to the effects of spatial and temporal variability in radiation receipt and meteorological conditions, differences in internal energy state and SWE are likely to have an important influence on snowmelt rates and timing. The model was used to examine and gain insight on how variability in the snowpack state affects the computation of snowmelt at a point, under the same applied melt energy. To do this, a number of simulations were carried out at each site based on a range of different initial SWE conditions, while using the same parameter values and meteorological forcing variables as previously described. Model outputs of a number of variables such as SWE, internal energy change (i.e., dU/dt), snowpack cold content (i.e., the energy deficit, or energy required to bring the pack to 0 °C), and snowmelt were then compared over time. In each case, the model was run continuously from initial conditions beginning on March 1, and the simulation ended once the snow disappeared. Thus, snowmelt associated with shallow snow later in the melt period was based on the remaining snowpack from simulations with greater initial SWE values, rather than initializing the model with shallow snow at later times in the melt period.

Figure 5.14 shows some of the results for the early melt period in 2008, just as the snowpack in most locations was beginning to become ripe and produce melt. The model

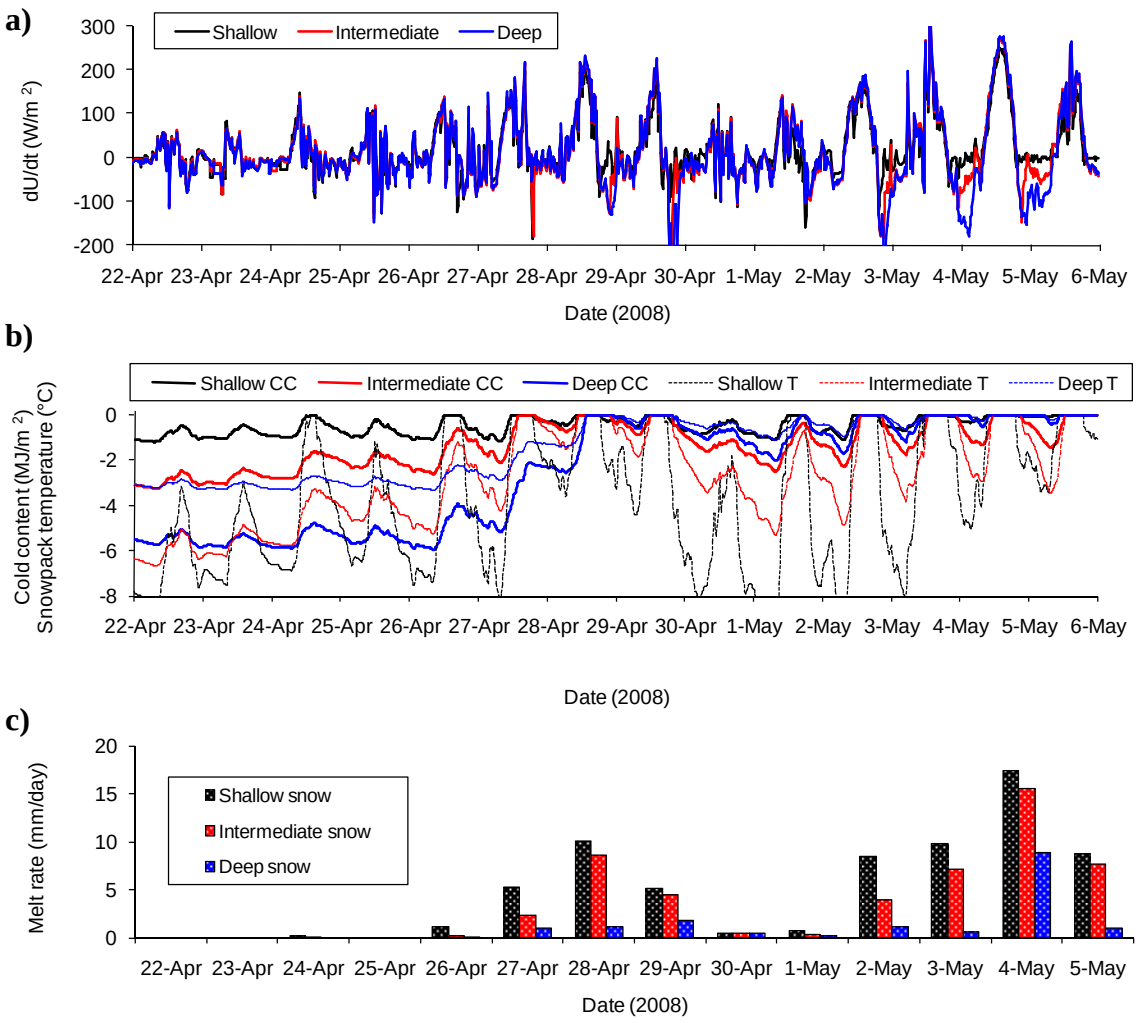

Figure 5.14. Simulated internal energy changes, snowpack temperature, and snowmelt rates in the early melt period of 2008 for conditions at the ridge-top site. Computations were made for three classes of SWE depth: shallow (i.e., ~70 mm on April 22), intermediate (~235 mm), and deep (~850 mm).

is clearly sensitive to the snowpack state and the initial conditions, and produces considerably different timing of melt onset and melt rates depending on these conditions. For the first several days of the period shown in Fig. 5.14, the simulated internal temperatures for all snowpacks were below zero and an energy deficit existed. The shallow snowpack had the coldest internal temperature and was subjected to the greatest diurnal temperature range due to its smaller "thermal mass" (i.e., it responds to variations

in energy receipt and air temperature relatively fast in comparison to a deeper snowpack; Fig. 5.14b). At the same time, the shallow snow had the smallest internal energy deficit because of the relatively small mass of SWE. Deeper snow, in contrast, had relatively warmer initial internal temperatures with greatly reduced diurnal variability, and had greater energy deficits to overcome. The magnitude and variation in dU/dt was very similar for all simulations before snowmelt began (Fig. 5.14a). This was due to the fact that meltwater generation and subsequent overnight refreezing had not yet begun to occur in a significant amount for any of the hypothetical snowpacks represented here.

Snowmelt began as early as April 26, and in more appreciable amounts (i.e., >5 mm/day) by April 27 – 28 for the simulation based on a shallow snowpack. There was a greater lag for the deeper snow to produce similar quantities of melt (i.e., one to two days for intermediate snow and over one week for the deep snowpack; Fig. 5.14c). This was due to the larger cold contents of the deeper snow. Initially, energy inputs to shallow snow were expended on melt, while inputs to deeper snow were used towards warming and ripening the pack. In addition to the differences in melt timing, computed melt rates exhibited variability between the different simulations over time. Throughout this early ripening and melt period, there was a clear diurnal pattern of energy inputs to the surface, increasing internal energy content, and in some instances snowmelt during the day, followed by energy losses, cooling, and refreezing overnight. Because of the smaller mass of shallow SWE, the overnight energy deficits were not as significant (despite the greater decline in snowpack temperature), and thus more of the energy the following day was used towards producing melt.

After April 29, when all simulations had reached isothermal conditions and snowmelt had begun to occur, the refreezing of meltwater and release of latent heat became more important, and resulted in differences in the internal energy changes for different SWE depths (Fig. 5.14a). Overnight energy deficits were generally the least for the shallowest snow, again because of its very small mass of SWE at this time. Interestingly, the intermediate snowpack developed the greatest overnight cold contents. This is because of the slower thermal response of the deepest snow, and differences in the refreezing of meltwater and energy requirements for the latent heat of fusion within the pack. Melt rates were not as significant for the deepest snow, however, since it was still

in the ripening phase and only just beginning to reach its specified liquid water holding capacity.

Figure 5.15 shows how simulated melt rates varied across a range of initial SWE values at different times in the melt period, and at different locations on Fisera Ridge. Conditions for the early melt event in late April – early May are shown in the graphs on the left hand side, while selected melt events later in May and June are shown at right. Local patterns in the variability of simulated melt at each site showed the same broad pattern as observed for the ridge-top, but with differences in timing and rates of snowmelt over the range of SWE values due to the variability in applied energy between sites. In general, for given values of initial SWE the timing of melt onset was later and the melt rates were lower for the north facing location.

At later times in the melt period, Figure 5.15 shows the patterns to change from those simulated earlier in the spring. Following a heavy snowfall event in early May, all simulated snowpacks quickly reached isothermal and ripe conditions, and began to produce melt between the 16th and 18th of May. The negative association between melt rates and SWE that was observed earlier had become reduced and disappeared within one or two days of active melting conditions. At certain times a slight positive association was even predicted by the model (e.g., May 18), which was due to the fact that a shallower snowpack developed a greater overnight cold content due to refreezing at these times.

5.5 Discussion of Snowmelt Modelling Considerations

5.5.1 Energy Balance Terms and Spatial Variability of Simulated Melt

The evaluation of the simulated energy balance shows that a large amount of the total energy for snowmelt here is derived from net radiation, and in particular, net shortwave radiation. In the Rocky Mountain Front Ranges and other similar environments, spatial variability in incident solar radiation is relatively pronounced in comparison to very humid/cloudy environments, or locations with very little topographic relief or variability. This leads to a higher degree of variability in energy receipt between slopes of different

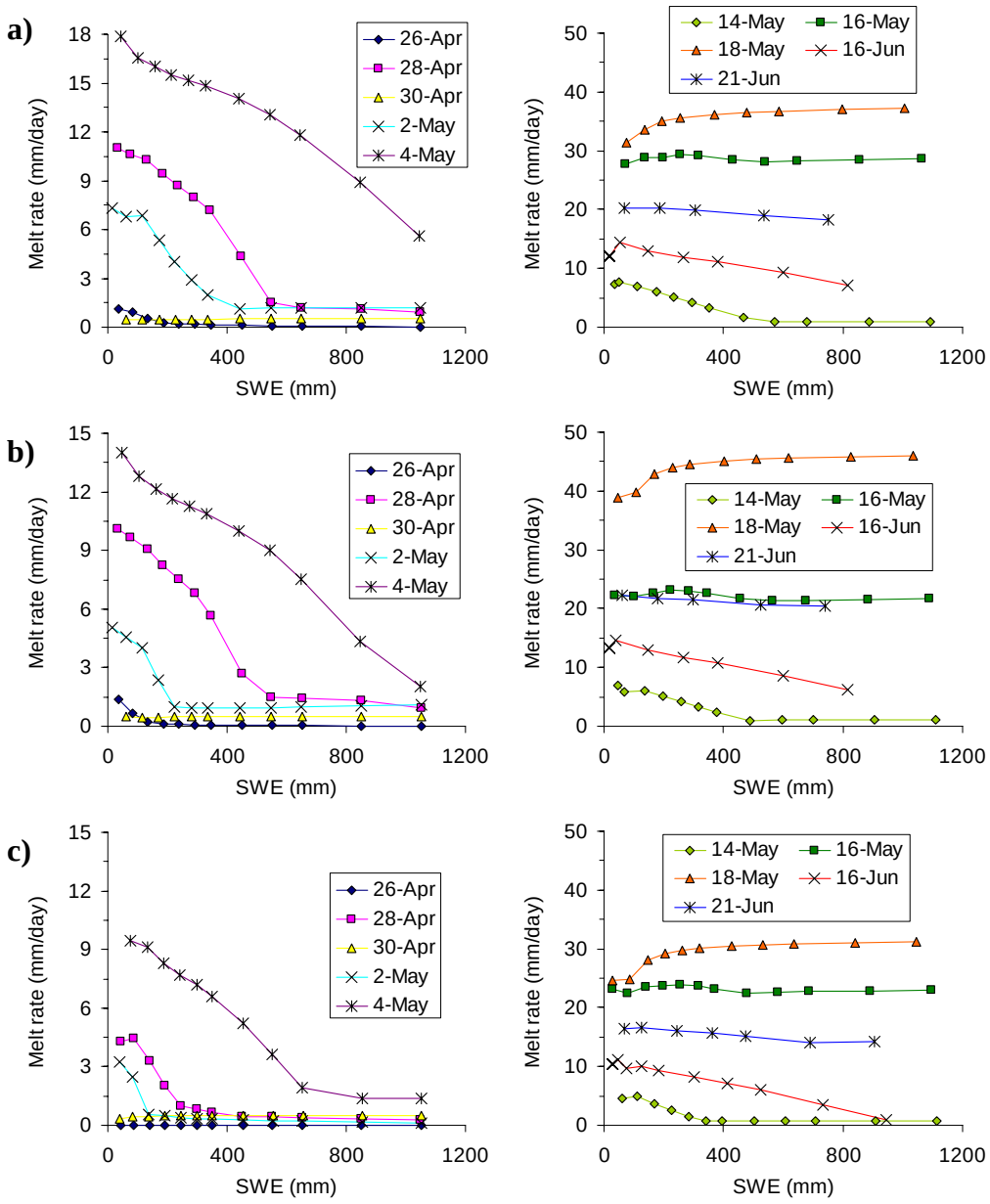

Figure 5.15. Plots of simulated melt rates vs. SWE on consecutive dates at various times throughout the melt period in 2008 at Fisera Ridge: a) ridge-top location; b) south-east facing location; and c) north facing location.

orientation. Pomeroy et al. (2003) reported considerable variability in melt energy and snow ablation rates between different slopes in a subarctic mountainous catchment, and showed that this was primarily a result of differences in the radiation regime. Under clear, sunny conditions with high levels of insolation, dramatically higher ablation rates

were found on a south facing slope in comparison to a valley bottom and north facing slope. Under cloudy conditions later in the melt period, these rates were virtually identical between slopes. The same pattern is apparent over Fisera Ridge and within the Upper Middle Creek Basin. Here, the highest rates of snowmelt occur during warm and sunny periods, while at the same time the variability in melt rates is typically also near a maximum. This suggests that it is highly important to consider and account for differences in local slope orientation and the associated effects on solar radiation receipt to properly represent the spatial – temporal variability in snowmelt energy and melt rates, as shown by Dornes et al. (2008a, b).

Reflection from and differences in local shading by adjacent terrain may also have an influence on the variability of incident solar radiation (e.g., Dozier, 1980). These factors were not accounted for here because it was expected that the effect would be minimal in comparison to the differences due to slope and aspect variability and mainly captured by the local radiometer measurements at Fisera Ridge, and also because the *Global* and *Slope_Qsi* modules together take into account slope self-shading effects. However, in more rugged terrain where cliffs or high surrounding peaks cast shadows over extended periods of the day, it would likely be of greater importance to represent this effect. Accounting for multiple reflections from the surrounding terrain is exceedingly complex, and the reflected radiation should account for only a very small fraction of the total radiation to a given location. It is therefore of greater importance to focus modelling efforts on proper accounting of the primary sources of variability in incoming solar radiation over the landscape.

The net shortwave radiation to the surface also depends on the albedo, α, which is an important parameter for snowmelt computation and must be properly represented in modelling applications. The parameterization approach used here allowed α to decline to artificially low values for a pure snow surface, but in doing so represented the effective mixed surface supplying energy to the melting snow. Wind-blown debris and snow algae have been frequently observed on the snow surface here later in spring, so that even values as low as 0.3 – 0.4 may not be entirely unrealistic. It is also important to account for the effects of fresh snow on α at any time during melt in this environment. The increase in α following these events has a large influence on net shortwave radiation and

delays melt for up to several days or more afterward. The minimum value of 10 mm fresh snow to restore α seemed to work well here. Essery and Etchevers (2004) also found that the 10 mm value of new snowfall to refresh the albedo worked well at several different sites within a wide range of environments for the Snow Model Intercomparison Project (SnowMIP).

Variations in the receipt of longwave radiation over the landscape due to differences in the sky view factor and exposure to the surrounding terrain is also an important source of variability for snowmelt energy. Olyphant (1986), Plüss and Ohmura (1997), and Sicart et al. (2006) showed that longwave irradiance from surrounding terrain is an important component of the energy balance of an alpine snowcover. Atmospheric conditions and the surface temperature of the surrounding terrain are both important in controlling the contribution from adjacent slopes. Thus, taking these effects into account along with local differences in exposure to surrounding terrain is likely to improve the simulated incoming longwave component to the snow surface, and yield better predictions of the snowmelt energy balance. The approach used here approximated the temperature of the surrounding terrain using mean daily air temperature, but differences in the effective surface temperature of the terrain that snow is exposed to could lead to further spatial variation in longwave irradiance. For example, the north facing slopes on Fisera Ridge and within the Upper Middle Creek Basin are exposed to a large south facing slope on Mt. Collembola that typically has large areas of bare ground, which have a low albedo and are heated by the sun. Exposed soil, rocks, and vegetation can be significantly warmer than melting snow ($\leq$ 0 °C) or the mean daily air temperature, especially during clear days. In the spring of 2008 under warm and sunny conditions, temperatures of exposed rocks and bare ground of over 22 °C were measured on this slope using a thermal infrared camera. Thus, as different parts of the terrain become free of snow at different rates and times, the effect could be to increase, or alternatively dampen, the spatial variation in longwave irradiance. Further work may be necessary to determine the magnitude of these effects and their influence on snowmelt modelling in the Rocky Mountains, for instance, by using terrestrial thermal imaging and spatially distributed pyrgeometer measurements to measure the variability of longwave receipt over the landscape.

For the most part, the contributions of latent and sensible heat fluxes to the energy balance are not significant in comparison to the net radiation. The turbulent fluxes are generally of approximately equal magnitude with opposite sign, and thus tend to cancel on average. There are times, however, when these fluxes do not cancel and they may contribute significant amounts of energy to the melting snowpack. The results of the modelling here indicate that in the early melt period, latent heat fluxes tended to dominate slightly over the sensible heat flux, but that later in spring, with warmer air temperatures and greater humidity, the pattern was reversed and sensible heat fluxes were generally greater. This pattern was also found by Marks et al. (2008) under a pine canopy within the Fraser Experimental Forest, Colorado. Therefore, although the fluxes tend to cancel over long periods on average, the short term variability and temporal trends in the magnitude and direction of these fluxes are important in the energy balance of the snowcover over time.

Another source of variability in snowmelt energetics and melt rates over the landscape is the local scale advection of sensible heat from exposed areas of bare ground, vegetation, and rocks. This was not explicitly accounted for or parameterized here, and may have influenced melt rates computed for other parts of the basin where local measurements of air temperature, humidity, and wind speed were not available (i.e., the slopes with Upper Middle Creek Basin). Many studies have shown that the effects of local advection and lateral transport of energy increase as the fraction of SCA decreases during the spring (Liston, 1995; Marsh and Pomeroy, 1996; Shook and Gray, 1997a; Pohl and Marsh, 2006; Grünewald et al., 2010). Although the modelling approach used here did not explicitly account for this effect, the parameterization of the snow surface albedo effectively accounted for the increase in available energy over time from the broader surface by allowing α to decline to artificially low values for pure snow. The spatial variability of energy contributions from local advection is highly complex and difficult to parameterize. The relative contributions depend on factors such as upwind features (e.g., snow, ground, and vegetation patches, and fetch distance), local wind speed and direction, variability in radiation receipt to the landscape, etc. (Shook et al., 1993; Liston, 1995; Neumann and Marsh, 1998; Winstral and Marks, 2002; Pohl et al., 2006). These will change markedly over the spring and over the course of a day, and there is

uncertainty at the present time regarding the spatial scales these processes operate at in this environment and the magnitude of their effects on the overall surface energy balance. Thus there is a need for further research on the relative importance of local advection on snowmelt here.

Overall, the snowmelt modelling at various locations over the alpine landscape within this Front Ranges basin shows that there is a considerable amount of spatial and temporal variability in melt timing, rate, and duration, and that much of this is due to the variation in net radiation, and particularly incoming solar radiation. Differences in simulated melt rates were as high as ~12 mm/day between north and south facing slopes, and the timing of melt onset for the shallow–intermediate depth snowpacks varied by over one week between these slopes. Over the spring and early summer period, the total accumulated potential melt depths differed by over 300 mm between the north and south facing slopes. This variation is significant and likely to have an important influence on the timing and rate of areal SCD over the landscape. Further, due to the non-linear nature and interaction of the processes involved in areal snowmelt beyond the point-scale (e.g., Blöschl, 1999), it is unlikely that the spatial average energy inputs would yield the spatial averages of melt onset and timing, melt rate, or melt duration beginning from initial SWE conditions. Therefore, it should be important to resolve this variability over the land-scape in upscaled modelling applications. The appropriate scale and location for applying point-scale snowmelt computations over the broader landscape is investigated in more detail in Section 6.2 of this thesis.

5.5.2 Snow Mass, Internal Energy Content, and Inhomogeneous Melt

The results of the simulations at a point under the same external forcing (i.e., applied energy) in Section 5.4.2 show that differences in the computation of snowmelt rates and timing can be quite large due to the effects of snow mass (SWE) and internal energy. The model used here indicates that the variability in melt rates due solely to these differences in snowpack state can be, at certain times, comparable to or even greater than the spatial variability in melt rates resulting from differences in radiation receipt between slopes. Further, the timing of melt onset was simulated to vary by more than one week as

a result of differential warming and ripening of the snowpack, which is also comparable to the differences in melt timing noted for a given SWE depth on opposing slopes. The effects of snow mass and internal energy differences are particularly important in the early spring just as the snowcover ripens and begins to produce melt; however, as was shown here, these effects can persist throughout most of the melt period as a result of differences in the night-time cooling and refreezing for different SWE depths. In prairie and low relief arctic environments, where the receipt of solar radiation is more uniform across the landscape, it has been shown how melt is first produced from shallow snow, and that these areas may be snow-free by the time that areas with deeper snowpacks begin to actively melt (Gray and O'Neil, 1974; Male and Gray, 1975; Marsh and Pomeroy, 1996; Pohl and Marsh, 2006). In the open and windswept alpine landscape of the Front Ranges, differences in local snowpack depth and SWE may vary tremendously over horizontal distances of only several meters, and can be up to an order of magnitude greater than found in the prairies. Coupled with the much larger spatial variability in snowmelt energy than that across most prairie and arctic environments, the effects can lead to a highly significant degree of spatial variability in snowmelt characteristics.

These findings are of interest and have important implications for upscaled snowmelt simulations. First, this indicates that it is not physically realistic to simulate areal snowmelt over an initially cold and highly redistributed snowcover by basing melt rate computations on a single snowpack state and neglecting differences in the internal energy content (e.g., Horne and Kavvas, 1997). Because of the tendency of melt from deeper snowpacks to be delayed and occur at an initially lower rate, there is an inherent non-linearity which will affect the upscaled representation upon aggregation by $\overline{SWE}$ and average melt timing/rates. Parameterization of covariance between melt rates and SWE has been previously suggested (Faria et al., 2000; Pomeroy et al., 2001, 2004; Essery and Pomeroy, 2004b), which could potentially resolve this problem in upscaled simulations. However, the results here have indicated that the association is non-linear and not stable over time, and therefore it would be difficult or impossible to characterize in terms of a constant linear covariance term and the parameterization would be intractable over the duration of the melt period. Such an approach is better suited for

conditions involving an association between applied melt energy and SWE that persists over time.

The results also have implications for snowmelt modelling over time from late winter through the spring and early summer. Snowmelt energy balance models are often restricted to so-called ripe periods after the snowcover has reached an isothermal state and is ready to produce melt (Fierz et al., 2003), whereas temperature index methods generally do not even account for the warming and ripening of the snow. Following the onset of melt, model consideration of internal processes and energetics may be neglected for the remainder of the simulation period or until final snow disappearance. The results here, as well as in numerous other studies (Section 2.3.3), show that not only does the snowcover reach this condition at different times depending on the initial state, but that even after this condition has been reached, the internal energy term remains highly important to the energy balance. Within environments characterized by large night-time surface energy losses (particularly on clear nights), changes in the internal energy content lead to an energy deficit that must be satisfied before melt can begin again the following day. Differences in the overnight cold content, which depend primarily on snow mass, may then become manifested as differences in melt timing and overall rate the following day. Shallow snow tends to undergo large diurnal variations in internal energy due to overnight cooling and refreezing, in contrast to deeper snow, which takes longer to warm in spring, but exhibits relatively damped diurnal variation of internal energy content due to its greater thermal mass. Therefore, the effects of snow mass on the energy balance and snowmelt should not be neglected after the initial time when the snowpack reaches isothermal conditions.

In particular, and what has not been previously considered in detail, are the implications of this variation in the energy balance, melt rates, and melt timing due to snow mass on parameterizations of areal SCD based on applying point-scale melt rate computations over a distribution of SWE. Representation of these effects must be considered in combination with the considerable spatial variability in both SWE and snowmelt energetics over exposed alpine terrain. The theoretical framework developed in Section Three provides a tool for examining the effects of this variability on areal snowmelt and SCD. The following section of this thesis addresses these issues.

6. Simulation of Areal Snowcover Depletion and Surface Meltwater Generation

6.1 Introduction

The results presented in the previous section of this thesis clearly show that snowmelt timing and melt rates are subject to considerable spatial – temporal variability in the alpine zone of MCRB, primarily due to differences in net radiation. Snowmelt is also affected by the internal energy state and mass of the snowpack. These features, coupled with the high degree of spatial variability of the pre-melt alpine snowcover, will have a significant influence on areal snowcover depletion (SCD) and the generation of meltwater inputs over the landscape. The purpose of this section is to examine the influence of this variability in upscaled simulations within the Upper Middle Creek Basin, using the snowmelt model described in Section Five together with the theoretical developments presented in Section Three. This will fulfill the second and third objectives of this thesis.

This section begins by examining the spatial pattern of variability in both pre-melt snowcover and energy inputs to the surface during the melt period. Following this, the effects of both of these sources of variability are investigated for areal SCD, and the appropriate scale and configuration of landscape stratification for such modelling is determined. The effects of this variability on meltwater generation over the basin are then explored in terms of the meltwater generating area and the volume of meltwater production. Lastly, the findings here are discussed in the context of alpine snowmelt modelling and improvements to the current state of model development.

6.2 Spatial Variability of SWE and Snowmelt Energy

6.2.1 Spatial Distribution of Maximum Accumulation SWE

To investigate spatial patterns and variability in the snowcover over Fisera Ridge and the Upper Middle Creek Basin, the snow survey and snow pit measurements described in Section 4.3.1 were analyzed statistically. SWE values were derived from depth and density measurements, and analysis of these data focused on some of the relevant parameters such as $\overline{\text{SWE}}$ and CV in order to quantify the variability. Figure 6.1 presents some of the survey measurements around the time of maximum accumulation in the alpine zone at MCRB in 2008, while Table 6.1 provides the associated statistical parameters describing the variability of SWE. It is clear from these survey measurements that SWE varies considerably at the time of peak accumulation, ranging from 10's or 100 mm to over 1100 mm in depth over horizontal distances as short as ~10 m or less. The variability exhibits distinct spatial patterns and structure, which are strongly related to the variation in the underlying surface topography. For example, deep drifts form in the surface depressions and hollows, downwind of small breaks in the micro-topography and exposed alpine shrubs, or on lee slopes, while shallow accumulations are found in more windswept and exposed locations. It is beyond the scope of this thesis to develop relationships between these patterns and the underlying physical factors or to investigate the spatial structure of variability through the use of geo-statistics or fractal analysis (as in many previous studies; e.g., see Sections 2.1.2 and 2.1.3). However, it is noted that the patterns here display many of the same features that have been commonly reported for seasonal snowcovers in open environments.

Both the mean and standard deviation of SWE values are relatively high, producing moderate CV values (Table 6.1). SWE variability over some surveys is not stationary, and therefore the surveys were broken into distinct segments based on slope orientation and the statistical parameters were determined for the individual segments. In many instances this resulted in a reduction in the variability as expressed by the CV, supporting the suggestion by Steppuhn and Dyck (1974) that such stratification based on landform features has merit. However, this was not the case for most of the

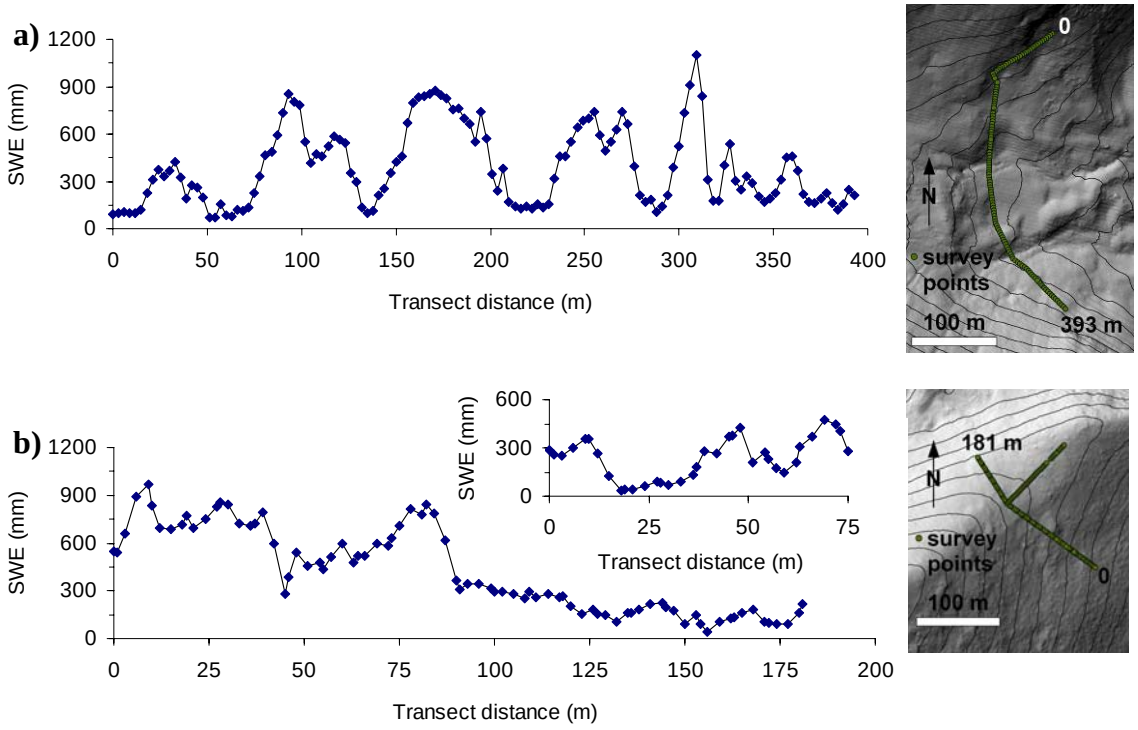

Figure 6.1. Variability of SWE on May 16 and 17, 2008 over survey transects within the Mt. Allan Cirque in Upper Middle Creek Basin (a) and across Fisera Ridge (b). Inset in (b) shows SWE values for the ridge-top "T-Section" of the survey; diagrams at right show the spatial layout of the survey transects over a shaded relief map with 10 m contours (see Fig. 4.5 also).

Table 6.1. Statistical parameters of SWE for snow surveys on May 16 and 17, 2008 at Fisera Ridge and within the Mt. Allan Cirque in Upper Middle Creek Basin. Lumped results for each survey are given along with results derived by splitting surveys into slope-based units.

	Fisera Ridge			Mt. Allan Cirque		
$\overline{SWE}$	367			389		
CV	0.67			0.64		
	S-E facing	Ridge-top	N facing	S facing	Bottom	N facing
$\overline{SWE}$	637	236	158	410	402	329
CV	0.27	0.54	0.36	0.64	0.56	0.72

survey within the cirque. Here, it appears the variability is linked more with the presence of gulleys and depressions, rather than wind loading onto lee slopes as at the ridge.

The surveys were chosen primarily for accessibility, with the secondary criteria being representativeness of the surrounding terrain. Because they characterize only

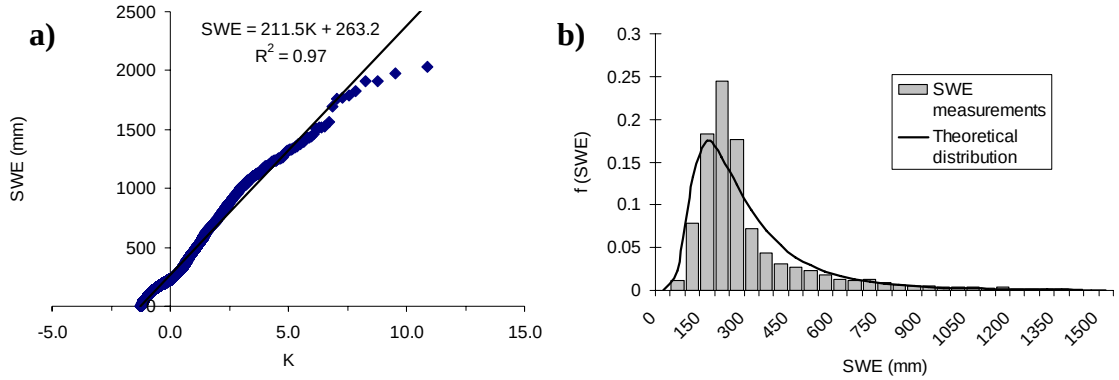

Figure 6.2. Maximum SWE distribution over the entire alpine portion of Upper Middle Creek in 2008: a) Plot of *K* vs. SWE and fitted regression line through the points; b) histogram and theoretical lognormal distribution based on the measured values of $\overline{SWE}$ and CV.

Table 6.2. Statistical parameters of SWE over the alpine landscape of Upper Middle Creek Basin for maximum accumulation in 2008.

Slope unit	$\overline{SWE}$ (mm)	st. dev. (mm)	CV
Entire alpine zone	263	213	0.81
S facing	223	159	0.71
N facing	290	270	0.93
E facing	294	188	0.64
Cirque floor	364	281	0.77

limited portions of the landscape, it was necessary to examine the SWE variability at a broader scale over the landscape using the repeat LiDAR dataset. Spatial patterns of SWE were determined for the time of peak accumulation based on the correspondence between LiDAR and survey measurements at the time of data acquisition, along with the changes observed over time at the surveys. Based on this information, the LiDAR-derived SWE measurements were adjusted to represent the patterns at this time in 2008.

Analysis of the SWE variability derived from the LiDAR dataset was performed to examine the form of the frequency distribution. Figure 6.2 shows the distribution of SWE based on values sampled on a 10 m grid from across the whole cirque and alpine portion of Upper Middle Creek. The SWE values plot against *K* along a straight line with few deviations, while the histogram is highly skewed and corresponds well with the theoretical lognormal distribution based on the same parameters as the measured SWE

(given in Table 6.2). The slope and intercept of the best fit line in Fig. 6.2a match the measured standard deviation and $\overline{SWE}$ very closely. Therefore, it is clear that the lognormal distribution provides a useful approximation to the SWE variability, although it is possible that a better fit might be achieved by a different distribution. That is beyond the scope of this work however, as here the main concern is only to find a simple and yet physically plausible distribution.

To investigate differences in the variability of SWE between individual slopes, the alpine portion of the basin was disaggregated into several distinct units based on slope and aspect (Fig. 6.3). These include a north, south, and east facing slope, as well as the cirque floor area in the alpine zone. SWE values on each unit were then analyzed separately. Figure 6.4 shows the distributions for the south and north facing slopes, while Table 6.1 provides the relevant statistical parameters for all slopes. The lognormal distribution provides a useful approximation for the SWE distribution on each of the individual slopes, as seen for the north and south facing slopes, but the parameters of the distribution differ between slope units. Further, the stratification of the landscape by slope and aspect has led to reduction in the CV values for most of the individual slopes. These results also show that the surveys, covering limited parts of the alpine landscape, are not representative of the SWE patterns and variability over the broader slopes.

6.2.2 Spatial Variability of Incident Solar Radiation

Much of the spatial variability in snowmelt that was examined in Section 5.4.1 was due to the variation in incoming shortwave radiation receipt with slope and aspect. Therefore, the spatial pattern of potential clear-sky incident solar radiation over the landscape was examined to gain insight on this variability at a larger scale. This was done using Spatial Analyst and the *Area Solar Radiation* tool in ESRI® ArcMap™ 9.3. This tool accounts for the latitude, time of year and day, local orientation, and horizon of the terrain as it computes the accumulated radiation over a specified period. Default parameters were used; this includes the uniform sky model for diffuse radiation (set at 0.3 of global normal radiation), and atmospheric transmittivity (i.e., the fraction of radiation passing through the atmosphere averaged over all wavelengths) set at 0.5.

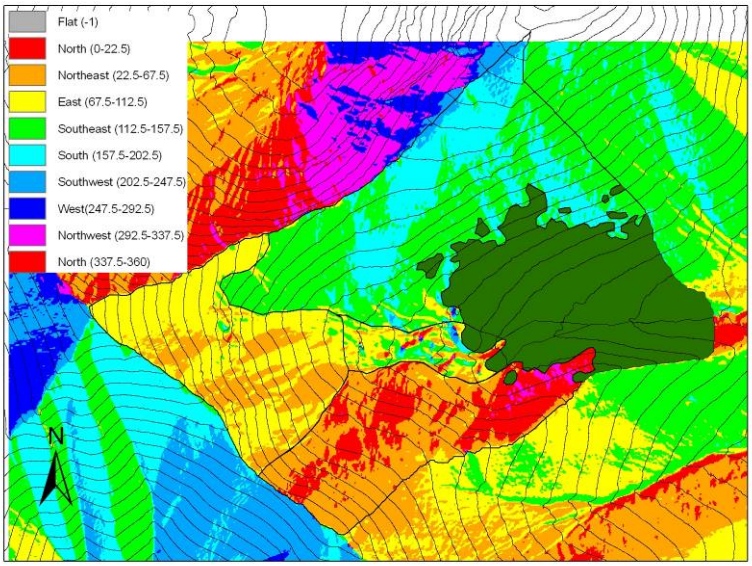

Figure 6.3. Local aspect values over the Upper Middle Creek Basin and division of basin into slope/aspect based terrain units. Lower forested parts of the basin are filled in dark green.

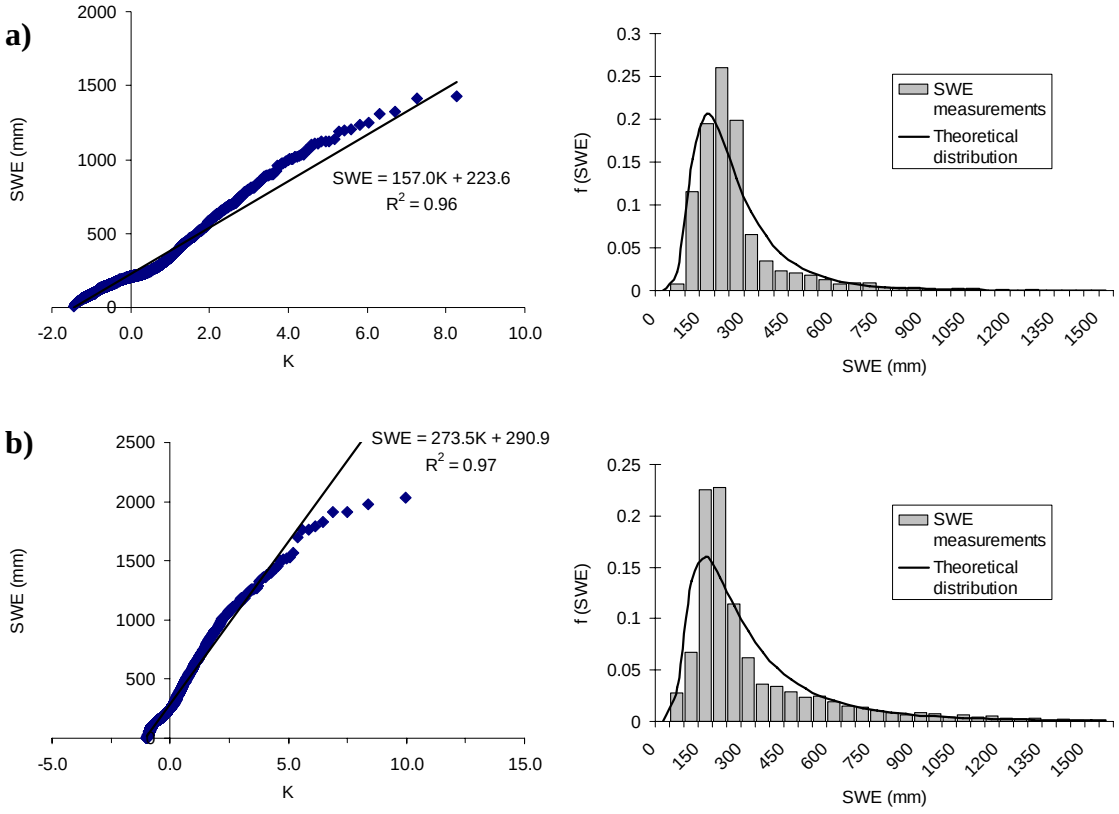

Figure 6.4. Maximum SWE distributions as in Fig. 6.2 for the south facing slope (a) and north facing slope (b) in 2008.

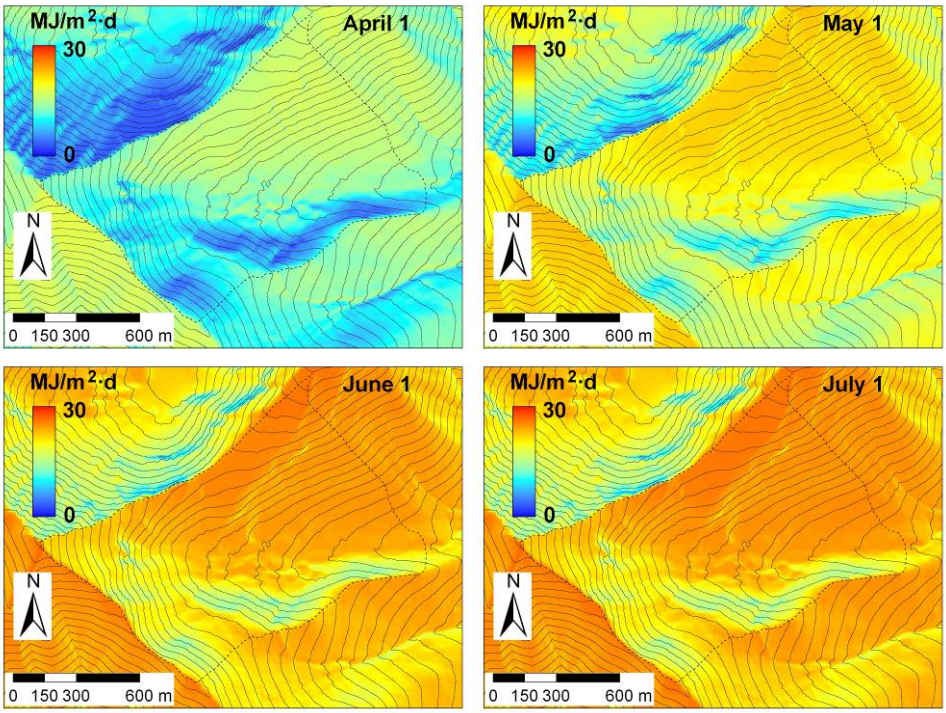

Figure 6.5. Spatial patterns of daily potential clear-sky solar radiation at different times throughout the spring and early summer over the Upper Middle Creek Basin.

The spatial patterns in solar radiation receipt are shown in Figure 6.5 for several different times throughout the snowmelt period. A clear pattern emerges, with the highest and lowest radiation totals on south and north facing slopes respectively, and intermediate values on west and east facing slopes. The patterns change over time as well. For example, earlier in spring, the variability is more pronounced over the landscape, and as time progresses towards the summer solstice, the pattern of radiation receipt becomes more spatially uniform.

This variability in shortwave radiation over the landscape was examined in more detail by extracting the computed values from the raster images and calculating summary statistics (Table 6.3). The variability within individual slope units is, in general, much less than the variability between slopes. By disaggregating the alpine portion of the basin into broad slope and aspect based units, a considerable reduction in both the range of daily radiation values and the variability of these values over individual slopes was achieved. This is a useful result, and shows that the same stratification approach that was

Table 6.3. Summary statistics of daily incident solar radiation ($MJ/m^2 \cdot d$) over different parts of the landscape for specific dates during the spring over the Upper Middle Creek Basin.

Slope unit	1-Apr				1-Jun			
	Mean	Max	Min	CV	Mean	Max	Min	CV
Entire alpine zone	12.5	17.4	2.8	0.30	21.9	26.0	11.7	0.14
S facing	15.9	17.4	5.0	0.06	24.6	26.0	16.1	0.03
N facing	7.9	15.1	2.8	0.28	18.5	25.6	11.7	0.14
E facing	10.9	15.8	5.8	0.16	20.5	25.8	13.4	0.05
Cirque floor	12.8	15.9	7.1	0.09	23.0	24.5	17.5	0.04

used for defining distinct SWE distributions and reducing the CV values over the landscape also resolves a large portion of the variability in incoming shortwave radiation. Most of the remaining variability is due to small scale variations in the local slope and aspect over the broader terrain units, which would require far more spatially explicit stratification to improve resolution of the variability further.

6.3 Areal Snowcover Depletion

The differences and variability of SWE, SWE distributions, and incident solar radiation over the landscape that were reported in the previous section have a significant influence on the patterns of areal SCD. In this section the effects of this variability are examined in detail using daily observations from the terrestrial-based photography together with the tools and results developed in previous sections of the thesis.

6.3.1 Observations of Areal Snowcover Depletion

Measurements of snowcovered area (SCA) were made using the terrestrial-based digital photographs during the spring and early summer for three years (2007, 08, 09) to derive areal SCD curves. (Appendix B describes this procedure in more detail). These are shown in Figure 6.6, and indicate broadly similar patterns between the different years. For example, SCA is typically high throughout May until maximum accumulation, as snowfall events are frequent at this time and act to maintain or refresh the snowcover. The main period of SCD begins in late May and lasts throughout June, but storms in late

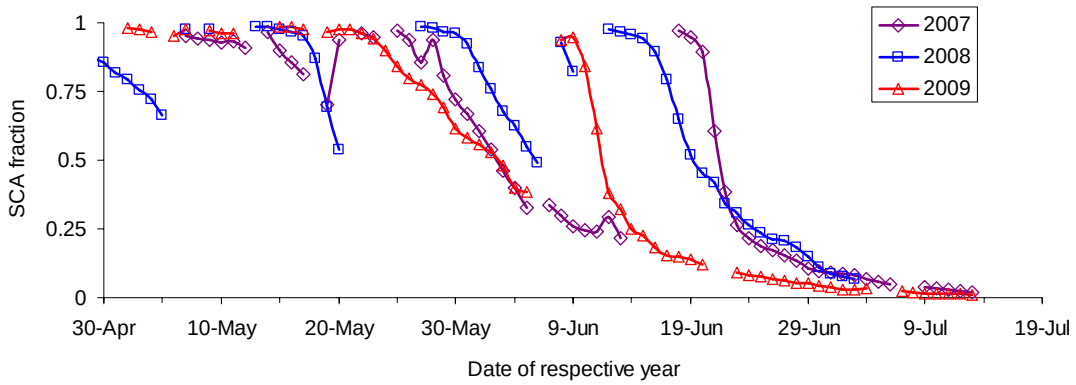

Figure 6.6. Snowcover depletion curves representing the alpine portion of Upper Middle Creek Basin derived from the terrestrial-based photography for the spring period in each of the years of field observations.

May and June, mid-way through melt, often bring heavy snowfall and again refresh the snowcover. By early July only a small fraction of the landscape still remains covered by late lying drifts. The spatial patterns of depletion are also consistent between years, such that drifts and scoured areas are found in the same locations and with the same geometry. Figure 6.7 shows how the snowcover pattern in mid- to late-June appears almost identical in each year, and how this pattern is closely linked to the snow depth over the landscape. The areas of late lying snowcover are the same areas where the deepest accumulation of snow was observed based on the LiDAR snow depth raster image. Spatial patterns of SWE variability are primarily controlled by the surface topographic and vegetation characteristics together with the prevailing wind direction (which is relatively consistent over time). The stability of the spatial SCA patterns from year to year reflects the fact that SWE variability exhibits similar characteristics in different years as controlled by these features.

SCD curves were also derived from the re-projected images separately for each of the individual slope-based terrain units in the Upper Middle Creek Basin. These curves are shown in Figure 6.8 for each of the years of field observations, while Figure 6.9 shows spatial SCA patterns at selected times during the melt period in 2008. It is clear that patterns of SCA and the timing and rate of areal SCD exhibit considerable differences between individual slopes within the basin. In general, the snowcover begins to decline earlier and at a much faster rate over the south facing slope in comparison to

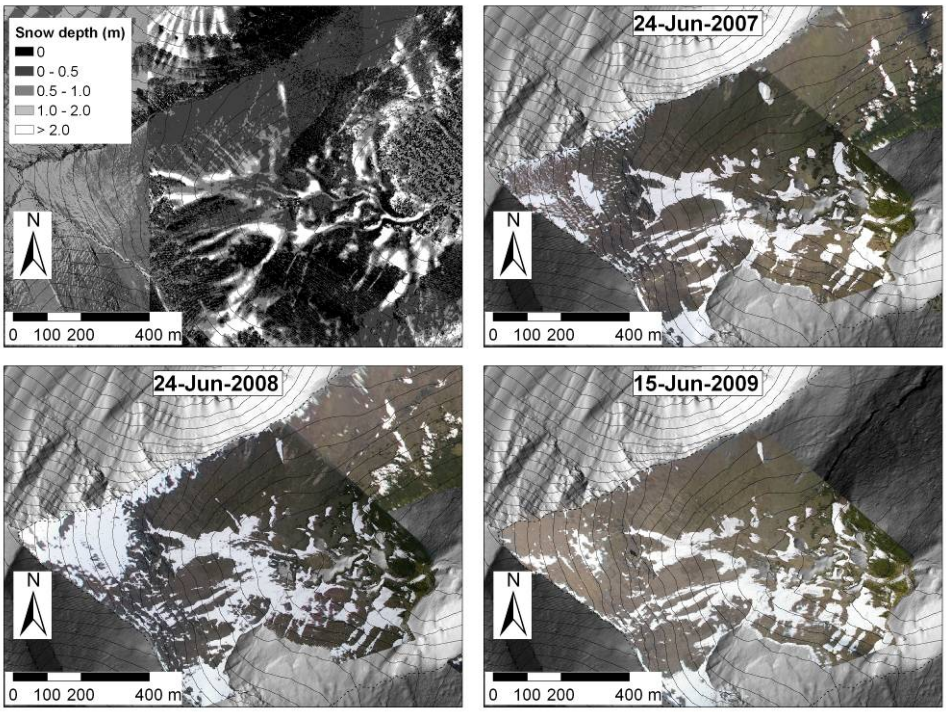

Figure 6.7. Spatial snowcover patterns in the Mt. Allan Cirque in the late spring for each observation year. Image at top left is the snow depth raster image produced from the LiDAR data obtained in late March 2008.

the other slopes. The south facing slope is characterized by large areas of windswept terrain, and this slope generally holds only relatively small drifts that form in local hollows and in the lee of exposed krummholz vegetation in the treeline area. In contrast, the other slope units tend to develop more extensive drifts and deep snowpacks in gulleys and depressions, and on wind-loaded slopes. Areal SCD tends to begin later and progress more slowly on these other slopes, especially the north facing slope. The slow melt-out of areas with relatively deep snowpacks leads to a more gradual decline of SCA through late June and into July on these slopes.

6.3.2 Influence of Spatial Variability of SWE and Snowmelt

To examine the relative influence of spatial variability of both SWE distribution and snowmelt on areal SCD in the alpine part of the basin, the theoretical framework developed in Section Three of this thesis was used together with the snowmelt model

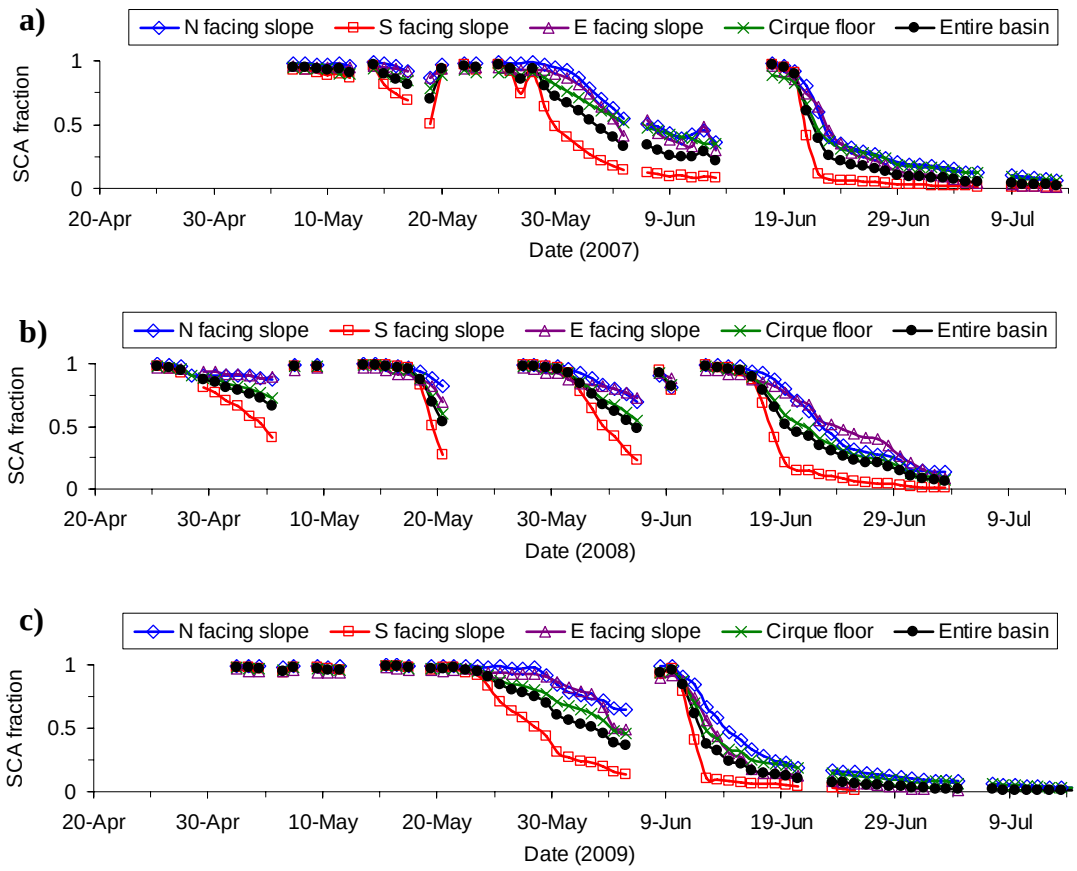

Figure 6.8. Snowcover depletion curves of individual slope units in the basin derived from the terrestrial photography for each of the respective study years. (The Fisera Ridge met station and camera failed on July 4, 2008; no photos were available for the remainder of that season).

described in Section Five. The framework was applied using approximations of the SWE distributions over the alpine part of the basin as well as for each of the individual terrain units at the time of maximum accumulation in each of the study years. These were approximated as being lognormal, and the parameters were defined in each case based on the observed spatial patterns and distributions from the 2008 LiDAR data, along with information from the snow surveys and point measurements at the stations on Fisera Ridge. Since the observed spatial snowcover patterns were broadly similar in each year, it was assumed that the CV values at peak accumulation are conserved from year to year. Then, the parameters of each distribution could be based on the value of $\overline{SWE}$ for the terrain unit, which in turn was estimated based on information from available measurements (snow surveys, point measurements at the stations) at that particular time.

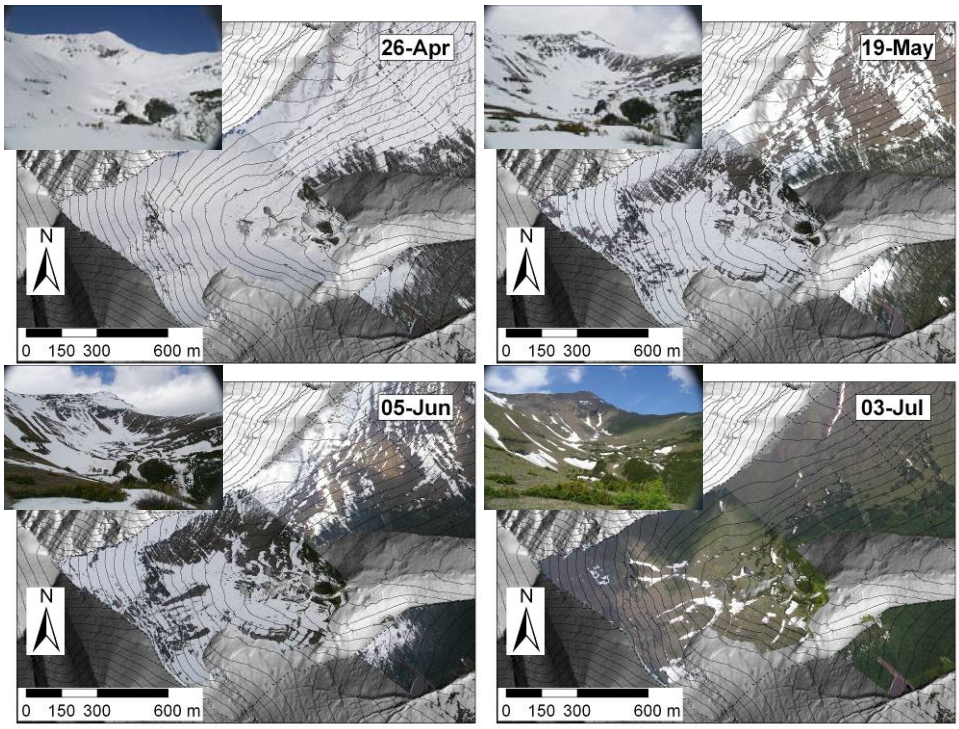

Figure 6.9. Spatial snowcover patterns over the basin at selected times during the spring and early summer of 2008. Corresponding original photos from the ridge-top site are also shown.

Snowmelt computations to be applied to the distributions were made using the model within the CRHM platform together with the snowpack and albedo decay parameter values listed in Section 5.3.2. Terrain parameters were defined for each slope-based unit using ESRI® ArcMap™ 9.3 GIS as described in Section 5.3.2, and are listed in Table 6.4. The same approach for snowmelt modelling on slopes away from the measurement sites on Fisera Ridge was adopted for use in the SCD simulations here. The model was run in a point-scale mode based on a number of different initial SWE conditions beginning March 1 of each respective year, and forced using the corrected observations for each terrain unit. Changes of SWE from simulations based on different initial conditions were then applied to the corresponding SWE values over each distribution according the methods described in Section 3.3.2. The effects of fresh snowfall during the melt period were handled using the rescaling technique for K – SWE plots described in Section 3.3.3, with a value of 50% of the new snow applied at the original K_{min}. Therefore, half of the new snowfall would have to melt before any depletion of the snowcover began after these events, and the curve subsequently followed

Table 6.4. Spatial average values of terrain parameters over each of the individual slope-based units in the alpine part of Upper Middle Creek Basin.

Parameter	N facing slope	S facing slope	E facing slope	Cirque floor
Terrain slope (°)	28	26.5	33	12.3
Aspect (° clockwise from north)	24	155	76	106
Elevation (m)	2427	2463	2575	2338
% permanent snow-free area	2	2	5	0
Sky view factor	0.72	0.74	0.72	0.66
Area (10^5 m^2)	2.33	4.05	2.41	0.73

a linear reversion to the original depletion curve with further melt. Finally, to exclude areas of steep terrain that are typically snow-free, a terrain classification similar to that of Blöschl et al. (1991) was performed to identify areas with a slope gradient >50°. Calculated SCA values were then multiplied by the fraction of the total area with a slope less than this critical value.

Figure 6.10 shows some of the results of this modelling for the 2008 snowmelt period following the peak accumulation in mid-May. In this case, the simulated "overall" curve was derived based on the SWE distribution representing the entire alpine area (Fig. 6.2, Table 6.2) with snowmelt computations based on the ridge-top site and applied uniformly over the landscape. This spatially uniform melt simulation captured the initial decline in SCA following maximum accumulation reasonably well, but later following a series of snowfall events the simulation produced rates of SCD that were too rapid and values of SCA were under predicted for most of the remainder of the simulation (Fig. 6.10a). Improvements in the predicted SCD curves resulted from applying slope-corrected melt rates to individual SWE distributions on the different slope units (Figs. 6.10b–d). Rates and timing of simulated areal SCD, and magnitude of SCA were generally closer to the observed values for individual slopes, and the model performance based on *NS* and *RMSE* was improved in most cases. Despite these improvements, however, some errors still remained on individual slopes in terms of the timing, rate, and magnitude of SCD. For example, the simulated depletion on the south facing slope

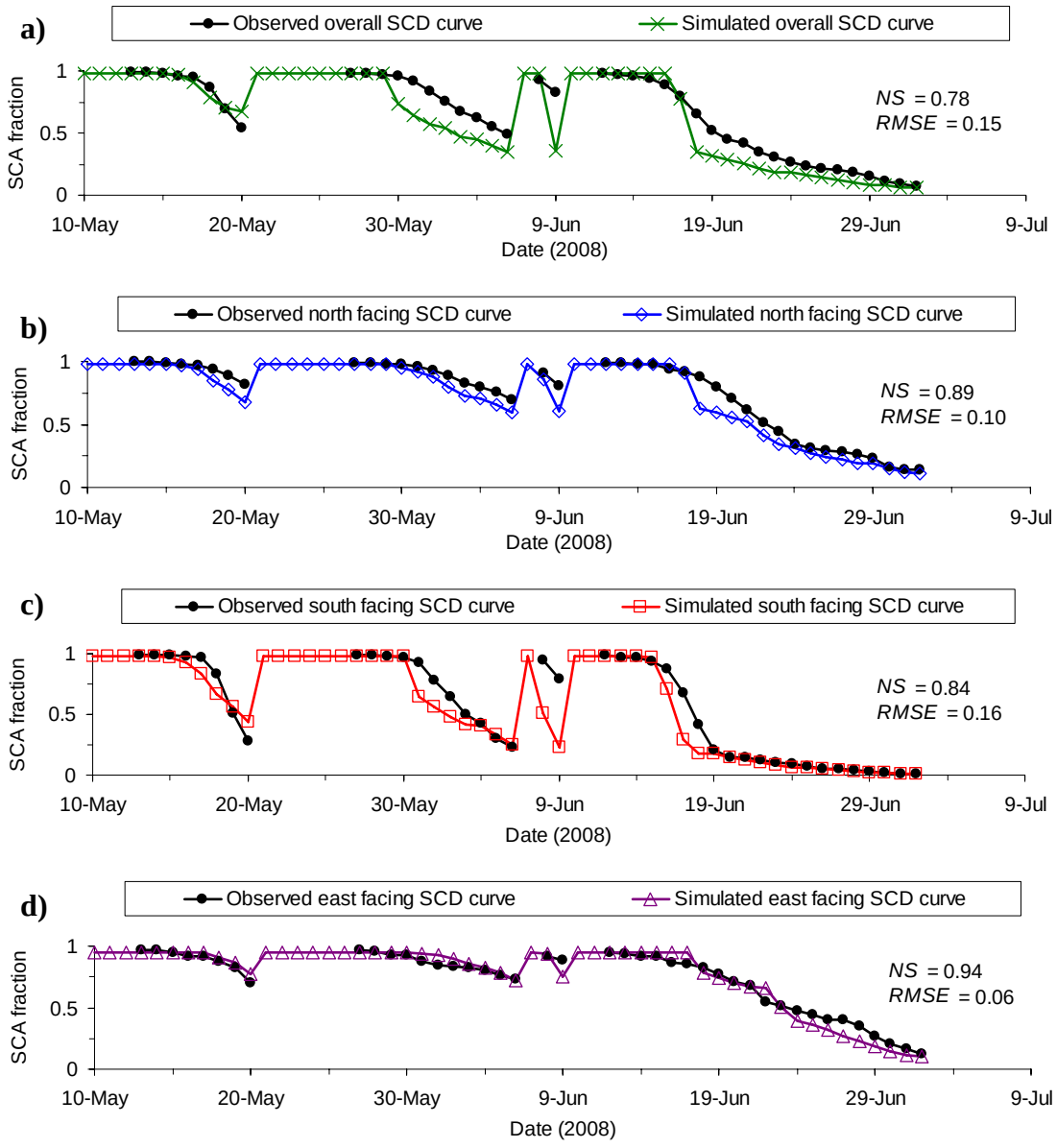

Figure 6.10. Simulated and observed snowcover depletion curves in 2008 following maximum accumulation for the overall alpine area in Upper Middle Creek Basin (a), and the individual north, south, and east facing slope units (b – d respectively).

generally occurred too early and SCA was initially too low following snowfall events, while values of SCA on the north facing slope were too low throughout the latter half of June.

Several different simulation approaches were used to examine the sensitivity of the results and the influence of spatial variability in SWE distributions and snowmelt at

Table 6.5. Summary descriptions of each simulation approach for predicting SCD curves on each slope and for the overall alpine basin.

Simulation Approach	Description
Variable SWE dist. – Variable Melt	SWE distributions defined for each slope unit, with slope-corrected melt rates applied to distribution on each slope unit
Fixed SWE dist. – Variable Melt	Single overall SWE distribution for the landscape, with slope-corrected melt rates applied to each slope unit
Variable SWE dist. – Uniform Energy	SWE distributions defined for each slope unit, with spatially uniform energy (based on ridge-top) applied to each slope
Fixed SWE dist. – Uniform Energy	Single overall SWE distribution for the landscape, with spatially uniform energy (based on ridge-top) applied to distribution

the slope unit and basin scales (Table 6.5). The first of these involved applying slope-corrected snowmelt computations to individual SWE distributions on the slopes (Variable SWE dist. – Variable Melt). Another approach used slope-corrected snowmelt applied to the overall alpine area SWE distribution (Fixed SWE dist. – Variable Melt), while a third used melt rate computations from the ridge-top applied to individual SWE distributions on each slope (Variable SWE dist. – Uniform Energy). Finally, the last approach involved using both a spatially uniform SWE distribution and uniform energetics, with ridge-top energy applied to the overall SWE distribution (Fixed SWE dist. – Uniform Energy). The latter two approaches were termed uniform applied energy rather than uniform melt to distinguish that the simulations still allowed for inhomogenous melt over the individual SWE distributions due to internal energy effects (this is explored further in the next section). Except for the Fixed SWE dist. – Uniform Energy approach, individual SCD curves that were generated for each slope unit were aggregated to represent the overall depletion of SCA in the alpine area by taking their area-weighted average.

Some of the results for individual slope units in 2008 are shown in Figure 6.11, and the aggregated curves for the overall alpine part of the basin for each year are shown in Figure 6.12. The degree of correspondence between the various simulation results and the observed SCA values is quantified in terms of the *NS* and *RMSE* values, which are given for the individual slope units in Table 6.6 and for the aggregated simulations in Table 6.7. These show that for the individual slope units, the best model results were obtained by either the Variable SWE dist. – Variable Melt or the Fixed SWE dist. –

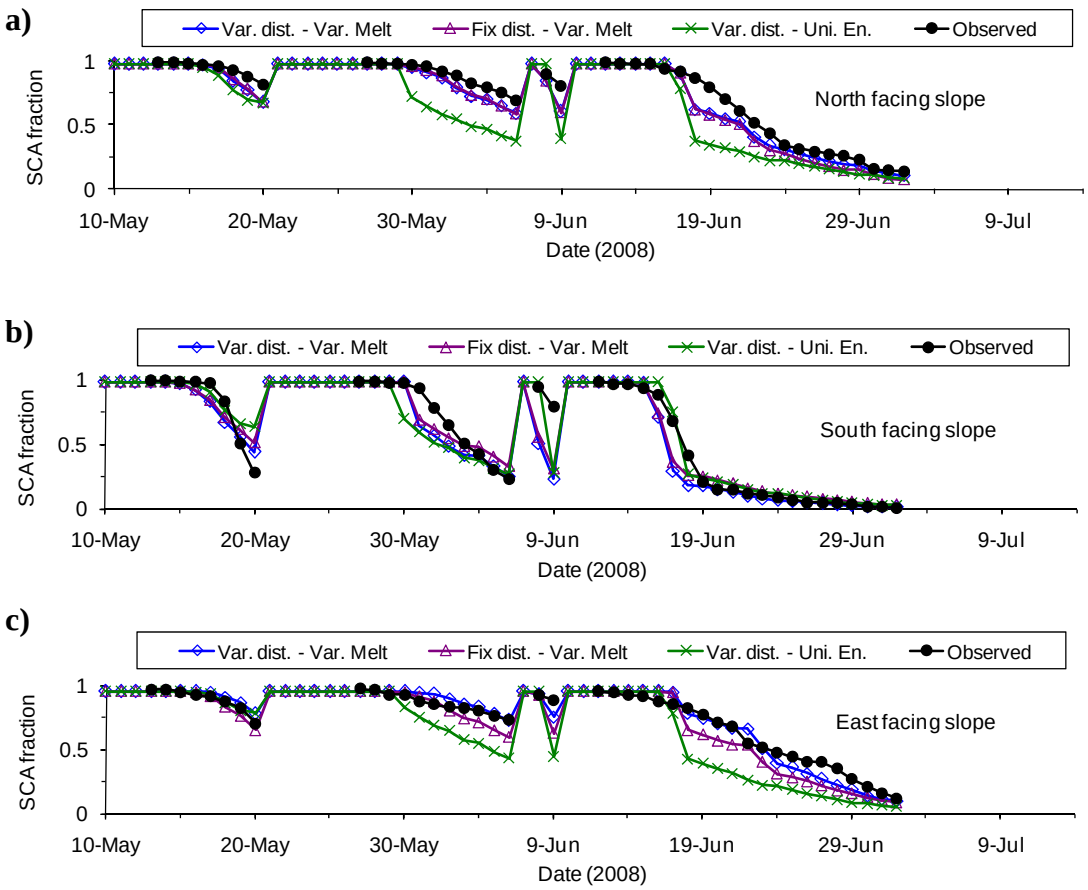

Figure 6.11. Simulated and observed SCD curves over the north facing (a), south facing (b), and east facing (c) slope units in 2008. The different simulation approaches, explained in the text and in Table 6.5, are: Variable SWE dist. – Variable Melt (Var. dist. – Var. Melt), Fixed SWE dist. – Variable Melt (Fix dist. – Var. Melt), and Variable SWE dist. – Uniform Energy (Var. dist. – Uni. En.).

Variable Melt approaches, while the Variable SWE dist. – Uniform Energy approach produced poorer results. Despite the consideration of differences in SWE distributions between slope units, the Variable SWE dist. – Uniform Energy simulations had the lowest values of *NS* and the highest *RMSE* values in almost all cases (Table 6.6). It is clear that including representation of snowmelt variability between the slope units is more important than separate SWE distributions towards improving the simulations on each slope. The fact that the fully distributed approach did not consistently yield the optimum results may be explained by uncertainty in the peak SWE distributions on each slope, over-parameterization of the model, or by other uncertainties or errors such as

Table 6.6. *NS* and *RMSE* values between simulated and observed SCA values on individual slope units (NF – north facing, SF – south facing, EF – east facing, CF – cirque floor) for the various simulation approaches of Fig. 6.11 in each of the three modelling years.

	Approach	*NS*				*RMSE*			
		NF	SF	EF	CF	NF	SF	EF	CF
2007	Var. dist. – Var. Melt	0.97	0.88	0.93	0.97	0.06	0.13	0.09	0.06
	Fix dist. – Var. Melt	0.97	0.90	0.97	0.98	0.06	0.13	0.06	0.06
	Var. dist. – Uni. En.	0.38	0.92	0.60	0.71	0.28	0.11	0.23	0.19
2008	Var. dist. – Var. Melt	0.89	0.84	0.94	0.94	0.10	0.16	0.06	0.07
	Fix dist. – Var. Melt	0.89	0.87	0.83	0.93	0.10	0.14	0.10	0.08
	Var. dist. – Uni. En.	0.40	0.87	0.34	0.70	0.22	0.14	0.20	0.16
2009	Var. dist. – Var. Melt	0.98	0.97	0.95	0.98	0.05	0.07	0.09	0.05
	Fix dist. – Var. Melt	0.97	0.95	0.88	0.85	0.07	0.09	0.15	0.14
	Var. dist. – Uni. En.	0.80	0.88	0.82	0.88	0.17	0.14	0.18	0.13

from the approach for handling the effects of fresh snowfall during melt, for example.

When the individual SCD curves are aggregated to represent the overall basin scale curve, the first two approaches (based on distributed snowmelt computations) yield the best results. However, neither produced consistently better results, which again may be due to uncertainties in the SWE distributions, rescaled depletion, etc. The results also show that nearly all of the improvement in the results is due to the representation of spatial variability of snowmelt, as the SCD curves and the model performance for the Variable SWE dist. – Uniform Energy and Fixed SWE dist. – Uniform Energy approaches are virtually the same (Fig. 6.12, Table 6.7). This feature may be partly attributable to the cancellation of some errors in the individual SCD curves in the aggregation process. This is also partly due to the fact that with the exception of the cirque floor area (which occupies a relatively small portion of the total basin area), none of the individual distributions on any of the slopes were significantly different from the overall distribution representing the entire alpine area. Thus, only minor differences in areal SCD were achieved when accounting for the different distributions under the same snowmelt conditions, and these were most likely averaged out in the aggregation process.

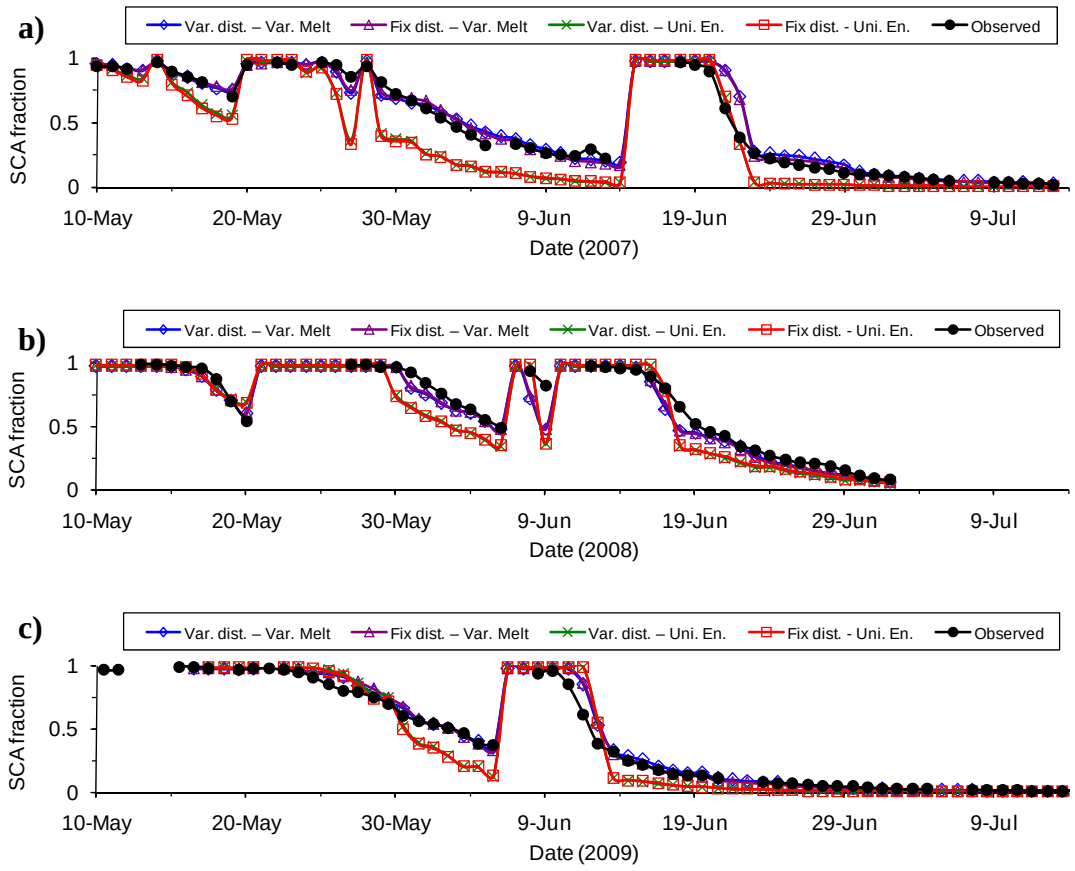

Figure 6.12. Simulated and observed SCD curves for the overall alpine area in the basin in each of the modelling years. Individual SCD curves from each of the different simulation approaches were aggregated to produce these curves.

Table 6.7. *NS* and *RMSE* values between daily simulated and observed SCA values for the overall alpine area using the various approaches of Fig. 6.11 in each of the modelling years.

Approach	*NS*			*RMSE*		
	2007	2008	2009	2007	2008	2009
Var. dist. – Var. Melt	0.96	0.92	0.98	0.07	0.09	0.05
Fix dist. – Var. Melt	0.97	0.93	0.98	0.07	0.08	0.06
Var. dist. – Uni. En.	0.77	0.78	0.91	0.17	0.15	0.11
Fix dist. – Uni. En.	0.76	0.78	0.91	0.18	0.15	0.11

6.3.3 Influence of Inhomogeneous Melt

As shown in Section 5.4.2 and discussed in other parts of this thesis, differences in SWE and internal energy content over a SWE distribution can have a considerable effect on the

timing and rate of snowmelt under the same applied energy. To examine how this may influence the depletion of SCA over individual slope units and at the basin scale, simulations were carried out using computations for a single initial value of SWE applied uniformly over the distribution (i.e., homogeneous melt). The magnitude of the variability in computed melt rates tends to be greatest in the early snowmelt period when the snowcover is warming and ripening, and it is therefore at this time when the effects on areal SCD are expected to be most significant.

A number of early melt and SCD events were observed in April and early May during the three year study period, but during most of these events blowing snow and wind scouring of the snowcover was occurring, which made it difficult to isolate the influence and effects of inhomogeneous melt. However, early in the 2008 snowmelt period, a depletion event was observed where the effects of blowing snow were minimal and which provided a useful test case to apply the framework for areal SCD. This event occurred prior to the time of maximum accumulation, so the parameters for the SWE distribution had to be adjusted to represent the snowcover at this time. Values of $\overline{SWE}$ were estimated based on survey and station measurements around this time, while CV values were assumed to be the same as those for peak accumulation. Snowmelt computations were made for SWE values at 50 mm intervals (bins) over the shallow part of the distributions for inhomogeneous snowmelt simulations, while homogeneous, or uniform simulations were based on a single value of SWE. Several different initial values of SWE were used for snowmelt computations, and changes in SWE from each were applied uniformly over the distributions for the homogeneous simulations. These included initial values of 150, 300, and 850 mm to represent shallow, average, and deep snowpacks respectively. The different homogenous melt simulations were done to compare the effects of basing melt computations on a range of different initial SWE depths, and examine what influence this has on the timing and magnitude of areal SCD.

The results of these simulations on some slopes are shown in Figure 6.13, and Table 6.8 provides *NS* and *RMSE* values to evaluate the success of the various approaches in predicting SCA over time. Depending on the approach and specific value of SWE used for melt computations, large differences in the timing and magnitude of areal SCD are apparent over some slopes. The best results were obtained by using the

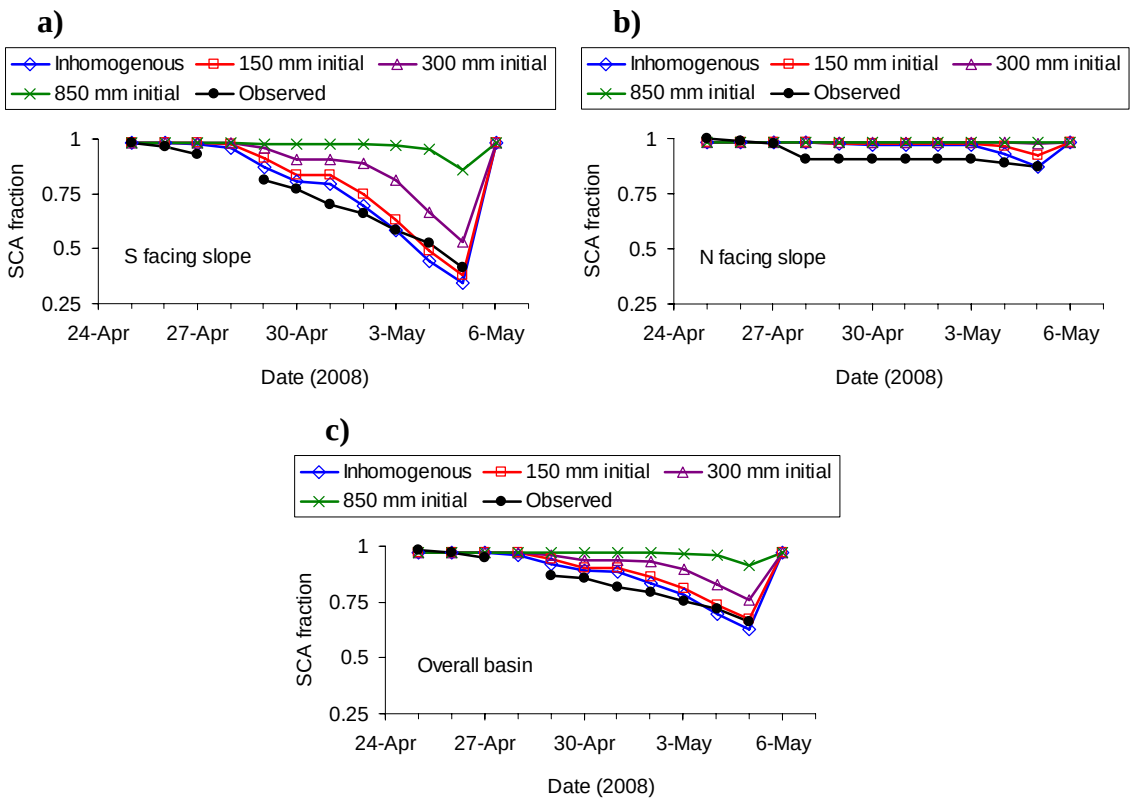

Figure 6.13. Simulated and observed SCD curves during an early snowmelt event in 2008 over the south facing (a), north facing (b), and overall alpine part of the basin. Homogeneous melt simulations were based on approximate values of SWE of 150, 300, and 850 mm on April 25.

approach that accounts for the variability in melt rates across the SWE distribution, particularly over the south facing slope. This initial phase of areal SCD on the south facing slope was due mainly to the melt and disappearance of shallow snow over a large portion of the slope, while adjacent deeper snow was still warming to 0 °C. Thus the simulations based on a single computation of snowmelt for deeper snow poorly represented the decline of SCA during this period. Over the north facing slope at this time, SCD was limited and due mainly to blowing snow and wind scouring of the snowcover on April 27 (which is not accounted for in the approach). Melt of the shallow snow did not begin until May 3, at which time the model based on inhomogeneous melt, and to a lesser extent that based on uniform melt and an initial value 150 mm SWE, predicted a small decline in SCA. The results for individual slope units were aggregated to produce the overall SCD curves for the basin. In this case, as for the individual slopes

Table 6.8. *NS* and *RMSE* values between daily simulated and observed SCA values over each slope for different simulation approaches in 2008. Values are given for both the early melt and SCD event (25-Apr – 5-May), and the remainder of the snowmelt period following peak accumulation. Uniform simulations were based on approximate initial average SWE values (~150 mm for early event, ~250 mm for maximum accumulation), and initially deep SWE (~850 mm in both cases).

	Slope unit	Early SCD event			Post-maximum accumulation SCD		
		Inhomo-geneous	Average (uniform)	Deep (uniform)	Inhomo-geneous	Average (uniform)	Deep (uniform)
NS	North facing	0.30	–0.02	–0.41	0.89	0.77	0.76
	South facing	0.91	0.86	–1.30	0.84	0.88	0.86
	East facing	0.50	–0.38	–0.65	0.94	0.93	0.88
	Cirque floor	0.84	0.70	–1.31	0.94	0.91	0.88
	Entire basin	0.88	0.77	–1.31	0.92	0.91	0.89
RMSE	North facing	0.05	0.06	0.07	0.10	0.14	0.14
	South facing	0.05	0.07	0.28	0.16	0.14	0.15
	East facing	0.02	0.03	0.04	0.06	0.06	0.09
	Cirque floor	0.04	0.05	0.13	0.07	0.09	0.10
	Entire basin	0.04	0.05	0.16	0.07	0.10	0.11

during this early melt event, an improvement in the results was achieved using the inhomogeneous melt approach from that based on deeper SWE and uniform melt over the distribution, which can be seen by the considerable increase in *NS* values and decrease in *RMSE* values. Therefore representation of melt rate variability with SWE is important for properly representing the SCD on individual slopes and at the basin scale at this time.

Simulations were carried out similarly for the remainder of the snowmelt period to examine how the effects change or persist over time. The distribution parameters for maximum accumulation (Table 6.2) were used within the modelling framework following the snowfall events between May 6 and May 11. An important issue that arises in the case of uniform melt simulations based on a single initial value of SWE is the fact that the snowpack for point-scale simulations will melt out and disappear at some time prior to the end of the snowmelt and SCD period. Thus, computations must be based on very deep SWE to avoid this problem. Alternatively, melt rates can be based on shallower snow, but this still requires carrying out several simulations for different initial

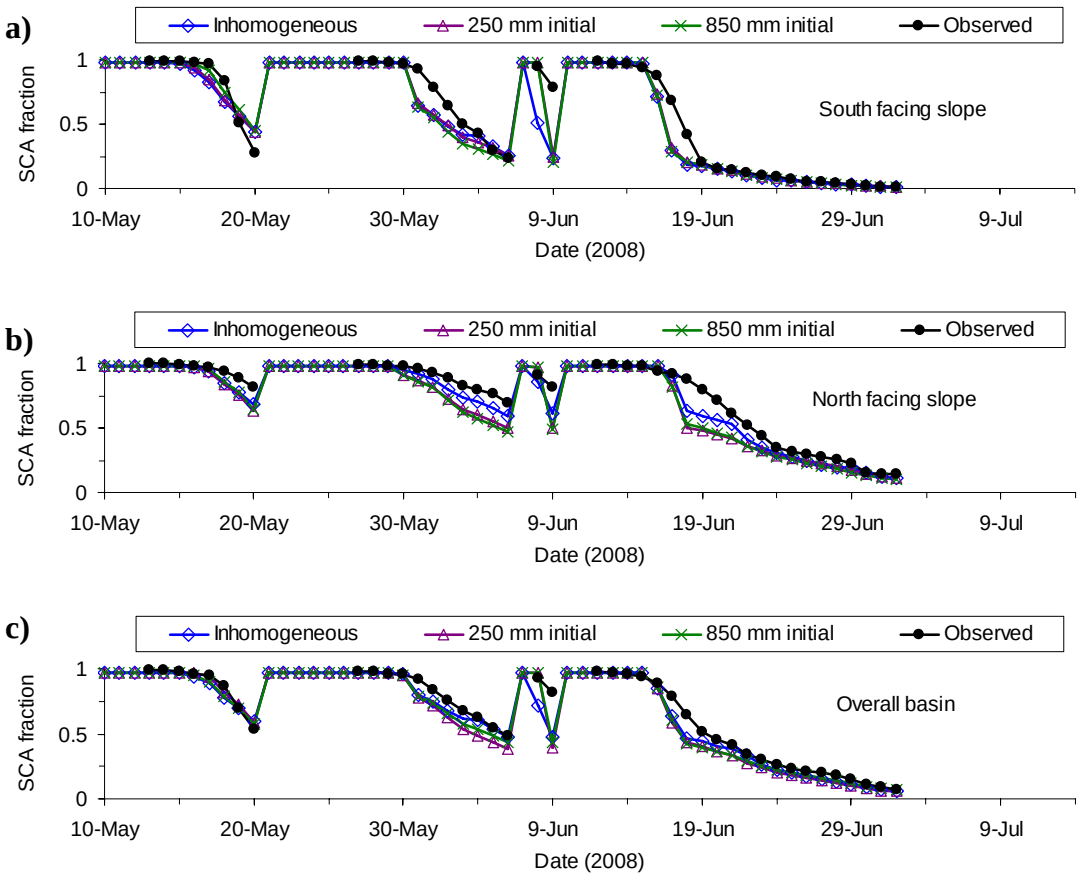

Figure 6.14. Simulated and observed SCD curves following maximum accumulation in 2008 over the south facing (a), north facing (b), and overall alpine part of the basin. Homogeneous melt simulations were based on approximate values of SWE of 250 and 850 mm on ~May 12.

values of SWE or re-initializing a model at some time during the melt period. For the uniform melt simulations carried out here, SWE values of ~850 mm (representing deep snow) and ~250 mm (representing average snow) at maximum accumulation were used to base melt computations. In the latter case, once the snowpack was depleted, melt rates to be applied to the distribution for the remainder of the simulation were based on the computations for the deeper SWE.

Figure 6.14 shows the results for these simulations and Table 6.8 provides the *NS* and *RMSE* values. For most slopes and for the basin as a whole, the results indicate a slight improvement using the inhomogeneous snowmelt framework, but the improvements are only minor and not significant in comparison to those achieved using this framework for the early melt and SCD event. This is due to the fact that the

variability in computed snowmelt rates and timing over the SWE distribution is considerably less at most times later in the melt period. Interestingly, on some slopes at certain times the approach using uniform melt resulted in a more rapid depletion of SCA because greater melt rates were predicted for the deeper snow. At other times following cooler periods and new snowfall, the inhomogeneous melt approach resulted in accelerated SCD due to the earlier and more rapid melt of shallower snow.

6.4 Meltwater Generation

So far it has been shown how the variability of both SWE and snowmelt over the landscape has a significant influence on the timing and rate of areal SCD on different slope units. This variability will also control the timing, rate, location, and overall magnitude of meltwater generation and snowmelt runoff across the landscape during the spring. Here the framework for areal SCD and snowmelt runoff is used towards examining the influence and effects of such variability on meltwater inputs over the landscape. To demonstrate this influence, simulations and analyses focused on the spatial extent and location of various *meltwater generating areas* (MGAs) over the landscape with time, and the timing and volume of meltwater generation within different parts of the basin. The simulated meltwater inputs over the basin can be used within the context of a hydrological model for simulation of the snowmelt hydrograph, which is the focus of Section 7 of this thesis.

6.4.1 Meltwater Generating Areas

The MGA represents the source area for meltwater generation and input to the landscape surface, and is limited to areas within a basin that are: a) snowcovered, and b) undergoing active meltwater generation (i.e., ripe snow with meltwater outflow from the base of the pack). The extent of this source area can be expressed as a fractional area within a landscape unit or over a basin in the same manner as the SCA. Expressed in this way, the MGA is equivalent to the fraction of the initial SWE distribution that is characterized by non-zero SWE and active meltwater generation at a given time during the snowmelt

period. From the previous analysis and discussion on inhomogeneous melt, it is clear that not all areas of the snowcover will produce meltwater at the same time and rate, even within a single landscape or slope unit. Thus, there is not necessarily a simple distinction between meltwater generating and non-meltwater generating areas of the snowcover, but rather, there may be a variety of different rates of meltwater generation with different and continuously changing areal extents over the landscape.

To examine the variability in timing, rates, and location of meltwater generation over the Upper Middle Creek Basin, various MGA's were defined based on analysis of the meltwater production from the point-scale snowmelt simulations for different SWE depths over the distribution on each slope unit. Melt computations were based on initial SWE values of 0, 50, 100, 150, 200, 250, 300, 400, 500, 600, 800, 1000, and 1500 mm, which were used to define the SWE classes over the distribution on each slope. This provided a higher resolution (50 mm) for the shallow to average parts of the SWE distributions where melt timing and rate vary most strongly, and coarser resolutions (100, 200, and 500 mm) for above average to very deep SWE over the landscape, as the variation in snowmelt rates is progressively reduced in this range of the distribution. The fraction of the initial distribution (or landscape area) occupied by the various SWE classes was then determined by the difference in exceedence probability of the upper and lower K values for that class. Rates of snowmelt were grouped into four different classes to distinguish areas of the snowcover producing different daily meltwater amounts, ranging from minimal or no melt, to high rates of meltwater generation (i.e., 0 – 5, 5 – 10, 10 – 20, and >20 mm/day). The use of four classes was adopted primarily for ease of visualization of the extent of these different zones. To define the extent of the various areas generating meltwater at different rates for the alpine part of the basin as a whole, the area-weighted average (based on slope unit area) for each slope and meltwater class was taken. In all cases, the combined areal extent of each class of meltwater production was equal to the SCA, and the extent of individual classes ranged from zero to the SCA fraction.

Figures 6.15 and 6.16 respectively show the relative area fraction and the spatial extent of the different generating areas over time during the early snowmelt and SCD period in 2008. Spatial patterns were mapped based on the LiDAR-derived snow depth

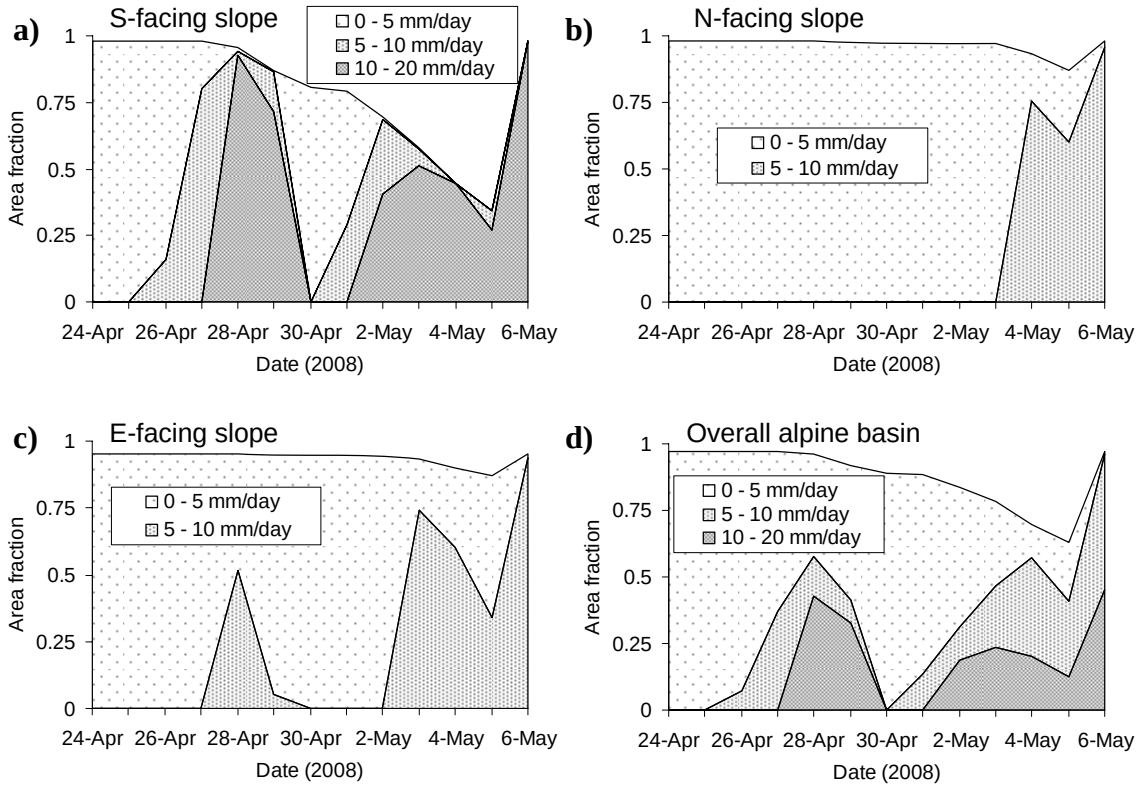

Figure 6.15. Temporal evolution and relative areal extent of MGAs producing different rates of snowmelt inputs on different slopes in the early melt period of 2008. a) south facing slope, b) north facing slope, c) east facing slope, d) overall alpine basin.

raster model by accounting for the melt and depletion of different SWE depths over time on each of the slope units. The temporal evolution of these areas differed considerably between slopes at this time as a result of the differences in the timing and rate of snowmelt on the individual slopes and over the different SWE distributions. For example, simulated meltwater generation began to occur in appreciable quantities (i.e., >5 mm/day) on the south facing slope one week before that on the north facing slope. Due to the differences in warming and ripening over the variable snowcover on each slope, areas of meltwater generation were initially limited in extent to a small fraction of the south facing slope and cirque floor. These areas then expanded as an increasing fraction of the SWE distribution on these slopes began actively melting, but at the same time, the depletion of SCA on these slope units partially counteracted this expanding area of active meltwater generation. Once areas with a shallow snowcover on the north and east facing slopes began to produce melt, areal SCD that had occurred on the other slopes

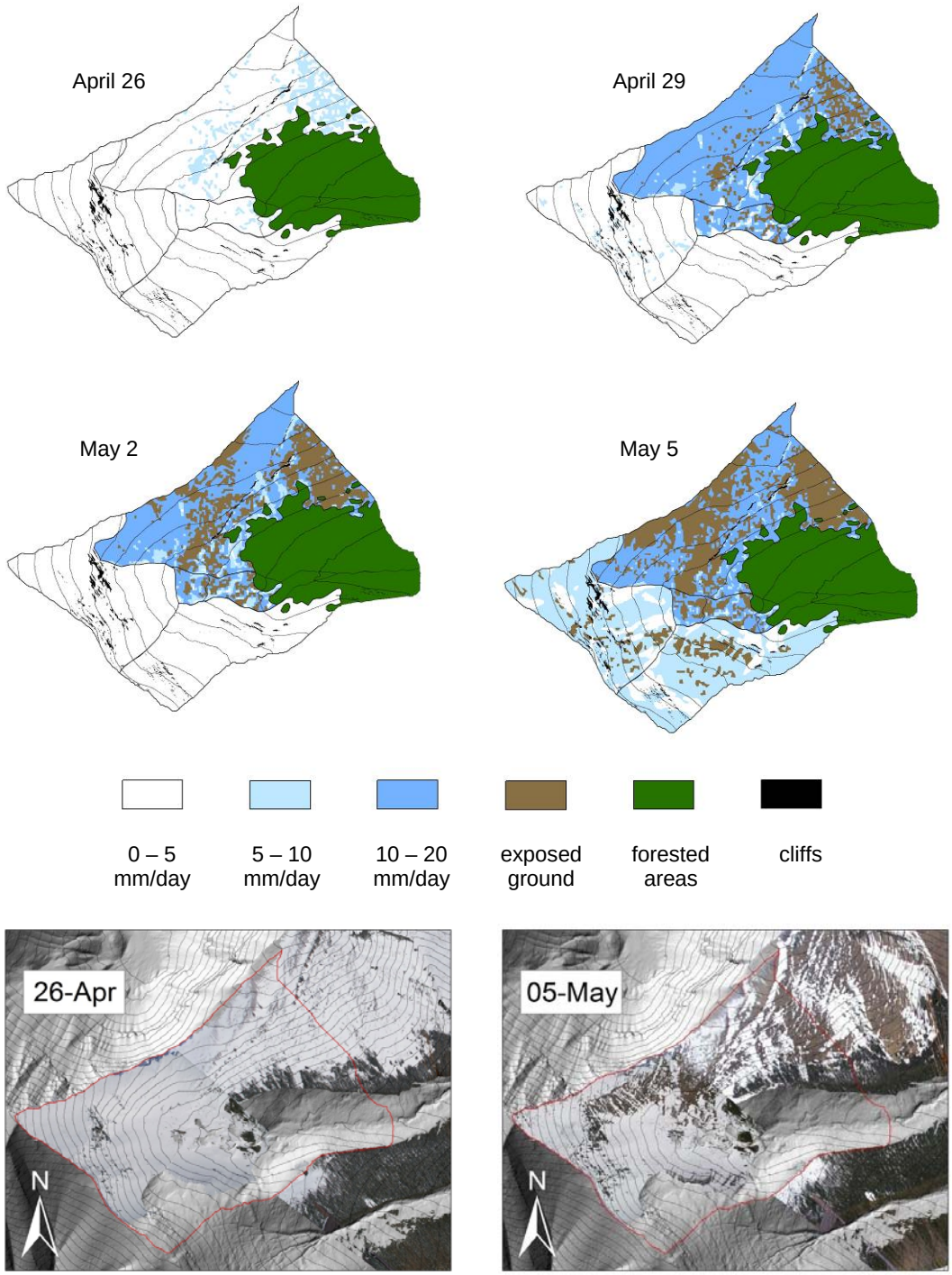

Figure 6.16. Simulated and observed spatial snowcover and simulated MGA patterns over the different slopes units within the Upper Middle Creek Basin during the early melt period in 2008. Patterns were mapped based on the spatial distribution of snow depth and SWE derived from the repeat LiDAR data. Snow melt patterns were not simulated in the densely forested or cliff areas.

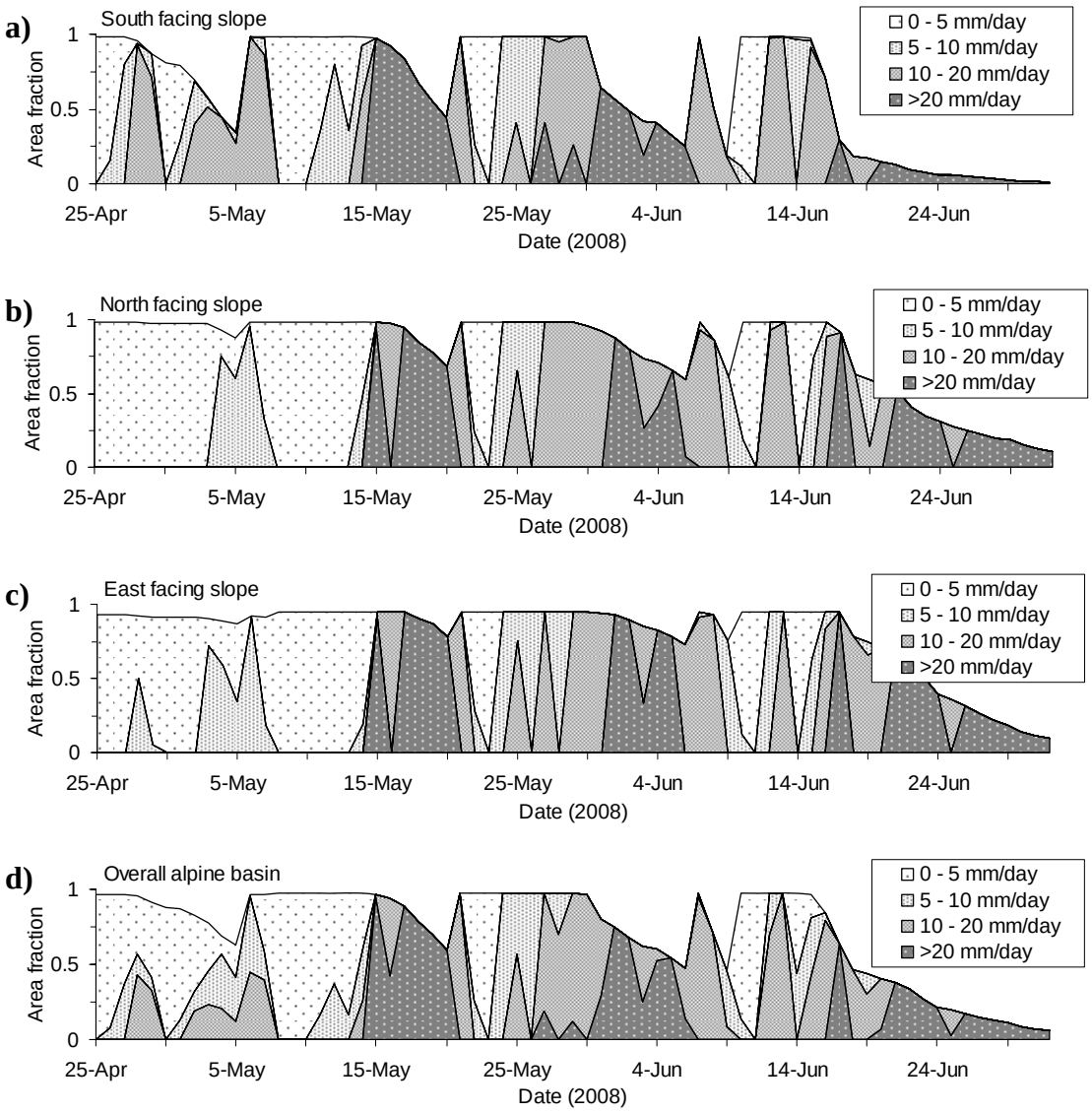

Figure 6.17. Temporal evolution and relative areal extent of MGAs producing different rates of snowmelt inputs on different slopes over most of the melt period in 2008. a) south facing slope, b) north facing slope, c) east facing slope, d) overall alpine basin.

limited the source areas for meltwater generation there. Thus, the overall extent of areas with active meltwater generation on the north and east facing slopes was greater than that over the other slopes, although the magnitude of melt rates was less for these generating areas.

Figure 6.17 shows the results of these simulations carried out on different slopes for the remainder of the snowmelt period in 2008. Differences in snowmelt rate and

timing are apparent between the different slopes over time, and within individual slopes as a result of inhomogeneous melt. In general, melt rates on a given slope and time following the time of maximum accumulation were relatively uniform, but there were a number of instances following periods of cooler weather and snowfall, or overnight refreezing, when the differences in melt amongst different SWE classes over the remaining distribution again became important. At the scale of the overall basin, encompassing multiple slope units and SWE depths over these units, the combined variability in snowmelt had a considerable influence on the temporal development of the different MGAs. Together these results show how the differences in melt and depletion of SCA between slope units and over SWE distributions within these units controls the overall timing, extent, and location of the areas generating different rates of snowmelt input over the landscape.

6.4.2 Spatial – Temporal Variability of Meltwater Generation

Analysis was also done to examine the variability in the overall magnitude of meltwater generation across the alpine landscape in the Upper Middle Creek Basin. The volume of melt was determined by integrating the daily meltwater depths over the area of each of the SWE classes defined from the maximum accumulation SWE distribution on each slope. The depletion of SCA was not accounted for within individual SWE classes. Rather, point-scale snowmelt computations were applied over the areas of the different classes, and once the snow from a simulation representing a specific SWE class melted out, predicted meltwater input over the area of that particular class ceased. For comparison with this distributed approach, simulations based on uniform snowmelt over the landscape and single values of SWE (overall basin $\overline{\text{SWE}}$ at maximum accumulation) were carried out for each of the three study years. In this case, the simulations were based on uncorrected meteorological conditions from the ridge-top stations and applied uniformly to the overall alpine area of the basin. For both simulation approaches fresh snowfall during the melt period was assumed uniform over the landscape.

Figure 6.18 shows the simulated meltwater inputs from each of the individual slope units, together with inputs based on the spatially uniform SWE/melt representations

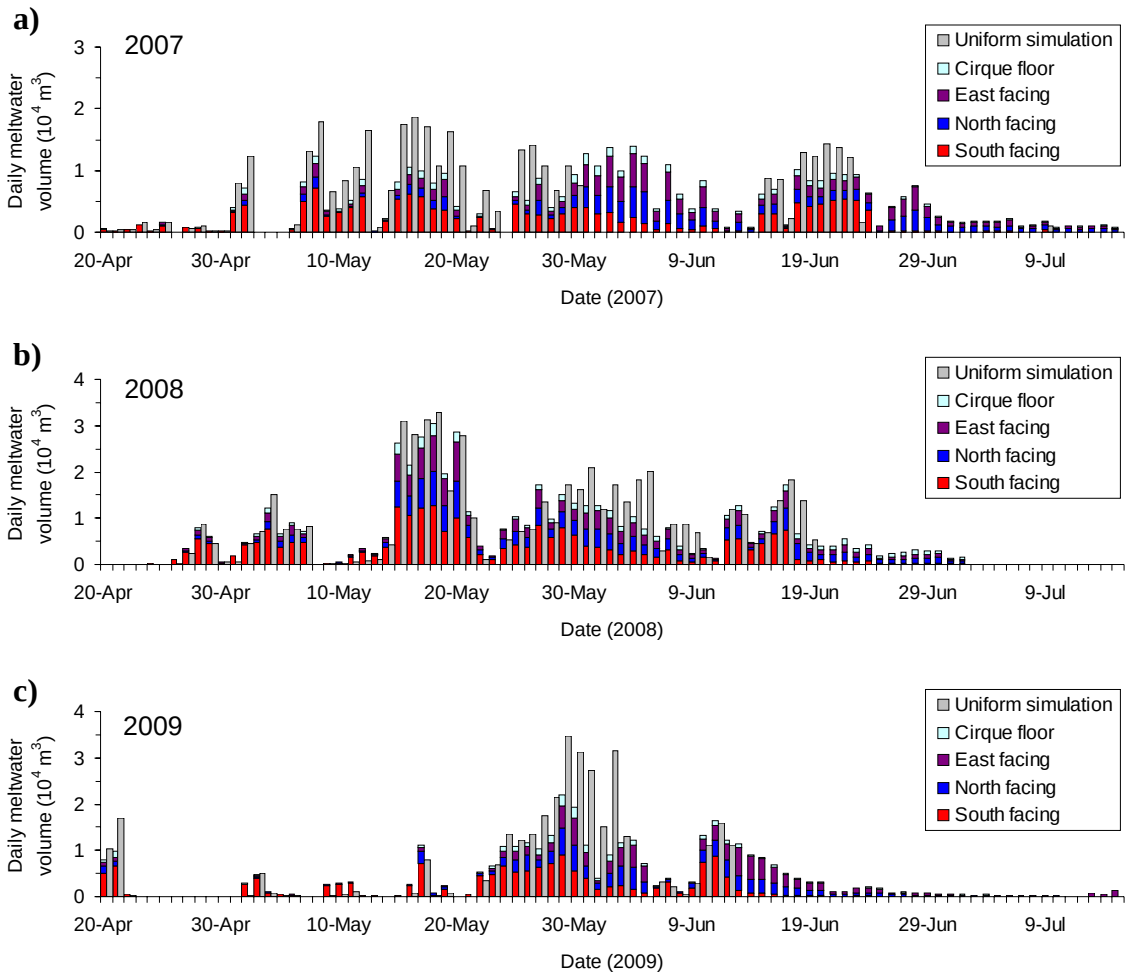

Figure 6.18. Temporal variability of simulated meltwater volume from the different slope units in the spring – early summer seasons of a) 2007, b) 2008, and c) 2009. Results from the uniform simulations are shown for comparison.

over the course of the spring and early summer in each of the study years. Table 6.9 provides the values of accumulated meltwater depth and volume on the individual slopes for different periods during the spring and early summer. This includes the earlier times in the melt period up to May 31 of each year, the later melt period following June 1, and the entire snowmelt season. Simulated meltwater generation differed considerably in terms of timing and magnitude between the three years represented, despite the broad similarity in spatial and temporal patterns of areal SCD noted in Section 6.3.1. The 2008 snowmelt season was characterized by greater meltwater generation than the other years because of the relatively warm conditions and heavy snowfall over the course of the

Table 6.9. Accumulated depth and volume of snowmelt inputs over the individual slope units and their combined total for different times during the melt period in each of the simulation years. Results are also shown for the uniform snowmelt simulations based on average SWE depth and melt over the landscape.

		Up to May 31		After June 1		Entire melt period	
	Slope unit	(mm)	(10^4 m^3)	(mm)	(10^4 m^3)	(mm)	(10^4 m^3)
2007	S Facing	236	9.6	143	5.8	379	15.4
	N Facing	101	2.4	302	7.0	403	9.4
	E Facing	119	2.9	301	7.2	419	10.1
	Cirque Fl	284	2.1	309	2.3	593	4.3
	Total	176.9	16.9	234.5	22.3	411.5	39.2
	Uniform	303.4	28.9	108.2	10.3	411.5	39.2
2008	S Facing	431.4	17.5	155.6	6.3	587.0	23.8
	N Facing	317.0	7.4	240.2	5.6	557.2	13.0
	E Facing	302.9	7.3	197.1	4.8	500.0	12.1
	Cirque Fl	347.8	2.5	342.7	2.5	690.5	5.0
	Total	364.5	34.7	201.2	19.2	565.7	53.9
	Uniform	353.0	33.6	212.6	20.3	565.7	53.9
2009	S Facing	247.7	10.0	104.8	4.2	352.5	14.3
	N Facing	148.7	3.5	214.0	5.0	362.7	8.5
	E Facing	106.7	2.6	253.1	6.1	359.9	8.7
	Cirque Fl	217.7	1.6	167.2	1.2	384.8	2.8
	Total	185.5	17.7	173.8	16.6	359.3	34.2
	Uniform	214.7	21.8	144.7	12.4	359.3	34.2

spring and early summer. In contrast, melt and runoff were more delayed in the spring of 2009, resulting in rapid melt towards the end of May and fast depletion of the thinner snowcover at that time. Other differences in meltwater generation patterns between the three years were due to the timing of the various melt and snowfall events during the course of each spring. One similarity between the years was that from late June and into July, meltwater generation declined towards zero following the last snowfall events of the season as isolated remaining snow patches melted out and disappeared.

There were also clear differences in the timing and magnitude of meltwater generation between the different slopes in each year. Meltwater inputs typically began in significant quantities earliest on the south facing slope. Meltwater was also generated relatively sooner on the cirque floor area, but the small area of this unit limited the total volume. From Table 6.9 it can be seen that according to the simulations, most of the

meltwater generation from these two slope units occurred in the earlier part of the melt season prior to May 31. Production of meltwater began in significant amounts relatively later over the north and east facing slopes, and continued later into the spring and summer as the contribution from the south facing slope diminished. Most of the meltwater simulated from the north and east facing slopes was produced in the later spring after June 1 (Table 6.9), and from late June on, these were the primary runoff contributing areas in the alpine part of the basin (Fig. 6.18). Over the entire snowmelt period in each year, the total volume of meltwater production was greatest from the south facing slope, least from the cirque floor area, and intermediate and roughly equivalent in magnitude from the north and east facing slopes. These differences were primarily controlled by the area of the different slope units, and to a lesser extent, differences in the SWE distributions and $\overline{\text{SWE}}$ at maximum accumulation.

The uniform SWE and snowmelt simulations produced notably different results from the combined total of the individual slopes in the distributed simulations. Although the total volume was the same by both approaches (because the $\overline{\text{SWE}}$ and meltwater volume over the basin area are conservative quantities), the timing and magnitude of melt over the course of the spring differed. For example, the uniform approach generally produced greater meltwater inputs earlier in the melt period and less at later times. Inputs to the basin up to May 31 each year were 74, 62, and 60 % of the seasonal total for 2007, 2008, and 2009 respectively, as compared to 26, 38, and 40 % of the seasonal total after June 1 for the same years (see Table 6.9). In contrast, the approach based on differential melt amongst the various slopes and SWE distributions over them yielded meltwater inputs of 43, 64, and 52 % of seasonal volumes up to May 31, and 57, 36, and 48 % of total seasonal meltwater after June 1 for the three respective years. So with the exception of 2008, the uniform approach predicted greater inputs in the early melt period than the distributed approach, with a difference of up to 31% of the seasonal total in 2007. For shorter periods (up to several days) at certain times during the snowmelt period, simulations using a single melt rate applied uniformly to a single value of SWE over the landscape produced more meltwater than the distributed approach. This was because the distributed simulations accounted for the declining SCA and contributing area over the individual slopes, while the contributing area for the uniform approach was constant and

equal to the total basin area. For this same reason, runoff ceased earlier due to the effect of the instant melt out and disappearance of the snowcover by the uniform approach. After the last snowfall events in each of the simulation years, no further meltwater generation was predicted by the uniform simulations from mid to late June and afterward (Fig. 6.18). These are obvious deviations from reality based on the known patterns of snowcover at these times.

6.5 Discussion of Implications for Model Upscaling

6.5.1 Spatial Variability of Melt Energy and SWE, and Landscape Stratification

The results have shown that there is a significant amount of variability in the pre-melt snowcover and SWE depth, as well as the energy available for snowmelt during the course of the spring. The variation in SWE over the landscape is mainly a result of blowing snow redistribution by wind as influenced by the surface topography and exposed alpine shrubs and vegetation, while the variability in melt energetics are due primarily to the differences in net radiation over the landscape, the patterns and magnitude of which are controlled predominantly by incoming shortwave radiation. Properly accounting for or resolving this combined variability is important for snowmelt modelling and SCD/snowmelt runoff simulations in open alpine terrain; in the Canadian Rocky Mountains, for example, these landscapes occupy roughly 50 – 60% of the total area, and contribute disproportionately more to the total generation of runoff. Therefore, this is of prime importance for model representation of the regional hydrology.

Disaggregation of the terrain into spatial units or a grid system is a useful means for handling some of the primary sources of variability, and the appropriate scale to which this should be done depends on the associated scale dependence of both snow accumulation and snowmelt processes. In this work, as well as in many other studies in such environments, it was shown that snow redistribution processes lead to a late winter snowcover that exhibits substantial variation over short distances (i.e., order of magnitude differences in SWE over horizontal scales of 10 m or less). To explicitly represent this in hydrological models would require the use of fully distributed simulations applied at

similarly small spatial scales. Alternatively, model spatial units can be larger, and snow variability within the unit can be parameterized for simulations of snowmelt and areal SCD, as in this study. Major variations in the applied energy due to variations in radiation receipt, as well as air temperature variation with elevation, occur at the scale of individual slope units (i.e., ~250 to ~800 m horizontal length scales in this instance). Therefore, to apply a sub-grid, or sub-model unit parameterization based on the assumption of uniform applied energy to the snowcover, this approximate scale should be considered an upper limit, beyond which explicit spatial representation is necessary. The appropriate landscape stratification is not only scale dependent (e.g., Cline et al., 1998), but also location dependent so as to conform to the underlying variations in the terrain that are responsible for the variation in snow processes and energy receipt (e.g., distinct, broadly homogeneous units based on slope and aspect, sky exposure, elevation, etc.). This provides a basis for the distinction and delineation of HRUs within such alpine landscapes. However, the scale and locations for consideration of snowcover and snowmelt processes may need to be smaller in very highly complex and rugged landscapes, where the terrain does not tend to approximate broadly homogeneous and planar units.

Based on analysis of a LiDAR-derived raster of snow depths (and conversion to SWE depths) over the Upper Middle Creek Basin, it was found that the spatial distribution of maximum accumulation SWE could be approximated reasonably well by the theoretical lognormal distribution. Further, by stratifying the landscape and considering SWE variation separately over different slope-based units, it was shown that the distributions on the individual units exhibit strong lognormal characteristics and that the CV of SWE values was reduced in general compared to the overall basin scale distribution. Steppuhn and Dyck (1974) suggested that reduction of the CV by landscape stratification is useful as this improves the confidence in the fitted distribution about the sample mean, reduces the number of snow courses needed while improving their representativeness over the landscape unit or class, and increases the likelihood that the snowcover distribution is similar over each areal unit. An even greater reduction in the CV of values of potential incident solar radiation over the landscape was achieved by this stratification. The fact that the same approach to reducing the variability about the mean

of the SWE distributions also resulted in significantly greater uniformity of shortwave radiation inputs provides strong support for disaggregation of the landscape by slope and aspect for snowmelt and SCD simulation above treeline in the alpine zone.

It was also observed here that spatial snowcover and SWE patterns tended to be rather consistent from year to year, as has been found in other alpine and windswept environments (McKay and Gray, 1981; Winstral and Marks, 2002; Deems et al., 2008), primarily due to the underlying influence of terrain features, vegetation, and prevailing wind directions. This inter-annual consistency leads to more reliable estimates of SWE distribution parameters, such as CV, which should remain stable from year to year over different parts of the landscape. Thus, differences in accumulation and variability of SWE may be effectively tracked based solely on $\overline{\text{SWE}}$ over different landscape units, while the standard deviation or CV can be estimated from previous survey data or from similar, "representative" landscapes (e.g., Pomeroy et al., 1998; Liston, 2004; Clark et al., 2011). Values of CV observed in this study (Section 6.2.1; Appendix A) corresponded well with those from other studies over windswept alpine terrain. The notion of transferring representative CV values has potentially high value for extending snowmelt and areal SCD modelling applications far beyond intensively studied research basins, and the approach developed in this work provides a useful tool for this as it only depends on $\overline{\text{SWE}}$ and CV. This is even further supported by the results here, which showed that areal SCD predictions are not highly sensitive to the precise value of CV (e.g., based on either slope-specific or alpine basin average CV for above treeline areas). However, it may be necessary to distinguish highly wind-loaded slopes, such as those in the Upper Twin Creek Basin, for example.

Taken together, the findings show that the approach developed in this thesis for handling the combined effects of snowcover and snowmelt variability provides a useful and robust means for areal SCD simulation. Improvements seen in the simulated SCD curves result from considering the separate SWE distributions and snowmelt rates on different slopes, compared to curves derived from a single (basin scale) SWE distribution and uniform applied melt. By using objective means to stratify the landscape, the major sources of deterministic variability in the radiative components of snowmelt energetics are explicitly accounted for, leading to better overall predictions of snowmelt timing and

rates. Dornes et al. (2008a, 2008b) also showed that this approach works well in a subarctic mountainous landscape. At smaller spatial scales (i.e., sub-landscape unit), the SCD and meltwater generation framework based on the lognormal distribution provides a useful stochastic means for handling the remaining variability in SWE. Thus, a simple modelling strategy that that employs recognition of the important sources of deterministic variability, and that considers both top-down understanding of system behaviour and bottom-up representation of physical processes, can be very successful (Sivapalan et al., 2003; Dornes et al., 2008a, 2008b; Savenije, 2009). This type of approach is necessary to be able to extend such simulations over broader parts of the Rocky Mountains, and other alpine regions, as fully distributed simulations carried out at the scale necessary to explicitly capture the essential process variability have great difficulty in producing the initial conditions (i.e., spatial SWE end-of-winter patterns). Here, all that are needed are reliable estimates of $\overline{SWE}$ and CV. At the same time, the approach here avoids the problems common to traditional HRU-based methods, which either do not account for the sub-HRU variability in SWE at all, or do not account for the variation in snowmelt due to the internal energetics of different SWE classes within an HRU. This is discussed further in the next section.

6.5.2 Effects of Inhomogeneous Melt on Areal Snowcover Depletion

In Section Five it was shown that it is not physically realistic to apply a single snowmelt computation over a highly redistributed and initially subfreezing snowpack due to the effects of differences in the internal energetics and snowpack state. This has important implications for areal snowmelt modelling applications based on a stochastic sub-grid representation of the small scale variability in SWE, which were explored in more detail here. Under conditions of uniform applied energy over a distribution of SWE, shallow snow tends to ripen earlier in spring and melt faster than the deeper snow; this is due to the greater cold content of the deep snow. The effect of this negative association between SWE and melt timing/rates on the pattern of simulated areal SCD is to cause an initial acceleration in the rate of snowcover decline in comparison to that derived from uniform applied melt based on computations for average or deep snowpacks. As the melt period

progresses and the effects of variable SWE and internal energy differences become reduced, melt rates over a given slope (and SWE distribution over the slope) become more uniform and consideration of melt differences amongst SWE classes becomes less important.

It is noted, however, that this variability can be important again at other times, such as following spring snowfall events (which are common in this environment and refresh the snowcover), or periods of cold weather. Even night-time cooling and refreezing due to longwave radiation losses (particularly on clear nights) can have a considerable effect on internal snowpack energetics and become manifested as differences in melt timing and rate amongst different SWE depth classes the following day.

Previously, the effects of internal snowpack energetics on areal SCD have only been represented with the use of fully spatially distributed models at very fine scales. Other HRU approaches have only resolved differences in snowpack state at the scale of the HRU. The work in this thesis has provided an approach to effectively bridge the gap between these two methods, capturing the important aspects of inhomogeneous melt over a SWE distribution and retaining physical integrity, while at the same time retaining spatial simplicity and requiring only inputs of $\overline{\mathrm{SWE}}$ and CV (as well as other parameters that would be common to any physically based snowmelt model). The scale at which this is applied (i.e., slope unit) allows the separation of differences in snowmelt rate and timing due to both applied energy at the snowcover surface and differential warming and ripening of the snowpack, which could not otherwise be resolved without resorting to a fully distributed approach. Therefore, this provides a novel means of carrying out areal SCD simulations over larger regions, and outside of intensively studied research basins. Given the importance of realistic predictions of the SCA in many applications requiring sound estimates of surface energy fluxes (e.g., SCA may be as important or more than melt rates), the benefit and utility of this new approach are potentially high.

Realistic simulation of the extent of meltwater generating areas over the landscape also requires proper representation of the SCA, which limits their maximum extent. Net meltwater production also depends on the fraction of the remaining SWE distribution that is actively melting and generating meltwater. The flow of meltwater

through, and release from the snowpack also depends on the depth, density, and cold content of the snow (Colbeck, 1972; Colbeck and Davidson, 1973; Marsh and Woo, 1984). Consideration of differences in melt timing and rates over a non-isothermal SWE distribution is therefore also important in this regard. As described previously, earlier and initially faster melt of the shallow snow depletes the snowcover and exposes the ground more rapidly in these sites. Thus, the effect of the earlier melt of shallow areas of snow, which initially expands the area producing melt, is somewhat counteracted by the fact that these areas become more rapidly snow-free, and the MGA is then limited by the SCA. At the basin scale, which generally encompasses multiple slope units of different aspect, gradient, and elevation, the pattern is even more complex. Snowmelt and areal SCD begin first over areas with shallow snow on south facing slopes or level lower elevation sites, and then proceed to deeper snow within these areas and shallow snow on other slopes. By the time that most of the snowcover on the remaining slopes begins to melt, much of the snowcover on the south facing slopes may have disappeared. Subsequent spring snowfalls add even more complexity to these patterns as the snowcover is re-established over the landscape and the MGA must again evolve. The importance of this variability for simulation of the basin hydrograph is examined in the following section of this thesis.

7. Streamflow Modelling and Hydrograph Comparative Analysis

7.1 Introduction

The last two sections of this thesis have explored the combined variability of SWE and snowmelt energetics, along with the effects on snowmelt timing and rate, areal SCD, and meltwater generation at different spatial scales over the alpine landscape. The considerable spatial and temporal variability of melt rates and SWE has a significant influence on the timing, rate, magnitude, location, and duration of meltwater production, which can be well-represented by the previously described approach. The purpose of this section of the thesis is to take this further and demonstrate how this framework can be applied within a hydrological model to represent the snowmelt runoff hydrograph at the basin outlet. In this context, the purpose is not to develop an explicit and detailed model to represent every aspect of the system, but rather to use a simple process-based and conceptual model towards examining the effects of different snowcover and snowmelt representations on the basin hydrograph, and thereby fulfill the final thesis objective.

Here, a hydrological model that includes both physical and conceptual process descriptions is first presented and described. The model's spatial structure is based on the HRUs of the previous section and the concepts developed in Section 3.4 of this thesis, thereby retaining spatial simplicity but physical process integrity. Next, the calibration and validation of the model are discussed; this was performed using distributed snowmelt inputs and observed hydrographs at the gauge site on Upper Middle Creek from 2007 and 2009 (due to the failure of streamflow measurements in 2008, the model was not applied in that year). Following this, the model is used to examine the changes and sensitivity of the simulated hydrographs to different approaches of representing the variability of snowmelt and SWE over the basin. The section ends with a discussion of the results and implications for hydrological modelling in such environments.

7.2 Model Description

7.2.1 CRHM Modules and Analytical Structure

The general modelling framework here is an extension of the point-scale snowmelt model described in Section 5.2, with additional CRHM modules coupled to the melt routines to represent the movement of meltwater and rainfall through the basin to the stream outlet. The transfer of water from the base of the snowpack through the basin was simulated using modules to represent infiltration to frozen soils (or other porous media), evaporation and soil moisture balance, snow interception and radiation attenuation by the forest canopy (where present), groundwater recharge, and routing of the meltwater through the basin and stream channels. Modules dealing with meltwater infiltration, evaporation, and snow–canopy processes are physically based, whereas those for soil moisture balance and flow routing are conceptual and based on unit hydrograph concepts. These are described individually in more detail below.

The infiltration of meltwater into frozen and unfrozen soils during the spring was handled using the module *FrozenAyers* within the CRHM library. In some cases this may not necessarily correspond to well-developed and mature soils, but the algorithm can be applied to represent all porous media, including poorly developed alpine soils and regolith, till and talus, etc. The frozen soil algorithm in this module was proposed by Zhao and Gray (1999) and Gray et al. (2001), and is based on extensive research by the Division of Hydrology, University of Saskatchewan, which suggests the infiltration regime of frozen soils can be grouped into three broad categories: restricted, limited, and unlimited. Restricted conditions occur when an impermeable layer, such as a basal ice lens, impede infiltration and result in immediate surface runoff, while unlimited conditions are found for soils with high porosity and numerous macropores, such that all meltwater infiltrates and surface runoff is negligible. Under limited conditions, infiltration is governed by the SWE and the initial temperature and moisture content (water + ice) of the uppermost 0.4 m soil layer. Here the total snowmelt infiltration (*INF*; mm) is determined as:

$$INF = C \cdot S_0^{2.92}(1 - S_I)^{1.64}\left(\frac{273.15 - T_I}{273.15}\right)^{-0.45} t_0^{0.44}, \quad (7.1)$$

where C is a coefficient, S_0 is the surface saturation (mm^3/mm^3), S_I is the average soil saturation in the upper 0.4 m soil layer, T_I is the initial average temperature (K) of this layer, and t_0 is the infiltration opportunity time (h), which is governed by the duration of melt, and thus SWE. The rate that a frozen soil infiltrates meltwater ($d(INF)/dt$) can be determined under limited conditions by a change in infiltration by Equation (7.1) in an incremental increase in infiltration opportunity time. The routine is disabled once the remaining SWE is less than 5 mm.

Infiltration during thawed soil conditions following snowmelt was represented using the Ayers (1959) approach within the *FrozenAyers* module. This method does not require surface ponding conditions, as in other infiltration approaches such the Green–Ampt approach, and bases infiltration amount on the net infiltration capacity for the HRU as set for different soil profile conditions and ground cover. These are specified as parameters within the module.

Evapotranspiration was estimated using the *Evap* module, which is based on the algorithm of Granger and Gray (1989) and Granger and Pomeroy (1997). Their formulation is an extension of the Penman equation for unsaturated conditions under minimal advection, where the aridity of the atmosphere is used to index the ability of soil and vegetation to supply water for evaporation. The total evapotranspiration is segregated into losses of intercepted rain from the canopy, evaporation from the surface, and transpiration by vegetation (i.e., from deeper soil layer), with the transpiration losses limited by the soil moisture module described below.

To account for the variation in soil moisture, the module *Soil*, which conceptually represents the soil as a two-layer profile (Pomeroy et al., 2007), was incorporated within the model. Again, as for *FrozenAyers*, this module may be used to represent all porous media such as poorly developed alpine soils and debris. Inputs to this module are provided by *FrozenAyers* for both periods with snowcover and following melt under thawed soil conditions, and infiltration occurs only when there is available moisture capacity within the soil profile. The upper layer, or recharge layer is first satisfied by surface infiltration before water moves to the lower layer; evaporation only occurs from

the recharge layer, while water for transpiration is withdrawn from the entire profile. Surface runoff is generated by the module when the soil can no longer infiltrate water, while excess moisture from both soil layers goes first towards satisfying a specified daily groundwater recharge and flow, and then towards sustaining subsurface flow. The subsurface flows are represented by a linear reservoir approximation where outflow rate is proportional to storage. *Soil* requires the field capacity to be specified as a parameter representing the maximum soil moisture capacity for the two layers.

Because some of the lower portions of Upper Middle Creek Basin are forested, it was necessary to include a module to represent canopy processes such as radiation transfer through the foliage and interception/unloading of snow. The module *Canopy-Clearing*, which includes several algorithms described in detail by Ellis et al. (2010), was therefore incorporated within the model for forested HRUs. The module was also incorporated within the model structure for other HRUs as well, but a parameter was set to neglect any canopy effects for non-forested slopes. In this module, net all wave radiation at the snow surface under a needleleaf forest canopy is determined from above canopy observations of incoming shortwave and longwave radiation. Shortwave radiation transmitted through the canopy is based on the formulation of Pomeroy and Dion (1996) for forest transmittance, τ, as follows:

$$\tau = \exp\left(-\frac{1.08\theta\cos(\theta)LAI'}{\sin(\theta)}\right), \tag{7.2}$$

where θ is the solar angle above the horizon, and LAI' is the effective leaf area index. Simulation of the longwave radiation to the snow surface, $L{\downarrow}_f$, is made as the sum of sky and forest longwave emissions weighted by the sky view factor as:

$$L{\downarrow}_f = \upsilon L{\downarrow} + (1-\upsilon)\varepsilon_f \sigma T_f^4, \tag{7.3}$$

where υ is the canopy sky view factor, $L{\downarrow}$ is the above canopy downward longwave radiation, ε_f is the emissivity of the canopy elements, σ is the Stefan-Boltzmann constant, and T_f is the absolute forest temperature. The canopy interception is modelled using a coupled forest snow interception, sublimation, and unloading routine after Hedstrom and Pomeroy (1998) and Parviainen and Pomeroy (2000).

Outflow from an HRU, comprised of both surface and subsurface runoff, was routed through the HRU and stream network using the lag and route approach of Clark

(1945) in the module *Netroute*. This approach is based on unit hydrograph concepts, with the outflow from a channel reach being linearly related to the storage in the reach. Essentially, the outflow at a given timestep is computed by lagging the inflow by the travel time, and then routing it through an amount of linear storage using the following expressions:

$$S = K_s \cdot O, \tag{7.4}$$

and,

$$\frac{I_1 + I_2}{2} - \frac{O_1 + O_2}{2} = \frac{K_s(O_2 - O_1)}{\Delta t}, \tag{7.5}$$

where S is storage, I is inflow, O is outflow, the subscripts 1 and 2 refer to the beginning and end of the routing interval Δt, and K_s is the storage constant. The value of O_2 can then be solved based on the inflows and the previous outflow, along with the storage constant, which is set by calibration.

Figure 7.1 provides a summary of the linkages of the modules within CRHM to construct the process-based hydrological model used for hydrograph simulation at Upper Middle Creek. Using this specific model structure, parameters and state variables were set and computed for the individual component modules, and variables representing mass and energy flow through the system were transferred amongst these modules as depicted in the figure. This analytical modelling framework was applied consistently to each individual hydrological response unit (HRU) with the exception of canopy representation, which was not used for exposed alpine HRUs. The next section discusses the spatial model structure and representation of these HRUs over Upper Middle Creek Basin.

7.2.2 Spatial Modelling Structure

The landscape was represented by HRUs of relatively homogeneous slope, aspect, vegetation, and location with respect to the drainage channel as in Section Six of this thesis. However, to represent the sub-HRU scale variability in snowcover and snowmelt over the SWE distribution on each unit, further stratification by SWE classes was made using the *group* functionality in CRHM (i.e., a group is a collection of modules executed in sequence that can be used in place of specific individual modules; Pomeroy et al.,

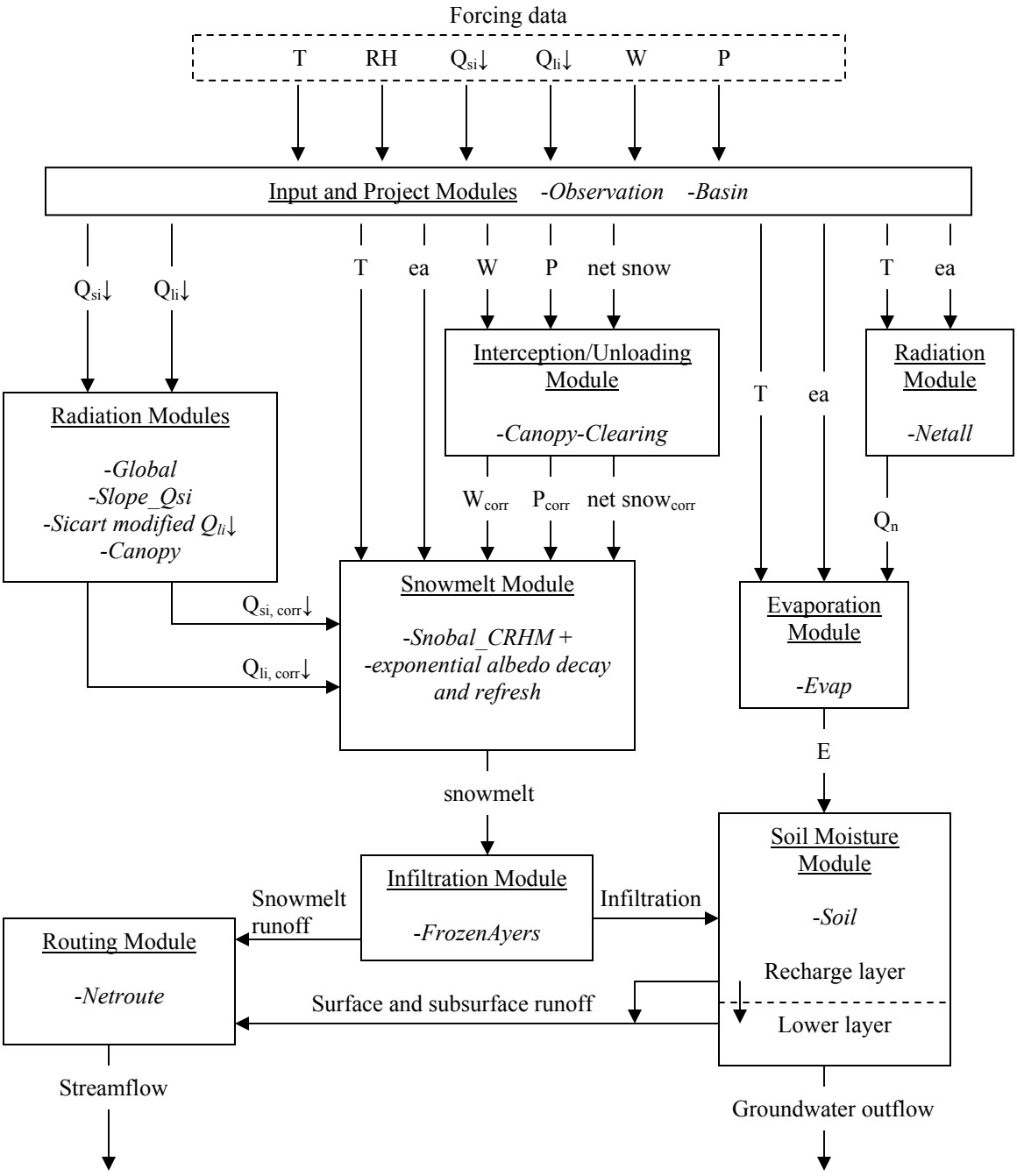

Figure 7.1. Flow diagram of the modules and linkages within CRHM used to construct a complete snowmelt runoff and streamflow hydrograph simulation model for Upper Middle Creek.

2007). Using the *CreateGroup* command in the macro edit menu of CRHM, an existing project consisting of a specified number of HRUs can be converted to a group, and the project can be added multiple times to create more groups. The number of HRUs in each

group is determined from the project that the group was originally created from. In this way, the landscape can be represented by a number of groups (individual projects or module sequences) to represent the various landscape units of slope, aspect, etc., while individual HRUs within each group can be used to represent the different SWE classes over the SWE distribution within a unit.

To represent the spatial variability in landscape units and SWE classes using this approach, landscape parameter values (discussed in Section 7.3.1) were set uniformly for the HRUs within individual groups, but varied between groups to represent differences in terrain, vegetation, and soils/surface cover. The only exception to this was the area of the individual HRUs within each group. This was set according to the approximated SWE distributions at the time of maximum accumulation on each of the landscape units, thereby allowing inter-annual differences in accumulation and snowcover to be represented by differences in the area of SWE classes (see Section 3.4). By determining the fraction of the total distribution represented by specific SWE classes and multiplying by the total landscape unit surface area, the area (m^2 or km^2) of the individual classes could be determined.

Figure 7.2 illustrates how this landscape stratification was carried out for the Upper Middle Creek Basin. Slope and aspect (Fig. 7.2a) were used first to disaggregate the terrain as in Section Six of this thesis, while landcover type (Fig. 7.2b) was used to further distinguish exposed alpine slopes higher in the basin from forested lower parts of the basin. As shown in Section 6.2, disaggregation of the basin into these units led to a reduction in the CV of both SWE and incident solar radiation, and provided a satisfactory fit to the lognormal distribution for SWE values. It was noted in that section that improving resolution of the variability further would require far more spatially explicit stratification. Table 7.1 provides the average value for several key terrain parameters over the landscape units, and lists the predominant landcover types over each unit.

For each year, approximated lognormal SWE distributions on each of the units were used to define the area of individual SWE classes. To maintain a moderate level of spatial model complexity while still representing the effects of inhomogeneous melt and SWE variability over individual landscape units, four SWE classes were considered for melt and runoff simulations. These were based on exceedence probability over the initial

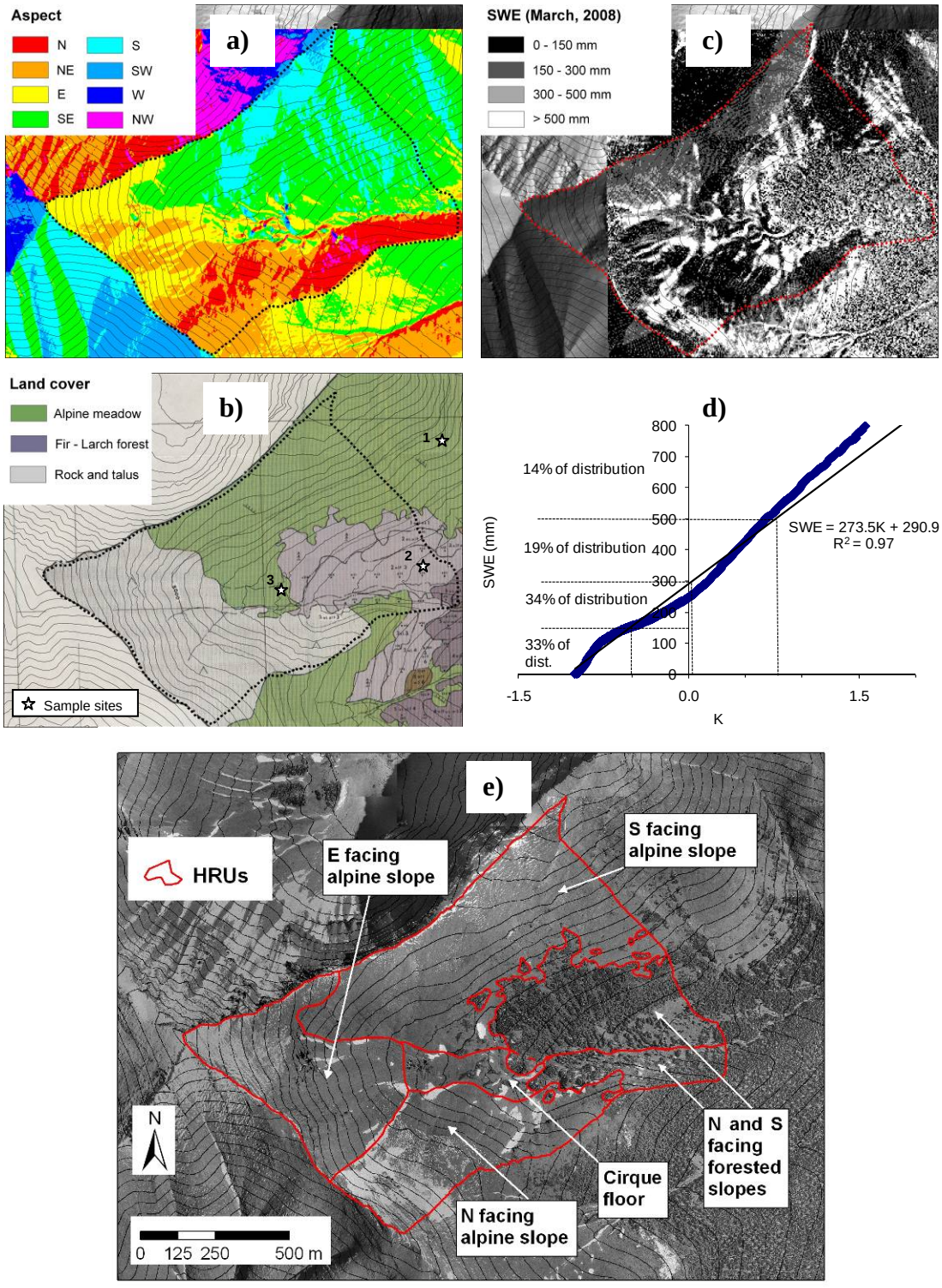

Figure 7.2. Illustration of landscape disaggregation approach and HRU selection: a) surface aspect; b) landcover type and approximate location of soil sampling sites by Beke (1969); c) LiDAR-derived SWE patterns; d) *K* – SWE plot for N-facing alpine slope; e) Upper Middle Creek HRU's based on landcover and topography (25 m contour interval).

Table 7.1. Spatial average values of terrain parameters over each of the individual slope-based landscape units in the alpine part of Upper Middle Creek Basin.

Parameter	N facing slope	S facing slope	E facing slope	Cirque floor	N facing forest	S facing forest
Terrain slope (°)	28	26.5	33	12.3	22	20
Aspect (° clockwise from N)	24	155	76	106	5	150
Elevation (m)	2427	2463	2575	2338	2254	2287
Sky view factor	0.72	0.74	0.72	0.66	0.54	0.68
Predominant landcover type	rock/talus	meadow	rock/talus	meadow	Fir–Larch	Fir–Larch
Area (10^4 m^2)	23.3	40.5	24.1	7.3	6.3	20.0
Area (% of basin)	19.2	33.3	19.8	6.0	5.2	16.5

distributions at peak accumulation; Figure 7.2c and 7.2d show an example of the spatial patterns of pre-melt SWE and a K – SWE plot for basing areas of different SWE classes. Table 7.2 provides estimated peak accumulation values of $\overline{\text{SWE}}$ and CV over the various landscape units, as determined from snow survey information and the LiDAR snow patterns, assuming that the early spring CV values are conserved between years (Appendix A). The table also shows the upper limits of SWE classes used to break up the distributions and the percent of the distribution (and thus area) represented by each class. With the exception of the lower forested slopes, the class limits were defined so that between 25 – 35% of the total distribution fell within each of the first three classes, and 7 – 15% within the deepest SWE class, while ensuring that no class represented too narrow a range of SWE (i.e., <100 mm). SWE classes were grouped more closely in forested areas due to the considerably less redistributed SWE patterns, as compared to windswept alpine areas. This approach improved resolution of the small areas with the deepest snow drifts, and the use of four classes produced similar timing and volume of meltwater generation over the landscape units as compared with the use of 12 classes in Section 6.4. This approach therefore helps to preserve model simplicity. By the stratification approach described here, the model represents the different landscape units in a spatially explicit manner, but the spatial structure of the SWE classes within these units is not considered. All HRUs were defined to drain directly to the stream network since during the spring surface meltwater streams formed in each landscape unit and were directly connected to the main stream channel.

Table 7.2. Mean and coefficient of variation of approximated lognormal SWE distributions on each areal landscape unit at the time of maximum accumulation in both streamflow simulation years. SWE class limits to break up the distribution are also given, along with area represented by each of the classes.

Landscape Unit	2007					2009				
	$\overline{SWE}$ (mm); CV	**SWE classes (mm)**; *Class area (% of unit)*; Class area (10^4 m^2)				$\overline{SWE}$ (mm); CV	**SWE classes (mm)**; *Class area (% of unit)*; Class area (10^4 m^2)			
N facing alpine slope	220; 0.93	**100**; *27.3*; 6.3	**200**; *33.5*; 7.7	**500**; *31.6*; 7.3	**>500**; *7.6*; 1.7	230; 0.93	**100**; *25.4*; 5.8	**200**; *33.2*; 7.6	**500**; *33.0*; 7.6	**>500**; *8.4*; 1.9
S facing alpine slope	170; 0.71	**100**; *30.5*; 12.5	**175**; *33.8*; 13.9	**300**; *24.4*; 10.0	**>300**; *11.3*; 4.6	160; 0.71	**100**; *33.9*; 13.9	**175**; *33.8*; 13.9	**300**; *22.7*; 9.3	**>300**; *9.6*; 4.0
E facing alpine slope	230; 0.64	**140**; *29.0*; 7.0	**225**; *31.1*; 7.5	**450**; *32.4*; 7.8	**>500**; *7.5*; 1.8	235; 0.64	**140**; *27.7*; 6.6	**225**; *30.9*; 7.4	**450**; *33.3*; 8.0	**>500**; *8.0*; 1.9
Cirque floor	294; 0.77	**150**; *25.9*; 1.8	**275**; *33.7*; 2.4	**500**; *27.2*; 1.9	**>500**; *13.3*; 0.9	305; 0.77	**150**; *24.2*; 1.7	**275**; *33.3*; 2.3	**500**; *28.2*; 2.0	**>500**; *14.3*; 1.0
N facing forest slope	320; 0.3	**225**; *14.6*; 0.9	**300**; *32.5*; 1.9	**400**; *34.7*; 2.1	**>400**; *18.2*; 1.1	330; 0.3	**225**; *12.4*; 0.7	**300**; *30.6*; 1.8	**400**; *35.9*; 2.2	**>400**; *21.1*; 1.3
S facing forest slope	320; 0.3	**225**; *14.6*; 2.9	**300**; *32.5*; 6.5	**400**; *34.7*; 6.9	**>400**; *18.2*; 3.6	330; 0.3	**225**; *12.4*; 2.5	**300**; *30.6*; 6.1	**400**; *34.7*; 7.2	**>400**; *18.2*; 4.2

7.3 Model Parameterization and Validation

7.3.1 Initialization and Parameterization of Model

The model was run using point-scale snowmelt simulations applied separately to each of the individual SWE classes on the different landscape units. These were initialized to give the mean value for a given SWE class at the time of maximum accumulation, and were used to represent the areal snowmelt over the extent of these classes on each unit. Hydrograph simulations were carried out for the 2007 and 2009 spring periods, but due to the failure of streamflow measurements in 2008, the model was not applied in that year. For both years, the areas of individual SWE classes were set according to Table 7.2.

The model parameters used within the snowmelt routines are listed in Table 5.2 of Section 5.3.2, which were left unchanged in the simulations described here, and Table 7.1 above. The use of the same parameters for Snobal maintains internal model consistency and reduces the degrees of freedom for remaining modules, as the parameters and structure of the snowmelt routines worked well at the point-scale and for areal SCD simulation on different slopes. Here, parameter selection and validation was focused on the modules described in Section 7.2.1; the selection for physically based modules such as *FrozenAyers* and *Canopy-Clearing* could mainly be based on measureable or estimated values, while those for conceptual modules such as *Soil* and *Netroute* were primarily derived through trial and error calibration. Table 7.3 provides some information on alpine soils in and adjacent to Upper Middle Creek Basin from Beke (1969) used to estimate some of the parameter values, and Table 7.4 summarizes the key parameter values used in the model for both years on the various landscape units.

The values for C and S_0 in Equation (7.1) describing the infiltration to frozen soil were set as 2.0 and 1.0 respectively, following previous studies using this routine (Zhao and Gray, 1999; Gray et al., 2001; Dornes et al., 2008a). The value for S_I, the initial soil saturation in the upper zone of the soil column, was estimated from both pre-melt soil moisture content and soil porosity. Pre-melt soil moisture was determined from water content time-domain reflectometer measurements collected manually in some lower parts of the basin during the fall, representing moisture conditions prior to freezing. Soil type, depth, and porosity in parts of the alpine zone of Marmot Creek were reported by Beke (1969), and this information was used for estimation of initial soil saturation, S_I. The value was set as 0.6, which is a moderately high value for wetter alpine soils in comparison to values of between 0.2 and 0.34 used by Dornes et al. (2008a) in a subarctic mountain basin, 0.4 used by Zhao et al. (1997) in a prairie environment, and 0.13 to 0.57 for prairie and boreal forest environments reported by Zhao and Gray (1999). It is noted that there is some uncertainty as to the value of these parameters over the primarily rock and talus covered north and east facing alpine slopes; however, meltwater and rainfall does infiltrate into porous till and surface regolith in the lower parts of these slopes, and these are relatively wet areas found near the base of the slopes. Thus the infiltration algorithm represents the best approach to dealing with the process here, despite that these

Table 7.3. Soil characteristics from soil sample sites within and near Upper Middle Creek Basin based on analysis by Beke (1969). See Fig. 7.2b for site locations.

Site	Soil type	Saturated capacity (mm)	Porosity (%)	depth to bedrock (cm)
1	Alpine Dystric Brunisol (Class B)	214	53	40
2	Alpine Dystric Brunisol (Class A)	287	41	70
3	Cumulic Regosol	176	40	44

Table 7.4. Model parameters used for *FrozenAyers* (FA), *Canopy-Clearing* (C-C), *Soil*, and *Netroute* modules over the Upper Middle Creek Basin. Canopy representation was only applied to the lower forested slopes.

Parameter	Module	N and E facing alpine slopes	S facing alpine slope and cirque floor	N and S facing forested slopes
Environment coefficient, (C; dimensionless)	FA	2.0	2.0	2.0
Surface saturation, (S_0; mm^3/mm^3)	FA	1.0	1.0	1.0
Initial soil saturation, (S_I; mm^3/mm^3)	FA	0.6	0.6	0.6
Initial soil temperature, (T_I; K)	FA	269.15	269.15	269.15
Net thawed infiltration capacity, (mm/hour)	FA	7.6	7.6	76.2
Canopy height, (h; m)	C-C	-	-	5.0
Effective leaf area index, (LAI'; m^2/m^2)	C-C	-	-	0.91
Maximum canopy snow interception, ($\overline{S}$; kg/m^2)	C-C	-	-	6.6
Maximum soil water capacity (mm)	Soil	100	200	250
Initial soil water capacity (mm)	Soil	75	150	187.5
Excess soil groundwater drainage factor (mm/day)	Soil	5	5	5
Linear storage coefficient (K_s; days)	Netroute	4	4	4
Runoff lag (hours)	Netroute	0	0	0

are not mature and well-developed true soils. Initial soil temperature was based on soil thermocouple measurements at Fisera Ridge prior to snowmelt, and was roughly –4 °C at this time. Infiltration opportunity time was calculated by model simulation of snowmelt duration.

For infiltration under thawed conditions, net infiltration capacity (i.e., maximum infiltration rate) was set based on values for various generalized soil categories following Ayers (1959). The soils are classified as consisting of coarse and medium textured soils over sand and gravel glacial deposits or coarse till, which was shown in this part of Marmot Creek by Beke (1969). Ground cover condition was set as either forested for the

lower basin or bare soil for upper slopes of the basin. The maximum thawed soil infiltration rates for these conditions are given in Table 7.4.

Canopy-Clearing parameters include vegetation height and *LAI'*, the effective leaf area index. These were based on the work of MacDonald et al. (2010) at Fisera Ridge, who reported an average canopy height of 2.3 m and an average *LAI'* of 0.91 for spruce forest down-slope of the south-east facing meteorological station. The same *LAI'* value was used here, but an average canopy height of 5 m was taken as more representative of the treeline forest in the Upper Middle Creek Basin. The maximum canopy intercepted snow load was set as 6.6 kg/m^2 following Hedstrom and Pomeroy (1998).

Soil and routing parameters were conceptual in nature, and were estimated or calibrated. Soil parameters in alpine meadow and forested areas were based on information on soil type, and their depth and porosity in the alpine zone of Marmot Creek (e.g., Beke, 1969). The capacity of the soil column was approximated from the depth and porosity of several soil profile measurements in different parts of the basin, which showed depths of between 40 cm and one metre, and porosity values from 40 to 60% (Table 7.3). From this information, average maximum soil moisture capacities for the soil profile on the different landscape units were defined (Table 7.4). The deepest soils are found in the lower parts of the basin in forested areas, and in the cirque floor area and the south facing alpine slope. Upper reaches of the basin on the north and east facing alpine slopes are characterized by poorly developed and thin soils, and mostly rock and talus. Using soil information from Beke (1969), the initial value of soil moisture in forested and meadow areas was assumed to be 75% of the maximum capacity, representing wetter alpine soils, in contrast to Pomeroy et al. (2010) who assumed this value to be 50% in the drier Wolf Creek basin, Yukon. Similar to their study, however, the soil recharge zone was assumed to be saturated. The same proportions were used for the rock and talus slopes, but the total capacity was reduced to half of that in meadow areas (Table 7.3). Again, there is uncertainty with these values and this approach, however, the module is conceptual and does not necessarily represent true soils in all cases, but rather the storage within all porous media.

Percolation to groundwater was set as a maximum of 5.0 mm d^{-1} for times when there is soil water excess. This amount is difficult to determine and may be higher than

in reality in some areas, but was set to conceptually represent strong surface – subsurface water connections in the basin and the large volume of water that percolates into the groundwater reservoir in areas with surface deposits of glacial till and talus at the base of slopes. *Soil* also contains algorithms for routing of the subsurface flows and groundwater percolation by a linear storage term, but these were left as the default of zero in the model, and all flows were routed based only on the storage term within the Netroute module. Routing of flow through the HRU and drainage network was based on the lag and route approach, and a value for K_s of four days was found to give a good fit of simulated streamflow with the observed hydrograph. The runoff lag, or delay, was left as zero as this produced the optimum results for hydrographs during the primary snowmelt period. In an alpine meadow – talus complex along the continental divide in the Rockies, McClymont et al. (2010) found that input volume of snowmelt and rainfall to the small basin is several times larger than its groundwater storage capacity, resulting in a rapid response of the water table and streamflow to water inputs in spring. Storr (1974) noted that storage capacity at Marmot Creek is usually filled in June from the combination of snowmelt and rainfall, resulting in rapid excess of runoff and flow into channels. Thus, during this time at Upper Middle Creek there is little delay between water inputs and streamflow response, and the calibrated value of K_s conceptually represents the relatively fast transmission of water through overland and subsurface pathways to the stream outlet. However, because it is calibrated specifically for the spring snowmelt period, it likely does not provide a good representation of the storage and transmission of water through the basin during other times such as late summer and fall.

7.3.2 Evaluation of Model Performance

The model was evaluated for its ability to represent characteristics of the observed hydrograph, including the magnitude and timing of flow, and the volume of runoff over the snowmelt period. The 2009 snowmelt period was used to calibrate specific parameters in *Soil* and *Netroute*, while the 2007 period was used as a validation year for the model. Figure 7.3 shows a comparison of the simulated and observed snowmelt hydrographs for these two years. The model captured the basic characteristics of the

measured hydrographs, such as the magnitude and peak flow of individual snowmelt runoff events and the decline to low flow conditions, as well as the timing of hydrograph rise following melt events. In 2009, the simulated hydrograph corresponded very well to the main snowmelt hydrograph following the break-up of ice and snow in the stream channel, but there were problems in terms of the response, timing, and recession of flow following a rainfall event in early July. This may have been due to increasing lags between surface water inputs and streamflow resulting from thawing soils and longer flow pathways with longer storage times as thaw increased. For the 2007 snowmelt period, the simulated hydrograph generally followed the major hydrograph peaks and the recession to baseflow in July, but the model had some problems in representing the short term variability of flow as it produced too rapid of a rise in flow rates (i.e., too "flashy" response) with the onset of snowmelt events and failed to adequately represent the hydrograph peak in late June. The error may be partly attributed to uncertainty in the streamflow measurements and stage–discharge rating curve used to predict flow rate, but is more likely due to model error, such as misrepresentation of changing lag times.

A quantitative assessment of the model performance was made using criteria including the Nash–Sutcliffe model efficiency (*NS*; see Section 5.3.3) and Model Bias (*MB*), which is given by:

$$MB = \frac{\sum \mathrm{dis}_{sim}}{\sum \mathrm{dis}_{obs}} - 1, \tag{7.6}$$

where dis_{sim} and dis_{obs} are the simulated and observed (i.e., measured) 15 minute discharge values respectively. Positive and negative *MB* values indicate the fraction by which discharge is either overestimated or underestimated throughout the simulation, and thereby describes the reproduction of total runoff. These were computed over the period from the beginning of flow measurements following ice and snow-free channel conditions to July 31 of each season, and are provided in Table 7.5. In addition, the total volume of discharge was determined by accumulating the flow rate over this same time period. The results indicate a good overall correspondence between simulation results and measurements in terms of the *MB*, while the moderate *NS* values indicate that the model did reasonably well at capturing the observed variability, but that it still produced errors in short term flow variations and magnitudes. The overall simulated volume of

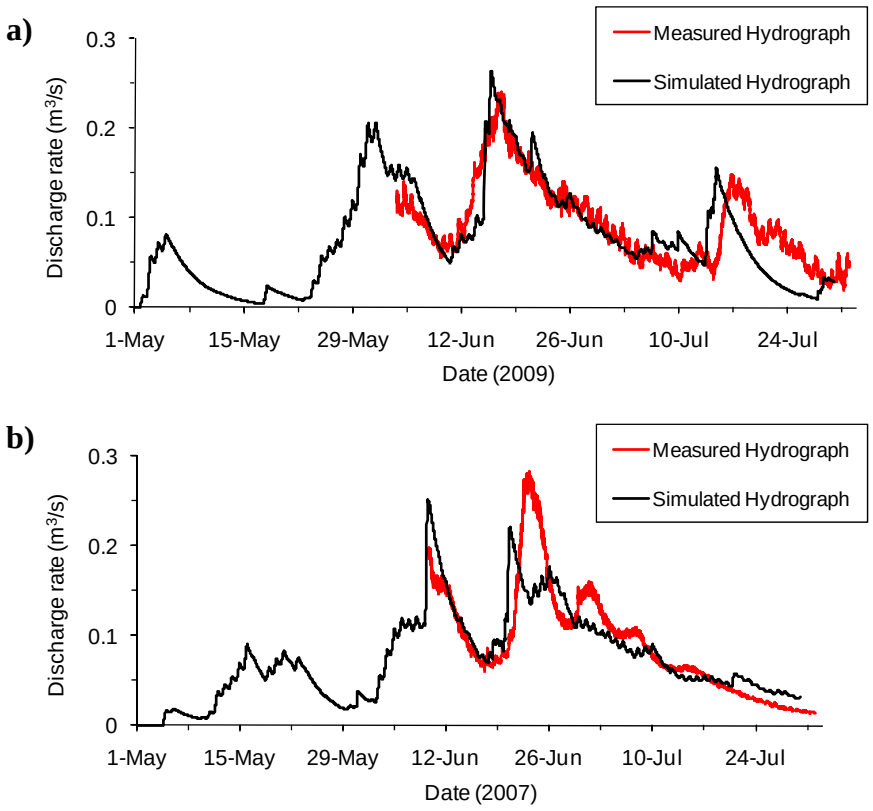

Figure 7.3. Comparison of measured and simulated hydrographs at the gauge site for Upper Middle Creek Basin in a) 2009 (model calibration year), and b) 2007 (validation year).

Table 7.5. Model Bias and Nash–Sutcliffe values, and comparison of simulated and measured runoff volumes for the calibration (2009) and validation (2007) years. Runoff ratio is the ratio of simulated total runoff to snowmelt and rainfall inputs.

Simulation year	Model Bias	Nash-Sutcliffe	Simulated total discharge		Measured total discharge		Runoff ratio
			(10^4 m^3)	(mm)	(10^4 m^3)	(mm)	
2009	–0.08	0.52	46.7	384	47.5	390	0.70
2007	–0.02	0.36	42.8	352	41.7	343	0.78

runoff during the snowmelt period in each season closely corresponds to the measured volume (i.e., within <10%), which itself suggests the model performs well and provides a well calibrated and good conceptual representation of the storages and transfers in this basin. The runoff ratios (i.e., the ratio of discharge/inputs) for both years are also provided in Table 7.5, and show that not all of the snowmelt and precipitation inputs

immediately contribute to runoff. In 2007 and 2009 respectively, approximately 22% and 30% of the inputs were abstracted and stored in the basin. This ultimately sustains baseflow later in summer and throughout the fall and winter. Although the total snowmelt inputs computed in Section 6.4.2 and the discharges here are comparable in magnitude, there was also an additional 127 and 159 mm of rain during the spring melt periods of 2007 and 2009 respectively.

This evaluation was based on the model being executed in a spatially distributed manner and accounting for the distributions of SWE on each landscape unit. The good performance of the model shown here indicates that it provides a simple, yet conceptually and physically reasonable approach for representing the transfer of snowmelt runoff through the basin and stream network. In the following section the model group and HRU structure, and snowmelt representations are altered to provide several different spatial representations of SWE and snowmelt variability over the landscape. Comparison of the results with the simulations from this distributed approach yields insight on the sensitivity and error of the integrated basin scale snowmelt hydrograph from these various approaches.

7.4 Hydrograph Comparative Analysis

7.4.1 Landscape Unit Component Hydrographs

The snowmelt hydrograph at the basin outlet is composed of the runoff from each of the individual landscape units within the basin. Each of these produces meltwater at different rates and times as shown in Section 6.4, with the magnitude of snowmelt runoff varying considerably over time and space in the small basin. The combined flows originating from the different slopes influence the overall shape and magnitude of the hydrograph at the basin outlet, and therefore examination of the simulated streamflow contributions from the individual slope units may be useful towards characterizing the effects of landscape representation in the model.

Figure 7.4 shows the simulated component hydrographs from each landscape unit for the two simulation seasons. There are considerable differences in the timing and

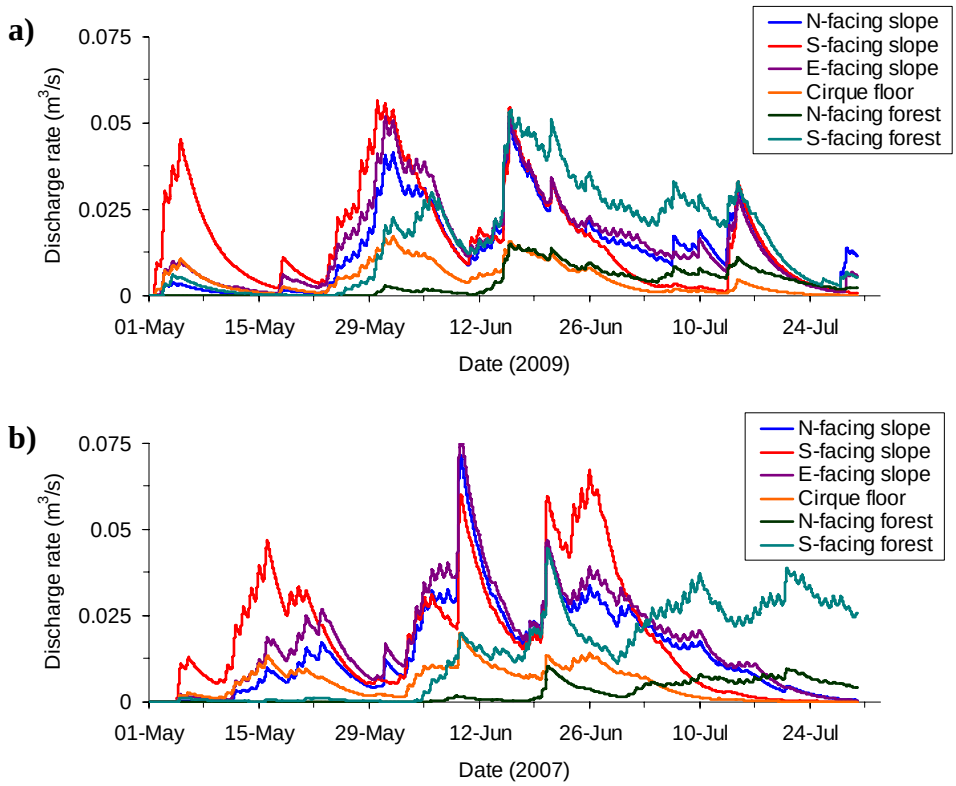

Figure 7.4. Simulated component hydrographs from each of the individual slope, aspect, and vegetation based landscape units in Upper Middle Creek Basin: a) 2009 snowmelt hydrographs; b) 2007 snowmelt hydrographs.

magnitude of flow from the different units, just as shown in Section 6.4.2 for the meltwater inputs. In both seasons, the most significant overall contributions were from the south facing slope (including both the forested and the above-treeline alpine components) due to the relatively large area of this landscape unit in comparison with the others. Runoff from the exposed alpine component of the south facing slope is important in controlling the initial hydrograph rise in mid to late-May, when the contribution from other slopes is less significant. Also, runoff from this slope represents an important component of the overall hydrograph during periods of snowmelt following spring snowfall and rainfall events because it has a large total area. However, the more rapid melt and decline of the snowcover on the windswept alpine part of the south facing slope results in reduced runoff contributions later on in the spring and early summer. The forested area on the south facing slope develops deep accumulations of relatively uniformly distributed SWE, which begin to melt somewhat later in spring due to the

influence of the canopy on snowmelt energy, but provide a significant source of meltwater and runoff later in the spring. In terms of the overall volume of streamflow, the forested south facing slope unit represents an important area for snowmelt runoff generation, as it contributes a comparable amount of melt and runoff as the exposed alpine part of the south facing slope, despite occupying approximately only half of the area (33% vs. 16% of total basin area; Table 7.1). This attests to the high relative importance of the treeline region for trapping and accumulating windblown snow from the alpine zone, and producing melt and runoff that sustains streamflow later into the spring.

The component hydrographs of the north and east facing alpine slopes are broadly similar in timing and magnitude during the course of the spring, despite some minor differences in the timing and magnitude of runoff. These slopes begin to contribute to streamflow in early June, and sustain runoff later into July from the slower and later melt from drift areas here. Together, these two slope units provide the most significant contribution to the overall hydrograph in late June and early July, which highlights the importance of local depressions and gullies in some parts of the alpine landscape for collecting snow and sustaining late-spring runoff. The effect is amplified where these drifts form in areas such as north facing slopes with lower energy receipt and later and slower melt of deep snow. Because the area of both the north and east facing alpine slope units is roughly equivalent, and the SWE accumulation patterns are not substantially different, the total volumes of streamflow originating from these slopes are similar in magnitude.

Finally, the contributions from the cirque floor area and the north facing forested slope are smaller in magnitude due to the relatively minor area of each unit in comparison to other slopes (Table 7.1). However, runoff from these units still has an important influence on the overall hydrograph shape and magnitude at certain times. The cirque floor area is important in contributing melt and runoff that supply early season flows in mid to late-May, as well as sustaining flow due the melt of deep drifts through June and into July. Melt does not begin until much later under the canopy of the north facing forested slope. The deep accumulation of snow on this relatively small unit, and the

delayed and slow rate of melt here, make it an important source area for late season runoff generation.

This analysis has shown that there are considerable differences in the timing and magnitude of flow originating from the various landscape units. The hydrology of this system is characterized by a highly non-linear response, and as indicated by the model here, the spatial–temporal runoff dynamics vary considerably on both a seasonal and an inter-annual basis as controlled by snow accumulation patterns and spring meteorological conditions. Therefore proper representation of the differential rate and timing of inputs from different parts of the basin is likely important for realistic simulations of streamflow here. This is explored in more detail in the following section.

7.4.2 Effects of Representation of Spatial Snowmelt and SWE Variability

To investigate the sensitivity of the simulated hydrographs to the representation of spatial snowcover and snowmelt variability, several different model scenarios were explored as in Section 6.3.2. In addition to the distributed approach previously described, these involved simulations based on a single fixed distribution of SWE over the entire basin together with distributed snowmelt energy to each slope unit (Fixed SWE dist. – Variable Melt), separate distributions on each slope with uniform applied energy based on the ridgetop (Variable SWE dist. – Uniform Energy), and a fixed SWE distribution together with uniform applied energy (Fixed SWE dist. – Uniform Energy). Uniform applied energy approaches are distinguished from uniform melt in that inhomogeneous melt over the SWE distribution due to internal energy effects is still possible (this is considered further in the next section). This is similar to the scenario analysis of Dornes et al. (2008b), who investigated the effects of different aggregation approaches of initial SWE conditions and forcing variables in a subarctic environment. For each of the simulations, the same model structure and parameters (Table 7.4) were used for the six slope/landscape units over the Upper Middle Creek Basin as previously described. Thus, canopy and soil parameters varied between the landscape units for all the model scenarios here, while other parameters were set uniformly over the basin. For simulations based on uniform applied melt energetics, the terrain was modelled as being flat, with no

corrections applied for slope, aspect, and sky view effects on incoming short and longwave radiation, and using the observed forcing data from the main station on Fisera Ridge. However, meltwater and flow routing through the basin was the same as for the distributed approach since the model structure was unchanged. Simulations based on a fixed distribution of SWE used an approximation for the overall basin distribution, and the area of different SWE classes on individual slope/landscape units was set according to this single distribution.

Figures 7.5 and 7.6 show the simulated hydrographs from each of these modelling approaches in the two seasons, and compare them with the measured hydrographs at the basin outlet. Table 7.6 provides *MB* and *NS* values for each of the simulations as a quantitative measure of the success of the approach in each instance. In all cases, the model reasonably captured the observed shape and timing of the major peaks in streamflow after the end of May, although the magnitude of simulated flow varied depending on the approach. The key differences that were observed amongst the different simulations involved the timing and magnitude of early flows in May, the magnitude of peak flow events during and after major snowmelt events and rainstorms, and the magnitude of flow and rate of recession towards the end of the snowmelt period. In both years, comparison of the four scenarios described above showed that the best results were achieved using the approach with variable SWE distributions and variable applied snowmelt energy, while the poorest model performance was associated with the fixed SWE distribution and/or uniform applied energy simulations. This is clear based on visual comparison of the simulated and measured hydrographs along with the Model Bias and Nash–Suttcliffe values, although in 2007 the fixed SWE dist. – Uniform Energy approached yielded the highest *NS* value.

Approaches based on spatially uniform applied energy (c and d in Figs. 7.5 and 7.6) tended to produce higher early spring peak flows and more streamflow in the month of May before measurements were available. High predicted discharge rates through May was also a problem for the simulations using variable snowmelt energy (a and b in Figs. 7.5 and 7.6), but less so than for the uniform approaches. Although there were no actual discharge data to confirm that the simulated flow was too high in some cases for mid to late May, the observations in the field suggested that flow was minimal prior to

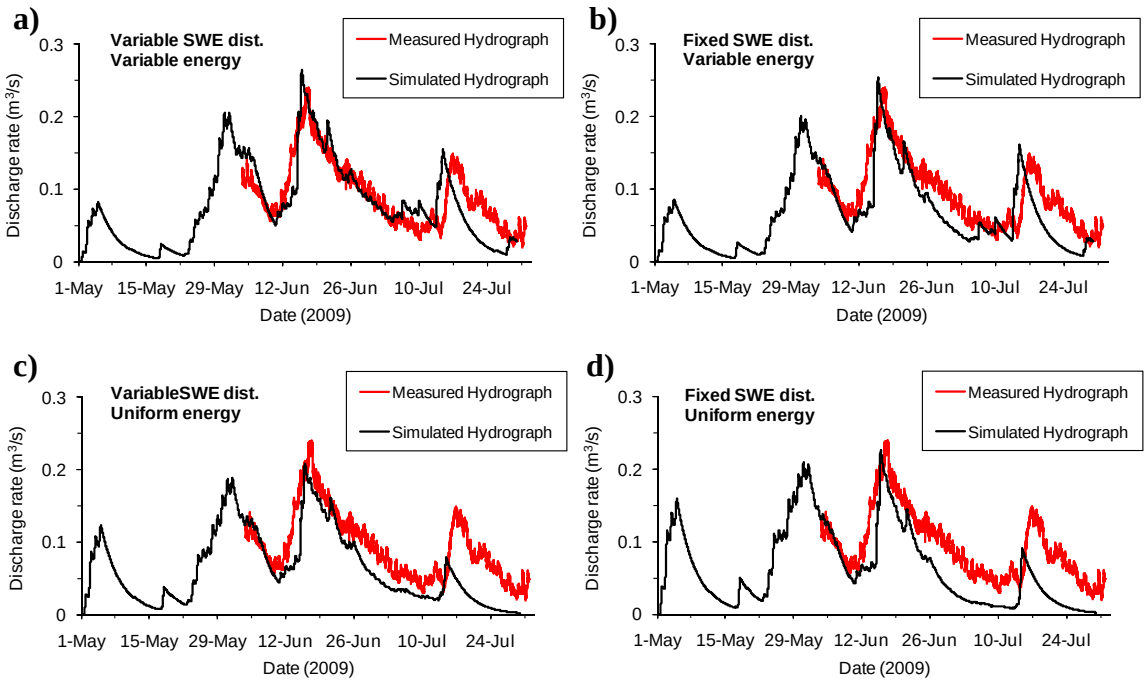

Figure 7.5. Comparison of simulated and observed hydrographs using different modelling approaches for representation of SWE and melt energy variability in the spring of 2009.

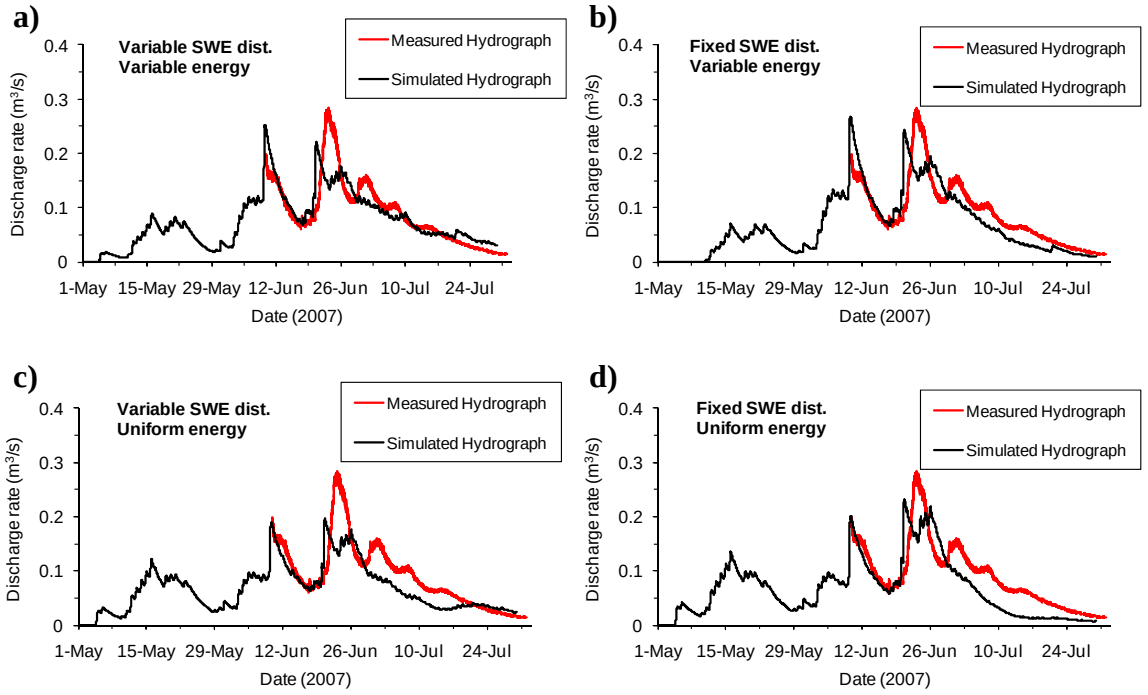

Figure 7.6. Comparison of simulated and observed hydrographs using different modelling approaches for representation of SWE and melt energy variability in the spring of 2007.

Table 7.6. Model Bias (MB) and Nash–Sutcliffe (NS) values for simulated hydrographs generated from the different modelling approaches shown in Figs 7.5 and 7.6.

Year	Variable SWE dist. Variable Melt		Fixed SWE dist. Variable Melt		Variable SWE dist. Uniform Energy		Fixed SWE dist. Uniform Energy	
	MB	NS	MB	NS	MB	NS	MB	NS
2009	–0.08	0.52	–0.25	0.36	–0.39	0.15	–0.47	–0.08
2007	–0.02	0.36	–0.10	0.26	–0.10	0.42	–0.23	0.39

just before the start of measurements. At these times the channel was entirely snow-filled and stream discharge was only occurring as saturated basal flow through the snow and through small voids in ice along the channel bottom. Discharge rates at these times would have been roughly the same magnitude or less than those during the baseflow conditions following snowmelt. The issue of snow damming of channels was not addressed in the model as techniques to simulate it do not exist. The use of uniform applied energy based on ridgetop melt energy lead to earlier and greater snowmelt runoff on north and east facing slopes, while delaying melt to some degree on south facing slopes. The net effect of this was to produce more melt and runoff over the basin during May. This also led to reduced meltwater inputs later in June and July due to the fact that snow on north and east facing slopes melted and became depleted sooner in the spring. As shown in the previous section, snowmelt runoff contributions from areas of deep drifts and snow-filled gullies on these slopes are important in sustaining late spring flow after peak runoff events. This partly explains the misrepresentation and under-prediction of the recession flows and return to baseflow in late June and throughout much of July for the uniform energy scenarios.

The approach based on a fixed distribution of SWE for the basin together with spatially distributed snowmelt rates produced better results than those based on uniform applied energy. Hydrographs from the fixed SWE dist. – Variable Melt simulations were very similar to those from the variable SWE distribution and melt simulations due to the fact that for the exposed alpine slopes, the individual distributions on each slope were not significantly different. However, SWE distributions within lower forested parts of the basin differed considerably from those over the windswept alpine slopes. Because of this, the fixed distribution approach led to some errors in the simulated late spring and

summer flows following peak melt since deeper and more uniform accumulations of snow in the tree-line areas were misrepresented. As for the drift areas higher on the north and east facing alpine slopes, later contributions of snowmelt runoff from these areas are relatively important towards the end of the spring.

These scenarios only considered the effects of spatial differences in snowcover variability and applied energy, while landscape parameters describing soil properties and vegetation were not changed. To investigate the combined influence of variability in snowcover, surface energy receipt, soils, and vegetation on the snowmelt hydrograph at the basin scale, two further simulations were carried out using spatially lumped soil and canopy representations. Initial and maximum soil moisture content were uniformly set as 150 and 200 mm respectively, and the entire basin was represented as having no canopy (since the dominant surface cover is exposed alpine meadow, tundra, and rock). The first approach assumed variable distributions of SWE and distributed energy receipt to the different landscape units, and the second approach used a fixed SWE distribution for the basin and uniform snowmelt energy based on the ridgetop site. Figure 7.7 shows the predicted hydrographs from these two simulations in each model year, and Table 7.7 provides the *MB* and *NS* values from the simulations.

The approach based on variable SWE distributions and melt energy together with uniform soils and canopy produced higher streamflow values in the early melt period and less towards the end of the melt period. This was mainly due to the earlier and more rapid melt of snow in the forested areas, which were represented as open, and the earlier disappearance of snow in these areas that would have augmented the late spring flows. Model performance decreased for the 2007 simulation, and although it was not significantly affected in the 2009 simulation, this was for the wrong reasons due to the cancellation of errors. The approach based on a fixed distribution of SWE and spatially uniform snowmelt energy together with uniform soils and canopy produced very poor results with greatly excessive flows in the early spring and insufficient streamflow in the later part of the spring. In these simulations, the effects of uniform melt energy and timing of melt onset and snow depletion over the basin were very pronounced. In reality, the effects of lower melt energy to north and east facing slopes, together with the effects of the tree-line area forest canopy in both trapping windblown snow and delaying melt

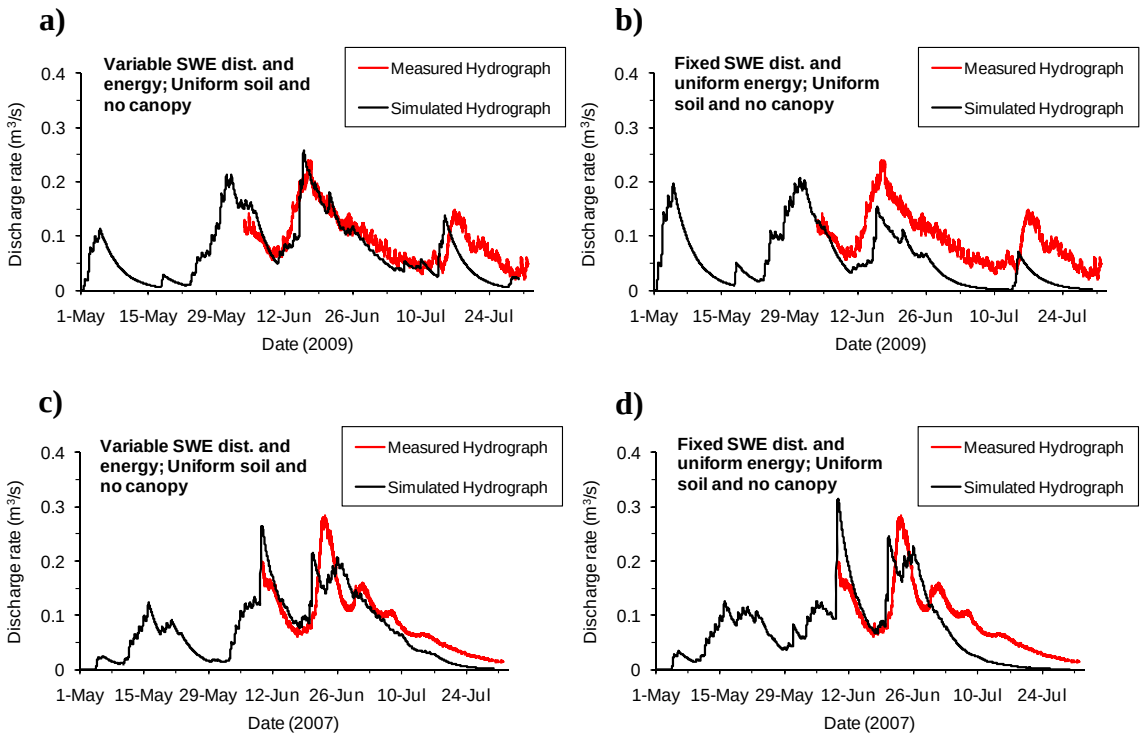

Figure 7.7. Comparison of simulated and observed hydrographs in 2007 and 2009 using distributed and uniform approaches of melt and applied energy, together with uniform soils and vegetation parameters.

Table 7.7. Model Bias (*MB*) and Nash–Sutcliffe (*NS*) values for simulated hydrographs generated from the different modelling approaches shown in Fig. 7.7.

Year	Distributed SWE and forcing; Uniform soil and canopy		Uniform SWE and forcing; Uniform soil and canopy	
	MB	*NS*	*MB*	*NS*
2009	–0.20	0.46	–0.62	–0.71
2007	–0.09	0.28	–0.18	0.01

leads to areas of persistent snowcover into the early summer. With no forest canopy cover represented by the model, and uniform melt energy to all slopes, there was no remaining snowpack to provide meltwater contributions after mid to late-June, unless a

new snowfall event occurred. Therefore, some of the success of the previous model approaches based on uniform snowmelt energy can be partly attributed to the fact that limited areas of forest canopy were still represented such that there was slower melt in forested areas. For cases where a fixed SWE distribution was used, representation of forest canopy and/or spatially variable snowmelt still had the effects of moderating early spring runoff and delaying melt in some areas to provide greater late season flows. This helps to show how misrepresentation of certain characteristics of the snowmelt hydrology here may not necessarily lead to large errors since this can be partially offset depending on the approach taken to resolve the variability.

7.4.3 Influence of Inhomogeneous Melt

The effects of non-uniform melt rates and timing due to differences in the warming and ripening over a cold, redistributed snowcover have been examined in other parts of this thesis at the point-scale and for simulations of areal SCD. Here the influence of this phenomenon on the snowmelt hydrograph is examined to see how differences in the internal energy and snowmelt over SWE distributions are manifested in the runoff characteristics at the basin outlet. To do this, melt rates and meltwater discharge from the base of the snowpack were simulated as uniform for each SWE class being represented, and the surface inputs were handled in the same way by the other model routines to derive the hydrograph. Timing and rate of meltwater generation was represented by the deepest SWE class to ensure that the model produced runoff until the end of the snowmelt period, but the duration of melt over each of the separate SWE classes within the distribution was limited by the time to melt and deplete the initial SWE in each class. An export file was created from an initial model run to produce the melt rates and meltwater input, as well as remaining SWE in each of the classes for each time step, and this was then fed back into the model using a macro in the CRHM project (Appendix D). Instead of running the modules for snowmelt computation in the second simulation, the macro takes the specified inputs of melt rate and SWE from the file and uses these as the inputs to *FrozenAyers*, *Soil*, and *Netroute* modules to derive the snowmelt hydrograph.

Figure 7.8 shows the hydrographs produced by the model in the two years under both inhomogeneous melt (as previously shown) and homogeneous melt, where melt rates and meltwater generation were represented uniformly over the SWE distribution and the SCA on each slope unit. Table 7.8 provides the *MB* and *NS* values from these simulations. The primary difference between the hydrographs in each year from inhomogeneous and homogenous melt simulations is that melt and runoff generation was initially more limited in May, and then greater runoff was produced later in the spring and early summer. In both years, neither approach produced consistently better results according to the *MB* and *NS* values (Table 7.8). However, from inspection of the hydrographs, the 2007 homogeneous melt simulation tended to over-predict the recession flows through July and did no better at representing short term streamflow variability than the inhomogeneous approach during May and June. The reason for the initially more limited runoff generation during the early spring was that large areas covered by shallow or average depths of SWE were represented as melting more slowly according to the rates for the deeper snow. In late April and early May, the available storage capacity in the soil and surface debris cover took longer to fill due to the delay in melt onset and meltwater generation of the deep snowcover. Because these areas were represented as melting out initially later and more slowly than they otherwise would have under inhomogeneous melt, the remaining snowcover persisted later into the spring under homogeneous melt and led to a slight increase in the later season flows.

Although the effects of inhomogeneous melt are apparent in the snowmelt hydrograph, the magnitude of error resulting from neglecting these effects is not as great as that for areal SCD. This is likely because as additional processes are considered, the effects become less emergent in the overall response. Further, it cannot be determined from these results which approach produced better overall results due to the lack of discharge measurements during May in both years. This is when the largest differences between simulation results were observed. Given the anecdotal observations of very low channel flow rates at this time, the simulations based on homogeneous melt seemingly produced better early season streamflow values. This suggests a problem that is most likely associated with improper representation of snow obstructing the channel network, and not the representation of snowmelt processes.

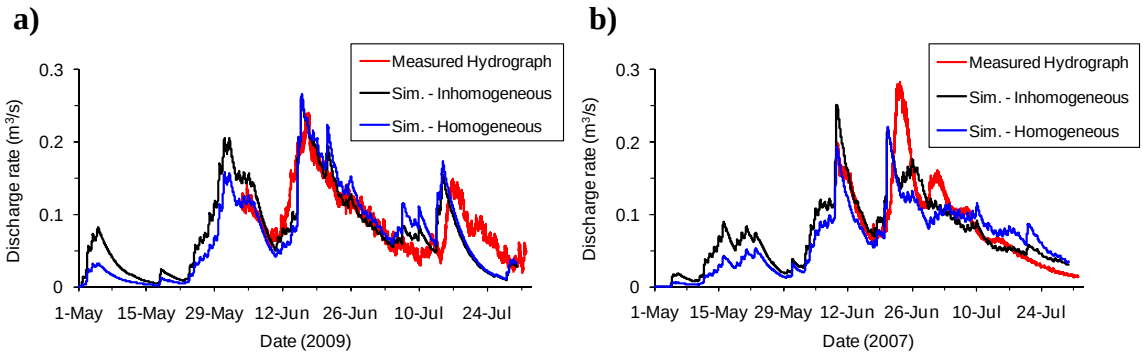

Figure 7.8. Comparison of simulated and observed hydrographs in 2007 and 2009 for inhomogeneous melt and homogeneous melt over SWE distributions. For both cases, simulations used variable SWE distributions and applied melt energy between slopes.

Table 7.8. Model Bias (*MB*) and Nash–Sutcliffe (*NS*) values for simulated hydrographs generated from the different modelling approaches shown in Fig. 7.8.

Year	Inhomogeneous Melt		Homogeneous Melt	
	MB	*NS*	*MB*	*NS*
2009	–0.08	0.52	0.01	0.36
2007	–0.02	0.36	–0.04	0.41

7.5 Discussion of Hydrological Modelling Considerations

7.5.1 Variability of Surface Meltwater Inputs

The spatial and temporal dynamics of meltwater generation and runoff over the landscape have a major influence on the magnitude, shape, and timing of the snowmelt hydrograph at the basin outlet. It was shown here by simulation that the variability in pre-melt snowcover and snowmelt energy patterns over the spring, together with the presence of forest surface cover in the lower part of the basin, largely control the timing and location of the different source areas for snowmelt runoff. Model performance was generally found to decrease when the simulation approach did not account for the spatial variability

in any or all of these features, since the definition and development of the source areas were not properly represented. However, there were instances where the model seemed to perform reasonably well in comparison to the approach based on both variable SWE distributions and snowmelt energy, and produced realistic appearing hydrographs despite misrepresenting some of the variability in snowmelt over different parts of the basin. The success could be partly attributed to the cancellation of errors in melt timing, rate, and location, and the fact that in some cases, simply representing forest canopy in the lower basin or spatially variable snowmelt energy could offset what would otherwise have been greater errors. In this respect, the various analyses carried out here helped to show how the correct results can sometimes be obtained, but for the wrong reasons.

An advantage in this study was that the snowmelt routines within the model had been developed and validated up from the point-scale (i.e., melt rate and timing on individual slopes) to the slope unit and alpine basin scale (i.e., simulation of areal SCD), as shown in Sections Five and Six. This provides confidence in the internal validity, or "correctness" of the hydrological model in terms of its alpine snow components. Thus, not only could the hydrograph be reasonably well-represented, but the variability in the timing and rate of snowmelt and areal SCD on different slopes within the basin was also captured, which is often not the case in many hydrological model applications. Rather, modellers frequently base the structure and parameters solely on relationships between input forcing data and basin-scale snowmelt hydrograph features, and are therefore likely to misrepresent important aspects of the variability of surface meltwater inputs. Such a "black box" approach might fail to capture critical non-linear scaling effects and changes in system behaviour under different modelled climate and landcover scenarios, for example. By preserving internal consistency and correctness in snowmelt routines, it is possible to improve parameter identifiability and analytical structure for the remaining non-snow components, and as the models are subsequently transferred to other scales, locations, and climatic or landcover conditions, it is more likely that realistic hydrographs will be produced.

Many studies in a range of environments have shown that explicit consideration of source areas based on surface cover and topography over a basin are key towards the prediction of basin discharge (Gray and O'Neil, 1974; Marsh and Pomeroy, 1996; Marks

et al., 2002; Pohl et al., 2005, 2006; Pohl and Marsh, 2006; Davison et al., 2006; Dornes et al., 2008a, 2008b). It is especially important to represent the differential contributions from various parts of the basin when there are underlying associations between snow accumulation patterns and melt energy. The approach presented and applied here provides a useful, yet spatially and computationally simple method of representing these source areas within the landscape, while requiring relatively little information for initialization (i.e., $\overline{\text{SWE}}$ and CV). As discussed in Section 6.5.1, the transferability of CV values based on representative landscape types (e.g., Pomeroy et al., 1998; Liston, 2004; Clark et al., 2011) makes this a potentially valuable technique for representing snowmelt inputs to the land surface in models applied outside of well-studied research basins. This is much simpler than attempting to initialize a distributed, grid-based model, which would have to have a very fine spatial resolution (i.e., 10 – 25 m maximum) to effectively capture the relevant variability in snowmelt processes and areal SCD. Here, a total of 24 computational units (Table 7.2) based on the SWE distributions over six landscape units were sufficient to characterize the variability of the snowcover for melt and runoff simulation.

A final point to discuss here is that the differences in predicted hydrographs under the inhomogeneous and the homogeneous melt simulations were not significant. This is likely because as pathways through the basin become longer, and as further hydrological processes become involved, the hydrograph response to surface meltwater inputs becomes increasingly controlled by these other basin factors. Inhomogeneous melt over the SWE distribution (at least that within individual landscape slope units) therefore appears to be a non-emergent feature in basin scale hydrographs, whereas it is directly relevant for the simulation of areal SCD (Section 6.3.3), and especially important early in spring. Thus, if the primary goal of model application is simply to obtain the hydrograph, representation of this feature might be omitted (although variability of snowmelt amongst slope-based landscape units is still essential).

7.5.2 Routing, Groundwater, and Other Model Components

Although the main focus and objectives of this thesis do not involve the development of new hydrological process modules other than a surface meltwater input framework, it is useful here to briefly discuss some key components that could be improved for future generations of similar models. In this study, existing modules within CRHM were used to assemble a simple conceptual, or for some processes, physically based approach for transferring snowmelt and rainfall inputs through the basin to generate the streamflow hydrograph in the spring and early summer. However, some of the important processes involved in the movement of water through various subsurface pathways and along the channel drainage network may not have been ideally represented. In particular, consideration of storage delays and the gradual release of water moving through glacial and post-glacial surficial deposits, and the surface runoff delays caused by snow within the gullies and stream channels could likely be improved.

Subsurface flow is a highly important aspect of the hydrology of Marmot Creek. Swanson et al. (1984) reported that most of the streamflow is fed by transient subsurface flow from glacial deposits, which moderates hydrograph peaks and sustains baseflow. Recent hydro-chemical and tracer studies by the Centre for Hydrology, University of Saskatchewan on Upper Middle Creek have shown that there is a substantial subsurface and groundwater component to streamflow. Therefore, it is important for future work to focus explicitly on characterizing the subsurface hydrology using a physically based approach. The current representation of groundwater in the *Soil* module is conceptual, including a term for quantifying the maximum daily seepage loss to the groundwater reservoir, and characterizing subsurface outflows by a lag and route approach. Physical aquifer properties, changes in groundwater storage, and non-linear storage–discharge relationships are not accounted for, which is a potential limitation that should be explored further in the future.

In the model here, attenuation and storage delays were represented using *Netroute* and the lag and route approach. Best fit values for the lag and linear storage term, K_s, were set by calibration, and these are meant to conceptually account for watershed properties and the natural storages that feed streamflow after surface water inputs have

ceased. Although this can produce reasonable hydrograph recessions immediately following snowmelt, it is recognized that the linear reservoir model of watershed response that this approach is based on is valid only over a limited range of the recession period (Tallaksen, 1995). Further, the value of the storage term may vary over time as storages and hydrological pathways in the basin change from the snowmelt period into the summer and fall. For example, Carey and DeBeer (2008) observed the linear storage, or recession coefficient to strongly increase over time in a subarctic basin, and suggested that hydrological models using such parameters in calibration should consider their temporal dependent nature.

Another important characteristic of the snowmelt hydrology at Upper Middle Creek is the filling of stream channels and gullies with deep accumulations of snow over winter. This plays a key role in the evolution of the surface drainage network and the timing of spring hydrograph rise at the basin outlet. Woo (1998) discussed how snow within the channels in arctic environments affects the integration of the drainage network and influences the lag time between snowmelt and streamflow initiation. The observations over the course of this thesis work suggest that the channel network does not become clear of snow and capable of effectively draining the basin until early or mid-June, despite significant snowmelt conditions occurring through May. The model used here did not account for this phenomenon in any way, and may have overestimated the flows in the early spring before measurements were available. Delays between surface meltwater inputs and streamflow were represented in an indirect way by setting the initial soil moisture as 75% of the maximum capacity, thus requiring a certain amount of melt before any runoff and streamflow was simulated. This is a clear misrepresentation of the actual processes that would likely influence the performance of the model, and requires further study and perhaps algorithm development for subsequent models. There is not presently a snow-damming module with the CRHM library, but it may be necessary in future to develop a module to account for storage and delay within the stream network up until the time of channel clearance.

8. SUMMARY AND CONCLUSIONS

The purpose of the final section of this thesis is to synthesize the main findings and significance of this work, and to provide insight and direction for future studies to carry the work forward. The section begins with a brief overview summary of the work, including the approach and key results. More detail is then provided on specific developments and findings throughout the thesis, along with the significance and implications for related work in alpine and other environments. The section ends with a brief discussion of the limitations of this study and of future directions for research and modelling of alpine snow hydrology.

8.1 Summary of Key Developments and Findings

8.1.1 Thesis Overview

This thesis has focused on the melt and areal depletion of alpine snowcovers, beginning with the development of a new theoretical framework for areal SCD and snowmelt runoff, and then application of the framework over a small (~1.2 km^2), well-studied basin in the Canadian Rocky Mountains. The focal site was the Upper Middle Creek Basin and adjacent Fisera Ridge within the Marmot Creek Research Basin, Kananaskis, Alberta. An intensive field monitoring campaign was carried out here to collect the necessary data to apply and test the framework, where measurements included point and areal snowpack and spatial snowcover monitoring, along with detailed hydro-meteorological observation, and streamflow observation at the basin outlet. A physically based point-scale snowmelt model was developed using the Cold Regions Hydrological Model (CRHM) platform and used to drive upscaled simulations of areal SCD and snowmelt runoff, based on the theoretical framework. Various simulations were carried out to examine different aspects of the timing and rate of snowmelt over the landscape, and the effects of variable pre-melt SWE and melt rates on areal SCD. Finally, a process-based hydrological model was developed using CRHM and the snowmelt runoff framework was used together with this

model to simulate the streamflow hydrograph at the outlet of the basin. In this way, the basic modelling approach of this work has essentially been to proceed upwards from point-scale snowmelt computations, to areal snowmelt and SCD simulation at the scale of individual slopes and for the basin as a whole, and finally to snowmelt runoff and streamflow simulation at the basin scale. This provided validation of the model framework at various stages along the course of its development.

8.1.2 Significance and Implications of Findings

Some components of this research have not been considered in detail in previous studies, and make a contribution towards advancing both the conceptual understanding and model representation of alpine snow hydrology. Here, the significance and implications of the developments and findings throughout this thesis are discussed.

The first objective of this thesis involved the development of a theoretical framework for areal SCD and snowmelt runoff in open alpine environments, and was addressed in Section Three. As discussed in the Introduction and Literature Review sections of this thesis, there are a number of difficulties encountered in the representation of complex alpine snow processes at the appropriate spatial scales in hydrological models, which makes application of these models over broad regional scales difficult and challenging. Areal SCD and snowmelt runoff depend strongly on the pre-melt spatial snowcover variability, as well as the surface energetics and resulting melt rates throughout the spring. The framework that was developed here accounts for the combined spatial–temporal variability of pre-melt SWE and snowmelt rates over the alpine landscape by resolving areal units with relatively uniform applied melt energetics (i.e., slope-based landscape units), and representing sub-unit variability in SWE according to a statistical frequency distribution. It is based on the theoretical lognormal distribution, for which a reasonable approximation can be given by the parameters $\overline{SWE}$ and CV, although it can be extended to include any parametric or empirical distribution. Some notable advantages of the lognormal distribution are that it has been found widely applicable, its parameters are easily obtained, and studies have noted the transferability of typical CV values amongst similar landscapes, leaving differences in accumulation

patterns primarily a function of $\overline{SWE}$ only. This makes the framework easily and more reliably transportable – a key advantage for extending modelling applications beyond well-studied research basins.

What is truly unique and novel with this framework is that melt rate computations may be based on different SWE and initial snowpack state values over the distribution, in order to allow representation of local-scale differences in melt timing and rate due to the associated differences in warming and ripening, or overnight cooling and refreezing, under the same externally applied surface energetics. No previous models have included sub-grid representation of these effects on areal SCD, although it is known that they are important for an initially sub-freezing and heterogeneous snowcover. Rather, this has only been possible in the past through the use of fully distributed simulations. Therefore, the theoretical framework developed here captures, in a spatially and computationally simple way, an essential characteristic that applies to all "cold" snowcovers; in the North American context, this is expected to be relevant from the northern U.S. Rockies and central plains to Alaska and the Arctic, becoming increasingly important northward.

The second and third thesis objectives were concerned with applying the framework to a test basin (Upper Middle Creek Basin) to determine how the combined variability in pre-melt SWE and spring melt rates affect the generation of snowmelt runoff. These were addressed throughout Sections Five and Six of the thesis. First, the work in Section Five on point-scale snowmelt modelling helped to demonstrate the dominant terms in the snowmelt energy balance (i.e., radiative surface energy balance components). It revealed the differences in magnitude and timing of melt rates on slopes of different orientation and exposure due to spatial variation of this energy, and further, it provided insight, through simulation, on snowmelt variability due solely to differences in initial snowpack state. It was shown that although there are large differences in melt timing and rate amongst different slopes, due mainly to differences in shortwave radiation receipt (and already well-understood), at times such as the early spring, the differences due to snowpack state alone were of similar or greater magnitude than that due to slope effects. This is an important finding that suggests it is not physically realistic to simulate areal snowmelt over an initially cold and highly redistributed snowcover by basing melt rate computations on a single snowpack state and neglecting

differences in the internal energy content. Another important implication of the results obtained here is that the effects of joint melt rate and SWE variability cannot be parameterized in terms of a constant linear covariance term for the duration of snowmelt (e.g., obtained through statistical analysis), since melt rates, SWE, and the association between them are continuously changing over time.

The next section took this modelling further by applying the theoretical framework of Section Three for simulation of areal SCD over the test basin. First, the spatial variability in both pre-melt SWE and incident solar radiation were examined to gain insight on how to disaggregate the landscape and resolve the joint variability. The analyses showed that the SWE patterns over the landscape were well-described by the lognormal distribution, and that the CV values of both of SWE and potential solar radiation could be reduced by considering separate slope and aspect based landscape units. Subsequently, application of the theoretical framework showed that simulations of areal SCD were improved overall when SWE distributions and snowmelt energetics were separately accounted for, compared to using a basin-average SWE distribution and uniformly applied snowmelt energy. Nearly all of the improvement was due to representation of surface energy differences, as the SWE distributions on most slopes did not differ substantially from the basin-average distribution, and the predicted SCD curves did not appear overly sensitive to the precise values of CV. As the values of CV found at this site closely corresponded with those found for similar landscapes in other regions (e.g., Pomeroy et al., 1998; Clark et al., 2011), this suggests that the notion of transferring CV values from "representative" landscape types, together with a framework for areal SCD such as in this thesis, can provide a valuable approach for extending model applications across broader regional scales.

At times, including the early spring period, it was found that representation of the effects of inhomogeneous melt (i.e., melt differences due to internal energetics) is crucial for reliable model prediction of areal SCD. This effect causes an acceleration of the decline in SCA due to the earlier and more rapid melt of areas with a relatively shallow snowcover, which cannot be represented by basing snowmelt computations on deeper classes of SWE. In land surface and climatological applications, which require reliable

estimates of surface energy fluxes, the value of SCA may be more important overall than snowmelt rates themselves, and thus this effect in models should not be neglected.

Further, the results of the modelling helped to show how the variability in both pre-melt snowcover and spring melt rates affect the generation of meltwater inputs to the surface over the landscape. The combined variability controls the timing, location, extent, and duration of meltwater generating areas over the basin, with snowmelt inputs first being generated over thin snowcovers in areas with greater energy receipt. Meltwater production then occurs from deeper snow in these areas and shallow snow in areas with lower amounts of incident radiation at the surface. As melt occurs over a greater portion of a SWE distribution, and over the landscape, areal SCD acts to reduce the area for snowmelt runoff generation. Later, towards the end of the melt period, only isolated drifts and snow-filled gullies continue to provide meltwater in the alpine areas. The effects of spring snowfall events add further complexity to these patterns and restore the areal snowcover temporarily. This analysis helped to demonstrate the spatial and temporal complexity of the evolution of meltwater generation and surface inputs over the landscape, but it would be necessary to use a hydrological model of the full basin response to determine the influence of these patterns on the snowmelt hydrograph.

The final objective of this thesis, addressed in Section Seven, involved determining this influence by incorporating the spatial snowmelt framework within a hydrological model, which was adapted to this particular basin. The conceptual/process-based model was developed using CRHM, and helped to show the differential contributions to runoff from different parts of the alpine basin (including forested lower elevation slopes). Although the best results were generally achieved by representing separate SWE distributions amongst landscape units, with differentially applied snowmelt energetics, similar appearing hydrographs were produced from other representations of snowcover and snowmelt, and were attributed to the cancellation of various model errors. It was noted that the development and validation of the alpine snowmelt routines upward from the point-scale to the slope unit and basin scales provided support that the model was internally valid, or "correct", and that therefore, the only model approach that produced a realistic hydrograph for the "right reasons" was that which accounted for the true variability in snowcover and melt rates, as described earlier in the thesis. This

implies that by properly representing surface snowmelt processes in a model, other components of the model can be improved, and their parameter selection made more reliable, thereby making them more transferrable and useful for regional hydrology applications. Finally, it was observed that hydrograph simulation approaches using either inhomogeneous, or homogeneous snowmelt computations (i.e., over a given SWE distribution on a slope-based unit) produced very similar results, neither of which could be shown to be consistently better. Although representation of inhomogeneous melt was shown to be very important for successful prediction of areal SCD in early melt, it is less likely to influence the overall basin runoff in a significant way due to the effects of other processes involved in the transfer of water through the basin. Therefore, for applications in which all that is sought is the hydrograph, this feature can likely be neglected.

8.2 Future Research Directions

The work done in this thesis has made some important advancements in alpine snow hydrology, which lead to some related issues that warrant further studies and investigation. Some problems involve the application of similar modelling over broader regional sales and in other basins with different physiographic characteristics, as well as for different climate and landcover scenarios. Difficulties also exist in coupling the framework with physically based simulations of the over-winter development of the snowcover, and in using it for continuous modelling over the course of a year. These issues are briefly discussed here to conclude this thesis.

Improved water management and water security in western Canada will involve modelling of Rocky Mountain snowmelt runoff at regional scales. It may not yet be feasible to apply such a detailed approach as in this work across the entire alpine zone of this region, as the success here was largely due to having high quality data and local meteorological records. The sparse observational network in the high alpine environment across the Rockies is presently a major limitation for driving physically based simulations of snow accumulation and ablation dynamics (Pomeroy et al., 2009a). Sound predictions of changes in the hydrology require consideration of the scale dependencies and complex snow process interactions and dynamics, which cannot be realistically represented much

beyond scales of individual slopes. Sharp regional and elevational climate gradients are also important as these exert an influence on the snow processes, while ongoing and future changes in climate and surface cover may not occur uniformly over these gradients. A possible initial approach to bridge this local – regional scale gap could be to select a number of "representative" basins that can be considered to reflect the general physiographic and climatological characteristics across the gradients. These could then be the focus of more intensive modelling work using approaches similar to that applied in this thesis, and where various sensitivity analyses can be carried out. Also, these test basins could be used to gain further information that may directly inform modelling initiatives for the larger surrounding region (i.e., representative CV values, soil and landcover characteristics, etc.). The new theoretical approach developed here could then provide a tool to be applied at the regional scale (while still maintaining slope-based landscape stratification as an upper limit). However, over sufficiently large areas, further computational efficiency could be made by repeating certain classes of terrain and snowcover (e.g., north-facing, south-facing,… slopes; low,… high elevation; shallow,… deep SWE; etc.).

Modelling together with remote sensing techniques, utilizing snowcover products from MODIS (Hall et al., 2002; Hall and Riggs, 2007), for example, represents an important step forward for alpine snow modelling in remote regions. This tool can provide useful information on the spatial and temporal depletion of the snowcover as well as the pre-melt SWE distribution, which are essential variables for snowmelt runoff prediction. This approach is beginning to see more widespread use (e.g., Kuchment et al., 2010; Homan et al., 2011), and will no doubt continue to undergo refinement in future studies. The work in this thesis is important and can be of use as these tools are further developed. For example, consideration of spatially variable melt timing and rate must be accounted for when applying melt computations over even small scales in alpine terrain. Of particular significance are the effects of inhomogeneous melt due to internal energy differences over cold and redistributed snowcovers. As shown in Section 3.6 of this thesis, established methods for determining modified depletion curves early in the spring (e.g., Rango and Martinec, 1982; Martinec, 1985) or estimation of pre-melt SWE distributions might be modified for handling such variation in melt timing and rate.

Simulations for climate and land use sensitivity analyses need to focus not only on changes in mean conditions, but on the projected extremes and the effects of changes in system behavior and coupled climate–vegetation responses. Of significance to alpine snow hydrology are warmer winter and spring air temperatures, potential increases in the amount and variability of winter precipitation, and shifts in the altitude or extent of treeline and alpine tundra ecozones. This could lead to increased frequency and magnitude of mid-winter melt events, earlier runoff timing in spring, and greater risk of flooding or drought. Analyses should be directed towards characterizing such extremes and investigating the hydrological response under changed surface conditions, which require physical approaches for representing snow–climate–vegetation dynamics. An improved understanding of accumulation and melt processes in key source areas of the alpine environment is therefore necessary. For example, within treeline stands of alpine larch and spruce, snow accumulation patterns are affected by wind-blown snow from alpine tundra and reduced interception losses for larch trees (e.g., Fisera, 1977). Small scale variability in melt energetics may result from increased net radiation near trees, where more complex relationships between melt rates and SWE may exist (Faria et al., 2001; Pomeroy et al. 2009b). The approach developed and applied in this work may not be ideally suited for simulating snowmelt dynamics in such areas, and further work should investigate how to effectively link process representations over the transition from alpine tundra to sub-alpine forest. Further, exposed alpine shrubs and krummholz vegetation beyond treeline significantly affect blowing snow redistribution and accumulation. Representing hydrological changes due to changes in the pattern and variability of the alpine snowcover requires explicit consideration of blowing snow, and linking this to a spatial snowmelt and SCD framework such as in this thesis.

In this environment, snow accumulation and snowmelt processes cannot be considered independently as winter and springtime phenomena. Applying this framework during the winter is important for investigating mid-winter melt events, while linking it with overwinter representation of the spatial–temporal snowcover development is important to avoid relying on model initialization near the end of winter. Blowing snow redistribution and sublimation are among the most important processes during and after snowfall events, which can occur at any time of year. Recent work by MacDonald

et al. (2010) has shown how physically based simulation of alpine blowing snow can yield reasonable predictions of mean snow accumulation over slope-based HRUs. This work might be extended in some ways to be better coupled with the areal SCD and snowmelt runoff framework here. For example, it would be useful to be able build up a distribution of SWE on a given landscape unit during the winter by assigning differential accumulation rates to different SWE/area classes, and/or redistributing snow amongst classes. A potential approach might involve basing the area of separate SWE bins on some characteristic value of CV that can be defined over a landscape unit, and adjusting inputs and redistribution according to the ratio of $SWE/\overline{SWE}$ for that part of the distribution, scaled by the probability of occurrence of blowing snow (e.g., Li and Pomeroy, 1997b). This would allow for the dynamic behavior of snow redistribution in relation to meteorology and snow conditions rather than a static drift multiplier approach as in previous studies. It also allows for the development over time of a distribution that approximates the lognormal or other parametric form of the frequency distribution. Finally, no work has previously considered sub-landscape unit areal SCD due to blowing snow and wind-scouring, although this is common in windswept alpine terrain such as Upper Middle Creek Basin. The approach to redistribute SWE amongst different classes or bins may be able to account for this. Further study is necessary to explore some of the conceptual and physical details of how such an approach could be implemented.

REFERENCES

Abbott, M.B., Bathurst, J.C., Cunge, J.A., O'Connell, P.E. and Rasmussen, J., 1986. An introduction to the European hydrologic system – système hydrologique Européen, ''SHE'', 1: history and philosophy of a physically based, distributed modelling system. *Journal of Hydrology*, **87**, 45–59.

Akyurek, Z., Surer, S., and Beser, Ö., 2011. Investigation of the snow-cover dynamics in the Upper Euphrates Basin of Turkey using remotely sensed snow-cover products and hydrometeorological data. *Hydrological Processes*, **25**, 3637–3648.

Alfnes, E., Andreassen, L.M., Engeset, R.V., Skaugen, T., and Undæs, H.C., 2004. Temporal variability in snow distribution. *Annals of Glaciology*, **38**, 101–105.

Anderson, E.A., 1968. Development and testing of snow pack energy balance equations. *Water Resources Research*, **4**, 19–37.

Anderson, E.A., 1973. *National Weather Service River Forecast System – Snow Accumulation and Ablation Model*, NOAA Technical Memorandum, NWS-HYDRO-17, U.S. Department of Commerce.

Anderson, E.A., 1976. *A Point Energy and Mass Balance Model of a Snow Cover*. NOAA Technical Report, NWS 19, U.S. Department of Commerce.

Anderton, S.P., White, S.M., and Alvera, B., 2002. Micro-scale spatial variability and the timing of snow melt runoff in a high mountain catchment, *Journal of Hydrology*, **268**, 158–176.

Anderton, S.P., White, S.M., and Alvera, B., 2004. Evaluation of spatial variability in snow water equivalent for a high mountain catchment. *Hydrological Processes*, **18**, 435–453.

Ayers, H.D., 1959. Influence of soil profile and vegetation characteristics on net rainfall supply to runoff. In: *Proceedings of Hydrology Symposium No. 1: Spillway Design Floods*, NRCC, Ottawa, 198–205.

Bales, R.C., Molotoch, N.P., Painter, T.H., Dettinger, M.D., Rice, R., and Dozier, J., 2006. Mountain hydrology of the western United States. *Water Resources Research*, **42**, doi:10.1029/2005WR004387.

Barnett, T.P., Adam, J.C., Lettenmaier, D.P, 2005. Potential impacts of a warming climate on water availability in snow-dominated regions. *Nature*, **438**, doi: 10.1038/ nature04141.

Barnett, T.P., Pierce, D.W., Hidalgo, H.G., Bonfils, C., Santer, B.D., Das, T., Bala, G., Wood, A.W., Nozawa, T., Mirin, A.A., Cayan, D.R., and Dettinger, M.D., 2008. Human-induced changes in the hydrology of the western united states. *Science*, **319**, 1080–1083.

Barry, R.G., 2008. *Mountain Weather and Climate*. 3rd Edition, Cambridge University Press, New York, NY, 506 p.

Bartelt, P. and Lehning, M., 2002. A physical SNOWPACK model for avalanche warning services – Part I: numerical model, *Cold Regions Science and Technology*, **35**, 123–145.

Beke, G.J., 1969. Soils of three experimental watersheds in Alberta and their hydrologic significance. PhD thesis, University of Alberta, Edmonton, 456 pp.

Beniston, M., 2003. Climatic change in mountain regions: A review of possible impacts. *Climatic Change*, 59, 5–31.

Beven, K.J., 1989. Changing ideas in hydrology – the case of physically-based models. *Journal of Hydrology*, **105**, 157–172.

Beven, K.J., and Binley, A.M., 1992. The future of distributed models: model calibration and uncertainty in prediction. *Hydrological Processes*, **6**, 279–298.

Billings, W.D., 1969. Vegetational patterns near alpine timberline as affected by fire-snowdrift interaction. *Vegetatio*, **19**, 192–207.

Blöschl, G., 1999. Scaling issues in snow hydrology. *Hydrological Processes*, **13**, 2149–2175.

Blöschl, G., 2005. Statistical upscaling and downscaling in hydrology. In: *Encyclopedia of Hydrological Sciences*, Anderson, M.G. (ed.), John Wiley and Sons: Chichester, Article 9, 2061–2080.

Blöschl, G., and Kirnbauer, R., 1992. An anlaysis of snow cover patterns in a small alpine catchment. *Hydrological Processes*, **6**, 99–109.

Blöschl, G., Kirnbauer, R., and Gutknecht, D., 1991. A spatially distributed snowmelt model for application in alpine terrain. In: *Bergmann, H., Lang, H., Frey, W., Issler, D., and Salm, B. (eds.), Snow, Hydrology and Forests in High Alpine Areas*, IAHS Publication No. 205, 51–60.

Blöschl, G., and Sivapalan, M., 1995. Scale issues in hydrological modelling: A review. *Hydrological Processes*, **9**, 251–290.

Brown, R.D., and Goodison, B.E., 2005. Snow cover. In: *Anderson, M.G., and McDonnell, J.J. (eds.), Encyclopedia of Hydrological Sciences*, John Wiley & Sons Ltd., Chichester, West Sussex, UK, 2463–2474.

Brubaker, K.L., and Menoes, M., 2001. A technique to estimate snow depletion curves from time-series data using the beta distribution. In: *Proceedings of the 58th Eastern Snow Conference*, **58**, 343–346.

Brun, E., David, P., Sudul, M., and Brunot, G., 1992. A numerical model to simulate snow-cover stratigraphy for operational avalanche forecasting. *Journal of Glaciology*, **38**, 13– 22.

Brun, E., Martin, E., Simon, V., Gendre, C. and Coleau, C., 1989. An energy and mass balance model of snow cover suitable for operational avalanche forecasting, *Journal of Glaciology*, **35**, 333–342.

Brun, E., Yang, Z.L., Essery, R.H., and Cohen, J., 2008. Snow-cover parameterization and modeling. In: *Armstrong, R.L., and Brun, E. (eds.), Snow and Climate: Physical Processes, Surface Energy Exchange, and Modeling*. Cambridge University Press, Cambridge, UK, 125–180.

Brutsaert, W., 2005. *Hydrology – an introduction*. Cambridge University Press, Canbridge, UK., 605 p.

Budd, W.F., 1966, The Drifting of Non-uniform Snow Particles, In: *Rubin, M. (ed.), Studies in Antarctic Meteorology*, American Geophysical Union, Antarctic Research Series, **9**, 59–70.

Budd, W.F., Dingle, R., and Radok, U., 1966. The Byrd Snow Drift Project: Outline and Basic Results, In: *Rubin, M. (ed.), Studies in Antarctic Meteorology*, American Geophysical Union, Antarctic Research Series, **9**, 71–134.

Carey, S.K., and DeBeer, C.M., 2008. Rainfall–runoff hydrograph characteristics in a discontinuous permafrost watershed and their relation to ground thaw. In: *Kane, D.L., and Hinkel, K.M., eds., Proceedings of the ninth International Conference on Permafrost*, University of Alaska, Fairbanks, 233–238.

Carey, S.K., and Woo, M., 1998. Snowmelt hydrology of two subarctic slopes, Southern Yukon, Canada. *Nordic Hydrology*, **29**, 331–346.

Cayan, D.R., Kammerdiener, S.A., Dettinger, M.D., Caprio, J.M., and Peterson, D.H., 2001. Changes in the onset of spring in the western United States. *Bulletin of the American Meteorological Society*, **82**, 399–415.

Chow, V.T., 1954. The log-probability law and its engineering applications. *Proceedings of the American Society of Civil Engineers*, **80**, 1–25.

Clark, C.O., 1945. Storage and the unit hydrograph. *Proceedings of the American Society of Civil Engineering*, **69**, 1419–1447.

Clark, M.P, Hendrikx, J., Slater, A.G., Kavetski, D., Anderson, B., Cullen, N.J., Kerr, T., Hreinsson, E.Ö., and Woods, R.A., 2011. Representing spatial variability of snow water equivalent in hydrologic and land-surface models: A review. *Water Resources Research*, **47**, doi: 10.1029/2011WR010745.

Cline, D.W., 1992. Modeling the redistribution of snow in alpine areas using geographical information processing techniques. In: *Ferrick, M. (ed.), Proceedings of the 1992 Eastern Snow Conference*, 13–24.

Cline, D., Elder, K., and Bales, R., 1998. Scale effects in a distributed snow water equivalence and snowmelt model for mountain basins. *Hydrological Processes*, **12**, 1527–1536.

Clow, D.W., Schrott, L., Webb, R., Campbell, D.H., Torizzo, A., and Dorblaser, M., 2003. Ground water occurence and contributions to streamflow in an alpine catchment, Colorado Front range, *Ground Water*, **41**, 937–950.

Colbeck, S.C., 1972. A theory of water percolation in snow. *Journal of Glaciology*, **11**, 369–385.

Colbeck, S.C., 1987. A review of the metamorphism and classification of seasonal snow cover crystals. In: *Salm, B., and Gubler, H. (eds.), Avalanche Formation, Movement and Effects*, IAHS Publication No. 162, 3–34.

Colbeck, S.C., and Davidson, G, 1973. Water percolation through homogeneous snow. In: *The role of Snow and Ice in Hydrology: Proceedings of the Banff Symposia*, Sept 1972, Unesco-WMO-IAHS, Geneva-Budapest-Paris, pp. 242–257.

Comeau, L., 2009. *Glacier contribution to the North and South Saskatchewan Rivers*. Unpublished MSc. Thesis. Department of Geography, University of Saskatchewan, Saskatoon, 222 p.

Corripio, J.G., 2003. Vectorial algebra algorithms for calculating terrain parameters from DEMs and solar radiation modelling in mountainous terrain. *International Journal of Geographic Information Science*, **17**, 1–23.

Corripio, J.G., 2004. Snow surface albedo estimation using terrestrial photography. *International Journal of Remote Sensing*, **25**, 5705–5729.

Dadic, R., Mott, R., Lehning, M., and Burlando, P., 2010. Wind influence on snow depth distribution and accumulation over glaciers. *Journal of Geophysical Research*, **115**, doi:10.1029/2009JF001261.

Davison, B., 2003. *Snow accumulation in a distributed hydrological model*. MSc Thesis, University of Waterloo, 124 p.

Davison, B., Pohl, S., Dornes, P., Marsh, P., Pietroniro, A., and MacKay, M., 2006. Characterizing snowmelt variability in a land-surface-hydrologic model. *Atmosphere–Ocean*, **44**, 271–287.

de Scally, F.A., 1996. Avalanche snow melting and summer streamflow differences between high-elevation basins, Cascade Mountains, British Columbia, Canada. *Arctic and Alpine Research*, **17**, 14–23.

DeBeer, C.M., and Pomeroy, J.W., 2009. Modelling snow melt and snowcover depletion in a small alpine cirque, Canadian Rocky Mountains. *Hydrological Processes*, **23**, 2584–2599.

DeBeer, C.M., and Pomeroy, J.W., 2010. Simulation of the snowmelt runoff contributing area in a small alpine basin. *Hydrology and Earth System Sciences*, **14**, 1205–1219.

Deems, J.S., Fassnacht, S.R., and Elder, K.J., 2006. Fractal distribution of snow depth from lidar data. *Journal of Hydrometeorology*, **7**, 285–297.

Deems, J.S., Fassnacht, S.R., and Elder, K.J., 2008. Interannual consistency in fractal snow depth patterns at two Colorado mountain sites. *Journal of Hydrometeorology*, **9**, 977–988.

Doekson, N.J., and Judson, A., 1997. *The SNOW booklet: A guide to the Science, Climatology and Measurement of Snow in the Unites States*. Colorado State University, Fort Collins, CO, 86 p.

Donald, J.R., Soulis, E.D., Kouwen, N., and Pietroniro, A., 1995. A land-cover based snow cover representation for distributed hydrologic models. *Water Resources Research*, **31**, 995–1009.

Dornes, P.F., Pomeroy, J.W., Pietroniro, A., Carey, S.K., and Quinton, W.L., 2008a. Influence of landscape aggregation in modelling snow-cover ablation and snowmelt runoff in a sub-arctic mountainous environment. *Hydrological Sciences Journal*, **53**, 725–740.

Dornes, P., Pomeroy, J.W., Pietroniro, A., and Verseghy, D.L., 2008b. Effects of spatial aggregation of initial conditions and forcing data on modeling snowmelt using a land surface scheme. *Journal of Hydrometeorology*, **9**, 789–803.

Dozier, J., 1980. A clear sky spectral solar radiation model for snow covered mountainous terrain. *Water Resources Research*, **16**, 709–718.

Dozier, J., and Painter, T.H., 2004. Multispectral and hyperspectral remote sensing of alpine snow properties. *Annual Reviews of Earth and Planetary Science*, **32**, 465–494.

Dyunin, A.K., 1959. *Fundamentals of the theory of snow drifting* Izvest. Sibirsk, Otdel. Akad. Nauk. USSR. No. 12, 11–24 [English translation by Belkov, G., National Research Council, Ottawa, Technical Translation, 952, 1961].

Dyunin, A.K., 1967. Fundamentals of the mechanics of snow storms. In: *ôura H., (ed.), Physics of Snow and Ice*, Vol. I, part 2, Institute of Low Temperature Science, Sapporo, Japan, pp. 1065–1073.

Egli, L., and Jonas, T., 2009. Hysteretic dynamics of seasonal snow depth distribution in the Swiss Alps. *Geophysical Research Letters*, **36**, doi:10.1029/2008GL035545.

Egli, L., Jonas, T., Grünewald, T., Schirmer, M., and Burlando, P., 2011. Dynamics of snow ablation in a small Alpine catchment observed by repeated terrestrial laser scans. *Hydrological Processes*, article published online, doi: 10.1002/hyp.8244.

Elder, K., Dozier, J., and Michaelsen, J., 1989. Spatial and temporal variation of net snow accumulation in a small alpine watershed, Emerald Lake Basin, Sierra Nevada, California, USA. *Annals of Glaciology*, **13**, 56–63.

Elder, K. Dozier, J., and Michaelsen, J., 1991. Snow accumulation and distribution in an alpine watershed. *Water Resources Research*, **27**, 1541–1552.

Elder, K., Rosenthal, W., and Davis, R.E., 1998. Estimating the spatial distribution of snow water equivalence in a montane watershed. *Hydrological Processes*, **12**, 1793–1808.

Ellis, C.R., Pomeroy, J.W., Brown, T., and MacDonald, J., 2010. Simulation of snow accumulation and melt in needleleaf forest environments. *Hydrology and Earth System Sciences*, **14**, 925–940.

Erxleben, J., Elder, K., and Davis, R., 2002. Comparison of spatial interpolation methods for estimating snow distribution in the Colorado Rocky Mountains. *Hydrological Processes*, **16**, 3627–3649.

Essery, R.H., 1999. Parametrization of heterogeneous snowmelt. *Theoretical and Applied Climatology*, **62**, 25–30.

Essery, R.H., and Etchevers, P., 2004. Parameter sensitivity in simulations of snowmelt. *Journal of Geophysical Research*, **109**, D20111.DOI: 10.1029/2004JD005036.

Essery, R.H., and Pomeroy, J.W., 2004a. Vegetation and topographic control of wind-blown snow distributions in distributed and aggregated simulations for an arctic tundra basin. *Journal of Hydrometeorology*, **5**, 735–744.

Essery, R.H., and Pomeroy, J.W., 2004b. Implications of spatial distributions of snow mass and melt rate for snow-cover depletion: theoretical considerations. *Annals of Glaciology*, **38**, 261–265.

Essery, R.H., Rutter, N., Pomeroy, J.W., Baxter, R., Stähli, M., Gustafsson, D., Barr, A., Bartlett, P., and Elder, K., 2009. SNOWMIP2: An evaluation of forest snow process simulations. *Bulletin of the American Meteorological Society*, **90**, 1120–1135.

Etchevers, P., Martin, E., Brown, R., Fierz, C., Lejeune, Y., Bazile, E., Boone, A., Dai, Y.J., Essery, R., Fernandez, A., Gusev, Y., Jordan, R., Koren, V., Kowalczyk, E., Nasonova, N.O., Pyles, R.D., Schlosser, A., Shmakin, A.B., Smirnova, T.G., Strasser, U., Verseghy, D., Yamazaki, T., and Yang, Z.L., 2004. Validation of the energy-budget of an alpine snowpack simulated by several snow models (SnowMIP project), *Annals of Glaciology*, **38**, 150–158.

Faria, D.A., Pomeroy, J.W., and Essery, R.H., 2000. Effect of covariance between ablation and snow water equivalent on depletion of snow-covered area in a forest. *Hydrological Processes*, **14**, 2683–2695.

Farinotti, D., Magnusson, J., Huss, and Bauder, A., 2010. Snow accumulation distribution inferred from time-lapse photography and simple modelling. *Hydrological Processes*, **24**, 2087–2097.

Fierz, C., Plüss, C, and Martin, E., 1997. Modelling the snow cover in a complex alpine topography, *Annals of Glaciology*, **25**, 312–316.

Fierz, C., Riber, P., Adams, E.E., Curran, A.R., Föhn, P.M.B, Lehning, M., and Plüss, C., 2003. Evaluation of snow-surface energy balance models in alpine terrain, *Journal of Hydrology*, **282**, 76–94.

Fisera, Z., 1977. Snow accumulation and melt pattern in tree line stands of Marmot Creek Basin. In: *Swanson, R.H., and Logan, P.A., (eds.), Alberta Watershed Research Program Symposium Proceedings, 1977*, Northern Forest Research Centre, Edmonton, AB, Report NOR-X-176, 97–109.

Föhn, P.M.B., and Meister, R., 1983. Distribution of snow drifts on ridge slopes: measurements and theoretical approximations. *Annals of Glaciology*, **4**, 52–57.

Freeze, R.A., and Harlan, R.L., 1969. Blueprint for a physically-based, digitally-simulated hydrologic response model. *Journal of Hydrology*, **9**, 237–258.

Garnier, B.J., and Ohmura, A., 1970. The evaluation of surface variations in solar radiation income. *Solar Energy*, **13**, 21–34.

Giorgi, F., and Bi, X., 2005. Regional changes in surface climate interannual variability for the 21st century from ensembles of global model simulations. *Geophysical Research Letters*, **32**, doi:10.1029/2005GL023002.

Golding, D.L., and Swanson, R.H., 1986. Snow distribution patterns in clearings and adjacent forest. *Water Resources Research*, **22**, 1931–1940.

Goodison, B.E., 1978. Accuracy of canadian snow gauge measurements. *Journal of Applied Meteorology*, **27**, 1542–1548.

Goodison, B.E., Ferguson, H.L., and MacKay, G.A., 1981. Measurement and Data Analysis. In: *Gray, D.M., and Male, D.H. (eds.), Handbook of Snow: Principles, Processes, Management & Use*. Pergamon Press, Toronto, ON, Chapter 6, 191–274.

Granger, R.J., and Gray, DM., 1989. Evaporation from natural non-saturated surfaces. *Journal of Hydrology*, **111**, 21–29.

Granger, R.J., and Pomeroy, J.W., 1997. Sustainability of the western Canadian boreal forest under changing hydrological conditions – 2-summer energy and water use. In: *Rosjberg, D., Boutayeb, N., Gustard, A., Kundzewicz, Z., and Rasmussen, P. (eds)*, *Sustainability of Water Resources under Increasing Uncertainty*, IAHS Publication No. 240., IAHS Press, Wallingford, 243–250.

Gray, D.M., 1979. Snow accumulation and distribution. In: *Colbeck, S.C., and Ray, M., (eds.), Proceedings of a Meeting on Modeling of Snow Cover Runoff*, Hanover, NH., U.S. Army Cold Regions Research and Engineering Laboratory, 3–33.

Gray, D.M., and Landine, P.G., 1988. An energy-budget snowmelt model for the Canadian Prairies. *Canadian Journal of Earth Sciences*, **25**, 1292–1303.

Gray, D.M., and O′Neill, A.J., 1974. Application of the energy budget for predicting snowmelt runoff, In: *Santeford, H.S., and Smith, J.L., (eds.), Advanced Concepts in Technical Study of Snow and Ice Resources*, U.S. National Academy of Sciences, Washington, D.C., 108–118.

Gray, D.M., Norum, D.I., and Dyck, G.E., 1970. Densities of prairie snowpacks. *Proceedings of the 38th Annual Meeting Western Snow Conference*, Victoria, BC, 24–30.

Gray, D.M., and Prowse, T. 1993. Snow and floating ice. In: *Maidment D.R. (ed.), Handbook of Hydrology*, McGraw-Hill Inc., New York, NY, 7.1–7.58.

Gray, D.M., Steppuhn, H.W., and Abbey, F.L., 1979. Estimating the areal snow water equivalent in the Prairie environment. In: *Proceedings of Canadian Hydrology Symposium: 79 – Cold Climate Hydrology*, Associate Committee on Hydrology, National Research Council of Canada, Ottawa, ON, 302–322.

Gray, D.M., Toth, B., Pomeroy, J.W., Zhao, L., and Granger, R.J., 2001. Estimating areal snowmelt infiltration into frozen soils. *Hydrological Processes*, **15**, 3095–3111.

Grayson, R., and Blöschl, G., 2000. Spatial modelling of catchment dynamics. In: *Grayson, R., and Blöschl, G., (eds.), Spatial Patterns in Catchment Hydrology*, Cambridge University Press, Cambridge, UK, 51–81.

Groot Zwaaftink, C.D., and Lehning, M., 2010. Sublimation of drifting snow in an Alpine catchment. Extended abstracts, 14th Conference on Mountain Meteorology, Lake Tahoe Vicinity, USA, American Meteorological Society, Paper 8.3.

Grünewald, T., Schirmer, M., Mott, R., and Lehning, M., 2010. Spatial and temporal variability of snow depth and ablation rates in a small mountain catchment. *The Cryosphere*, **4**, 215–225.

Gumbel, E.J., 1954. *Statistical theory of extremes and some practical applications*. U.S. National Bureau of Standards Applied Mathematics Series 33, U.S. Govt. Printing Office, Washington, D.C.

Gupta, H.V., Beven, K.J., and Wagener, T., 2005. Model calibration and uncertainty estimation. In: *Anderson, M.G., and McDonnell, J.J. (eds.), Encyclopedia of Hydrological Sciences*, John Wiley & Sons Ltd., Chichester, West Sussex, UK, 2015–2031.

Haegeli, P., and McClung, D.M., 2007. Expanding the snow-climate classification with avalanche-relevant information: initial description of avalanche winter regimes for southwestern Canada. *Journal of Glaciology*, **53**, 266–276.

Hall, D.K., and Martinec, J., 1985. *Remote Sensing of ice and snow*. Chapman and Hall Ltd., London, 189 p.

Hall, D.K., and Riggs, G.A., 2007. Accuracy assessment of the MODIS snow products. *Hydrological Processes*, **21**, 1534–1547.

Hall, D.K., Riggs, G.A., Salomonson, V.V., DiGirolamo, N.E., and Bayr, K.J., 2002. MODIS snow-cover products. *Remote Sensing of Environment*, **83**, 181–194.

Hamlet, A.F., Mote, P.W., Clark, M.P., and Lettenmaier, D.P., 2007. Twentieth-century trends in runoff, evapotranspiration, and soil moisture in the western United States. *Journal of Climate*, **20**, 1468–1486.

Harding, R.J., 1986. Exchanges of energy and mass associated with a melting snow pack. In: *Morris, E.M., (ed.), Modelling Snowmelt-Induced Processes*, IAHS Publication No. 155, IAHS Press, Wallingford, 3–15.

Harding, R.J., and Pomeroy, J.W., 1996. The energy balance of the winter boreal landscape. *Journal of Climate*, **9**, 2778–2787.

Hardy, J.P., Davis, R.E., Jordan, R., Li, X., Woodcock, C.E., Ni, W., and McKenzie, J.C., 1997. Snow ablation modeling at the stand scale in a boreal jack pine forest. *Journal of Geophysical Research*, **102**, 29,397–29,405.

Hauer, F.R., Baron, J.S., Campbell, D.H., Fausch, K.D., Hostetler, S.W., Leavesley, G.H., Leavitt, P.R., McKnight, D.M., and Stanford, J.A., 1997. Assessment of

climate change and freshwater ecosystems of the Rocky Mountains, USA and Canada. *Hydrological Processes*, **11,** 903–924.

Hedstrom, N.R., and Pomeroy, J.W., 1998. Accumulation of intercepted snow in the boreal forest: measurements and modelling. *Hydrological Processes*, **12**, 1611–1623.

Helgason, W.D., 2009. *Energy fluxes at the air–snow interface*. PhD thesis, University of Saskatchewan, Saskatoon, 171 p.

Hiemstra, C.A., Liston, G.E., and Reiners, W.A., 2002. Snow redistribution by wind and interactions with vegetation at upper treeline in the Medicine Bow Mountains, Wyoming, U.S.A. *Arctic, Antarctic, and Alpine Research*, **34**, 262–273.

Hiemstra, C.A., Liston, G.E., and Reiners, W.A., 2006. Observing, modelling, and validating snow redistribution by wind in a Wyoming upper treeline landscape. *Ecological Modelling*, **197**, 35–51.

Hinzman, L.D., and Kane, D.L., 1991. Snow hydrology of a headwater Arctic basin 2. Conceptual analysis and computer modeling. *Water Resources Research*, **27**, 1111–1121.

Hock, R., 2003. Temperature index modeling in mountain areas, *Journal of Hydrology*, **282**, 104–115.

Homan, J.W., Luce, C.H., McNamara, J.P., and Glenn, N.F., 2011. Improvement of distributed snowmelt energy balance modeling with MODIS-based NDSI-derived fractional snow-covered area data. *Hydrological Processes*, **25**, 650–660.

Hood, J.L., and Hayashi, M., 2010. Assessing the application of a laser rangefinder for determining snow depth in inaccessible alpine terrain. *Hydrology and Earth System Sciences*, **14**, 901–910.

Hood, J.L., Roy, J.W., and Hayashi, M., 2006. Importance of groundwater in the water balance of an alpine headwater lake. *Geophysical Research Letters*, **33**, L13405, doi:10.1029/2006GL026611.

Horne, F.E., and Kavvas, M.L., 1997. Physics of the spatially averaged snowmelt process. *Journal of Hydrology*, **191**, 179–207.

Janowicz, J.R., Gray, D.M., and Pomeroy, J.W., 2003. Spatial variability of fall soil moisture and spring snow water equivalent within a mountainous sub-arctic watershed. In: *Proceedings of the 60th Eastern Snow Conference*, Sherbrooke, Quebec, 127–139.

Jordan, R.E., 1991. *A one-dimensional temperature model for a snow cover*. U.S. Army Corps of Engineers, Cold Regions Research and Engineering Laboratory, Special Report 91-16.

Jordan, R.E., Albert, M.R., and Brun, E., 2008. Physical processes within the snow cover and their parameterization. In: *Armstrong, R.L., and Brun, E. (eds.), Snow and Climate: Physical Processes, Surface Energy Exchange, and Modeling*. Cambridge University Press, Cambridge, UK, 12–69.

Jordan, R.E., Andreas, E.L., and Makshtas, A.P., 1999. Heat budget of snow-covered sea ice at North Pole 4. *Journal of Geophysical Research*, **104**, 7785–7806.

Kampf, S.K., and Burges, S.J., 2007. A framework for classifying and comparing distributed hillslope and catchment hydrologic models. *Water Resources Research*, **43**, doi:10.1029/WR005370.

Kampf, S.K., Richer, E.E., and Moore, C.C., 2010. A scaling hierarchy for hydrologic response to snowmelt in mountain basins. American Geophysical Union, Fall Meeting 2010, abstract # H14B-07.

Kaufman, Y.J., Kleidman, R.G., Hall, D.K., Martins, J.V., and Barton, J.S., 2002. Remote sensing of subpixel snow cover using 0.66 and 2.1 μm channels. *Geophysical Research Letters*, **29**, DOI:10.1029/2001GL013580.

Killingtveit Å., and Sand, K., 1991. On areal distribution of snowcover in a mountainous area. In: *Prowse, T.D., and Ommanney, C.S.L., (eds.), Northern Hydrology: Selected Perspectives*, NHRI Symposium No. 6. National Hydrology Research Institute, Environment Canada, Saskatoon, SK, 189–204.

King, J.C., Pomeroy, J.W., Gray, D.M., Fierz, C., Föhn, P.M.B., Harding, R.J., Jordan, R.E., Martin, E., and Plüss, C., 2005. Snow–atmosphere energy and mass balance. In: *Armstrong, R.L., and Brun, E. (eds.), Snow and Climate: Physical Processes, Surface Energy Exchange, and Modeling*. Cambridge University Press, Cambridge, UK, 70–124.

Kirnbauer, R., Blöschl, G., Waldhäusl, P., and Hochstöger, 1991. An analysis of snow cover patterns as derived from oblique aerial photographs. In: *Bergmann, H., Lang, H., Frey, W., Issler, D., and Salm, B. (eds.), Snow, Hydrology and Forests in High Alpine Areas*, IAHS Publication No. 205, 91–99.

König, M., Winther, J.G., and Isaksson, E., 2001. Measuring snow and glacier ice properties from satellite. *Reviews of Geophysics*, **39**, 1–27.

Kouwen, N., Soulis, E.D., Pietroniro, A., Donald, J., and Harrington, R.A., 1993. Grouped response units for distributed hydrological modeling. *Journal of Water Resources Planning and Management*, **119**, 289–305.

Kuchment, L.S., and Gelfan, A.N., 1996. The determination of the snowmelt rate and the meltwater outflow from a snowpack for modelling river runoff generation. *Journal of Hydrology*, **179**, 23–36.

Kuchment L.S., and Gelfan, A.N., 1997. Statistical self-similarity of spatial snow accumulation variations and its application to snowmelt runoff models. *Russian Meteorology and Hydrology*, **7,** 53–60.

Kuchment L.S., and Gelfan, A.N., 2001. Statistical self-similarity of spatial variations of snow cover: verification of the hypothesis and application in the snowmelt runoff generation models. *Hydrological Processes*, **15**, 3343–3355.

Kuchment, L.S., Romanov, P., Gelfan, A.N., and Demidov, V.N., 2010. Use of satellite-derived data for characterization of snow cover and simulation of snowmelt runoff through a distributed physically based model of runoff generation. *Hydrology and Earth System Sciences*, **14**, 339–350.

Kuz'min, P.P., 1961. Protsess tayaniya shezhnogo pokrova (Melting of Snow Cover). Gidrometeorol. Izd. Leningrad (English translation TT71-50095, *Israel Program of Scientific Translations Ltd*., Jerusalem, 1972, 47–59.

Langham, E.J., 1981. Physics and properties of snowcover. In: *Gray, D.M., and Male, D.H. (eds.), Handbook of Snow: Principles, Processes, Management & Use*. Pergamon Press, Toronto, ON, Chapter 7, 275–337.

Lapen, D.R., and Martz, L.W., 1996. An investigation of the spatial association between snow depth and topography in a Prairie agricultural landscape using digital terrain analysis. *Journal of Hydrology*, **184**, 277–298.

Leavesley, G.H. and Stannard, L.G., 1995. The precipitation-runoff modelling system – PRMS. Chapter 9 in: Singh, V. P. (Ed.), Computer Models of Watershed Hydrology. Water Resources Publications, Highlands Ranch, Colorado, pp.281–310.

Lehning, M., Grünewald, T., and Schirmer, M., 2011. Mountain snow distribution governed by an altitudinal gradient and terrain roughness. *Geophysical Research Letters*, **38**, doi:10.1029/2011GL048927.

Lehning, M., Löwe, H., Ryser, M., and Raderschall N., 2008. Inhomogeneous precipitation distribution and snow transport in steep terrain. *Water Resources Research*, **44**, doi:10.1029/2007WR006545.

Leydecker, A., Sickman, J.O., and Melack, J.M., 2001. Spatial scaling of hydrological and biogeochemical aspects of high-altitude catchments in the Sierra Nevada, California, U.S.A. *Arctic, Antarctic, and Alpine Research*, **33**, 391–396.

Li, L., and Pomeroy, J.W., 1997a. Estimates of threshold wind speeds for snow transport using meteorological data. *Journal of Applied Meteorology*, **36**, 205–213.

Li, L., and Pomeroy, J.W., 1997b. Probability of occurrence of blowing snow. *Journal of Geophysical Research*, **102**, 21,955–21, 964.

List, R.J., 1968. *Smithsonian Meteorological Tables*, 6th edition. The Smithsonian Institute, Washington, DC, 527 pp.

Liston, G.E., 1995. Local advection of momentum, heat, and moisture during the melt of patchy snow covers. *Journal of Applied Meteorology*, **34**, 1705–1715.

Liston, G.E., 1999. Interrelationships among snow distribution, snowmelt, and snow cover depletion: Implications for atmospheric, hydrologic, and ecologic modeling. *Journal of Applied Meteorology*, **38**, 1474–1487.

Liston, G.E., 2004. Representing subgrid snow cover heterogeneities in regional and global models. *Journal of Climate*, **17**, 1381–1395.

Liston G.E., and Sturm M., 1998. A snow-transport model for complex terrain. *Journal of Glaciology*, **44**, 498–516.

Liu, F., Williams, M.W., and Caine, N., 2004. Source waters and flow paths in an alpine catchment, Colorado Front Range, United States, *Water Resources Research*, **40**, W09401, doi:10.1029/2004WR003076.

Lott, F.C., and Lundquist, J.D., 2008. Modeling spatial differences in snowmelt runoff timing. In: *Proceedings of the 76th anuual Western Snow Conference*, Hood River Oregon, April 15-17, 2008, 91–97.

Lowry, C.S., Deems, J.S., Loheide, S.P., and Lundquist, J.D., 2010. Linking snowmelt-derived fluxes and groundwater flow in a high elevation meadow system, Sierra Nevada Mountains, California. *Hydrological Processes*, **24**, 2821–2833.

Luce, C.H., and Tarboton, D.G., 2004. The application of depletion curves for parameterization of subgrid variability of snow. *Hydrological Processes*, **18**, 1409–1422.

Luce, C.H., Tarboton, D.G., and Cooley, K.R., 1998. The influence of the spatial distribution of snow on basin-averaged snowmelt. *Hydrological Processes*, **12**, 1671–1683.

Luce, C.H., Tarboton, D.G., and Cooley, K.R., 1999. Sub-grid parameterization of snow distribution for an energy and mass balance snow cover model. *Hydrological Processes*, **13**, 1921–1933.

Lundquist, J., and Dettinger, M.D., 2005. How snowpack heterogeneity affects diurnal streamflow timing. *Water Resources Research*, **41**, doi:10.1029/2004WR003649.

Lundquist, J., Dettinger, M.D., and Cayan, D.R., 2005. Snow-fed streamflow timing at different basin scales: Case study of the Tuolumne River above Hetch Hetchy, Yosemite, California. *Water Resources Research*, **41**, doi:10.1029/2004 WR003933.

MacDonald, M.K., Pomeroy, J.W., and Pietroniro, A., 2010. On the importance of sublimation to an alpine snow mass balance in the Canadian Rocky Mountains. *Hydrology and Earth Systems Sciences*, **14**, 1401–1415.

Male, D.H., 1980. The Seasonal Snowcover. In: *Colbeck, S.C. (ed.), Dynamics of Snow and Ice Masses*. Academic Press, New York, NY, 305–395.

Male, D.H., and Granger, R.J., 1979. Energy and mass fluxes at the snow surface in a prairie environment. In: *Colbeck, S.C., and Ray, M. (eds.), Proceedings of the Modelling of Snow Cover Runoff*, U.S. Army Cold Regions Research and Engineering Laboratory, Hanover, NH, 101–124.

Male, D.H. and Gray, D.M., 1975. Problems in developing a physically based snowmelt model, *Canadian Journal of Civil Engineering*, **2**, 474–488.

Male, D.H., and Gray, D.M., 1981. Snowcover ablation and runoff. In: *Gray, D.M., and Male, D.H. (eds.), Handbook of Snow: Principles, Processes, Management & Use*. Pergamon Press, Toronto, ON, Chapter 9, 360–436.

Mandelbrot, B., 1983. *The fractal Geometry of Nature*. W.H. Freeman and Co. 468 p.

Marchand, W.D., and Killingtveit, Å., 2003. Statistical properties of spatial snowcover in mountainous catchments in Norway. *Nordic Hydrology*, **35**, 101–117.

Marks, D., Domingo, J., Susong, D., Link, T., and Garen, D., 1999. A spatially distributed energy balance snowmelt model for application in mountain basins. *Hydrological Processes*, **13**, 1935–1959.

Marks, D., and Dozier, J., 1992. Climate and energy exchange at the snow surface in the alpine region of the Sierra-Nevada: 2. Snow cover energy balance. *Water Resources Research*, **28**, 3043–3054.

Marks, D., Kimball, J., Tingey, D., and Link, T., 1998. The sensitivity of snowmelt processes to climate conditions and forest cover during rain-on-snow: a case study of the 1996 Pacific Northwest flood. *Hydrological Processes*, **12**, 1569–1587.

Marks, D., Reba, M., Pomeroy, J.W., Link, T., Winstral, A., Flerchinger, G., and Elder, K., 2008. Comparing simulated and measured sensible and latent heat fluxes over snow under a Pine canopy to improve and energy balance snowmelt model. *Journal of Hydrometeorology*, **9**, 1506–1522.

Marks, D., Winstral, A., and Seyfried, M., 2002. Simulation of terrain and forest shelter effects on patterns of snow deposition, snowmelt and runoff over a semi-arid mountain catchment. *Hydrological Processes*, **16**, 3605–3626.

Marsh, P., and Pomeroy, J.W., 1996. Meltwater fluxes at an Arctic forest-tundra site, *Hydrological Processes*, **10**, 1383–1400.

Marsh, P., Pomeroy, J.W., and Neumann, N., 1997. Sensible heat flux and local advection over a heterogeneous landscape at an Arctic tundra site during snowmelt. *Annals of Glaciology*, **25**, 132–136.

Marsh, P., and Woo, M.K., 1984. Wetting front advance and freezing of meltwater within a snow cover 1. Observations in the Canadian Arctic. *Water Resources Research*, **20**, 1853–1864.

Martinec, J., 1980. Limitations in hydrological interpretations of the snow coverage. *Nordic Hydrology*, **11**, 209–220.

Martinec, J., 1985. Snowmelt runoff models for operational forecasts. *Nordic Hydrology*, **16**, 129–136.

Martinec, J., and Rango, A., 1987. Interpretation and utilization of areal snow-cover data from satellites. *Annals of Glaciology*, **9**, 166–169.

Martinec, J., Rango, A., and Roberts, R., 1998. Snowmelt Runoff Model (SRM) user's manual. In: *Baumgartner, M.F., and Apfl, G.M., (eds.), Geographica Bernensia*, Series P, No. 35, Department of Geography, University of Berne, 84p.

Martz, L., Bruneau, J., and Rolfe T. (eds.), 2007. *Climate Change and Water – SSRB Final Technical Report*. University of Saskatchewan, Saskatoon, SK. 252 pp.

McClung, D., and Schaerer, P., 1993. *The Avalanche Handbook*. The Mountaineers: Seattle, 271 p.

McClymont, A.F., Hayashi, M., Bentley, L.R., Muir, D., and Ernst, E., 2010. Groundwater flow and storage within an alpine meadow-talus complex. *Hydrology and Earth System Sciences*, **14**, 859–872.

McFadden, J.P., Liston, G.E., Sturm, M., Pielke, R.A., and Chapin, F.S., 2001. Interactions of shrubs and snow in arctic tundra: measurements and models. In: *Dolman A.J., Hall, A.J., Kavvas, M.L., Oki, T., and Pomeroy, J.W. (eds.), Soil-Vegetation-Atmosphere Transfer Schemes and Large-Scale Hydrological Models*, IAHS Publication No. 270, 317–325.

McKay, G.A., 1970. Precipitation. In: *Gray, D.M. (ed.), Handbook on the Principles of Hydrology*, Water Information Center, Syoset, 2.1–2.111.

McKay, G.A., and Gray, D.M., 1981. The distribution of snowcover. In: *Gray, D.M., and Male, D.H. (eds.), Handbook of Snow: Principles, Processes, Management & Use*. Pergamon Press, Toronto, ON, Chapter 5, 153–190.

Meiman, J.R., 1970. Snow accumulation related to elevation, aspect and forest canopy. In: *Snow Hydrology – Proceedings of a Workshop Seminar 1968*, Canadian National Committee for the International Hydrological Decade, Queens Printer, Ottawa, ON, 35–47.

Miller, D.H., 1976. *Spatial interactions produced by meso-scale transports of water in the atmospheric boundary layer*. Paper presented to the Annual Meeting, Association of American Geographers, New York, NY, April 1976.

Mittaz, C., Imhof, M., Hoelze, M., and Haeberli, W., 2002. Snowmelt evolution mapping using an energy balance approach over an alpine terrain. *Arctic, Antarctic, and Alpine Research*, **34**, 274–281.

Molotch, N.P., 2009. Reconstructing snow water equivalent in the Rio Grande headwaters using remotely sensed snow cover data and a spatially distributed snowmelt model. *Hydrological Processes*, **23**, 1076–1089.

Moore, R.D., 1996. Snowpack and runoff responses to climatic variability, southern Coast Mountains, British Columbia. *Northwest Science*, **70**, 321–333.

Moore, R.J., Bell, V.A., Austin, R.M., and Harding, R.J., 1999. Methods for snowmelt forecasting in upland Britain. *Hydrology and Earth System Sciences*, **3**, 233–246.

Moore J.N., Harper, J.T., and Greenwood, M.C., 2007. Significance of trends toward earlier snowmelt runoff, Columbia and Missouri Basin headwaters, western United States. *Geophysical Research letters*, **34**, doi: 10.1029/2007/GL031022.

Moore, R.D., and McKendry, I.G., 1996. Spring snowpack anomaly patterns and winter climatic variability, British Columbia, Canada. *Water Resources Research*, **32**, 623–632.

Mote, P.W., Hamlet, A.F., Clark, M.P., and Lettenmaier, D.P., 2005. Declining mountain snowpack in western North America. *Bulletin of the American Meteorological Society*, **86**, 39–49.

Mott, R., Schirmer, M., Bavay, M., Grünewald, T., and Lehning, M., 2011. Understanding snow-transport processes shaping the mountain snow-cover. *The Crysophere*, **4**, 545–559.

Mott, R., Egli, L., Grünewald, T., Dawes, N., Manes, C., Bavay, M., and Lehning, M., 2011a. Micrometeorological processes driving snow ablation in an Alpine catchment. *The Cryosphere Discussions*, **5**, 2159–2196.

Mott, R., Schirmer, M., and Lehning, M., 2011b. Scaling properties of wind and snow depth distribution in an alpine catchment. *Journal of Geophysical Research*, **116**, doi:10.1029/2010JD014886.

Neumann, N., and Marsh, P., 1998. Local advection of sensible heat in the snowmelt landscape of Arctic tundra. *Hydrological Processes*, **12**, 1547–1560.

Norum, D.I., Gray, D.M., and Male, D.H., 1976. Melt of shallow prairie snowpacks: basis for a physical model. *Canadian Agricultural Engineering*, **18**, 2–6.

O'Neil, A.D.J., and Gray, D.M., 1973. Spatial and temporal variations of the albedo of a prairie snowpack. In: *The Role of Snow and Ice in Hydrology: Proceedings of the Banff Symposium*, Sept 1972, Vol. 1, UNESCO-WMO-IAHS, Geneva-Budapest-Paris, 176–186.

Olyphant, G.A., 1986. The components of incoming radiation within a mid-latitude alpine watershed during the snowmelt season. *Arctic and Alpine Research*, **18**, 163–169.

Painter, T.H., Rittger, K., McKenzie, C., Slaughter, P., Davis, R.E., and Dozier, J., 2009. Retrieval of subpixel snow covered area, grain size, and albedo from MODIS. *Remote Sensing of Environment*, **113**, 868–879.

Parajka, J., Haas, P., Kirnbauer, R., Jansa, J., and Blöschl, G., in press. Potential of time-lapse photography of snow for hydrological purposes at the small catchment scale. *Hydrological Processes*, accepted article, doi:10.1002/hyp.8389.

Parviainen, J., and Pomeroy, J.W., 2000. Multiple-scale modelling of forest snow sublimation, initial findings. *Hydrological Processes*, **14**, 2669–2681.

Perla, R.I., 1980. Avalanche release, motion, and impact. In: *Colbeck, S.C. (ed.), Dynamics of Snow and Ice Masses*. Academic Press, New York, NY, 397–462.

Pietroniro, A., and Soulis, E.D., 2003. A hydrology modeling framework for the Mackenzie GEWEX programme. *Hydrological Processes*, **17**, 673–676.

Plüss, C., and Ohmura, A., 1997. Longwave radiation on snow-covered mountainous surfaces. *Journal of Applied Meteorology*, **36**, 818–824.

Pohl, S., Davison, B., Marsh, P., and Pietroniro, A., 2005. Modelling spatially distributed snowmelt and meltwater runoff in a small arctic catchment with a hydrology land-surface scheme (WATCLASS). *Atmosphere–Ocean*, **43**, 193–211.

Pohl, S., and Marsh, P., 2006. Modelling the spatial–temporal variability of spring snowmelt in an arctic catchment. *Hydrological Processes*, **20**, 1773–1792.

Pohl, S., Marsh, P., and Liston, G.E., 2006. Spatial–temporal variability in turbulent fluxes during spring snowmelt. *Arctic, Antarctic, and Alpine Research*, **38**, 136–146.

Pomeroy, J.W., 1988. *Wind Transport of Snow*. PhD thesis, University of Saskatchewan, 226 p.

Pomeroy, J.W., 1989. A process-based model of snow drifting. *Annals of Glaciology*, **13**, 237–240.

Pomeroy J.W., 1991. Transport and sublimation of snow in wind-scoured alpine terrain. In: *Bergmann, H., Lang, H., Frey, W., Issler, D., and Salm, B. (eds.), Snow, Hydrology and Forests in High Alpine Areas*, IAHS Publication No. 205, 131–140.

Pomeroy, J.W., Bewley, D.S., Essery, R.H., Hedstrom, N.R., Link, T., Granger, R.J., Sicart, J.E., Ellis, C.R., and Janowicz, J.R., 2006. Shrub tundra snowmelt. *Hydrological Processes*, **20**, 923–941.

Pomeroy, J.W., and Brun, E., 2001. Physical properties of snow. In: *Jones, H.G., Pomeroy, J.W., Walker, D.A., and Hoham, R.W. (eds.), Snow Ecology – An Interdisciplinary Examination of Snow-Covered Ecosystems*, Cambridge University Press, Cambridge, UK, Chapter 2, 45–126.

Pomeroy, J.W., and Dion, K., 1996. Winter radiation extinction and reflection in a boreal pine canopy, measurements and modelling. *Hydrological Processes*, **10**, 1591–1608.

Pomeroy, J.W., Essery, R.H., and Toth, B., 2004. Implications of spatial distributions of snow mass and melt rate for snow-cover depletion: observations in a subarctic mountain catchment. *Annals of Glaciology*, **38**, 195–201.

Pomeroy, J.W., and Goodison, B.E., 1997. Winter and Snow. In: *Bailey, W.G., Oke, T.R., and Rouse, W.R., (eds.), The Surface Climates of Canada*. McGill-Queen's University Press, Montreal, QC, 68–100.

Pomeroy, J.W., and Gray, D.M., 1990. Saltation of snow. *Water Resources Research*, **26**, 1583–1594.

Pomeroy, J.W., and Gray, D.M., 1995. *Snowcover: Accumulation, Relocation and Management*. National Hydrology Research Institute Science Report No. 7, Saskatoon, SK, 144 p.

Pomeroy, J.W., Gray, D.M., Brown, T., Hedstrom, N.R., Quinton, W.L., Granger, R.J., and Carey, S.K., 2007. The cold regions hydrological process representation and model: a platform for basing model structure on physical evidence. *Hydrological Processes*, **21**, 2650–2667.

Pomeroy, J.W., Gray, D.M., and Landine, P.G., 1993. The prairie blowing snow model: characteristics, validation, operation. *Journal of Hydrology*, **144**, 165–192.

Pomeroy, J.W., Gray, D. M., Shook, K. R., Toth, B., Essery, R. L. H., Pietroniro, A., and Hedstrom, N., 1998. An evaluation of snow accumulation and ablation processes for land surface modelling, *Hydrological Processes*, **12**, 2339–2367.

Pomeroy, J.W., Hanson, S., and Faria, D.A., 2001. Small-scale variation in snowmelt energy in a boreal forest: an additional factor controlling depletion of snow cover? In: *Proceedings of the 58th Eastern Snow Conference*, **58**, 85–96.

Pomeroy, J.W., and Li, L., 2000. Prairie and Arctic areal snow cover mass balance using a blowing snow model. *Journal of Geophysical Research*, **105**, 26619–26634.

Pomeroy, J.W., MacDonald, M.K., DeBeer, C.M., and Brown, T., 2009a. Modelling alpine snow hydrology in the Canadian Rocky Mountains. In: *Proceedings of the 77th Western Snow Conference*, **77th**, 20–23 April 2009, Canmore, AB., 3–11.

Pomeroy, J.W., Marks, D., Link, T., Ellis, C., Hardy, J., Rowlands, A., and Granger, R., 2009b. The impact of coniferous forest temperature on incoming longwave radiation to melting snow. *Hydrological Processes*, **23**, 2513–2525.

Pomeroy, J.W., Semenova, O.M., Fang, X., Vinogradov, Y.B., Ellis, C., Vinogradova, T.A., MacDonald, M., Fisher, E.E., Dornes, P., Lebedeva, L., and Brown, T., 2010. Wolf Creek Cold Regions Model Set-up, Parameterisation and Modelling Summary. Centre for Hydrology Report No. 8, Centre for Hydrology, University of Saskatchewan, Saskatoon, Canada and State Hydrological Institute, Saint Petersburg, Russia, 107 pp.

Pomeroy, J.W., Toth, Granger, R.J., Hedstrom, N.R., and Essery, R.H., 2003. Variation in surface energetics during snowmelt in a subarctic mountain catchment. *Journal of Hydrometeorology*, **4**, 702–718.

Purves, R.S., Barton, J.S., Mackaness, W.A., and Sugden, D.E., 1998. The development of a rule-based spatial model of wind transport and deposition of snow. *Annals of Glaciology*, **26**, 197–202.

Rademacher, L.K., Clark, J.F., Clow, D.W., and Hydson, G.B., 2005. Old groundwater influence on stream hydrochemistry and catchment response times in a small Sierra Nevada catchment: Sagehen Creek, California. *Water Resources Research*, **41**, doi: 10.1029/2003WR002805.

Rango, A., and Martinec, J., 1982. Snow accumulation derived from modified depletion curves of snow coverage. In: *Gen, J.W. (ed.), Hydrological Aspects of Alpine and High-Mountain Areas*, IAHS Publication No. 138, 83–90.

Rango, A., and Martinec, J., 1995. Revisiting the degree-day method for snowmelt computations. *Water Resources Bulletin*, **31**, 657–669.

Rango, A., and van Katwijk, V., 1990. Development and testing of a snowmelt-runoff forecasting technique. *Water Resources Bulletin*, **26**, 135–144.

Rosenthal, W., and Dozier, J., 1996. Automated mapping of montane snow cover at subpixel resolution from the Landsat Thematic Mapper. *Water Resources Research*, **32**,115–130.

Sauchyn, D., and Kulshreshtha, S., 2008. Prairies. In: *Lemmen, D.S., Warren, F.J., Lacroix, J., and Bush E. (eds.), From Impacts to Adaptation: Canada in a Changing Climate 2007*, Government of Canada, Ottawa, ON, 275–328.

Savenije, H.H.G., 2009. The art of hydrology. *Hydrology and Earth Systems Sciences*, **13**, 157–161.

Schaerer, P.A., 1981. Avalanches. In: *Gray, D.M., and Male, D.H. (eds.), Handbook of Snow: Principles, Processes, Management & Use*. Pergamon Press, Toronto, ON, Chapter 11, 475–518.

Scherer, D., Hall, D.K, Hochschild, V., König, M., Winther, J.G., Duguay, C.R., Pivot, F., Mätzler, C., Rau, F., Seidel, K., and Walker, A., 2005. Remote Sensing of Snow Cover. In: *Dugay, C.R., and Piteroniro, A. (eds.), Remote Sensing in*

Northern Hydrology: Measuring Environmental Change, Geophysical Monograph 163, American Geophysical Union, Washington, D.C., 7–38.

Schirmer, M., and Lehning, M., 2011. Persistence in intra-annual snow depth distribution: 2. Fractal analysis of snow depth development. *Water Resources Research*, **47**, doi: 10.1029/2010WR009429.

Schirmer, M., Wirz, V., Clifton, A., and Lehning, M., 2011. Persistence in intra-annual snow depth distribution: 1. Measurements and topgraphic control. *Water Resources Research*, **47**, doi: 10.1029/2010WR009426.

Schmidt, R.A., 1972. *Sublimation of wind-transported snow – a model.* Research Paper RM-90, USDA Forestry Service, Rocky Mountain Forest and Range Experimental Station, Fort Collins, CO.

Schmidt, R.A., 1986. Transport rate of drifting snow and the mean wind speed profile. *Boundary Layer Meteorology*, **34**, 213–241.

Schmidt, R.A., and Troendle, C.A., 1992. Sublimation of intercepted snow as a global source of water vapour. In: *Proceedings of the 60th Western Snow Conference*, **60**, 1–9.

Schmidt, S., Weber, B., and Winiger, M., 2009. Analyses of seasonal snow disappearance in an alpine valley from micro- to meso-scale (Loetschental, Switzerland). *Hydrological Processes*, **23**, 1041–1051.

Shook, K.R., 1995. *Simulation of the ablation of prairie snowcovers*. PhD thesis, University of Saskatchewan, 189 p.

Shook, K.R., and Gray, D.M., 1996. Small-scale spatial structure of shallow snowcovers. *Hydrological Processes*, **10**, 1283–1292.

Shook, K.R., and Gray, D.M., 1997a. Snowmelt resulting from advection. *Hydrological Processes*, **11**, 1725–1736.

Shook, K.R., and Gray, D.M., 1997b. Synthesizing shallow seasonal snow covers. *Water Resources Research*, **33**, 419–426.

Shook, K.R., Gray, D.M., and Pomeroy, J.W., 1993. Temporal variation in snowcover area during melt in prairie and alpine environments. *Nordic Hydrology*, **24**, 183–198.

Sicart, J.E., Pomeroy, J.W., Essery, R.L.H., and Bewley, D., 2006. Incoming longwave radiation to melting snow: observations, sensitivity and estimation in northern environments. *Hydrological Processes*, **20**, 3697–3708.

Sivapalan, M., Blöschl, G., Zhang, L., and Vertessy, R., 2003. Downward approach to hydrological prediction. *Hydrological Processes*, **17**, 2101–2111.

Skaugen, T., 2007. Modelling the spatial variability of snow water equivalent at the catchment scale. *Hydrology and Earth System Sciences*, **11**, 1543–1550.

Skaugen, T., Alfnes, E., Langsholt, E.G., and Undæs, H.C., 2004. Time-variant snow distribution for use in hydrological models. *Annals of Glaciology*, **38**, 180–186.

Solomon, S., and 29 others, 2007. Technical Summary. In: *Climate Change 2007: The Physical Science Basis. Contribution of Working Group I to the Fourth Assessment Report of the Intergovernmental Panel on Climate Change* [Solomon, S., Qin, D., Manning, M., Chen, Z., Marquis, M., Averyt, K.B., Tignor, M., Miller, H.L., (eds.)]. Cambridge University Press, Cambridge, United Kingdom and New York, NY, USA.

Sommerfeld, R.A., and LaChapelle, E., 1970. The classification of snow metamorphism. *Journal of Glaciology*, **9**, 3–17.

Steppuhn, H., 1981. Snow and agriculture. In: *Gray, D.M., and Male, D.H. (eds.), Handbook of Snow: Principles, Processes, Management & Use*. Pergamon Press, Toronto, ON, Chapter 3, 60–125.

Steppuhn, H.W., and Dyck, G.E., 1974. Estimating true basin snowcover. In: *Santeford, H.S., and Smith, J.L., (eds.), Advanced Concepts in Technical Study of Snow and Ice Resources*, U.S. National Academy of Sciences, Washington, D.C., 314–328.

Stevenson, D.R., 1967. *Geological and groundwater investigations in the Marmot Creek experimental basin of southwestern Alberta, Canada*. MSc Thesis, University of Alberta, Edmonton, Alberta.

Stewart, I.T., 2009. Changes in snowpack and snowmelt runoff for key mountain regions. *Hydrological Processes*, **23**, 78–94.

Stewart, I.T., Cayan, D.R., and Dettinger, M.D., 2004. Changes in snowmelt runoff timing in western North America under a 'Business as Usual' climate change scenario. *Climatic Change*, **62**, 217–232.

Stewart, I.T., Cayan, D.R., and Dettinger, M.D., 2005. Changes towards earlier streamflow timing across western North America. *Journal of Climate*, **18**, 1136–1155.

Storr, D. 1967. Precipitation Variations in a Small Forested Watershed. *Proceedings of the Annual Western Snow Conference*, **35th**, 18-20 April 1967, Boise, Idaho, 11–17.

Storr, D., 1974. Relating sub-surface water storage to streamflow in a mountainous watershed. Canadian Meteorological Research Report 4/74, 14 pp.

Strasser, U., Bernhardt, M., Weber, M., Liston, G.E., and Mauser, W., 2008. Is snow sublimation important in the alpine water balance? *The Cryosphere*, **2**, 53–66.

Sturm, M. 1992. Snow distribution and heat flow in the taiga. *Arctic and Alpine Research*, **24**, 145–152.

Sturm, M., and Holmgren, J., 1998. Differences in compaction behavior of three climate classes of snow. *Annals of Glaciology*, **26**, 125–130.

Swanson, R.H., and Golding, D.L., 1982. Snowpack management on Marmot Watershed to increase late season streamflow. In: *Proceedings of the Western Snow Conference,* **50th**, 20-23 April 1982, Reno, Nevada, 215–218.

Swanson, R.H., Golding, D.H., Rothwell, R.L., and Bernier, P.Y., 1984. Hydrological effects of clear-cutting at Marmot Creek and Streeter Watersheds, Alberta. Canadian Forest Service, Northern Forestry Centre, Edmonton, Alberta. Int. Rept. NOR-X.

Tabler, R.D., 1975. Estimating the transport and evaporation of blowing snow. In: *Symposium on Snow Management on the Great Plains (Bismarck, ND; July, 1975)* Proceedings, Great Plains Agricultural Council Publication No. 73, 85–104.

Tabler, R.D., Pomeroy, J.W., Santana, B.W., 1990. Drifting Snow. In: *Ryan, W.L., and Crissman, R.D. (eds.), Cold Regions Hydrology and Hydraulics*, American Society of Civil Engineers, New York, NY, 95–146.

Tallaksen, L.M., 1995. A review of baseflow recession analysis. *Journal of Hydrology*, **165**, 349–370.

Tarboton, D., Blöschl, G., Cooley, K., Kirnbauer, R., and Luce, C., 2000. Spatial snow processes at Kütai and Reynolds Creek. In: *Spatial Patterns in Catchment Hydrology: Observations and Modelling*, Grayson, R., and G. Blöschl, eds., Cambridge University Press, 158–186.

Tarbotan, D.G., and Luce, C.H., 1996. *Utah Energy Balance Snow Accumulation and Melt Model (UEB)*. Computer model technical description and users guide, Utah Water Research Laboratory and USDA Forest Service Intermountain Research Station.

Toews, D.A., and Gluns, D.R., 1986. Snow accumulation and ablation on adjacent forested and clearcut sites in southeastern British Columbia. In: *Proceedings of the 54th Western Snow Conference*, **54**, 101–111.

Turpin, O., Ferguson, R., and Johansson, B., 1999. Use of remote sensing to test and update simulated snow cover in hydrological models. *Hydrological Processes*, **13**, 2067–2077.

U.S. Army Corps of Engineers, 1956. *Snow Hydrology: Summary Report of the Snow Investigations*. U.S. Army Corps of Engineers, North Pacific Division, Portland, Oregon.

Verseghy, D.L., 1991. CLASS – A Canadian land surface scheme for GCMs – 1: Soil model. *International Journal of Climatology*, 11, 111–133.

Viviroli, D., Archer, D.R., Buytaert W., Fowler H.J., Greenwood, G.B., Hamlet, A.F., Huang, Y., Koboltschnig, G., Litaor, M.I., López-Moreno, J.I., Lorentz, S., Schädler, B., Schreier, H., Schwaiger, K., Vuille, M., and Woods, R., 2011. Climate change and mountain water resources: overview and recommendations for research, management and policy. *Hydrology and Earth System Sciences*, **15**, 471–504.

Walker, D.A., Billings, W.D., and DeMolenar, J.G., 2001. Snow – vegetation interactions in tundra environments. In: *Jones, H.G., Pomeroy, J.W., Walker, D.A., and Hoham, R.W. (eds.), Snow Ecology – An Interdisciplinary Examination of Snow-Covered Ecosystems*, Cambridge University Press, Cambridge, UK, Chapter 6, 266–324.

Walland, D. J., and Simmonds, I., 1996. Sub-grid-scale topography and the simulation of Northern Hemisphere snow cover. *International Journal of Climatology*, **16**, 961–982.

Warren, S.G., and Wiscombe, W.J., 1980. A model for the spectral albedo of snow. II: Snow containing atmospheric aerosols, *Journal of the Atmospheric Sciences* **37**, 2734–2745.

Water Survey of Canada, 2010. *Archived Hydrometric Data*, http://www.wsc.ec.gc.ca /hydat/H2O/index_e.cfm?cname=main_e.cfm, accessed July, 2010.

Wigmosta, M.S., Vail, L.W., and Lettenmaier, D.P., 1994. A distributed hydrology-vegetation model for complex terrain. *Water Resources Research*, **30**, 1665–1679.

Winstral, A., Elder, K., and Davis, R.E., 2002. Spatial snow modeling of wind-redistributed snow using terrain-based parameters. *Journal of Hydrometeorology*, **3**, 524–538.

Winstral, A., and Marks, D., 2002. Simulating wind fields and snow redistribution using terrain-based parameters to model snow accumulation and melt over a semi-arid mountain catchment. *Hydrological Processes*, **16**, 3585–3603.

Woo, M.K., 1998. Arctic snow cover information for hydrological investigations at various scales. *Nordic Hydrology*, **29**, 245–266.

Woo M.K., and Marsh, P., 1978. Analysis of error in the determination of snow storage for small high arctic basins. *Journal of Applied Meteorology*, **17**, 1537–1541.

Woo, M.K., and Steer, P., 1986. Monte Carlo simulation of snow depth in a forest. *Water Resources Research*, 22, 864–868.

Woo, M.K., and Thorne, R., 2006. Snowmelt contribution to discharge from a large mountainous catchment in subarctic Canada. *Hydrological Processes*, **20**, 2129–2139.

Wood, E.F, Sivapalan, M., Beven, K., and Band, L., 1988. Effects of spatial variability and scale with implications to hydrological modeling. *Journal of Hydrology*, **102**, 29–47.

World Meteorological Organization, 1986. *Intercomparison of models of snowmelt runoff*. Operational Hydrology Report 23, WMO No. 646, 36 p.

Zappa, M., Pos, F., Strasser, U., Warmerdam, P., and Gurtz, J., 2003. Seasonal water balance of an alpine catchment as evaluated by different methods for spatially distributed snowmelt modelling. *Nordic Hydrology*, **34**, 179–202.

Zhao, L., and Gray, D.M., 1999. Estimating snowmelt infiltration into frozen soils. *Hydrological Processes*, **13**, 1827–1842.

Zhao, L., Gray, D.M., and Male, D.H., 1997. Numerical analysis of simultaneous heat and mass transfer during infiltration into frozen ground. *Journal of Hydrology*, **200**, 345–363.

APPENDIX A: SNOW SURVEY DATA AND DETERMINATION OF SWE VARIABILITY

A.1 Snow Survey and Snow Pit Measurements

This section presents some of the results of the snow surveys carried out over Fisera Ridge and within the adjacent cirque basin below Mt. Allan, along with the snow pits that were dug to measure snow density. Snow depth was measured repeatedly along fixed transects or once along unmarked survey lines (although GPS readings were taken to record the location of these surveys). SWE was determined from these depth measurements using density measured from nearby snow pits or from measurements made using the ESC-30 snow tube at points along the surveys. Parameters such as $\overline{SWE}$ and CV were derived from these surveys and used to quantify the variability of the snowcover at these times.

A.1.1 2007 Survey Data

In late March of 2007, an intensive survey campaign was carried out to measure the snowcover variability at Fisera Ridge and over parts of the alpine landscape in Upper Middle and Twin Creek basins. This consisted of a number of surveys chosen to represent different slopes, elevations, and landcover types, within the constraints of accessibility and terrain hazards. The locations of the surveys are shown in Fig. A.1, while Fig. A.2 and Table A.1 present some of the results. Most of the measurements showed a very poor relationship between snow depth and density, and therefore the average density was used to derive SWE using Equation (2.1) on p. 11. The variability in SWE was found to be strongly dependant on surface cover from these surveys (Table A.1), while spatial patterns of snowcover closely matched those found in subsequent years of this study along with the patterns of areal SCD observed in each year.

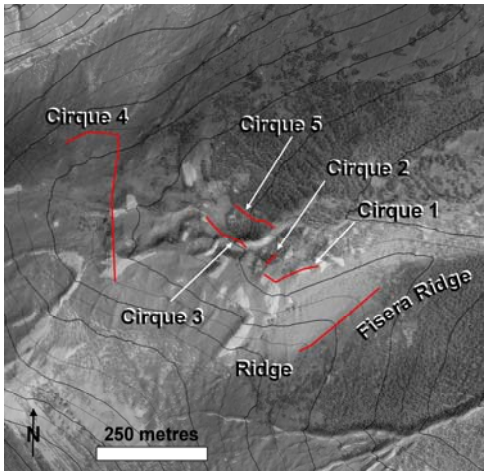

Figure A.1. Shaded relief map and air photo showing names and locations of snow survey transects across the alpine landscape in Upper Middle Creek basin on March 29–30, 2007.

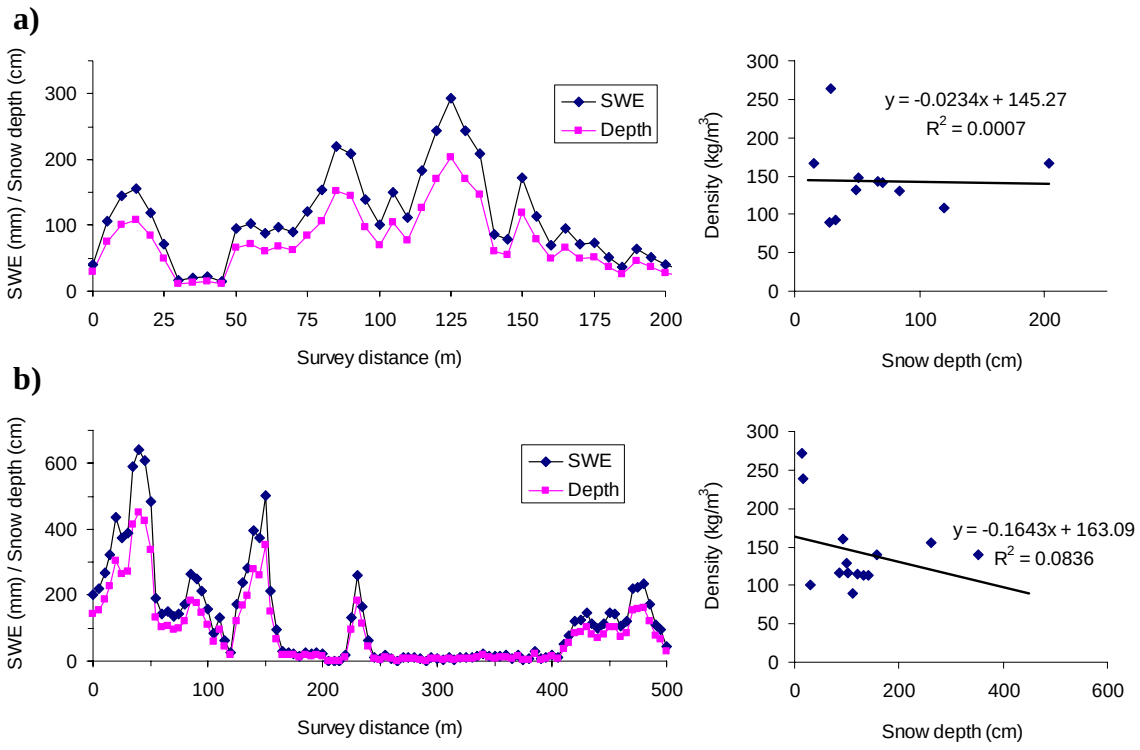

Figure A.2. Example snow survey transects carried out in parts of the alpine landscape in Upper Middle Creek basin on March 29–30, 2007: a) ridgetop survey up from the Fisera Ridge station (Ridge), b) survey crossing the cirque floor and moving up across the south-facing slope (Cirque 4). Plots of snow depth vs. density are also shown to illustrate the relationships found at this time.

Table A.1. Mean and coefficient of variation of SWE values measured along various transects carried out in parts of the alpine landscape in Upper Middle Creek basin on March 29–30, 2007.

Survey description – dominant landcover or surface type	$\overline{\text{SWE}}$ (mm)	CV
Crest of Fisera Ridge up from station (Ridge)	99	0.67
Foot of N-facing slope in cirque (Cirque 1)	294	0.39
Exposed shrubs in alpine zone (Cirque 2)	331	0.46
Prominent gulley in cirque floor (Cirque 3)	324	0.53
Cirque transect from cirque floor to S-facing slope (Cirque 4)	125	1.18
Exposed shrubs and dense krummholz in cirque floor (Cirque 5)	420	0.18

A.1.2 2008 Survey Data

In the late winter and spring of 2008, snow survey efforts were focused on the spatial – temporal variability at Fisera Ridge and across the cirque in Upper Middle Creek basin. The location of these two primary survey transects is shown in Fig. 4.6 (p. 86) and Fig. 6.1 (p. 134) for reference. The survey lines were staked with permanent markers at various points along both transects so that they could be repeated reliably, and these were spatially located using a differential GPS (Trimble Pro-XL) to accurately define their position. Snow pits were dug at selected locations along both of these surveys to measure snow density. Measurements were repeated approximately every second week during the spring melt period, and at times these were repeated two to three days apart in an attempt to derive snow ablation rates at each point.

Figures A.3 and A.4 show the density variations over time and with depth in the snowpack, as well as the total SWE measured nearby the SE-facing station on Fisera Ridge. The average density increased steadily over time at this location, which was most likely due to the increase in liquid water content within the pack. In addition, the density variation with depth throughout the snowpack tended to show a curved profile where the densest snow was in the middle and snow near the top and bottom of the pack were less dense. By fitting a linear trend over time to this data, the time variation of density was used to estimate SWE at the nearby station for measurements of snowmelt rates and validation of the model described in Section 5.3. Other snow pits over Fisera Ridge and

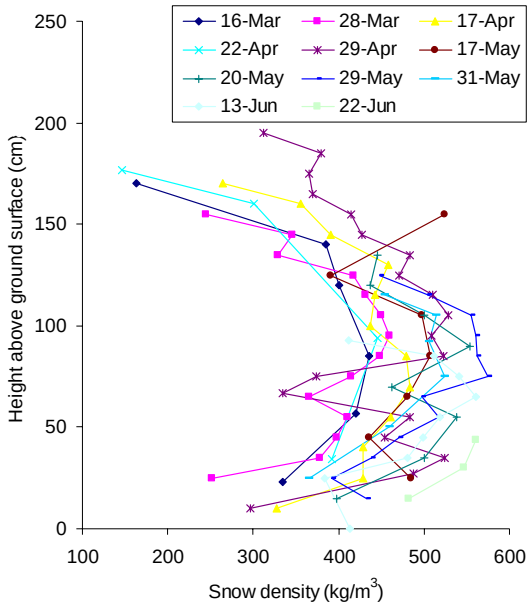

Figure A.3. Variation of snow density with depth (i.e., height above ground surface) in the snowpack measured in a pit near the SE-facing station at Fisera Ridge during 2008.

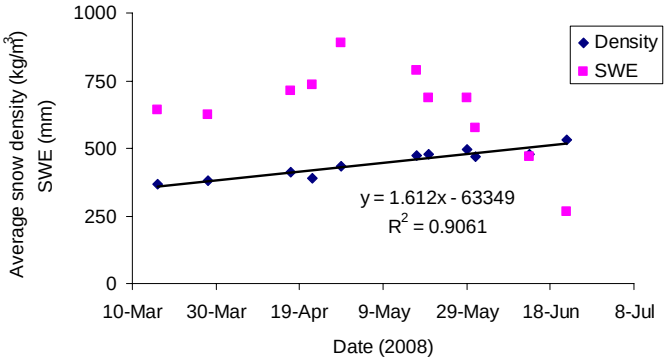

Figure A.4. Temporal variation of average snowpack density and total SWE at the snow pit near the SE-facing station during 2008.

within the cirque below Mt. Allan showed similar variation over time, and it was found that there was no discernible relationship between depth and density (although there was some spatial variation in density across the landscape). This was probably due to the snowpack becoming ripe holding water at its maximum capacity, which would tend to increase the density and make it more similar between deep and shallow snow, while

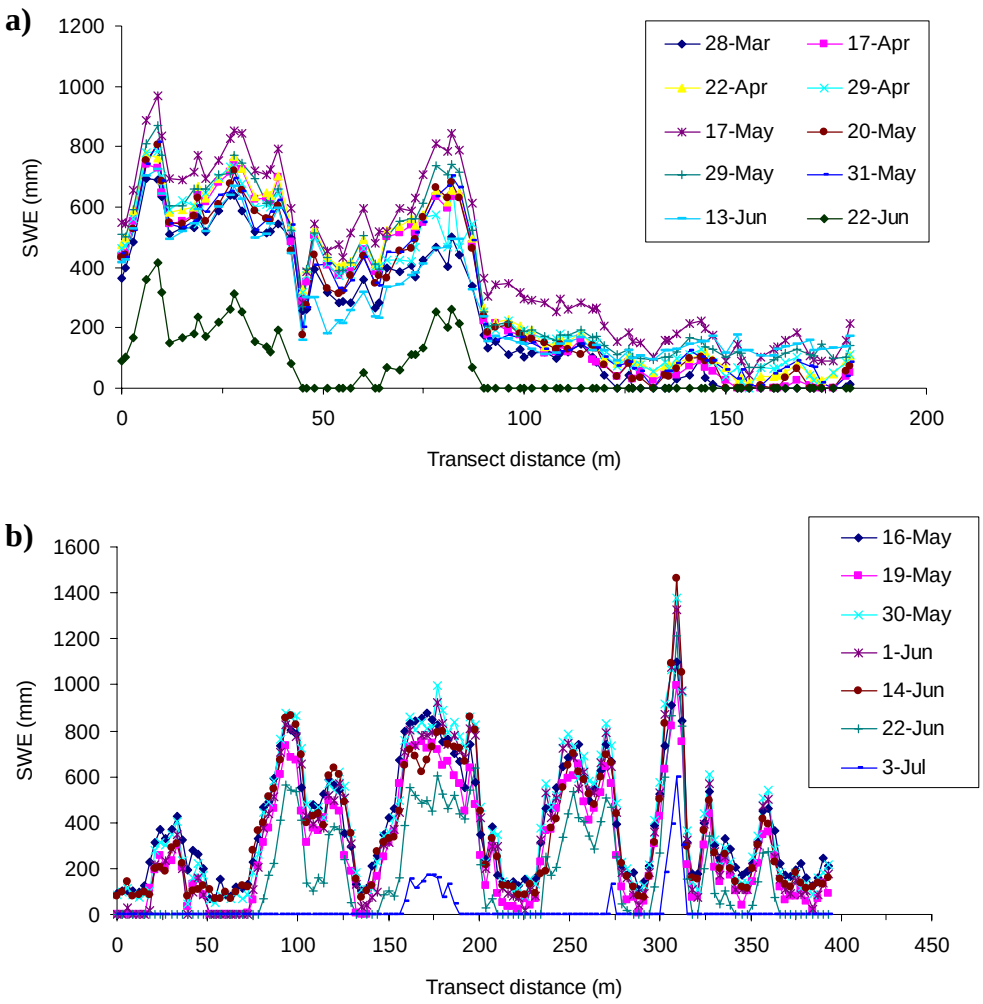

Figure A.5. Measurements of SWE over the survey transects at different times throughout the snowmelt period in 2008: a) transect crossing Fisera Ridge, b) transect within the Mt. Allan Cirque in Upper Middle Creek Basin.

differences in ripening and water movement through the pack on different slopes would lead to some spatial variation in density. The measurements from snow pits and from ESC-30 samples in some instances were used to determine the values of SWE at nearby points along the survey transects. Figure A.5 shows the results of these surveys over the course of the spring in 2008 and the spatial – temporal variation in SWE, while Tables A.2 and A.3 give the corresponding values of $\overline{SWE}$ and CV for each survey and for different slopes over Fisera Ridge.

Table A.2. Temporal variation in mean SWE and CV from the survey transect measurements on Fisera Ridge and within the adjacent cirque during the spring of 2008.

Fisera Ridge survey			Mt. Allan Cirque survey		
Date	$\overline{SWE}$ (mm)	CV	Date	$\overline{SWE}$ (mm)	CV
28-Mar	200	1.03	16-May	389	0.64
17-Apr	245	0.97	19-May	286	0.87
22-Apr	276	0.85	30-May	399	0.73
29-Apr	261	0.86	1-Jun	347	0.85
17-May	367	0.67	14-Jun	359	0.76
20-May	244	0.93	22-Jun	177	1.32
29-May	304	0.76	3-Jul	22	3.57
31-May	248	0.90			
13-Jun	250	0.70			
22-Jun	69	1.53			

Table A.3. Temporal variation in mean SWE and CV from different parts of the survey transect measurements on Fisera Ridge, representing different slopes during the spring of 2008.

SE-facing slope			N-facing slope			Ridge crest		
Date	$\overline{SWE}$ (mm)	CV	Date	$\overline{SWE}$ (mm)	CV	Date	$\overline{SWE}$ (mm)	CV
28-Mar	455	0.27	28-Mar	22	1.79	28-Mar	141	1.37
17-Apr	551	0.22	17-Apr	40	0.98	17-Apr	106	0.77
22-Apr	577	0.21	22-Apr	77	0.51	22-Apr	137	0.58
29-Apr	541	0.24	29-Apr	81	0.50	29-Apr	122	0.71
17-May	637	0.27	17-May	158	0.36	17-May	236	0.54
20-May	519	0.28	20-May	46	0.98	20-May	13	0.88
29-May	592	0.24	29-May	119	0.25	29-May	175	0.57
31-May	524	0.27	31-May	68	0.57	31-May	125	0.80
13-Jun	446	0.34	13-Jun	132	0.17	13-Jun	163	0.56
22-Jun	182	0.74						

A.1.3 2009 Survey Data

In 2009, the extent of snow surveys was more limited and focused primarily on Fisera Ridge and lower forested part of the Upper Middle Creek Basin. The same transect crossing Fisera Ridge was used to monitor snowcover patterns and temporal variability at this site, although in 2009 the same efforts and level of precision used to locate the exact points of each measurement were not undertaken as in 2008. Spacing was done by counting paces of the surveyors rather than measuring actual distances, although the approximate location of points was recording relative to features along the ridge and benchmarks such as the meteorological stations, prominent trees or shrubs, and marked posts. The purpose of these surveys was to monitor the spatial – temporal variability of $\overline{\text{SWE}}$ and CV rather to attempt to derive specific point–location ablation rates. The surveys were extended into the treeline forest stands on the SE-facing slope and along the ridgetop, and in addition, another survey transect was added in the lower part of the basin near the stream gauge site. Together these surveys provided information on the snowcover characteristics over time within representative forested parts of the basin.

Figure A.6 shows some of the survey data for the lower forest transect near the gauge and Table A.4 provides the corresponding values of $\overline{\text{SWE}}$ and CV. The data show that ablation rates under the forest canopy were relatively slow in general, averaging ~10 mm/day during the main melt period. It can also be seen that the value of CV near to the time of maximum snow accumulation was comparatively low with respect to values in the open windswept terrain (i.e., CV = 0.25 on May 17). The data from the Fisera Ridge surveys are provided in Table A.5, and show clear differences in accumulation and melt characteristics as reflected by the differences in $\overline{\text{SWE}}$ and CV. Notable are the high and low values of $\overline{\text{SWE}}$ and CV respectively for both the SE-facing and the forested parts of the transect. Most of the SE-facing part of the survey covered a large drift area on a lee slope. More exposed and windswept locations such as the N-facing and ridge crest locations had relatively low values of $\overline{\text{SWE}}$ and higher CV, and snowcover patterns were more transient in these areas. The patterns closely matched the observations in 2008, indicating the high year-to-year consistency in snowcover patterns

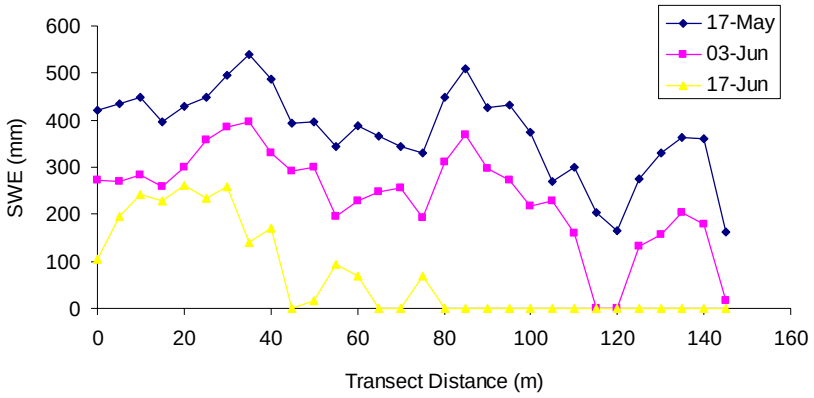

Figure A.6. Snow survey measurements of SWE in the lower forested part of the Upper Middle Creek Basin near the stream gauge site in 2009.

Table A.4. Mean and coefficient of variation of SWE values measured along the lower forested survey transect near the stream gauge site in 2009.

	17-May	03-Jun	17-Jun
$\overline{\text{SWE}}$ (mm)	376	238	70
CV	0.25	0.43	1.39

Table A.5. Temporal variation in mean SWE and CV from different parts of the survey transect measurements on Fisera Ridge, representing different slopes during the spring of 2009.

	N-facing		Ridge crest		SE-facing		Forested		Overall survey	
Date	$\overline{\text{SWE}}$ (mm)	CV	$\overline{\text{SWE}}$ (mm)	CV	$\overline{\text{SWE}}$ (mm)	CV	$\overline{\text{SWE}}$ (mm)	CV	$\overline{\text{SWE}}$ (mm)	CV
30-Mar	86	0.61	181	0.68	434	0.29	574	0.18	318	0.67
18-Apr	88	0.65	179	0.64	458	0.30	519	0.22	344	0.61
6-May	180	0.43	245	0.48	510	0.27	634	0.25	402	0.54
17-May	220	0.29	388	0.41	475	0.22	658	0.23	443	0.44
3-Jun	50	1.01	104	0.95	286	0.37	378	0.37	201	0.81
17-Jun	0		0		174	0.69	196	0.76	89	1.45

across the landscape here, which are due to the predominant direction of prevailing winds together with surface topography and vegetation characteristics across the landscape.

A.2 LiDAR-Derived Snow Depth Validation and Determination of SWE

In late March of 2008 snowcover patterns over Marmot Creek Basin were mapped using airborne LiDAR. Field validation of the data was carried out across the alpine part of the basin using snow surveys and snow pits, and measurements of snow density were used to determine spatial SWE patterns from the snow depth patterns. Figure A.7 shows the location of the surveys and snow pits done across the alpine zone within the Marmot Creek Research Basin. Survey locations were recorded using a Trimble Pro-XL differential GPS supplied by the University of Calgary Biogeosciences Institute. A permanent base station at the Biogeoscience Institute, roughly 20 km to the northeast, was used for differential correction of the readings. The software used for this correction was Trimble Pathfinder Office, and the base station software was the Trimble Community Base Station. It is noted that there was a failure of the base station at the time of the survey measurements, and therefore differential correction could not be applied. Therefore, the location of most of the alpine survey measurements is only precise to within ± 1–2 metres at best. However, the survey transect across Fisera Ridge was marked by a series of fixed stakes at known survey points, which were later returned to for differential measurements.

A detailed map of the Fisera Ridge transect used to validate the LiDAR depths is shown in Figure A.8 (see Section 4.4.2 for validation results). Snow depth measurements were taken at an interval of 3 m along the transect crossing the ridge, and at an interval of 2 m along the ridge. In addition, an extra measurement spaced 1 m apart from each 3rd point (across the ridge) was taken for the purpose of later examining fine scale variability without an excessive number of measurements being made. Fixed stakes placed at various locations along the transect were used as benchmarks to precisely repeat the surveys, and the location of these stakes was determined with the Trimble Pro-XL GPS operating in differential mode later in the spring. Based on these points, the location of each survey point was represented in ESRI® ArcGIS™ 9.3 by measuring the appropriate number and spacing of each point between the stakes. This method worked well, with the correct number and distance between points corresponding to the actual survey; thus the positional accuracy of individual points is likely accurate to within ~0.5 m or less.

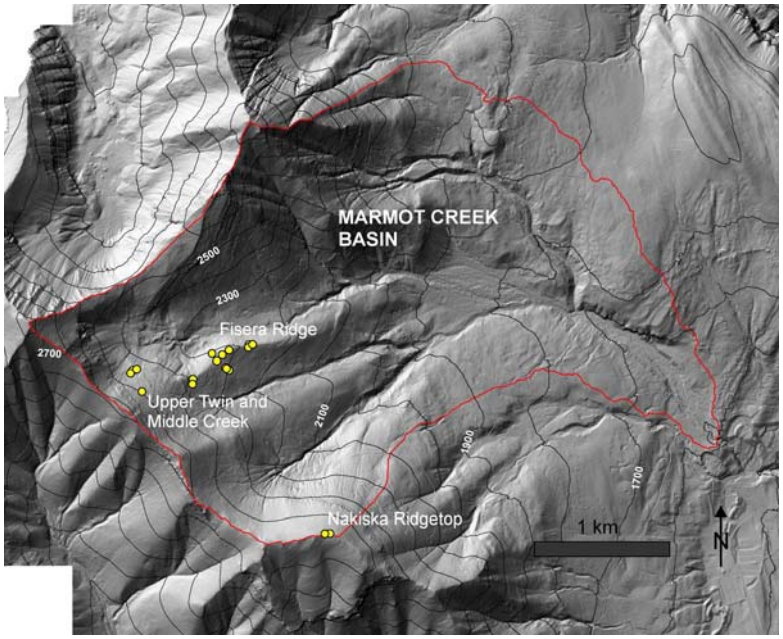

Figure A.7. Topographic relief map of the Marmot Creek Basin showing location of alpine snow surveys and snow pits on March 27–28, 2008, for validation of the LiDAR snow depth dataset.

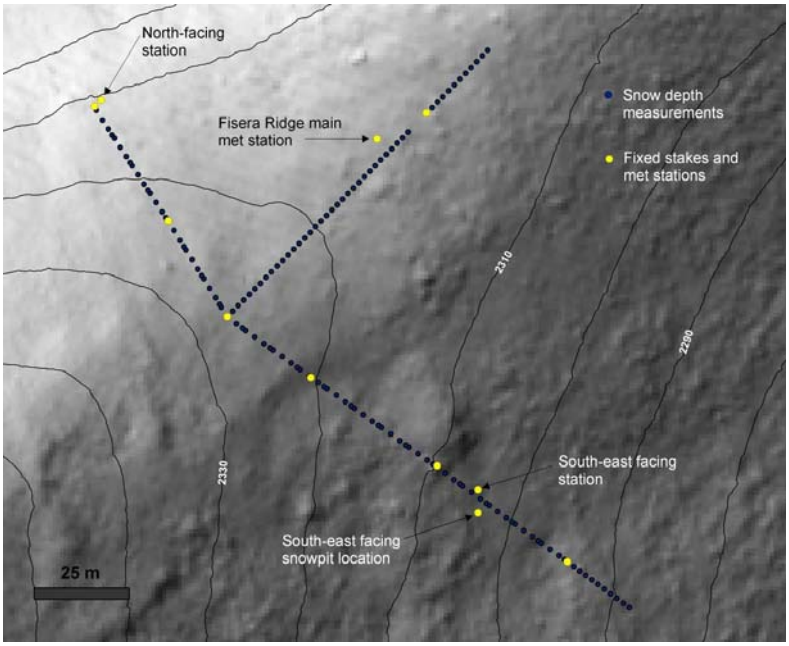

Figure A.8. Detailed map of the Fisera Ridge survey transect showing locations of each depth measurement and fixed stakes where differential GPS measurements were taken.

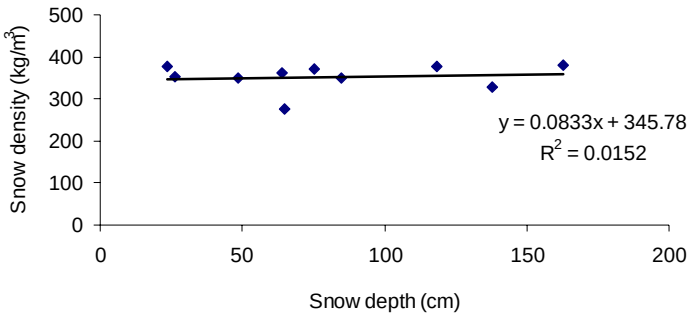

Figure A.9. Relationship between snow depth and density determined from snow pits carried out across the alpine zone in Marmot Creek on March 27–28, 2008.

To determine spatial SWE patterns from the snow depth raster image, density measurements from the various snow pits were used as described in Section 4.4.2. Most snow was hard and wind-packed across the open alpine zone and had a highly uniform density, as shown in Figure A.9. Therefore, mean snow density was used to convert snow depths to SWE based on Equation (2.1).

APPENDIX B: DETERMINATION OF SCA FROM TERRESTRIAL PHOTOS

The fraction of SCA over the landscape and SCD curves were derived from analysis of the corrected terrestrial oblique photographs taken from Fisera Ridge and from the chairlift station above treeline at Nakiska Ski Resort. The georeferenced photographs were then reclassified using ESRI® ArcGIS™ 9.3 by setting a brightness threshold to distinguish snowcovered from snow-free terrain in the images. This was done using the reclassify tool within the Spatial Analyst extension. Raster images representing the spatially corrected photographs were used as inputs and original cell brightness values ranging from 0 to 255 were reclassified as 0, 1, or 2, representing NoData, snow-free (bare ground), or snowcovered respectively. The threshold limit to distinguish snow from bare ground varied depending on the brightness conditions in the image and the presence of shadows covering parts of the landscape, and was set manually for each individual image. The results of the reclassification were then compared on screen by flickering between the original and the reclassified images to ensure that the corrected area and geometry of snow patches was properly represented. In cases where there were obvious and large errors the procedure was repeated using a different threshold value, ensuring a high degree of accuracy for each image. An example of this is shown in Figure B.1, which provides both the original and the reclassified image representing the snow patches. There is a clear correspondence between the extent and geometry of all snow patches. In general, the majority of the reclassified images produced in this manner had a similar correspondence and represented the snowcover extent very well.

To derive estimates of the fractional SCA over each slope, polygons representing the spatial extent of each slope unit (N-facing, S-facing, E-facing, and cirque floor) were created in ArcGIS (see Fig. 6.3). Grid cells from the reclassified raster images were extracted over the areas covered by each slope using the raster tools in ArcGIS toolbox, and were subsequently counted to derive an estimate of the SCA fraction on each day. An example of this calculation is provided in Table B.1, which provides the absolute and

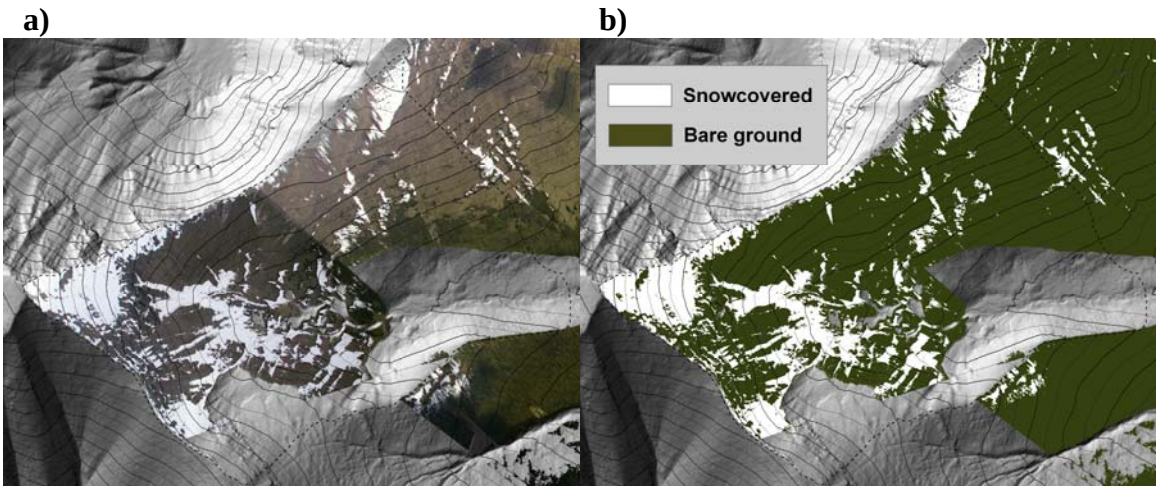

Figure B.1. Example of terrestrial photos from June 24, 2008 together with the reclassified image of snow vs. snow-free ground: a) original re-projected image, b) reclassified raster for SCA.

Table B.1. Example of SCA determination based on grid cell counts of snowcovered and bare ground for each of the major slope units in the alpine portion of Upper Middle Creek Basin (based on image acquired on June 24, 2008).

Slope unit	Area (km^2)	Area (% of total)	NoData cell count	Snow cell count	Non-snow cell count	SCA fraction
N-facing	0.23	24	161232	30295	41951	0.42
S-facing	0.41	43	13453	24726	206848	0.11
E-facing	0.24	25	6817	123042	111188	0.53
Cirque floor	0.07	8	11699	12367	29133	0.30
Alpine basin	0.95	100				0.30

relative area of each slope unit in the alpine portion of the basin, as well as cell counts for NoData, snowcovered, and snow-free cells on June 24, 2008. SCA was calculated as:

$$\mathrm{SCA} = \frac{\#\,\text{snow cells}}{\left(\#\,\text{total snowcovered} + \text{bare ground cells}\right)}. \qquad \text{B.1}$$

To determine the SCA for the entire alpine portion of the basin encompassing all slopes, the weighted average SCA from each slope was taken, rather than summing the total number of snowcovered and bare ground cells. The fact that the number of NoData cells

differed between slopes as a result of parts of the landscape being hidden from view of the cameras would have biased the results by simply summing these cells.

On some particular days there were cloud shadows partially covering the landscape, which made the classification of snowcovered vs. bare ground areas more difficult. In these instances, clearly identifiable snow patches may have been classified as bare ground if they were in shade, while light areas of soil and talus were classified as snow. To correct for these effects of shadows, the brightness thresholds were manually adjusted to obtain the best possible results, and where this still led to obvious errors (e.g., calculated SCA increasing from one to the next when in reality it did not), the value was based on interpolation between values from other days or from estimation based on interpretation of the change in snowcover pattern.

APPENDIX C: SPREADSHEET-BASED SCA CALCULATION

Calculations of snowcovered area (SCA) and areal snowcover depletion (SCD) were based on the theoretical framework presented and described in Section Three of this thesis. To derive daily SCA values from which SCD curves were generated, the point-scale model (Section Five) was run for different initial values of SWE on each of the major slope-based landscape units to represent the effects of inhomogeneous melt across the basin and across individual SWE distributions. Changes in SWE from each of the simulations were then applied to the corresponding SWE values over each distribution (i.e., on each slope unit) according the methods described in Section 3.3.2. This procedure is described here in more detail.

For each slope unit in each year, time series of SWE based on the point-scale modelling were exported from CRHM to be used for SCA prediction. Initial SWE values of 0, 50, 100, 150, 200, 250, 300, 400, 500, 600, 800, 1000, and 1500 mm, were used to base snowmelt computations and later define the SWE classes over the maximum accumulation SWE distribution on each slope for the reasons explained in Section 6.4.1 (p. 155). Values of SWE at midday were taken from the series to base daily SCA calculations. The parameters of the peak distribution (i.e., $\overline{\mathrm{SWE}}$ and CV for the lognormal distribution) where established and used to define K values for the SWE values in each series at this time according the following equation (see step two in Section 3.3.1):

$$K = \frac{\left(\mathrm{SWE} - \overline{\mathrm{SWE}}\right)}{\mathrm{CV} \cdot \overline{\mathrm{SWE}}}, \qquad \text{C.1}$$

where K is the corresponding value of the frequency factor for the particular value of SWE over the distribution. As SWE in each series decreased over time, the values were used to determine K_{min} corresponding to the condition where SWE = 0, in order to calculate the remaining SCA. This was determined as:

$$K_{min} = K - \frac{\mathrm{SWE}}{\mathrm{CV} \cdot \overline{\mathrm{SWE}}}, \qquad \text{C.2}$$

where K is the original frequency factor value corresponding to the value of SWE for that particular series at maximum accumulation, and SWE is in this case the new value at a later time in the series following some melt. The formulas in Equations (C.1) and (C.2) are simply different versions of the point–slope formula for a line, modified here to give the value of these specific variables at different times.

To determine the remaining SCA on each day, K_y values were determined using Equation (3.9) (p. 55), and $P(K_y)$ values, which are equivalent to P(SWE) and SCA, were determined as one minus the value of the standard normal cumulative distribution function evaluated for K_y. In Microsoft® Excel the standard normal cumulative distribution has the syntax NORMSDIST(z) where z is the value for which the user wants the distribution (i.e., K_y).

Once the first SWE series being used to base SCA calculations became zero, the next series based on a greater initial value of SWE was used to determine the values of K_{min}, K_y, and SCA. The same procedure was followed except that a new form of the point–slope expression for a line had to be used, since inhomogeneous melt would change the slope of the line between individual "nodes". Initially, the product $\overline{\text{SWE}} \cdot \text{CV}$ in the denominator of Equations (C.1) and (C.2) is equal to the standard deviation of the natural values of SWE, or the slope of the line in the plot of K vs. SWE. However, after some inhomogeneous melt, the value of the slope of the line between nodes changes, and can be calculated by Equation (3.10) (p. 58). This approach was taken, and so for times after the first series became equal to zero, the following expression was used in place of Equation (C.2) for K_{min}:

$$K_{min} = K - \frac{\text{SWE}}{\alpha}, \qquad \text{C.3}$$

where α is the new slope value calculated by Equation (3.10). The same procedures as above were then used to derive the remaining SCA.

The only remaining issue was how the rescaled SCD curves were derived for times following new snowfall during the melt period. This was implemented in the spreadsheet based on the theoretical approach described in Section 3.3.3. The "foot" of the line representing previously snow-free terrain was defined to extend between S_f (the new snowfall amount [mm]) at K_{min} just prior to the snowfall event and $0.5 \cdot S_f$ at the

original K_{min} for maximum accumulation. In the spreadsheet, the new snowfall depth was entered and a conditional statement was included to define the K_{min} and SCA over the rescaled portion until the value just prior to the snowfall event was reached. If the difference between the value of SWE following new snowfall and that just prior to the event was >50% of S_f, then K_{min} was set as the minimum initial value (i.e., SCA = $0.\overline{99}$). If this difference was <50% of S_f, the value of K_{min} was determined by:

$$K_{min} = K_i - \frac{\text{SWE}}{\alpha}, \tag{C.4}$$

where the subscript i refers to the value of K at K_{min} just prior to the snowfall event, SWE is the remaining new snow on each day, and α is the slope calculated by:

$$a = \frac{0.5 \cdot S_f}{K_{min,2} - K_{min,1}}, \tag{C.5}$$

where $K_{min,1}$ is the original value for the peak accumulation distribution, and $K_{min,2}$ is the value just prior to the snowfall event. This procedure produced the rescaled depletion curve, and was followed until the time at which the new snowfall was fully melted and the K_{min} value exceeded that from before the snowfall event.

APPENDIX D: CRHM PROJECT REPORT

The following lists are the macro group structure, which was used for the model spatial and analytical structure in all years, followed by the macro used to run the model for homogeneous melt simulations, and a report file output from CRHM providing model parameters and files for one of the model runs in 2009.

Group Structure

```
First_GrpA N-facing
declgroup 4
basin
global
obs
calcsun
Slope_QsiX#1
albedo_Richard
netall
evap
CanopyClearing#2
pbsmSnobal
SnobalCRHM#1
frozenAyers
Soil
Netroute
command
end
First_GrpB S-facing
declgroup 4
basin
global
obs
calcsun
Slope_QsiX#1
albedo_Richard
netall
evap
CanopyClearing#2
pbsmSnobal
SnobalCRHM#1
frozenAyers
Soil
Netroute
command
end
First_GrpC E-facing
declgroup 4
basin
global
obs
calcsun
Slope_QsiX#1
albedo_Richard
netall
evap
CanopyClearing#2
pbsmSnobal
SnobalCRHM#1
frozenAyers
Soil
Netroute
command
end
First_GrpD E-facing
declgroup 4
basin
global
obs
calcsun
Slope_QsiX#1
albedo_Richard
netall
evap
CanopyClearing#2
pbsmSnobal
SnobalCRHM#1
frozenAyers
Soil
Netroute
command
end
First_GrpE E-facing
declgroup 4
basin
global
obs
calcsun
Slope_QsiX#1
albedo_Richard
netall
evap
CanopyClearing#2
pbsmSnobal
SnobalCRHM#1
frozenAyers
Soil
Netroute
command
end
First_GrpF E-facing
declgroup 4
basin
global
obs
calcsun
Slope_QsiX#1
albedo_Richard
netall
evap
CanopyClearing#2
pbsmSnobal
SnobalCRHM#1
frozenAyers
Soil
Netroute
command
end
REW_Grp
declgroup 6
REW_route
command
end
```

Homogeneous Melt Macro

```
Chris_SnobalCRHM use melt from first HRU in each group
declvar, SWE, NHRU, "HRU SWE", (mm)
declvar, snowmeltD, NHRU, "HRU A snowmelt", (mm/d)
declreadobs, snowmeltDX, NOBS, description, (mm/d)
declreadobs, SWEX, NOBS, description, (mm/d)
// declputvar, *, SWE, NHRU, "HRU interval SWE", (mm)
command
if(STEP%FREQ == 0)
  snowmeltD[hh] = snowmeltDX[hh]
endif
   SWE[hh] = SWEX[hh]
end
```

CRHM Report File

```
CURRENT TIME: 11/7/2011 16:35

CRHM Version: CRHM 3.40c

PROJECT FILE NAME:

C:\CRHM_062410_TB\Projects_Feb_20
11\New_Sept_29_2011\2009_distribu
ted_soil_New.prj  dated 11/7/2011
15:55

DIMENSIONS:

nhru 4
nlay 1
nobs 4

OBSERVATIONS:

C:\CRHM_062410_TB\Projects_Feb_20
11\Fisera_snobal_2009_May-
1_(modified_precip).obs         (
5/1/2009 00:15 - 8/31/2009 23:44,
Interval = 00:15 )

DATES:

2009 5 1
2009 7 31

MODULES:

First_GrpA Macro04/20/06
First_GrpB Macro04/20/06
First_GrpC Macro04/20/06
First_GrpD Macro04/20/06
First_GrpE Macro04/20/06
First_GrpF Macro04/20/06
REW_Grp Macro04/20/06

PARAMETERS:

Shared - a1 <0 to 1E8>
1.08E7 1.08E7 1.08E7 1.08E7

Shared - a2 <0 to 1E8>
1E6 1E6 1E6 1E6

Shared - AlbedoCanopy <0 to 1>
0.1 0.1 0.1 0.1

Shared - Albedo_Bare <0 to 1>
0.17 0.17 0.17 0.17

Shared - Albedo_Snow <0 to 1>
0.85 0.85 0.85 0.85

Shared - amax <0 to 1>
0.85 0.85 0.85 0.85

Shared - amin <0 to 1>
0.3 0.3 0.3 0.3

Shared - A_S <0 to 2>
0.003 0.003 0.003 0.003

Shared - basin_area <1E-6 to 1E9>
0.2001

Shared - C <0 to 3>
2 2 2 2

Shared - CanopyClearing <0 to 1>
1 1 1 1

Shared - catchadjust <0 to 2>
0 0 0 0
```

```
Shared - cov_type <0 to 2>
1 1 1 1

Shared - distrib <-10 to 10>
0 0 0 0

Shared - evap_type <0 to 1>
0 0 0 0

Shared - fetch <300 to 1E4>
1000 1000 1000 1000

Shared - F_Qg <0 to 1>
0.1 0.1 0.1 0.1

Shared - groundcover <1 to 6>
1 1 1 1

Shared - gwKstorage <0 to 200>
0 0 0 0

Shared - gwLag <0 to 1E4>
0 0 0 0

Shared - hru_ASL <0 to 360>
24 24 24 24

Shared - hru_elev <0 to 1E5>
2450 2450 2450 2450

Shared - hru_GSL <0 to 90>
28 28 28 28

Shared - hru_lat <-90 to 90>
50.95 50.95 50.95 50.95

Shared - hru_names
'SWE_50' 'SWE_100' 'SWE_800'
'SWE_800'

Shared - HRU_nhru <1 to 1000>
4 0 0 0

Shared - HRU_OBS <1 to 100>
1 1 1 1

Shared - hru_rho_snow <50 to
1000>
100 100 100 100

Shared - hru_tsoil <223 to 273.1>
269.1 269.1 269.1 269.1

Shared - hru_T_g <-50 to 50>
-4 -4 -4 -4

Shared - Ht <0.001 to 100>
0.1 0.25 1 1

Shared - inhibit_bs <0 to 1>
1 1 1 1

Shared - inhibit_evap <0 to 1>
0 0 0 0

Shared - inhibit_subl <0 to 1>
0 0 0 0

Shared - INIT_STATE
''

Shared - Kstorage <0 to 200>
4 4 4 4

Shared - KT_sand <0.01 to 3>
1.65 1.65 1.65 1.65

Shared - Lag <0 to 1E4>
0 0 0 0

Shared - LAI <0.1 to 20>
2.2 2.2 2.2 2.2

Shared - lapse_rate <0 to 2>
0.75 0.75 0.75 0.75

Shared - max_h2o_vol <0 to 0.2>
0.01 0.01 0.01 0.01

Shared - max_z_s_0 <0 to 0.35>
0.1 0.1 0.1 0.1

Shared - N_S <1 to 500>
320 320 320 320

Shared - obs_elev <0 to 1E5>
2450 2450 2450 2450

Shared - order <1 to 1000>
1 2 3 4

Shared - ppt_daily_distrib <0 to
1>
1 1 1 1

Shared - rain_soil_snow <0 to 1>
0 0 0 0

Shared - rechr_ssr_K <0 to 100>
0 0 0 0

Shared - relative_hts <0 to 1>
0 0 0 0

Shared - runKstorage <0 to 200>
0 0 0 0

Shared - runLag <0 to 1E4>
0 0 0 0

Shared - RUN_END <0 to 1E5>
0

Shared - RUN_ID <-1E8 to 1E8>
1

Shared - RUN_START <0 to 1E5>
0
```

```
Shared - S0 <0 to 1>
1 1 1 1

Shared - Sbar <0 to 100>
6.6 6.6 6.6 6.6

Shared - Sdinit <0 to 1000>
0 0 0 0

Shared - Sdmax <0 to 1000>
0 0 0 0

Shared - Sd_ByPass <0 to 1>
0 0 0 0

Shared - Sd_gw_K <0 to 100>
5 5 5 5

Shared - Sd_ssr_K <0 to 100>
0 0 0 0

Shared - Si <0 to 1>
0.6 0.6 0.6 0.6

Shared - smin <0 to 20>
10 10 10 10

Shared - soil_gw_K <0 to 100>
5 5 5 5

Shared - soil_moist_init <0 to
2500>
75 75 75 75

Shared - soil_moist_max <0 to
5000>
100 100 100 100

Shared - soil_rechr_ByPass <0 to
1>
0 0 0 0

Shared - soil_rechr_init <0 to
250>
75 75 75 75

Shared - soil_rechr_max <0 to
250>
75 75 75 75

Shared - soil_ssr_runoff <0 to 1>
1 1 1 1

Shared - soil_withdrawal <1 to 4>
3 3 3 3

Shared - ssrKstorage <0 to 200>
0 0 0 0

Shared - ssrLag <0 to 1E4>
0 0 0 0

Shared - t0 <0 to 1000>
715.3 781.3 808.5 897.5

Shared - texture <1 to 4>
1 1 1 1

Shared - Time_Offset <-12 to 12>
0 0 0 0

Shared - tmax_allrain <-10 to 10>
1 1 1 1

Shared - tmax_allsnow <-10 to 10>
0 0 0 0

Shared - transp_limited <0 to 1>
0 0 0 0

Shared - t_ice_lens <-50 to 0>
-20 -20 -20 -20

Shared - unload_t <-10 to 20>
1 1 1 1

Shared - unload_t_water <-10 to
20>
4 4 4 4

Shared - whereto <0 to 1000>
0 0 0 0

Shared - Z0snow <0.0001 to 0.01>
0.01 0.01 0.01 0.01

Shared - Zref <0.01 to 100>
1.5 1.5 1.5 1.5

Shared - Zvent <0 to 1>
0.75 0.75 0.75 0.75

Shared - Zwind <0.01 to 100>
10 10 10 10

Shared - z_0 <0.0001 to 0.1>
0.001 0.001 0.001 0.001

Shared - z_g <0.1 to 1>
0.1 0.1 0.1 0.1

Shared - z_T <0 to 10>
1 1 1 1

Shared - z_u <0 to 10>
10 10 10 10

First_GrpA - basin_name
'N-facing'

First_GrpA - hru_area <1E-6 to
1E9>
0.074 0.061 0.067 0.03

First_GrpA - HRU_group <1 to
1000>
1 0 0 0
```

```
First_GrpB - basin_name
'S-facing'

First_GrpB - hru_area <1E-6 to
1E9>
0.155 0.129 0.092 0.028

First_GrpB - hru_ASL <0 to 360>
155 155 155 155

First_GrpB - HRU_group <1 to
1000>
2 0 0 0

First_GrpB - hru_GSL <0 to 90>
26.5 26.5 26.5 26.5

First_GrpB - soil_moist_init <0
to 2500>
150 150 150 150

First_GrpB - soil_moist_max <0 to
5000>
200 200 200 200

First_GrpB - soil_rechr_init <0
to 250>
150 150 150 150

First_GrpB - soil_rechr_max <0 to
250>
150 150 150 150

First_GrpC - basin_name
'E-facing'

First_GrpC - hru_area <1E-6 to
1E9>
0.044 0.071 0.087 0.039

First_GrpC - hru_ASL <0 to 360>
76 76 76 76

First_GrpC - HRU_group <1 to
1000>
3 0 0 0

First_GrpC - hru_GSL <0 to 90>
33 33 33 33

First_GrpD - basin_name
'Valley_bottom'

First_GrpD - hru_area <1E-6 to
1E9>
0.006 0.015 0.03 0.02

First_GrpD - hru_ASL <0 to 360>
0 0 0 0

First_GrpD - HRU_group <1 to
1000>
4 0 0 0

First_GrpD - hru_GSL <0 to 90>
0 0 0 0

First_GrpD - soil_moist_init <0
to 2500>
150 150 150 150

First_GrpD - soil_moist_max <0 to
5000>
200 200 200 200

First_GrpD - soil_rechr_init <0
to 250>
150 150 150 150

First_GrpD - soil_rechr_max <0 to
250>
150 150 150 150

First_GrpE - basin_name
'N-facing_forest'

First_GrpE - CanopyClearing <0 to
1>
0 0 0 0

First_GrpE - groundcover <1 to 6>
6 6 6 6

First_GrpE - hru_area <1E-6 to
1E9>
0.001 0.019 0.031 0.013

First_GrpE - HRU_group <1 to
1000>
5 0 0 0

First_GrpE - Ht <0.001 to 100>
5 5 5 5

First_GrpE - LAI <0.1 to 20>
0.91 0.91 0.91 0.91

First_GrpE - soil_moist_init <0
to 2500>
187 187 187 187

First_GrpE - soil_moist_max <0 to
5000>
250 250 250 250

First_GrpE - soil_rechr_init <0
to 250>
187 187 187 187

First_GrpE - soil_rechr_max <0 to
250>
187 187 187 187

First_GrpF - basin_name
'S-facing_forest'
```

```
First_GrpF - CanopyClearing <0 to
1>
0 0 0 0

First_GrpF - groundcover <1 to 6>
6 6 6 6

First_GrpF - hru_area <1E-6 to
1E9>
0.0001 0.032 0.1 0.068

First_GrpF - hru_ASL <0 to 360>
155 155 155 155

First_GrpF - HRU_group <1 to
1000>
6 0 0 0

First_GrpF - hru_GSL <0 to 90>
26.5 26.5 26.5 26.5

First_GrpF - Ht <0.001 to 100>
5 5 5 5

First_GrpF - LAI <0.1 to 20>
0.91 0.91 0.91 0.91

First_GrpF - soil_moist_init <0
to 2500>
187 187 187 187

First_GrpF - soil_moist_max <0 to
5000>
250 250 250 250

First_GrpF - soil_rechr_init <0
to 250>
187 187 187 187

First_GrpF - soil_rechr_max <0 to
250>
187 187 187 187

REW_Grp - Channel_shp <0 to 2>
0 0 0 0 0 0

REW_Grp - HRU_group <1 to 1000>
7 0 0 0 0 0

REW_Grp - HRU_nhru <1 to 1000>
6 0 0 0 0 0

REW_Grp - RB_area <1E-6 to 1E9>
1 1 1 1 1 1

REW_Grp - route_L <0.01 to 1E10>
3.69 3.69 3.69 3.69 3.69 3.69

REW_Grp - route_n <0.016 to 0.2>
0.025 0.025 0.025 0.025 0.025
0.025

REW_Grp - route_R <0.01 to 1E4>
0.5 0.5 0.5 0.5 0.5 0.5

REW_Grp - route_S0 <1E-6 to 1>
0.001 0.001 0.001 0.001 0.001
0.001

REW_Grp - watershed_area <1E-6 to
1E9>
6

REW_Grp - WS_gwLag <0 to 1E4>
0 0 0 0 0 0

REW_Grp - WS_gworder <1 to 1000>
1 2 3 4 5 6

REW_Grp - WS_gwwhereto <0 to
1000>
0 0 0 0 0 0

REW_Grp - WS_gwX_M <0 to 0.5>
0.25 0.25 0.25 0.25 0.25 0.25

REW_Grp - WS_Lag <0 to 1E4>
0 0 0 0 0 0

REW_Grp - WS_order <1 to 1000>
1 2 3 4 5 6

REW_Grp - WS_whereto <0 to 1000>
0 0 0 0 0 0

REW_Grp - WS_X_M <0 to 0.5>
0.25 0.25 0.25 0.25 0.25 0.25


INITIAL STATE:

C:\CRHM_062410_TB\Projects_Feb_20
11\2009_May-1(dist_Feb26-11).int

FINAL STATE:
```